Dissertation

submitted to the
Combined Faculty of Natural Sciences and Mathematics
at the Ruprecht-Karls University of Heidelberg,
Germany
for the degree of
Doctor of Natural Sciences (Dr. rer. nat.)

Presented by
Dipl.-Chem. Maximilian Paul Hanke
Born in Heidelberg, Germany

Oral examination: November 7th, 2014

HOW STEM CELLS ROLL:

A MICROFLUIDIC CHARACTERISATION OF THE CD44-HYALURONIC ACID INTERACTION AND ITS ROLE IN LEUKAEMIA

This dissertation was carried out at the

Department of Applied Physical Chemistry

University of Heidelberg

Referees:

Prof. Dr. Axel Rosenhahn

Prof. Dr. Joachim P. Spatz

ABSTRACT

Acute myeloid leukaemia is a malicious disease. Although the initial chemotherapeutic treatment often leads to a complete remission (a disappearance of all manifestations of disease), the effective survival rate is only (30-40) % over 4 years due to a high relapse rate. This relapse is attributed to leukaemic stem cells residing in the protective environment of the bone marrow niche. There are two major approaches aiming at achieving better long-term therapeutic results. The first is to make the leukaemic stem cells more susceptible to chemotherapeutic agents and the second is to increase the efficiency of haematopoietic stem cell transplants, which are used to regenerate the haematopoietic system after failure due to chemotherapy.

When searching for a receptor-ligand pair suitable as target for therapeutic agents, the prerequisite is that it must exhibit differences between the interaction it mediates in healthy and leukaemic cells. A detailed understanding of the mediated interaction and the differences would then allow exploitation of these to selectively mobilise the leukaemic stem cells increasing their susceptibility for chemotherapeutic drugs. In this work the flow-induced rolling interaction of leukaemic cells with hyaluronic acid was studied in detail using a suspension and an epithelial model cell line. It could be demonstrated, that the flow induced rolling interaction on hyaluronic acid observed for these cells was solely mediated by the cell surface receptor CD44 and that it was independent of the cell type tested. Next to a detailed validation and characterisation of this dependency and the properties of the interaction, the relevance of this interaction for the haematopoietic system and for leukaemic cells was evaluated. Therefore, the CD44 mediated interaction with hyaluronic acid of healthy haematopoietic progenitor cells from umbilical cord blood, mobilised peripheral blood and the bone marrow with that of leukaemic blasts was compared. Throughout the cell types tested two forms of interaction with hyaluronic acid were observed; a flow induced rolling and an immobile adhesion. It could be shown that while the rolling interaction was comparable for all cell types tested, the immobile adhesion to hyaluronic acid and its susceptibility to a monoclonal CD44 antibody (clone BU52) were not. The immobile adhesion was found predominantly in leukaemic cells, only playing a subordinate role in the interaction of healthy cells with hyaluronic acid. It could be demonstrated that a vicinity of the cells to the bone marrow upon isolation was directly correlated to an incomplete suppression of the immobile adhesion by BU52. Furthermore, this incomplete suppression could be linked to a non-response to induction chemotherapy and subsequently to a poor

therapeutic outcome. Besides investigating the interaction with surfaces artificially coated with hyaluronic acid, the possibility of using surfaces covered with mesenchymal stromal cells isolated from the bone marrow as more realistic binding partners was explored. Furthermore, the effect of a routinely used mobilisation reagent, namely Plerixafor®, on the migration and cell-surface interaction under flow was investigated. It is not only of great interest to understand the mechanisms of retention in the niche, but also to develop more sophisticated methods of *in vitro* stem cell expansion. In this context the slow and continuous release of *e.g.* cytokines or growth factors is of great interest. The cavities in porous materials present the unique opportunity of achieving just that by being pre-loaded with such agents. These can then under the right conditions be released to the cells. Amongst the porous materials the metal-organic frameworks protrude due to their high structural and chemical flexibility. In this work a novel 2-D metal-organic framework structure, namely SURMOF 2, was tested towards its biocompatibility and smart-release properties. It could be shown that SURMOF 2 was highly stable in protein free aqueous media and that its building units did not impair the growth of rat embryonic fibroblasts. Although the stability in cell culture medium is still limited, the water stability and the biocompatibility of the components are the starting point for future SURMOF 2 cell culture applications. A first application of SURMOF 2 as a smart-release matrix was achieved with the marine bacterium *Cobetia marina* under salt water conditions. The results demonstrated the general applicability of SURMOF 2 as bioactive substrates with responsive properties. For the future, fine-tuning of the stability of SURMOFs will allow to tailor drug release systems for cytokine or growth factor delivery in *in vitro* stem cell cultures.

KURZFASSUNG

Die akute myeloische Leukämie ist eine heimtückische Erkrankung. Obwohl die Induktionstherapie häufig zu einer kompletten Remission (der vollständige Wegfall aller Krankheitssymptome) führt, liegt die effektive Überlebenschance lediglich bei (30-40) % über einen Zeitraum von 4 Jahren. Dies geht auf eine hohe Rezidivrate zurück, welche auf die sogenannten leukämischen Stammzellen zurückgeführt wird. Diese leukämischen Stammzellen verweilen in der geschützten Umgebung der Knochenmarksnische. Es gibt zwei primäre Ansätze, die darauf abzielen bessere Langzeitresultate zu erreichen. Der eine ist es die leukämischen Stammzellen für Chemotherapeutika empfänglicher zu machen und der andere ist es die Effizienz der Transplantation gesunder hämatopoietischer Stammzellen zu verbessern. Diese Stammzelltransplantation dienen zur durch die Chemotherapie notwendigen Regeneration des hämatopoietischen Systems.

Wenn man ein Rezeptor-Liganden-Paar sucht, welches das Ziel therapeutischer Agenzien sein kann, ist die Grundvoraussetzung, dass es Unterschiede zwischen der Wechselwirkung aufweist, die es in gesunden und leukämischen Zellen mediiert. Ein genaues Verständnis der Wechselwirkung und der Unterschiede würde es dann ermöglichen diese auszunutzen um gezielt die leukämischen Stammzellen zu mobilisieren. Dies würde dann ihre Empfänglichkeit für chemotherapeutische Agenzien erhöhen. In dieser Arbeit wurde das flussinduzierte Rollen leukämischer Zellen auf Hyaluronsäure mit Hilfe einer Suspensions- und einer Epithelzelllinie *en détail* untersucht. Es konnte gezeigt werden, dass das flussinduzierte Rollen dieser Zellen auf Hyaluronsäure allein von CD44 mediiert wurde und dass es unabhängig von dem Zelltyp war bei dem es auftrat. Nebst einer sicheren Validierung dieser Abhängigkeit und einer Charakterisierung der Wechselwirkungseigenschaften wurde die Relevanz dieser Wechselwirkung für das hämatopoietische System und für leukämische Zellen untersucht. Dies wurde erreicht indem die CD44 mediierte Wechselwirkung gesunder hämatopoietischer Progenitorzellen aus Nabelschnurblut, mobilisiertem Peripherblut und dem Knochenmark mit Hyaluronsäure mit der leukämischer Blasten verglichen wurde. In allen getesteten Zelltypen konnten zwei Formen der Wechselwirkung mit Hyaluronsäure beobachtet werden; ein flussinduziertes Rollen und eine unbewegliche Adhäsion. Es konnte gezeigt werden, dass das Rollverhalten aller untersuchten Zelltypen vergleichbar war. Dies was für die unbewegliche Adhäsion und deren Empfänglichkeit für die Unterdrückung durch einen monoklonalen CD44 Antikörper (Klon BU52) nicht der Fall. Diese unbewegliche Adhäsion wurde vor allem in leukämischen Zellen beobachten. Für die Wechselwirkung gesunder

Zellen mit Hyaluronsäure spielte sie lediglich eine untergeordnete Rolle. Es konnte gezeigt werden, dass eine Nähe zum Knochenmark bei der Gewinnung der Zellen, direkt mit einer Unvollständigen Unterdrückung der unbeweglichen Adhäsion durch BU52 korrelierte. Des Weiteren, korrelierte die Resistenz gegen BU52 mit einem Misserfolg der Induktionstherapie und somit mit einem schlechten langfristigen klinischen Verlauf. Im Folgenden wurden erste Tests durchgeführt, die die Erweiterung der Analyse von künstlichen mit Hyaluronsäure beschichteten Oberflächen hin zu mit aus der Knochenmarksnische isolierten mesenchymalen Stammzellen bedeckten Oberflächen zum Ziel hatten. Zudem wurde der Einfluss des vielfach verwendeten Mobilisierungsreagenzes Plerixafor® auf die Migration und auf die Zell-Oberflächen Interaktion unter Fluss untersucht. Es ist nicht nur von großer Wichtigkeit die Mechanismen der Retention der Zellen in der Nische zu verstehen, sondern auch hochentwickelte Methoden zur *in vitro* Stammzellkultivierung zu entwickeln. In diesem Zusammenhang ist die langsame und kontinuierliche Freisetzung von beispielsweise Zytokinen oder Wachstumsfaktoren von großem Interesse. Die Hohlräume in porösen Materialien bieten die einzigartige Möglichkeit genau das zu erreichen indem sie vorab mit solchen Agenzien beladen werden. Diese können dann unter den richtigen Bedingungen an die Zellen abgegeben werden. Unter den porösen Materialien stechen die metall-organischen Gerüststrukturen durch ihre hohe strukturelle und chemische Flexibilität hervor. In dieser Arbeit wurde die neuartige 2-D metall-organische Gerüststruktur „SURMOF 2“ in Bezug auf ihre Biokompatibilität und *Smart-Release* Eigenschaften hin untersucht. Es konnte gezeigt werden, dass SURMOF 2 in proteinfreien wässrigen Medien äußerst stabil ist und dass die Bausteine das Wachstum von Fibroblasten in keiner Weise beeinträchtigt. Obwohl die Stabilität in Zellkulturmedium noch beschränkt war, waren die Wasserstabilität und die Biokompatibilität der Bausteine ein erster Schritt in Richtung der Applikation von SURMOF 2 in der Zellkultur. SURMOF 2 konnte jedoch nichtsdestotrotz bereits in Salzwasser mit dem marinen Bakterium *Cobetia marina* als *Smart-Release* Oberfläche zum Einsatz gebracht werden. Die Beobachtungen demonstrierten die generelle Anwendbarkeit von SURMOF 2 als bioaktives Substrat mit reaktiven Eigenschaften. In Zukunft wird das Feintuning der Stabilität von SURMOF 2 es erlauben gezielt *Drug-Release*-Oberflächen für die Zytokin- oder Wachstumsfaktorfreisetzung in der *in vitro* Stammzellkultivierung zu designen.

TABLE OF CONTENTS

1 INTRODUCTION

Acute myeloid leukaemia (AML) is the most common form of acute leukaemia in adults. The Swedish Acute Leukemia Registry lists 98 % of all patients diagnosed with AML between 1997 and 2005 in Sweden. Analysis of the data collected in this registry showed that approximately 15 new cases were diagnosed annually per 100,000 citizens under the age of 60. This value drastically increased with age reaching over 120 new diagnoses annually per 100,000 citizens between the age of 80 and 84. The median age of first diagnosis was 72.[1] This demonstrates the threat posed by this disease, especially for the elderly. While most patients treated for AML reach complete remission (CR) after initial chemotherapy, the relapse rate is high and the overall survival rate is only 30-40 % over 4 years. The general consent is that leukaemic cells are generated by stem cells, similar to healthy blood cells in haematopoiesis.[2-3] These leukaemic stem cells (LSC) are thought to share the haematopoietic stem cells (HSC) capability of self-renewal, their vicinity to the bone marrow (BM) niche and most inconveniently their chemotherapy resistance.[4] The proposed interactions of LSC with their niche are schematically depicted in Figure 1.

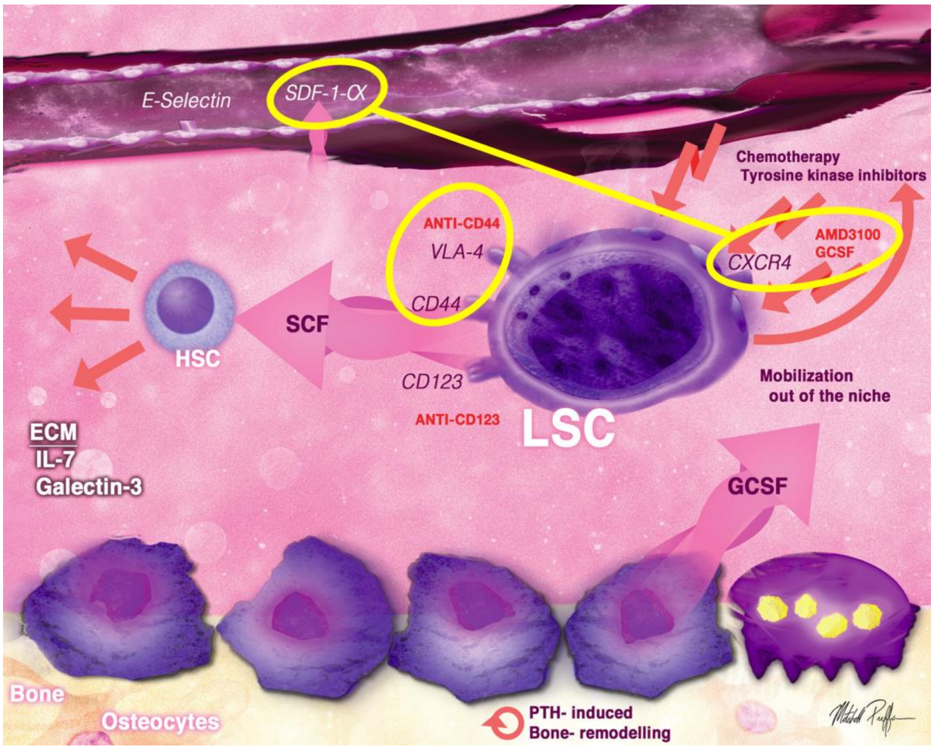

Figure 1: Schematic depicting the microanatomy of the leukemic stem cell niche and strategies to target the LSC in its niche. Strategies include the blocking of cytokines or adhesion molecules like CD44 or integrins, the mobilisation of LSCs out of their niche by GCS-F or AMD3100. Image taken from [5]. The interactions with the niche targeted in this work are marked in yellow.

The sketch also presents some strategies applicable when aiming at increasing the efficiency of the apoptosis induction in LSC by cytostatic and/or chemotherapeutic agents. Some of the targets studied in this work are marked in yellow. Thus far targeting of adhesion molecules, *e.g.* CD44 or integrins, could reduce the interaction of LSC with their niche[6-7] or the adhesion to fibronectin in the BM microenvironment,[8] respectively. Furthermore, the necessity of CD44 for the homing and engraftment of healthy haematopoietic progenitor cells (HPC) to the BM niche could be established.[9] Due to the apparent relevance of CD44 in this context the interaction of this receptor with its major ligand hyaluronic acid (HA) was the main focus of this work. The capability of leukaemic cells and HPC from umbilical cord blood expressing CD44 to exhibit a catch-bond like, flow-induced rolling interaction with HA under flow conditions was recently demonstrated in our workgroup.[10] A microfluidic shear force setup, developed by C. Christophis in our workgroup,[11-12] was applied to characterise this interaction. During the initial characterisation phase the general dependency of this form of interaction with HA on CD44 was verified and the properties of the CD44-HA interaction, such as the rolling velocity and its dependency on the availability of the receptor, were illuminated. Furthermore, it was determined whether this form of interaction is specific for suspension cells, such as HPC, or whether it can also be found in other CD44 expressing cells, such as epithelial liver cancer cells. Following the determination of the similarities and differences between these two fundamentally unalike cell types, a comparison was made between the CD44-HA interaction of HPC from different sources and leukaemic blasts (as surrogates for LSC as blasts can be acquired in larger quantities than LSC). In this context the interaction of HPC from umbilical cord blood, mobilised peripheral blood and the bone marrow was compared to that of leukaemic blasts isolated either from the peripheral blood or the BM. The aim was to identify differences that may in the future be targeted for the specific mobilisation of LSC from the niche. This would allow the application of milder chemotherapeutic agents, sparing the HSC, while still inducing apoptosis in the LSC and thereby preventing relapse of the leukaemia.

The BM niche, in which HSC and/or LSC dwell, is comprised of a variety of cells. All of these, less the HSC, can be derived from mesenchymal stromal cells (MSC).[13-14] For this reason MSC are widely used as model system for the BM niche. In the context of studying the CD44-HA interaction, MSC feeder layers were used instead of artificial HA-coated substrates. The aim was to establish a protocol for the growth and measurement procedure on MSC feeder layers and to investigate whether a similar interaction could be observed on MSC as it could on artificially coated HA surfaces.

The chemokine stem cell derived factor 1 alpha (SDF-1α) is secreted by MSC in the BM niche.[15] This chemokine and its receptor are reported to play a major role in the induction of chemotaxis in HPC[16-18] and in the process of homing of HSC to the BM niche.[19] Furthermore, as indicated in Figure 1, mobilisation of the LSC with granulocyte-colony stimulating factor (G-CSF)[20-22] or AMD3100 (also known as Plerixafor®), which antagonises SDF-1α,[23] has also proven promising in increasing chemotherapeutic success. First tests concerning the effect of Plerixafor® and SDF-1α on the migration of HPC and on the CD44-HA interaction were conducted in this study.

The haematopoietic stem cell transplantation (HSCT) is commonly applied in the treatment of patients with BM failure states often originating from high dosage chemotherapy. To achieve maximal tumour-kill efficiency higher doses of chemotherapeutic agents are applied and the haematopoietic organ is rescued by HSCT.[24] Today, over 350 centres in Europe perform a total of more than 18,000 HSCT per year.[25] One has to distinguish between autologous transplantations, which employ a patient's own BM tissue, and allogeneic transplantations, which are conducted between two genetically different individuals (with the rare exceptions of transplantations between identical twins; often referred to as syngeneic transplantations).[26] The possibility of conducting HSCT is often limited by the availability of a donor and by the amount of HSC in the graft, which is important to ensure successful engraftment.[27-28] To increase the amount of available HSC, it has often been attempted to culture HSC *in vitro*. Some studies could demonstrate modest, transient expansion of long-term repopulating HSC *in vitro* in response to particular cytokines. However, in most cases the *in vitro* proliferation of HSC led to differentiation or apoptosis.[29-34] Ideally the proliferation inducing cytokines should be added continuously, as would be the case *in vivo*. A possibility of doing so would be the application of porous materials such as *e.g.* zeolites or porous silicon. Due to the possibility of storing small molecules in their pores, these materials have often been applied in areas such as catalysis, sensors and gas filtering or storage.[35-42] Just this capability of storing small molecules could be the key to a continuous release of proliferation inducing cytokines during culture. Providing the pore size is sufficient, the cytokines would need to be loaded into the pores and then either a continuous release of the same or a slow degradation of the host structure, also slowly releasing the incorporated cytokines, would need to be induced. A class of porous materials which is highly flexible in its structural and chemical properties are the metal-organic frameworks.[43-45] In this study the first analysis of a novel 2-D surface bound metal-organic framework (SURMOF) structure, namely SURMOF 2, was conducted investigating the stability in aqueous media and the biocompatibility of the building units. Application a as smart-release surface that responds to the presence of bacteria under marine conditions demonstrated the potential of SURMOFs as bioactive surfaces for *in vitro* culture of HSC in the future.

2 THEORETICAL BACKGROUND

In this chapter the theoretical background relevant to this work is discussed. The roles of the haematopoietic stem cell and its niche as well as the question of what happens when haematopoiesis fails and an illness such as leukaemia arises are examined. The cell surface receptor CD44 is known to be involved in the homing and engraftment of both healthy haematopoietic and leukaemic stem cells. Therefore, the interaction mediated by this receptor is reviewed and in this context the mechanism of cellular rolling on surfaces as possibility for extravasation from the blood stream is discussed. Finally, possibilities to measure and analyse this interaction *in vitro* are presented and a class surface coatings, namely the surface bound metal-organic frameworks, which may find application in cell culture someday, are introduced.

2.1 HAEMATOPOIESIS, HAEMATOPOIETIC STEM CELLS AND THEIR NICHE

Blood is a highly complex bodily fluid composed of the blood plasma and blood cells. The plasma, which is mostly water, carries both nutrients such as proteins, glucose or minerals and the blood cells. The blood cells in turn are composed of myeloid cells, *e.g.* erythrocytes, granulocytes and macrophages, and lymphoid cells, *e.g.* T-lymphocytes, B-lymphocytes and natural killer cells. In a healthy adult human being each cubic millilitre of blood contains approximately (4-6) million cells that circulate in the blood stream for up to 120 days.[46] This limited cell life span makes it obvious that new cells must be produced continuously. This mammoth task is shouldered by a set of immature HSC located in the BM after birth.[47] The most striking characteristics of these HSC are the capability of self-renewal and the ability to differentiate into cells of multiple linages as schematically shown in Figure 2.[48-51] The differentiation is undergone in steps. The HSC develop from multi-potent progenitors (MPP also known and from here on referred to as haematopoietic progenitor cells HPC), which still possess the capability of self-renewal, over common myeloid progenitors (CMP) or common lymphoid progenitors (CLP) and a couple of further differentiation grades to the respective fully developed cell.[26,51] That this system is highly effective, can easily be seen from the fact that (2-3) million red blood cells alone are released into the blood stream from the BM every second in order to maintain steady state levels in the peripheral circulation.[46]

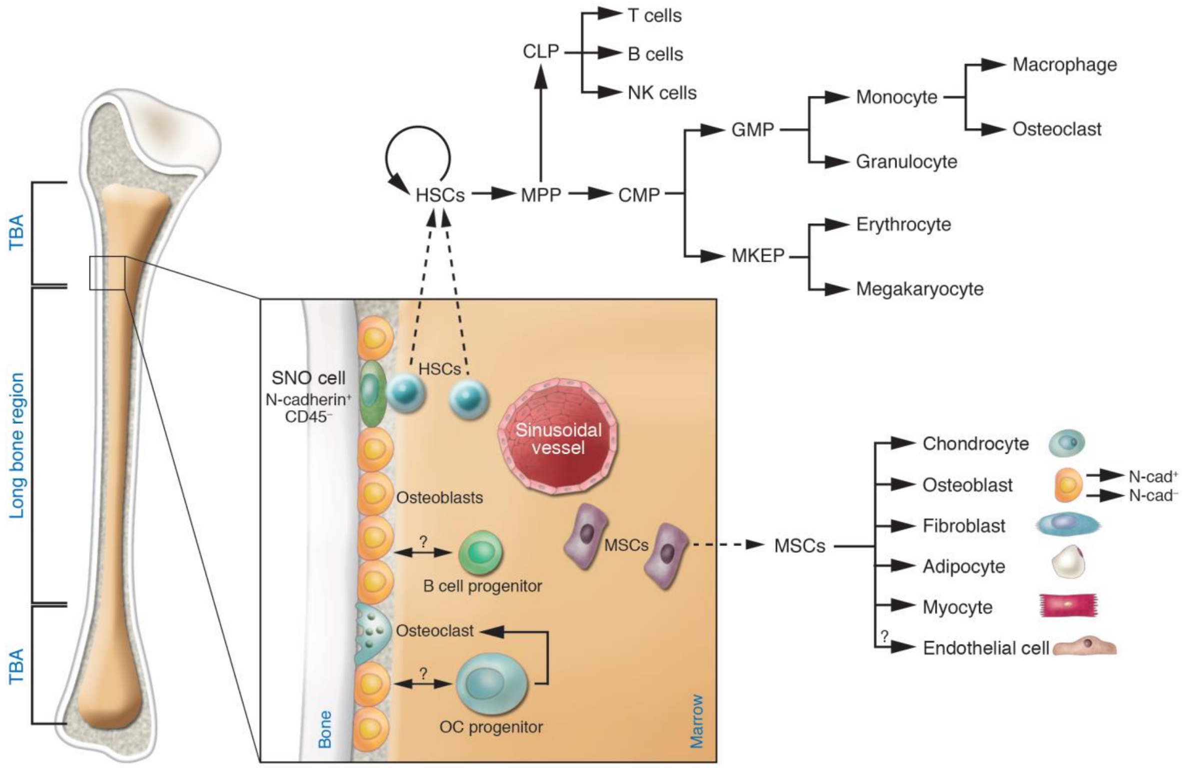

Figure 2: Haematopoiesis of bone cells and marrow stromal cells. Each differentiation of an HSC results in one daughter cell that leaves the marrow and differentiates and one that remains in the niche. The first daughter cell then differentiates via a multipotent progenitor (MPP) into various linages. In the marrow the HSC are surrounded by osteoblasts, endothelial cells and mesenchymal stromal cells (MSC). The differentiation scheme of the MSC is also depicted. Abbreviations used in this scheme: common myeloid progenitor (CMP); common lymphoid progenitor (CLP); granulocyte/macrophage progenitor (GMP); megakaryocyte erythroid progenitor (MKEP); multipotent progenitor stem cell (MPP); osteoclast progenitor (OC); spindle-shaped N-cadherin$^+$CD45$^-$ osteoblastic cell (SNO cell); trabecular bone area (TBA). Image taken from Yin *et al.*, 2006.[51]

The capability of HSC to self-renewal is the key to the constant cell division required for the generation of the vast amount of cells necessary to replenish the blood stream. The ability of HSC to an asymmetric division,[52] in turn, makes this continuous self-renewal possible. While one daughter cell remains a HSC populating the niche the other daughter cell undergoes further differentiation.[53] So far it is not fully understood what exactly governs the mechanism of self-renewal and differentiation. The importance of such a mechanism is clear, however, as the stem cell population would deplete in the case of cell differentiation overwhelming self-renewal. Similarly, unchecked self-renewal would lead to an increased risk of tumourigenesis.[51,54] The idea of a stem cell niche as a confined microenvironment in the BM was first described by Schofield in 1978.[55] This stem cell niche is thought to provide the conditions to control proliferation and differentiation of HSC. It could be demonstrated that a vicinity of HSC to a stem cell supporting microenvironment could induce asymmetric differentiation.[56-57] This could not be induced by cytokines alone[58] and thus demonstrates the relevance of the stem cell niche for the longevity of the HSC. If HSC are separated from the BM niche, *e.g.* by endogenous mobilisation,[59-60] induced mobilisation,[61] or after being transplanted[62] they migrate back to the BM niche. This process is known as 'homing'. Figure 3 shows the major steps involved in HSC homing. Similar to the homing of leukocytes to sites of inflammation (discussed in section 2.3),[63-67] homing of HSC to the BM niche involves tethering and rolling on the endothelium, then sticking and subsequent transmigration through the endothelium.

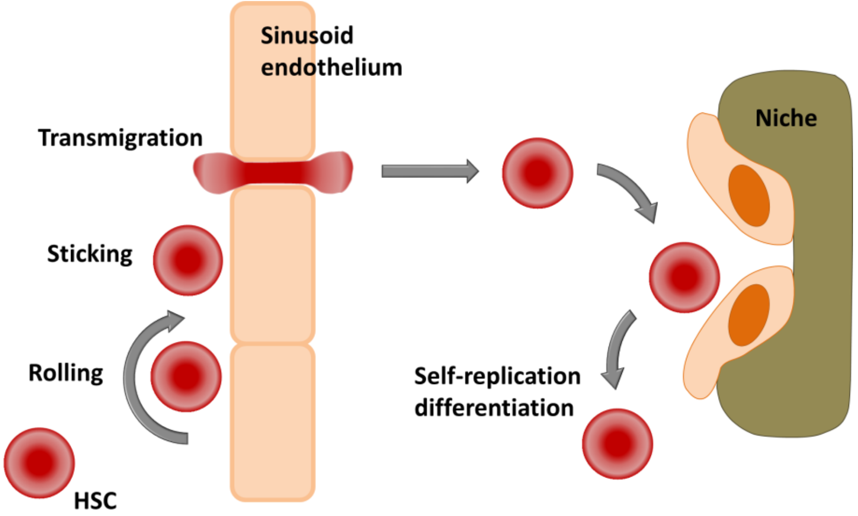

Figure 3: Schematic outlining the major steps in HSC homing. The process of HSC homing involves rolling on the endothelium, sticking and transmigration before the HSC migrates to the niche where it is capable of self-renewal and asymmetric division. Image inspired by Barrett *et al.*, 2008.[68]

In the context of homing it was shown that the cytokine stem-cell-derived factor-1 alpha (SDF-1α or C-X-C motif ligand 12; CXCL12) is essential for the process, as HSC home towards an SDF-1α gradient.[9,16,69-70] This is produced by a type of cells found in abundance in the BM niche; the mesenchymal stromal cells (MSC). In fact, MSC can differentiate into all cell types less the HSC found in the niche (indicated in Figure 2).[14,71] It was shown that MSC could fully re-establish the BM microenvironment in irradiated mice.[72] Considering the abundance of MSC in the BM niche, it is not surprising that they play a significant role for maintaining the self-renewal potential of HSC/HPC.[73-75] MSC are defined as plastic adherent under standard culture conditions. Furthermore, they must present the antigens CD73, CD90 and CD105 and lack haematopoietic antigens (CD45, CD34, CD14 or CD11b, CD79alpha or CD19 and HLA-DR surface molecules) and they must be capable of differentiating into osteoblasts, adipocytes and chondroblasts under *in vitro* conditions.[76-77] The mechanisms of interaction of HSC with the niche are vast. They range from cell-cell interactions, over interactions with the extracellular matrix (ECM) to the recognition of soluble factors.[78] Figure 4 shows an overview over some of the possible interactions between HSC and MSC, the ECM and some soluble factors expressed by MSC.[27]

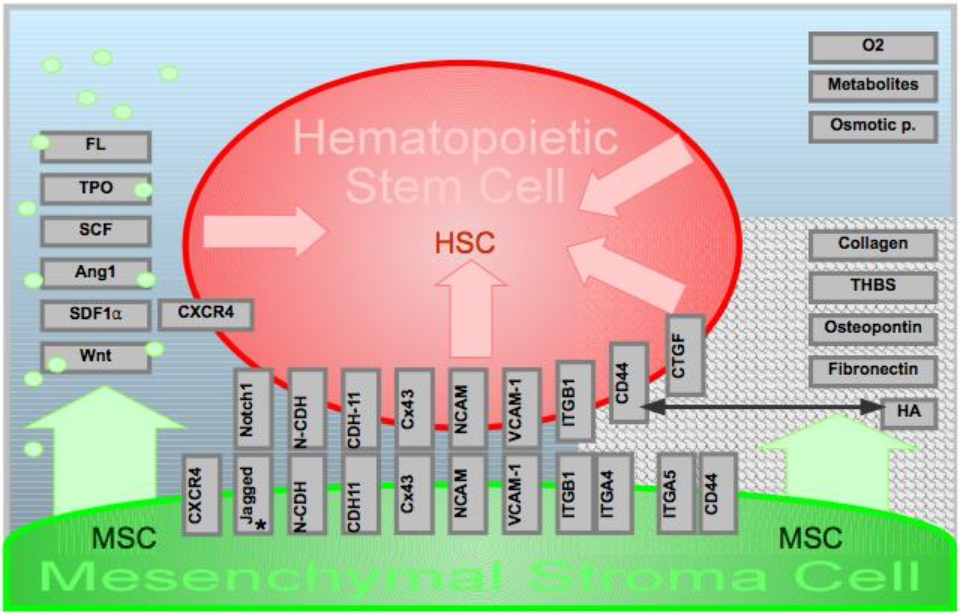

Figure 4: Interactions between HSC and their surrounding microenvironment. Interaction with the HSC takes place via soluble factors, cell-cell interactions, extracellular matrix components and metabolites and oxygen tension. The interaction between the receptor CD44 and HA is of special interest for this study and is therefore highlighted. Image taken from Wagner *et al.*, 2008.[27]

2.2 ACUTE MYELOID LEUKAEMIA

Leukaemia is a carcinoma of the blood. It has been suggested that leukaemia evolves when the proliferation of HSC, as described in the last section, is undergone in an uncontrolled manner by cells termed leukaemic stem cell (LSC). These cells originate from genetic (mutations of the DNA) and/or epigenetic (other heritable modifications) changes in HSC or progenitors. The undergone changes detach the LSC from the regulated haematopoietic system, thereby, enabling the uncontrolled proliferation of the cells, which in turn leads to the flooding of the BM niche and later the circulatory system with immature cells.[79-84] Figure 5 demonstrates the progression of leukaemia from healthy HSC to leukaemic blasts. With each cellular mutation the rate of proliferation can be increased. At some point the transformed cells no longer differentiate into mature cells, but rather remain at a very primitive level often even with the capability of self-renewal. These primitive blasts flood the haematopoietic system and interfere with normal haematopoiesis, resulting in anaemia, thrombocytopenia and neutropenia.

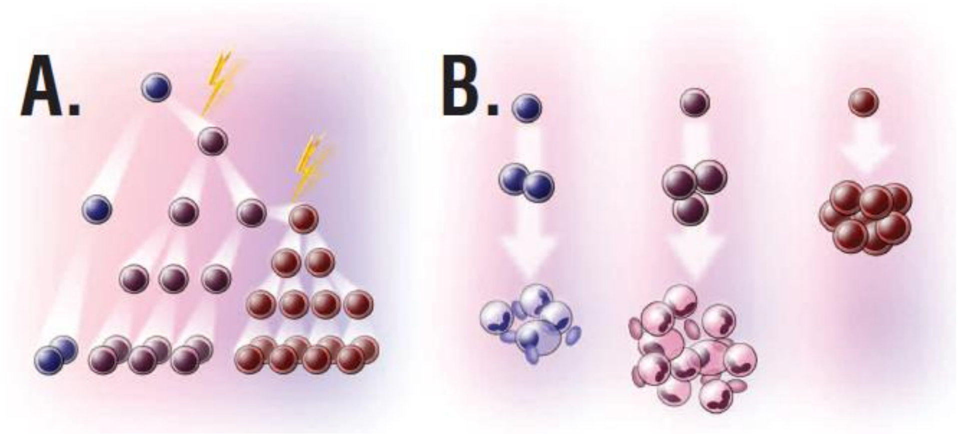

Figure 5: Leukaemic progression at the haematopoietic stem cell level. Proliferation of normal HSC yields 2 HSC, one of which undergoes differentiation. A) Preleukaemic progression of LSC development. Here two events are depicted. Each event (2 shown) leads to cells capable of outperforming healthy HSC in terms of proliferation. B) Proliferation of HSC leads to progenitors and mature cells (left). Partially transformed cells still yield progenitors and mature cells, but in far larger amounts (centre). In fully transformed cells the development of mature cells is blocked and large amounts of primitive blast cells are produced (right). These cells can be HSC-like or self-renewing transformed progenitors. Image taken from Yin *et al.*, 2006.[51]

Acute myeloid leukaemia (AML) is characterised by the uncontrolled production of myeloid blasts. Due to the many different differentiation stages in the myeloid differentiation pathway at each of which the leukaemic transformation can take place, AML is a highly heterogeneous disease. Though the predominant pathologic cell type is not the origin of the disease, different leukaemias are mostly classified by these cell types and/or the clinical course of the disease.[26] Two systems are widely used to classify the different AML. The French-American-British (FAB) system relies mainly on the final step of blast differentiation,[85-86] while the system of the World Health Organisation (WHO) takes cytogenetic and molecular factors into account that are known to impact the prognosis.[87-88]

Treatment of AML is undergone by induction chemotherapy (one to two intervals of intensive chemotherapy to achieve complete remission (CR)) followed by post-remission therapy (to sustain the results achieved during induction therapy). Generally treatment of AML with chemotherapy is highly effective and often results in CR. However, the relapse rate is also high, resulting in an overall survival rate of only (30-40) % over 4 years. The LSC are held responsible for this high relapse rate.[2-3] Lapidot *et al.* showed that $CD34^+/CD38^-$ cells (these are typical markers for HSC)[89-91] isolated from patients with AML could initiate AML in severe combined immunodeficiency (SCID) mice, thus, proving the relevance of these cells for the establishment of leukaemia in an organism. As these LSC share the vicinity to the niche and the chemotherapeutic resistance of the HSC,[4] high dosage chemotherapy is applied to achieve maximum tumour-kill efficiency. As this harms the whole haematopoietic system, it subsequently rescued by haematopoietic stem cell transplantation (HSCT).[24] This has been done since 1959.[26,92] For transplantation donor HSC are mobilised from the BM niche to the blood stream from where they can easily be isolated. In the clinical environment this is achieved by a treatment with Plerixafor® (syn.: AMD3100; 1,1-[1,4-phenylene-bis(methylene)]-bis-1,4,8,11-tetra-azacyclo-tetradecane).[93-95] Although the exact mechanism of the treatment with Plerixafor® is not yet fully understood,[96-97] it has been shown to block the CXCR4 receptor.[98] This is the receptor for the chemokine stem cell derived factor 1 alpha (SDF-1α), which is known to play a major role in the induction of chemotaxis in HPC[16-18] and in the process of homing of HSC to the BM niche.[19] Both are essential for the repopulation of the niche by HSC/HPC, *e.g.* after autologous or allogeneic HSCT.[99-101]

2.3 CELL ADHESION AND ROLLING

Cellular interactions are involved in a broad range of basic cell functions. Some of these are cell growth,[102] differentiation[103] and migration.[104] Furthermore, cell adhesion and changes of the same are involved in tissue development,[105] wound healing,[106] cancer metastasis[107] and the development of leukaemia.[108] The overall interaction of cells can be classified as firm adhesion and short-term adhesion.

Firm adhesion of cells is of great relevance for the connective tissue, wound healing, growth and immune defence processes. Cells express various receptors responsible for the binding to different substrates or cells. They may bind to other cells via *e.g.* tight junctions, desmosomes or adherence junctions or to the ECM via *e.g.* hemidesmosomes or focal contacts. The receptors involved in these binding patterns are selectins, integrins, cadherins or receptors from the immunoglobulin superfamily.[109-110]

In contrast to this firm, long-term adhesion stand methods of transient, short-term interactions, *e.g.* the rolling of cells over a surface such as the endothelium. For leukocytes, for example, rolling across endothelial cells in blood vessels is a key step in the extravasation process at sites of inflammation. Leukocyte rolling, adhesion and transmigration was described in the nineteenth century[111-112] and this selectin- and integrin-mediated extravasation has been extensively studied ever since.[63-67] A good overview is presented in the book ‘The selectins’.[113] A schematic overview of the steps of the extravasation process with the most important receptors and binding partners is given in Figure 6. Margination is the process of leukocytes moving away from the central blood stream towards the endothelium,[114] where the capture may take place. Upon inflammation, endothelial cells rapidly express P-selectin which can interact with the glycoprotein ligand 1 (PSGL-1) present on the surface of leukocytes.[115] Next to the mere presence of selectins and their ligands, threshold fluid shear forces of approximately

(0.4-0.5) dyn/cm² are required to promote the P-, E-, or L-selectin-mediated rolling of leukocytes on endothelial cells.[116-117] Beyond this value the number of rolling leukocytes increases with the shear stress until the optimum level is reached at shear stresses of approximately 1 dyn/cm². After surpassing this shear stress level the number of rolling cells was reported to then decrease with increasing shear stress.[118] These values correspond well with the wall shear stress found in postcapillary venules (approximately (1-4) dyn/cm²), where the extravasation of leukocytes mostly occurs.[119] L-selectin is supposed to play the most important role in capture and initiation of rolling. P-selectin is also reported to be involved in cellular capture, but its importance in this context is seemingly inferior to that of L-selectin. Only in the absence of L-selectin, the capture becomes P-selectin dependent.[120] The rolling velocity is greater though in this case, suggesting a weaker binding to L-selectin than to P-selectin.[113] The overall rolling velocity of leukocytes was found to be in the range of (20-40) µm/s under physiologic flow rates.[121] It was shown that this value is strongly dependent on the tissue with which the leukocytes interact. A span of (5-100) µm/s was observed for the rolling on different tissues.[113,122-126] Inflammatory endothelial cells also express E-selectin in response to the treatment with inflammatory cytokines. E-selectin participates in the conversion of rolling to firm adhesion. It binds to sialylated carbohydrates present in surface proteins of leukocytes and reduces the rolling velocity. This speed reduction is important for the leukocyte to firmly bind to the endothelium via integrins *e.g.* VLA-4, which binds to the receptor VCAM-1 present on the endothelial cells.[64]

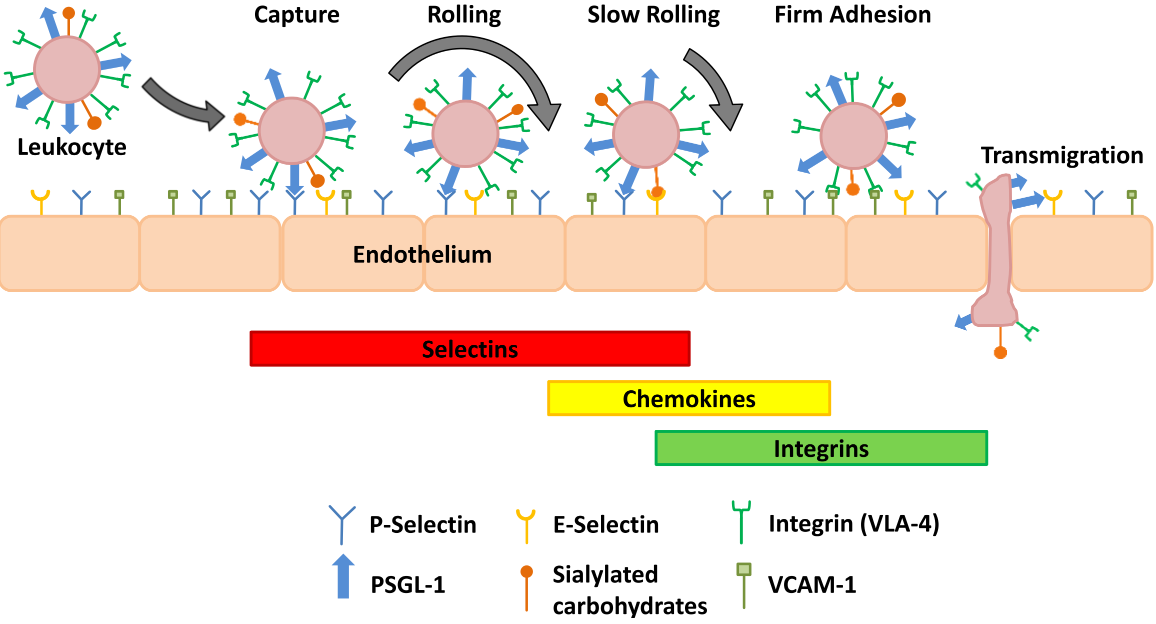

Figure 6: Leukocyte Extravasation. The process of leukocyte extravasation is mainly governed by the steps of cell capture, rolling, firm adhesion and transmigration of the cell through the endothelium. Image inspired by Ley *et al.*, 2007 and Albelda *et al.*, 1994.[64,115]

2.4 CELL SURFACE RECEPTOR CD44

However, not only the selectin family is capable of mediating a flow-induced interaction. It was shown that the transmembrane glycoprotein CD44 also mediates a flow-induced rolling interaction of cells on hyaluronic acid (HA). This could be demonstrated for the leukaemic suspension cell line KG-1a (Figure 7) on surfaces coated with HA in our workgroup by Christophis *et al.*.[10] It was shown that the flow induced interaction was only observed for the CD44 positive cell line KG-1a and only on HA. Furthermore, the characteristics of the rolling on HA were remarkably similar to those observed for the selectin mediated rolling of leukocytes discussed in section 2.3. For the CD44 positive cell line, flow induced rolling was observed beyond a threshold shear stress of approximately 0.2 dyn/cm², with the maximum fraction of interacting cells reached at a shear stress of roughly 1 dyn/cm².[10,12]

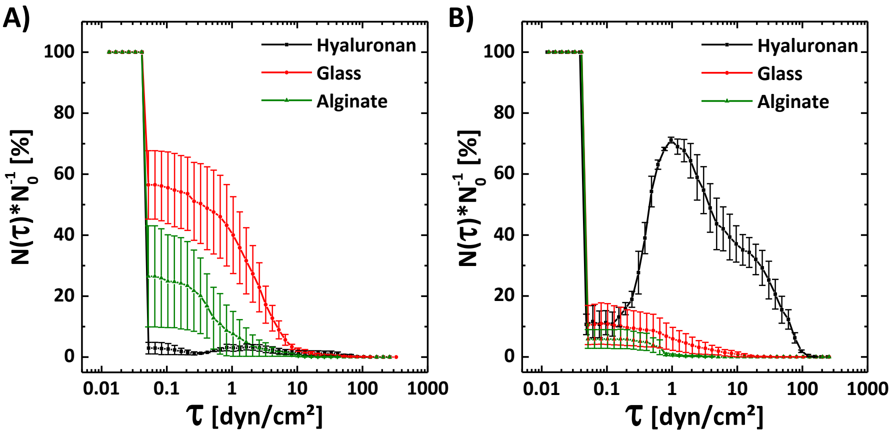

Figure 7: Interaction of CD44 negative and positive cells with different surfaces. The interaction of the CD44 negative leukaemic suspension cell line Jurkat (A) and of the CD44 positive leukaemic suspension cell line KG-1a (B) was analysed in the microfluidic setup also used in this study.[11-12] Only the KG-1a cells showed the flow induced interaction with HA and not with either of the control surfaces (alginate and glass). Image adapted from Christophis *et al.*, 2011.[10]

The cell surface receptor CD44, responsible for this interaction, is an integral membrane protein belonging to the link module superfamily.[127-128] It was first identified by Underhill and Toole.[129] CD44 mainly binds to HA,[130-132] but is also capable of recognising other binding partners,[133] such as collagen,[134] laminin,[134] fibronectin,[135] osteopontin[136] and itself.[137] As diverse as the binding partners of CD44 are, as diverse are its functions in the body. It has been reported to be involved in morphogenesis and organogenesis,[138-140] in haematopoiesis,[141-142] in migration,[143] in homing and proliferation of haematopoietic stem cells,[9,144-145] in cancer metastasis[146] and in the activation[141] and rolling[147] of leukocytes.

The structure of each receptor, as of every other protein generated in the body, is encoded in the genome. CD44 is encoded in a single gene containing 20 exons.[148] Alternative N- and O-glycosylation[149-155] as well as variability in the mRNA splicing lead to a variety of CD44variant isoforms. As shown in Figure 8 the standard isoform CD44s is composed of the first and last 5 exons (1-5 and 16-20, standard exon s1-10). This is not only the smallest but also the most common isoform. The remaining ten exons (6-15, variant exons v1-10) have the potential of being alternatively mRNA spliced during gene expression and added to the standard isoform as shown in Figure 9. This results in ten isoforms CD44v1-10.[148,156-158] Binding to HA is possible for all CD44variant isoforms, but it is strongest for CD44s.[159] The exact mode of interaction between the HA binding domain of CD44 and HA has been extensively studied by comparison to other HA binding sites, by NMR and by X-ray crystallography. HA is composed of repeating disaccharide units of N-acetyl-D-glucosamine and D-glucuronate, connected by β-1,4 and β-1,3 linkages. It was shown that at least three to five of these disaccharide units are required for binding to CD44, that the binding is dependent on the interaction of HA with arginine and tyrosine in the binding pocket and that the binding to HA induces a structural rearrangement in CD44.[160-164] These structural analyses also undermined the findings of a dependency of the CD44 activity on the grade of glycosylation. Glycosylation is, next to mitogens and the phosphorylation of specific serine-side chains in the cytoplasmic domain, an important regulator of CD44 activity in general. It is because of these dependencies that the presence of CD44 on a cell cannot be directly linked to an interaction with HA.[159,165-167] Such regulation is mandatory because of the high expression of CD44 in mammalian cells[130-132] and because of the variety of processes (mentioned above[9,138-147]) in which CD44 is involved. A good example for the regulation of the CD44 activity is that while it expressed in most haematopoietic cells in the mouse,[168] binding to HA is either often not detectable[169-170] or requires stimulation.[171]

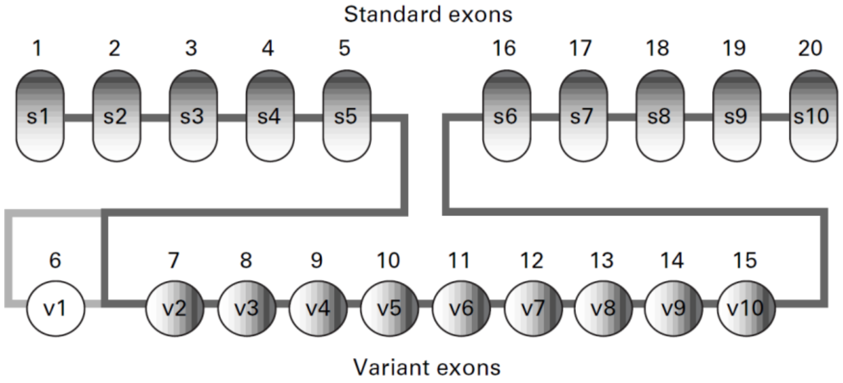

Figure 8: Scheme of the CD44 gene. The scheme shows the standard exons s1-10 and the variant exons v1-10. Alternative splicing occurs between s5 and s6. Image taken from Goodison *et al.*, 1999.[133]

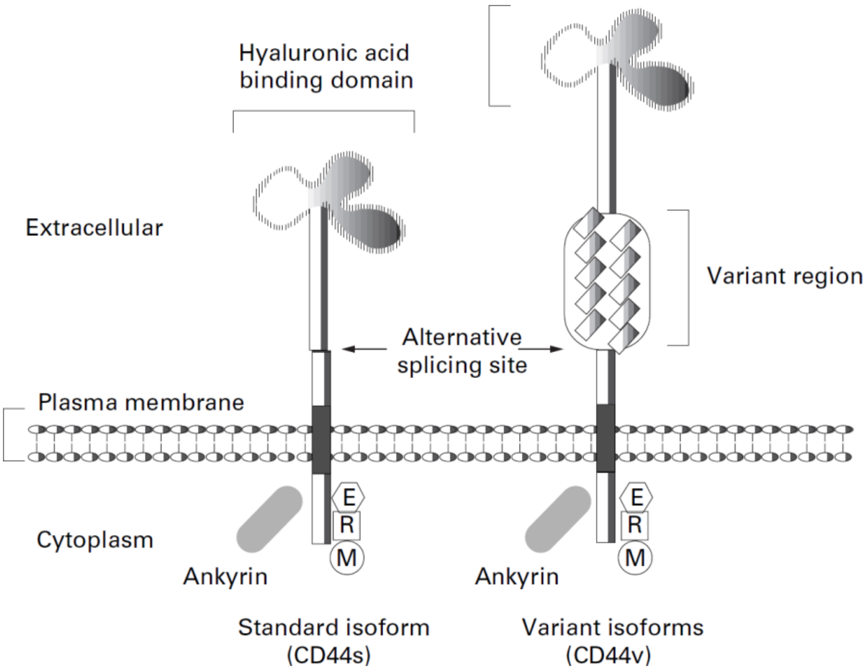

Figure 9: Scheme of the structure of CD44. The schematic shows the HA binding domain and the region at which the alternative slicing occurs. Image taken from Goodison *et al.*, 1999.[133]

2.5 ANALYSIS OF CELL-SURFACE INTERACTIONS

The methods of characterising the interaction between cells and surfaces are vast. This section gives an overview over the most common techniques used for analysis of these interactions.

2.5.1 TECHNIQUES FOR ADHESION STRENGTH MEASUREMENT

Analysis of the adhesion strength of cells interacting with surfaces varies dramatically with *e.g.* changes of the topography or surface energy. Measurement of the adhesion strength can be achieved by a centrifugal force assay or a variety of micromanipulation techniques (atomic force microscopes (AFM), microplates,[172] optical tweezers,[173] magnetic tweezers[174] and micropipette aspiration[175]) some of which shall briefly be described in this section.

The **centrifugal force assay** allows a high throughput screening of the adhesion strengths of cells under different conditions. Figure 10 gives an overview over the setup and the basic functional aspects. Multiwell plates are mounted in a centrifuge (each well can bare a different cell treatment such as antibodies, surface type and so forth) and is spun at a given rotational speed.

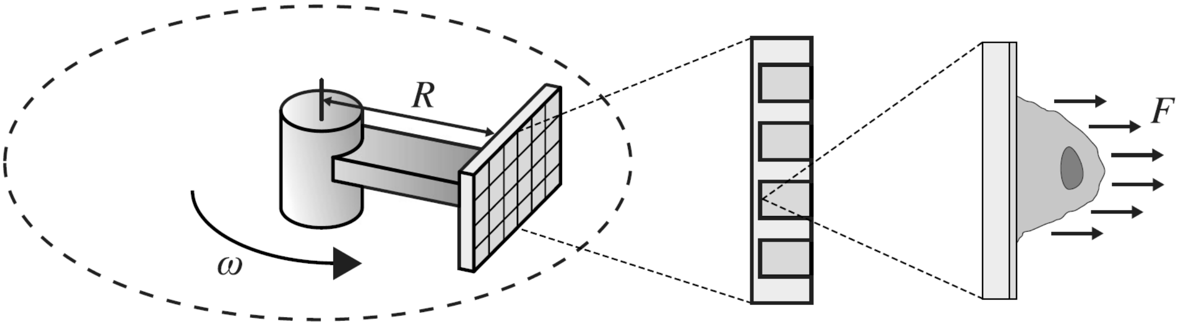

Figure 10: Centrifugal force assay. The cells are detached from the surface by centrifugal forces. Image taken from Christ *et al.*, 2010.[176]

The force F applied to the cells can be calculated from the cell volume V_{cell}, the relative centrifugal force RCF and the difference in density between the cell ρ_{cell} and the medium ρ_{medium}. The calculation of RCF in turn is based on the distance between the cell and the rotor centre R, the angular rotor speed ω and the gravitational acceleration g as shown in Equation (1). The formula for the overall force is shown in Equation (2).

$$RCF = \frac{R\omega^2}{g} \tag{1}$$

$$F = (\rho_{cell} - \rho_{medium}) \cdot V_{cell} \cdot RCF \tag{2}$$

The downside of the technique, opposing the large number of samples that can be studied simultaneously, is that only one force may be applied in each experimental run making it laborious to determine the actual adhesion strength of a cell sample.

The **cytodetachment** technique is a common example for a micromanipulation technique. Here a cantilever used in atomic force microscopy is used to detach a cell from a surface as shown in Figure 11.

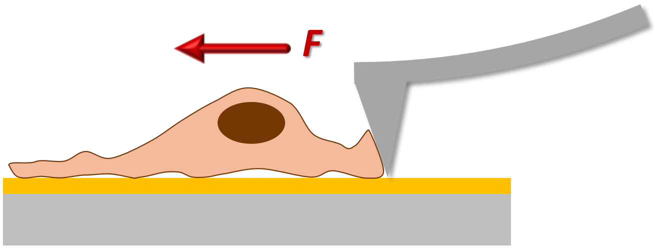

Figure 11: Cytodetachment technique. An AFM cantilever tip is used to detach a cell from a surface. Image inspired by Christ *et al.*, 2010.[176]

The force F applied to the cantilever in order to detach the cell from the sample surface is measured in form of the deflection of the cantilever d and the stiffness of the sample k as shown in Equation (3).

$$F = dk \tag{3}$$

This technique is highly flexible and can apply high forces, allowing the evaluation of the adhesion strength of even fully adhered cells.

2.5.2 HYDRODYNAMIC SHEAR FORCE ASSAYS

Hydrodynamic shear force assays are also applied for the measurement of the adhesion strength of cells to surfaces. The distinctiveness of these assays is, however, that they apply shear forces generated by the drag of a liquid along a wall and some of them can, therefore, in principle also be used for the observation of the interaction of cells with surfaces under shear force conditions. The flow is in all setups kept in the laminar flow region, as defined by a Reynold's number Re < 2300.[177]

The **spinning disc setup** allows the determination of the shear stress required to detach cells from a surface.[178-179] To achieve this cells are seeded on a circular disc (hence the name), which is then spun in a liquid. The rotation of the disc inside the liquid generates a shear stress τ that is, at a given rotational speed ω with the viscosity μ and density ρ of the fluid, dependent on the distance between the cell and the disc centre R as shown in Equation (4).

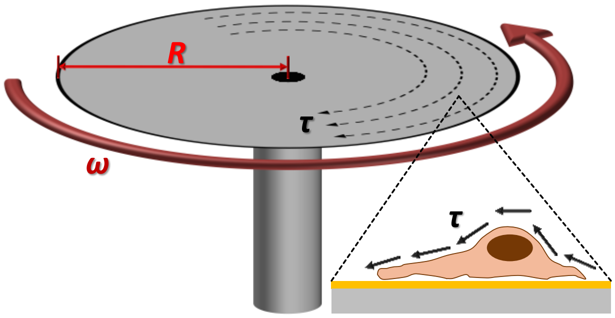

Figure 12: Spinning disc setup. The rotation of the disc inside a liquid induces a shear force on the cells. Image inspired by Christ *et al.*, 2010.[176]

$$\tau = 0.800R \cdot (\rho\mu\omega^3) \tag{4}$$

In the **radial flow chamber** the shear stress is generated by an active liquid flow. As shown in Figure 13 the liquid is injected at the centre of the chamber and then spreads homogeneously in all directions over the surface. With increasing distance from the chamber centre r the flow and directly proportional to that also the shear stress τ decreases.[180-182] This connection is easily deducible from Equation (5).[180,182]

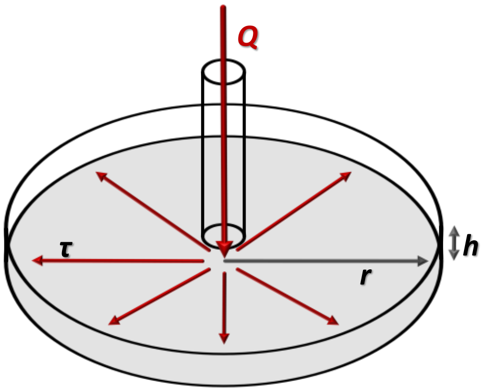

Figure 13: Radial flow setup. The liquid is injected at the middle of the chamber and flows in all directions. Image inspired by Christ *et al.*, 2010.[176]

$$\tau = \frac{3\mu Q}{\pi h^2 r} - \frac{3\rho Q^2}{70\pi^2 h r^3} \tag{5}$$

With Q being the flow rate, μ the viscosity and ρ the density of the liquid and h the distance between the top and bottom plate of the chamber.

The **parallel plate flow chamber** is in its theory closely related to the radial flow chamber. Liquid is moved through a rectangular channel system (Figure 14) either by hydrostatic pressure[183] or pumps.[184] The shear stress τ in a parallel plate flow chamber can be described according to Equation (6) if the width of the channel is far greater than its height.[185-188]

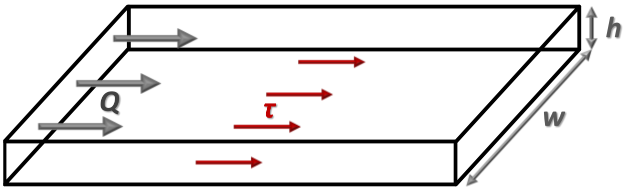

Figure 14: Parallel plate setup. The liquid flows through rectangular channel. Image inspired by Christ *et al.*, 2010.[176]

$$\tau = \frac{6Q\mu}{h^2 w} \tag{6}$$

With Q being the volume flow, μ the viscosity of the liquid, h the height and w the width of the chamber.

As the parallel plate flow chamber presents the theoretical basis of the channel system used in this work it shall be described in more detail later in section 3.8.3, where the microfluidic shear force device will be discussed, as well as in the Appendix (section 7.1.1.2 and 7.1.1.3).

2.6 SURFACE-BOUND METAL-ORGANIC FRAMEWORKS

Metal-organic frameworks (MOF), also known as porous coordination polymers (PCP), are a relatively new class of solid state inorganic-organic hybrid materials, which are typically characterised by a high crystallinity. They are extremely intriguing due to their structural specifications. Similar to zeolites they exhibit a high porosity though lacking the restrictions in reagent choice of zeolites. MOFs consist of metal ions or metal oxide clusters which coordinate organic linker molecules, hence the name. The combinational possibilities are vast resulting in a broad spectrum of MOFs structures with varying pore sizes and specific surface areas. According to IUPAC porous materials are classified according to the pore size *d* as micro- (< 2 nm), meso- (2-50 nm) and macroporous (> 50 nm).[189] So far micro- and meso-porous MOFs have been synthesised with pore sizes of up to 10 nm and specific surface areas of up to 6,000 m²/g clearly exceed those of zeolites.[190-191] MOF assembly generally follows the rules of Werner complexes. The classical method of MOF synthesis is the deposition from a solvothermal parent solution. Hereby, the metals are added to the reaction solution as precursors which coordinate the organic linkers to form structures dominated by the preferred coordination geometry of the metals.[192] After a short time at RT to 250 °C MOF crystals form from the solution, yielding the typical MOF powder. Variation of the metal precursor or the organic linker group allows the fine tuning of the MOF structure and properties. The variability was nicely demonstrated by Rowsell *et al.* at the example of a series of isoreticular MOFs (IRMOFs). The basis of this series was MOF-5, which is synthesised from tetrahedral Zn_4O^{6+}-metal clusters and terephthalate linkers. As shown in Figure 15 while all frameworks are of a cubic nature, variation of the organic linker allows the preparation of different pore sizes and functionalities.[193-194] Due to the presence of metals and/or metal oxides in the MOFs they can also exhibit electrical or magnetic properties.[195] Many applications such as size-, shape-, and enantio-selective catalysis, gas/vapour separation, drug storage and delivery or in sensors have been achieved or at least proposed.[191,196-200]

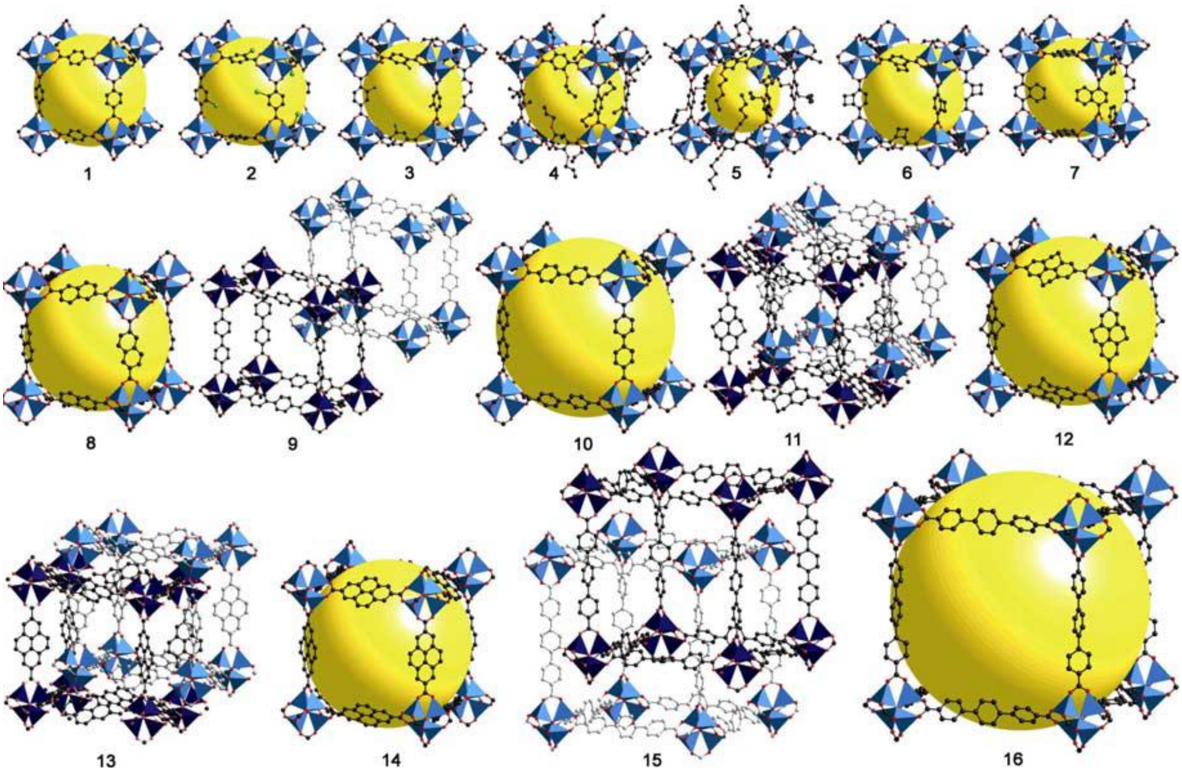

Figure 15: Variation of pore size and functionality by application of different organic linkers. A series of IRMOFs demonstrates how variable the synthesis of MOFs is. Image taken from Rowsell *et al.*, 2004.[194]

For some of these applications, *e.g.* the use in sensors, electrochemistry and chromatographic applications, the deposition of MOFs on solid substrates[201-202] in the form of thin films is of crucial importance. The first realisation of such a surface bound MOF (SURMOF) was the anchoring of MOF-5 on modified gold substrates.[203] Recently, a number of approaches have been presented to yield such porous coatings including quasi-epitaxial methods which lead to the formation of structurally nearly perfect, oriented and homogeneous coatings.[204-205] The liquid phase epitaxy is an easily controllable method for the synthesis of such SURMOFs.[206-209] Here a self-assembled monolayer (SAM) not only functions as anchor for the MOF to the surface, but it also controls the orientation in which the MOF crystal grows.[210] For synthesis the SAM is subsequently bought into contact with either a solution of the metal precursor or the organic linker as shown in Figure 16. Between each step the surface is cleaned, usually by rinsing with the solvent. This way, one layer of MOF can be generated in each step allowing for controlled growth of the MOF on the substrate and the variation of the building units used in each step.[206-210] The layer-by-layer method not only allowed the controlled growth of the SURMOF, but it also enabled the analysis of the growth in each step. This made an investigation of the influence of the structure of the metal precursor possible. Here, it was revealed that precursors already exhibiting the coordination sphere present in the MOF later strongly supported the growth of the MOF.[210]

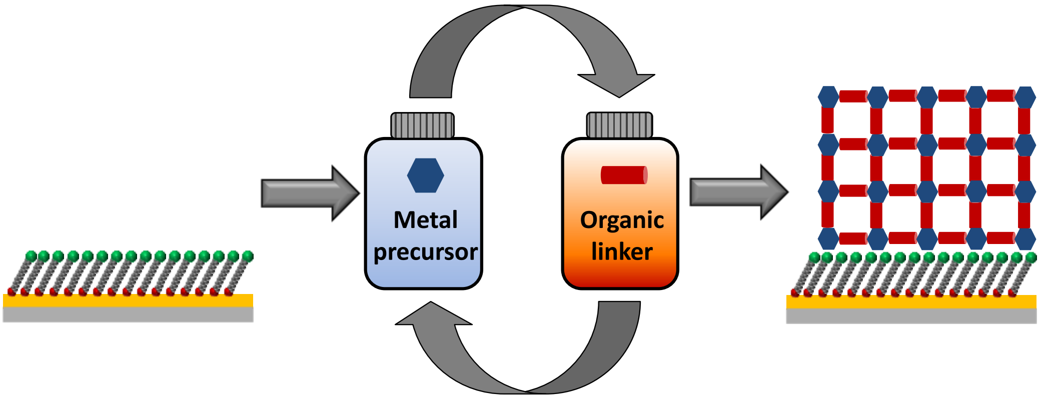

Figure 16: Liquid phase epitaxy for the synthesis of SURMOF structures. In the method of liquid phase epitaxy a SAM and later the SURMOF are brought in turn into contact with solutions of the metal precursor and the organic linker. In each step a defined layer of MOF is grown on the surface.[206-207,210] Image adapted from Shekhah *et al.*, 2010.[206]

3 MATERIALS AND METHODS

This chapter gives an overview over the techniques used in this work. The theoretical background and the practical parameters of the analytical techniques used to characterise the surfaces and cells are presented. Further, the methods of surface preparation and characterisation are outlined in this section. As a variety of cell lines and primary cell materials was used in this study, their isolation, culture and treatment protocols are also introduced in this section. Finally, the microfluidic shear force setup applied for the cell rolling and adhesion strength measurements is presented and the experimental details are discussed.

3.1 ANALYTICAL TECHNIQUES

3.1.1 CONTACT ANGLE GONIOMETRY

Contact angle goniometry is an easy technique to determine the wettability and thereby indirectly the free surface energy of a substrate.

In an ideal planar system without gravitational forces the interaction between a water droplet and a surface can be described by three surface tensions (solid/liquid γ_{SL}, solid/vapour γ_{SV}, liquid/vapourγ_{LV}) and Young´s contact angle θ_Y between the interfaces solid/liquid and liquid/vapour. The relation between these values is given by Young´s equation, shown in Equation (7).[211]

$$cos\theta_Y = \frac{\gamma_{SL} - \gamma_{SV}}{\gamma_{LV}} \tag{7}$$

As shown in Figure 17 surfaces with a high energy and high wettability have low water contact angles (0° < θ < 90°) and are known as hydrophilic, while low energy, non-wettable surfaces are known as hydrophobic surfaces and exhibit high water contact angles (90° < θ < 180°).

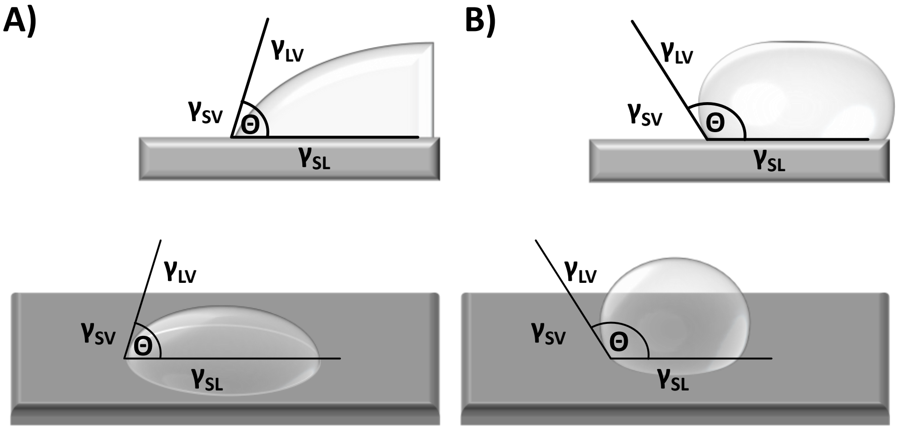

Figure 17: Contact angle of a hydrophilic surface (A) and a hydrophobic surface (B).

In non-ideal, non-planar systems the surface roughness must be taken into account. The first relation considering the surface roughness was the Wenzel equation.[212] Wenzel´s contact angle θ_W is related to Young´s contact angle θ_Y by a correction factor, the roughness ratio r_W, which is defined as the ratio between the absolute surface area and the projected surface area. The relation is shown in Equation (8).[212]

$$cos\theta_W = r_W \cdot cos\theta_Y \tag{8}$$

However, this model is only valid for fully wetted surfaces (Figure 18 A). In the case of incompletely wetted surfaces (Figure 18 B), wetting can be described by the Cassie-Baxter equation.[213] The Cassie-Baxter contact angle θ_{CB} is related to the material specific Young´s contact angle θ_Y via the surface contact fraction ϕ as shown in Equation (9). ϕ is defined as the ratio between the actually wetted surface area and the maximum possibly wettable surface area.

$$cos\theta_{CB} = \phi \cdot (cos\theta_Y + 1) - 1 \tag{9}$$

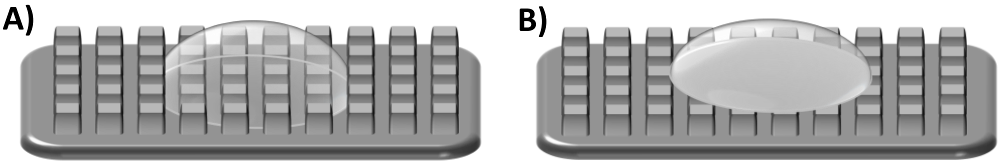

Figure 18: Theoretical contact of a water droplet as described by the Wenzel (A) and the Cassie-Baxter (B) model for wetting.

In this work contact angle goniometry was used to determine the water contact angles of SAMs and polysaccharides bound to surfaces and to thereby verify the quality of these substrates. Sessile water droplet contact angles were measured with a custom-built contact angle goniometer under ambient conditions.[12] At least three measurements were conducted on each sample. Contact between the tip and the droplet was avoided during measurement.

3.1.2 SPECTRAL ELLIPSOMETRY

Spectral ellipsometry is an optical technique that allows the determination of material properties, *e.g.* the thickness of thin layers or the refractive index, by measurement of the change of the polarisation state of light induced by the interaction with a substrate.[214]

Linearly polarised light (λ = 280 nm to 800 nm), resulting from the combination of s- (perpendicular to the plane of incidence) and p-polarised (parallel to the plane of incidence) light of the same phase and amplitude (Figure 19A), is reflected off the sample substrate and directed at a detector. Refraction in the substrate changes the phase of the beams components leading to a shift from linear polarisation to an elliptical polarisation (Figure 19B), hence the name 'spectral ellipsometry'. The reflected beam passes through an analyser and the phase shift of the beam components is measured. The change in polarisation can be expressed by the ratio *r* of the reflection coefficients r_p and r_s in the form of Equation (10).[215-216]

$$r = \frac{r_p}{r_s} = \tan(\psi)\exp(\mathrm{i}\mathit{\Delta}) \tag{10}$$

The phase shift between the *p* and *s* components is given by the parameter $\mathit{\Delta}$ and the amplitude ratio is denoted by $\mathit{\Psi}$. As the change between $\mathit{\Delta}$ and $\mathit{\Psi}$ is measured it is not necessary to measure a reference beam. This makes the setup robust against external disturbances and allows measurement at ambient conditions. The optical constants have to be calculated by regression analysis from the experimental data. Therefore a model has to be introduced representing the substrate with all known optical properties. With knowledge of the substrate´s thickness the optical constants can be determined and vice versa.[217] This method allows the calculation of layer thicknesses with sub-nanometre precision. In the case of multilayer systems each layer needs to be modelled separately.

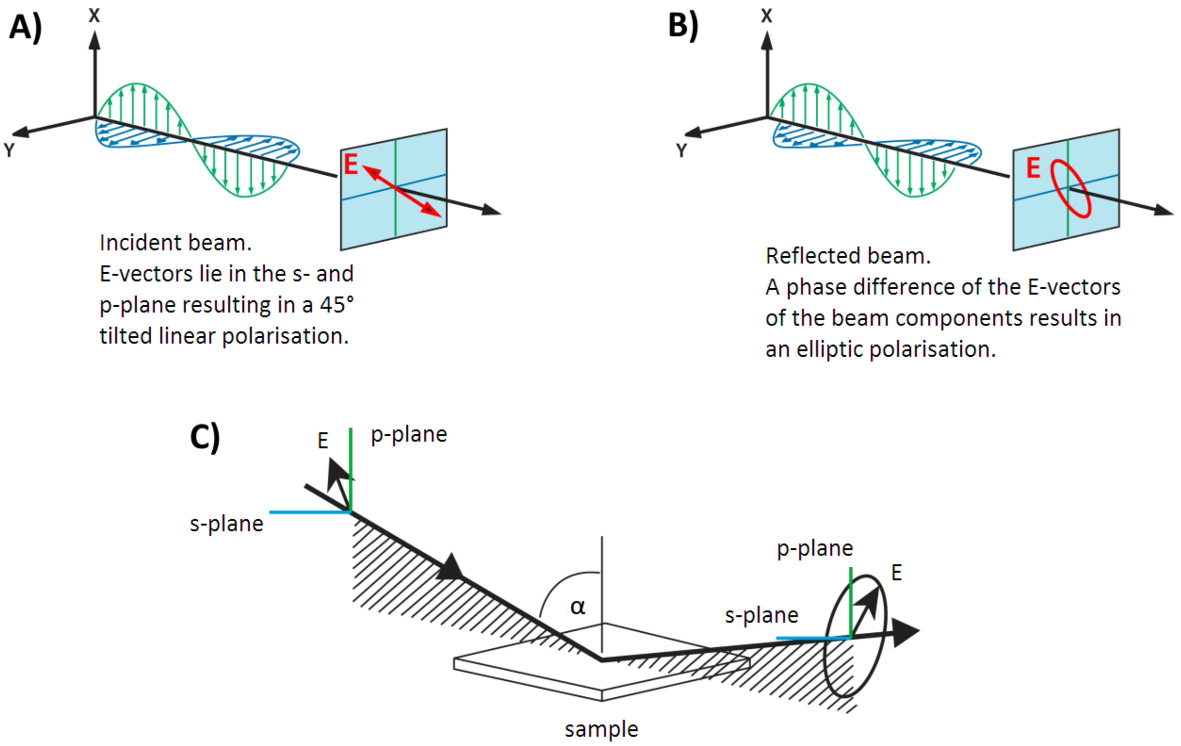

Incident beam.
E-vectors lie in the s- and p-plane resulting in a 45° tilted linear polarisation.

Reflected beam.
A phase difference of the E-vectors of the beam components results in an elliptic polarisation.

Figure 19: Polarisation of the light beam before (A) and after (B) being reflected on the sample surface. Image taken from S. Bauer (diploma thesis), 2011[218] adapted from jawoollam.com.[219]

In this study spectral ellipsometry was used to verify coupling reactions and to measure the thicknesses of SAMs and polysaccharides bound to glass substrates. The film thicknesses were measured using a M-44 multiple wavelength ellipsometer (J. A. Woollam Co., Inc., Lincoln, NE, USA) aligned at a nominal incidence angle of approximately 75 ° to the surface normal (Figure 19C). The light source used was a xenon lamp with a polychromatic spectrum. SAM and HA thicknesses were determined with the modelling software WVASE™ from J. A. Woollam Co. using a single ‘Cauchy’ model layer[214] on a underlying ‘void’ layer. The ‘Cauchy’ relationship shown in Equation (11) describes the wavelength dependent refractive index of transparent organic materials.

$$n(\lambda) = A + \frac{B}{\lambda^2} + \frac{C}{\lambda^4} \dots \tag{11}$$

Here, A, B and C are parameters which are adjusted to match the refractive index of the material. From literature values of the refractive index for protein film on surfaces are known to be in the range of 1.45-1.50.[220] From this the ‘Cauchy’ parameters were chosen as

$$A = 1.45 \qquad B = 0.01 \qquad C = 0$$

On each sample at least three measurements were conducted at different positions.

3.1.3 FLUORESCENCE ACTIVATED CELL SORTING

Fluorescence activated cell sorting (FACS) is a method that allows the high-throughput analysis and sorting of heterogeneous cell samples on a single cell basis. Each cell is separately passed by a laser beam in a liquid flow and analysed by measurement of the interaction with the light. The photons are scattered from the cells and both the scattering and the emission pattern are measured. From this different cell properties can be determined.

The intensity of the forward scattered light (FSC) is roughly proportional to the size of the cells. Strictly speaking this is only true for homogeneous spherical objects, which cells are not, but the relation is sufficient whatsoever. Light, which is scattered orthogonally to the incident beam, is known as side scattered light (SSC). Empirical measurements could show that the SSC is mainly scattered by internal cell structures and is therefore correlatable to the granularity of the cell. These cell properties are known as intrinsic features as they can be measured without the addition of exogenous reagents. Extrinsic features can be the presence of *e.g.* cell surface receptors. These must be marked with fluorescent antibodies prior to measurement. During FAC sorting, the fluorophor is excited and light is emitted in 360° around the cell. Typically this light is measured in the same optical system as the SSC. It is guided to different detectors, which measure the intensity at a given wave length, *i.e.* the presence of the stained receptor (Figure 20).[221]

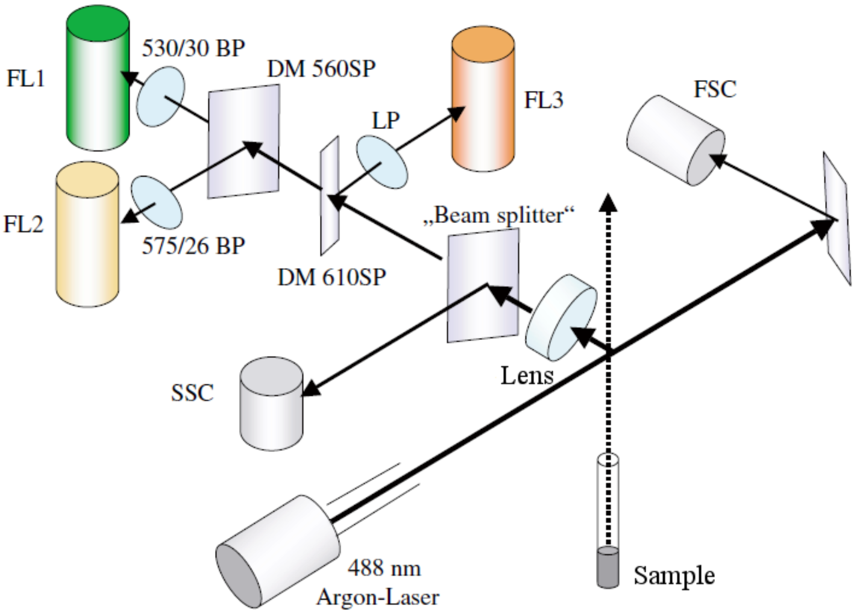

Figure 20: The optical setup of a single-laser flow cytometer with detection of 5 parameters. (FSC/SSC and three further parameters FL1, FL2, FL3). FSC = Forward Scatter; SSC = Side Scatter; DM = Dichroic Mirror; SP = Short Pass Filter; LP = Long Pass Filter; BP = Band Pass Filter. Image taken from Fruehauf *et al.*[221]

FACS analysis was used in this study to verify the binding of certain antibodies as well as to determine the presence of given receptors on cells. The measurements were performed on a FACScan flow cytometry system (Becton Dickinson, Heidelberg, Germany) by Isabel Hoffmann from the workgroup of Prof. Ho at the University Hospital Heidelberg.

3.1.4 SCANNING ELECTRON MICROSCOPY

The scanning electron microscope (SEM) was first designed in 1937[222] and has since been developed into one of the most commonly used analytical techniques.[223] The great advantage of the SEM over microscopic methods such as light microscopy is the far better spatial resolution. While the typical resolution limit of optical microscopes lies in the micrometre range, that of an SEM lies roughly three orders of magnitude below that. This is due to the use of an electron beam instead of light or more precisely the shorter wavelength of electrons compared to photons. Abbe´s diffraction limit δ is the minimal feature size that can be imaged. The formula to calculate δ is shown in Equation (12).[224]

$$\delta = \frac{\lambda}{2n \sin \vartheta} \tag{12}$$

The opening angle ϑ of the lens and the refractive index n of the medium, through which the beam travels, are the two factors unaffected by the use of electrons instead of photons. They are often found combined as the numerical aperture $NA = n \sin \vartheta$. The third variable in Equation (12) is the wavelength λ. The de Broglie relation,[225] which gives a relation between the wavelength and the impulse of a particle/wave, is given in Equation (13).

$$\lambda = \frac{h}{p} = \frac{h}{\sqrt{2mE_{kin}}} \tag{13}$$

Where h is Planck´s constant, p the impulse, m the particle´s/wave´s mass and E_{kin} the kinetic energy of the particle/wave. Together with Equation (12) it clearly demonstrates that higher energies of the particle/wave and larger masses lead to shorter wavelengths and thereby directly to a better resolution. If the wavelength of an electron that is accelerated with energies typical for SE microscopes (100 eV) is calculated, the result lies in the Angstrom regime. This is roughly three orders of magnitude below that of visual light (~ 400 nm to 800 nm).

SEM is applicable only for conductive samples, as the electrons interacting with the sample need to be removed preventing charging of the substrate. For this biological samples need to be coated with either graphite of gold in order to gain conductivity and contrast. The main components of a SEM are the electron gun, the optics, the measurement chamber and the detector with its electronics. The electron gun is a cathode from which electrons are emitted, either by heating (thermionic emission) or by applying high voltage (field emission), and an anode which is used to accelerate the electrons. The electron beam is then focused by electromagnetic fields and lenses. Scanning coils are used to deflect the beam, scanning the area of interest. An aperture is used to control the current density. The electrons then 'hit' the surface and are either deflected as back-scattered electrons (BSE) or induce the emission of secondary electrons (SE). These two types of electrons can be measured separately yielding different contrasts due to their different penetration depth.

The microscope used in this work was a LEO 1530 (Zeiss, Oberkochen, Germany). Images were recorded with Isabel Thomé and Linlin Xiao from our workgroup.

3.1.5 X-RAY PHOTOELECTRON SPECTROSCOPY

X-ray photoelectron spectroscopy (XPS) is an analytical technique used to investigate the chemical composition of surfaces. It is based on the photoelectric effect, which describes the capability of electromagnetic waves to induce the emission of electrons out of an atomic hull. The sample is probed with X-rays, thereby inducing the emission of electrons out of the hull of atoms in the top layers of the surface. Measurement of the kinetic energy of the emitted electrons can be used to characterise the elemental composition of the surface. This is possible because the binding energy of electrons is discrete and element specific. As shown in Figure 21 and in Equation (14), subtraction of the kinetic energy E_{kin} of the electrons and the work function of the device ϕ_{device} (a device specific constant) from the energy of the X-rays ($h\nu$, given by the electron source) results in the binding energy E_B. Therefore, measurement of E_{kin} allows the direct calculation of the binding energy of the core level electrons.

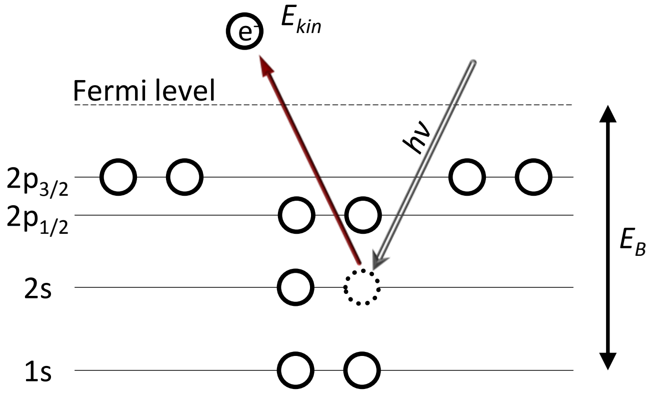

Figure 21: Scheme depicting the photoelectric effect. Interaction of X-rays of the energy $h\nu$ with electrons results in the emission of these from the atomic orbitals. Image based on Ratner et al., 2011[226]

$$E_B = h\nu - E_{kin} - \Phi_{device} \tag{14}$$

XPS not only allows the characterisation of the elemental composition of a substrate, but also the determination of the film thickness. For electromagnetic waves the empirically determined Lambert-Beer's law gives a correlation between the properties of the material through which the wave passes and the absorption in the same.[227] For thin film a slightly modified version of this law applies and allows the calculation of the thickness of the film based on the attenuation of the signal of the underlying substrate due to the film. This correlation is given by Equation (15).

$$d = \lambda_l \cos \Theta \ln \frac{I_0}{I(d)} \tag{15}$$

$I(d)$ is the signal intensity after attenuation, I_0 is the substrate signal intensity without a film present, λ_l is the attenuation length of photoelectrons with a given E_{kin} and Θ is the take-off angle. With knowledge of λ_l a measurement of the substrate without the film (I_0) and with the film ($I(d)$) is sufficient to calculate the film thickness. The attenuation length of the Au 4f signal (λ_l = 37.6 Å), as calculated for organic overlayers according to an empirical model presented by Seah and Dench,[228] was used for the calculation of the thickness of SAMs or protein layers on gold.

XP spectra were measured and analysed by Stella Bauer from our workgroup. Using a Leybold-Heraeus MAX 200 X-ray photoelectron spectrometer with a polychromatic magnesium anode as X-ray source (K_α = 1253.6 eV). Peak fitting was performed with the software *XPSPeak 4.1* (Prof. R.W.M. Kwok, Department of Chemistry, University of Hong Kong) after using a Shirley background subtraction.[229]

3.1.6 X-RAY DIFFRACTION

X-ray diffraction (XRD) spectroscopy is an analytical technique that allows the characterisation of crystalline materials. It is based on the diffraction of X-rays on ordered geometries such as crystals or quasicrystals. The diffraction can be described by the Bragg and Laue equations, which are equivalent. Bragg´s law is given in Equation (16).[230-231]

$$n\lambda = 2d \sin \theta \tag{16}$$

With n being the diffraction order (an integer), λ the wavelength of the beam, d the distance between the atomic planes and θ the angle between the incident beam and the atomic plane. As seen in Equation (16) and in Figure 22 the phase difference between the two reflected beams (the distance C-D-E) must be equal to $2d \sin \theta$ for the scattered waves to interfere constructively.

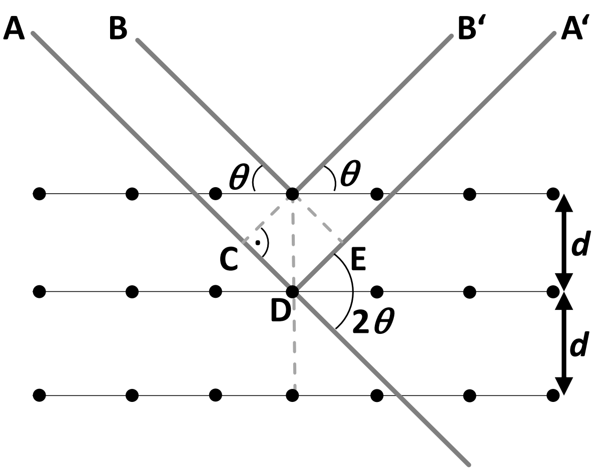

Figure 22: Geometry of a Bragg reflection. The incident beams A and B are reflected on the atoms of each atomic plane. If the path difference of the beams A' and B' is equal to a multiple of λ a constructive interference occurs.

Next to the determination of the crystallinity of a given sample XRD spectroscopy can be used to determine the distance between the atomic planes, the orientation of crystals, their periodicity, the lattice parameter or the space group of a given material.

In this study XRD spectroscopy was applied to determine the crystallinity of surface bound metal-organic frameworks (SURMOFs). Measurements were conducted by Hasan K. Arslan or Zhengbang Wang from the workgroup of Prof. Christof Wöll (IFG, KIT, Karlsruhe, Germany). For all SURMOF samples, out-of-plane XRD Θ-2Θ scans were recorded after synthesis and after the immersion into different solutions. XRD measurements were performed using a Bruker D8-Advance diffractometer with Θ-2Θ geometry and Cu K_α radiation (λ = 1.54 Å) as X-Ray source. Measurements were recorded by a PSD detector (MBraun, Garching, Germany) by a copper K_α radiation at 40 kV/30 mA, with a step size of 0.007° and scan time of 3 s in the range of 2Θ = (5-30)°.

3.1.7 INDUCTIVELY COUPLED PLASMA OPTICAL EMISSION SPECTROMETRY

Inductively coupled plasma optical emission spectrometry (ICP OES) is an analytical method which allows the rapid determination of the atomic composition of a sample.

For analysis the sample is injected into a plasma jet (typically argon plasma as this gas is comparatively cheap and chemically inert). This heat of the plasma jet (5,000 to 10,000 K depending on the region of the plasma) completely destroys that the sample with only atoms and ions remaining. This is of great benefit to the analysis as it eliminates all chemical effects such as *e.g.* the bond order. The plasma, furthermore, excites the atoms and ions to emit light. Spectral analysis of the emitted light gives information about the elements contained in the sample, with the intensity of the respective peak being proportional to the concentration of the element in the sample. As all elements are simultaneously exited they can also be detected simultaneously or in rapid succession. This results in very fast measurements (in the range of minutes). This inherent sample orientation of the ICP OES method is one advantage over element oriented methods such as atomic absorption spectroscopy where the samples are scanned for a certain element and not all elements are analysed at once. Next to the large working range of the ICP OES which typically comprises of six orders of magnitude (from sub-µg/L to g/L) is another noteworthy advantage of the ICP OES over other analytical techniques.[232]

Copper concentrations in SURMOF supernatants were measured by Marita Heinle from the workgroup of Prof. Matthias Franzreb (IFG, KIT, Karlsruhe, Germany) with an OPTIMA 8300DV (Perkin-Elmer, USA). The sample flow was set to 1 mL/min. The high frequency generator operated at 1400 W. Gas flows were 15 L/min for the plasma, 0.5 L/min for the thrust gas and 0.55 L/min for the vaporiser gas. The copper bands analysed were the signals at 327.393 nm and at 324.752 nm.

3.2 SURFACE PREPARATION TECHNIQUES

3.2.1 PREPARATION OF POLYSACCHARIDES ON GLASS

The glycosaminoglycans (GAGs) are a group of large polysaccharides without branching of the molecular structure.[128,233] Common to this type of polysaccharides are 1,4-linked disaccharide units containing at least one uronic acid (*e.g.* D-Glucuronic acid or L-Iduronic acid). This uronic acid is typically linked to an amino sugar by a β-1,3-glycosidic bond. The most prominent representatives are hyaluronic acid, chondroitin sulphate, keratin und heparin.[234]

Hyaluronic acid (HA) was first isolated from the vitreous humour of the eye by Meyer and Palmer in 1934.[235] The structure was solved 20 years later.[236] It is a large linear polymer based on a repeating disaccharide units consisting of N-acetyl-D-glucosamine and D-glucuronate, connected by β-1,4 and β-1,3 linkages. HA is one of the major components of the extracellular matrix. It was demonstrated in rats that HA can be found throughout a mammalian organism with the highest amounts located in the skin (~ 50 %), the bones and supporting tissues (~ 25 %) and the rest distributed in muscles and viscera.[237] This abundance of HA demonstrates its great importance and many functions in mammalian organisms. The most relevant for this study is surely its role as binding partner for CD44, which shall be examined in detail in section 4.

Chondroitin sulphate (CS), which also belongs to the GAG-family, can be found among others in the extracellular matrix (ECM)[238] or cartilage of mammals and in the slimy fluid covering many fish.[239] Each of its disaccharide subunits consists of N-acetyl-D-galactosamine (GalNAc) and glucuronic acid that are connected by β-1,3 and β-1,4 linkages. Due to the pronounced chemical similarities between HA and CS, CS presents an ideal reference when analysing the interaction of CD44 expressing cells with HA.

For cell interaction analysis a homogeneously coated surface, which can be used more than once, was of great interest. This could be realised by covalent coupling of the GAGs of interest to glass as shown in Figure 23. The GAGs (HA, CS) were coupled to NexterionB® glass slides according to previously published protocols.[240-243] Silicon wafers ([100], p-doped with boron, served as reflecting and conductive surfaces for spectroscopic characterisation (Table 1).

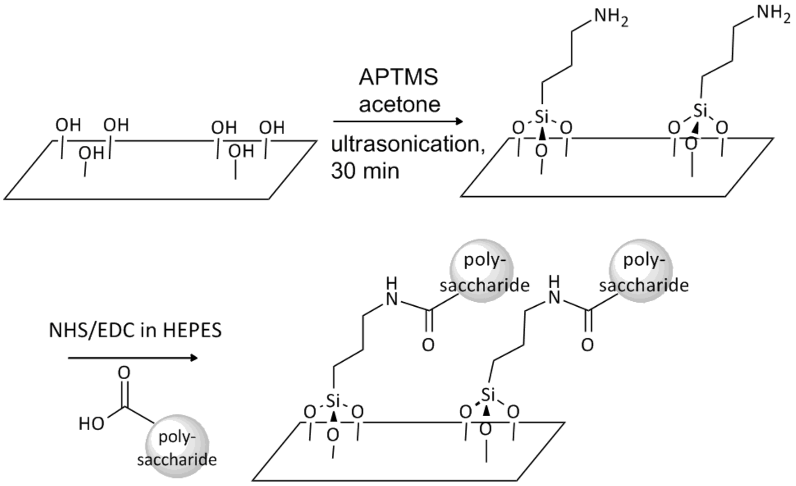

Figure 23: Schematic of the coating of glass slides with polysaccharides utilising the EDC/NHS chemistry. Image adapted from Bauer *et al.*, 2013.[244]

The substrates were cleaned and activated in an O_2-plasma (Pci PCCE, Diener plasma GmbH & Co. KG, Ebhausen, Germany) at 150 W power and 0.4 mbar O_2 pressure for 3 min. 3-Aminpropylotrimethoxysilane (APTMS) functionalisation was achieved by ultrasonification of the glass slides immersed in a solution of 5 % APTMS in dry acetone for 30 min. The surfaces were subsequently immersed in a solution of the GAG (1 mg/mL), N-hydroxysuccinimide (NHS, 0.01 M) and 1-ethyl-3-(3-dimethylaminopropyl) carbodiimide (EDC, 0.05 M) in 2-(4-(2-hydroxyethyl)-1-piperazinyl)-ethansulphonic acid (HEPES)-buffer (10 mM). The reaction took place on a vibrating Table (60 rpm) at room temperature (RT) and was quenched after 18 h by flooding with MilliQ® water (8x volume). Washing with MilliQ® water was repeated daily for 3 days, before the slides were stored in MilliQ® water until further use. After each step of the reaction, the surfaces were analysed by static contact-angle measurement and spectral ellipsometry to verify successful grafting.

Table 1 gives the film thickness and contact angle for the APTMS, the HA and CS layers prepared in this work. XP spectra of the prepared HA surfaces shown in Figure 24 were obtained by Stella Bauer from our workgroup. They clearly demonstrate the successful preparation of an APTMS layer and the binding of HA to that surface. The C 1s spectra of the APTMS layer show the signals for an aliphatic carbon and for a carbon with an adjacent electronegative (here the amino function) group. As expected from the chemical structure of APTMS the two signals are observed in a ration of roughly 2:1.

The XP spectrum of HA shows three species of carbon. This in line with the chemical structure of HA. A small aliphatic group of carbons is observed. This may also to a certain extent originate from the underlying APTMS layer. The two other species originate from carbons which have one (the centre peak; 287 eV) or two (the left peak; 288.5 eV) electronegative groups adjacent. The N 1s spectra show a small accumulation of nitrogen on the surface by coating with APTMS and an increased nitrogen occurrence after coating with HA. This too is in line with the chemical structure of the two molecules. Both APTMS and HA present one nitrogen atom in their monomer structure.

Table 1: Properties of GAG-coated surfaces.

Surface Type	**Film Thickness Ellipsometry [Å]**	**Contact Angle [°]**
APTMS layer	12 ± 4	38 ± 6
HA layer	19 ± 6	< 10
CS layer	24 ± 5	13 ± 5

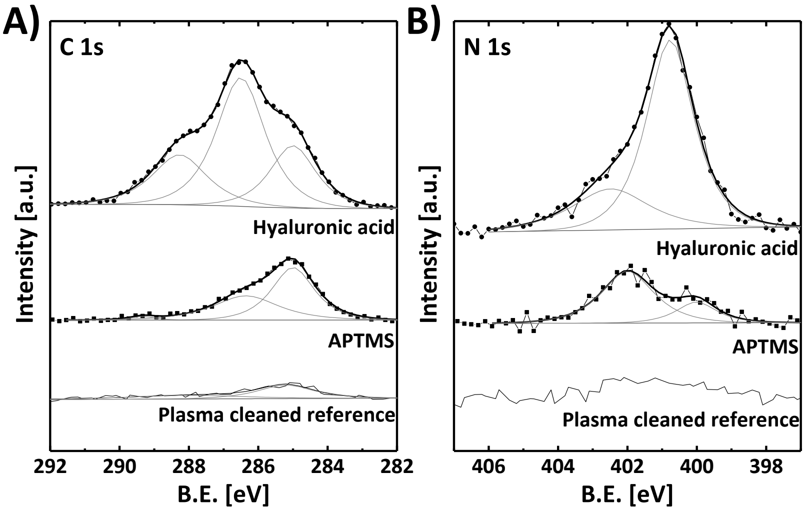

Figure 24: XPS analysis of the prepared HA films. The C 1s XP spectra (A) show the occurrence of increasing amounts of carbon on the surface. This together with the increasing amounts of nitrogen, as shown in the N 1s spectra (B), indicates the formation of the respective layers on the surface.

3.2.2 PREPARATION OF GOLD SUBSTRATES

Homogeneously coated flat gold substrates were required for the preparation of self-assembled monolayers. The gold substrates were obtained from PVD Beschichtungen (Silz, Germany). Thin polycrystalline gold films were prepared by thermal vapour deposition of 30 nm gold (99.99 % purity) onto polished float glass slides (Nexterion B®) predeposited with a 5 nm titanium adhesive layer. Evaporation was performed at a pressure of 2 x 10^{-7} mbar and a deposition rate of 0.5 nm/s resulting in a root-mean-square roughness of about 1 nm.[245] The gold substrates were kept in argon atmosphere until use.

3.2.3 PREPARATION OF SELF-ASSEMBLED MONOLAYERS ON GOLD

Self-assembled monolayers (SAMs) present easy to fabricate, highly reproducible surfaces with well-defined and tuneable properties.[246-247] While the term SAM describes a thin layer of self-organised organic molecules on a surface in general, the most common system used is an organic thiol that spontaneously self-assembles on a gold surface as shown in Figure 25.[247-250] In this system the driving force of assembly is the formation of an Au-S-bond,[249] which is an extremely strong surface bond (homolytic bond strength of ~ 44 kcal/mol).[251] Ordering of the layers is driven by van der Waals (VdW) forces between the alkane chains of the different molecules leading to the formation of crystalline monolayers.[251] In order to maximise the VdW forces the Organo-thiols are tilted by (30-35)°.[252] The surface properties are now dictated by the terminal functional group of the organo-thiol. This explains why the surface properties of SAMs are so easily controllable. The use of organo-thiols with different functional end groups results in differently terminated surfaces.

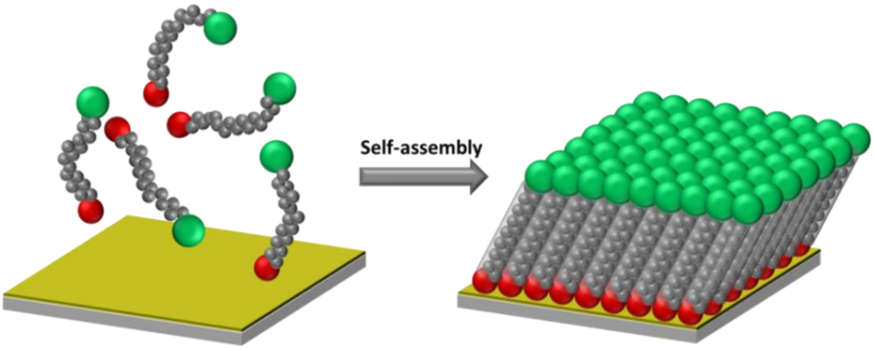

Figure 25: Self-assembly of organo-thiols on a gold surface. The organo-thiols are comprised of a thiol group (🔴), a CH2-linker group (⚪) and a terminal functional group (🟢). The thiol group interacts with the gold surface forming an Au-S-bond.[249] The SAM is formed by self-organisation of the molecules on the gold surface.

In this study SAMs were used as reference surfaces with defined surface properties and as anchoring group for metal-organic frameworks to surfaces. The SAMs used for the preparation of metal-organic frameworks were 16-Mercaptohexadecanoic acid (MHDA) and hexadecane1thiol (HDT) SAMs. These were prepared Hasan K. Arslan (MHDA and HDT) and Zhengbang Wang (MHDA) form the workgroup of Prof. Christof Wöll (IFG, KIT, Karlsruhe, Germany).

Prior to the SAM formation, the gold substrates where treated with UV radiation for 2-3 h for cleaning. The gold slides were then rinsed with EtOH *p.a.*, cleaned in EtOH *p.a.* in an ultrasonic bath for 3 min and again rinsed with EtOH *p.a.*. The substrates were then dried in a nitrogen stream. Each surface was measured as a reference for later ellipsometric measurement of the SAM layer thickness

MHDA SAMs was prepared on the Au coated glass slides using the following procedure: A solution of MHDA was prepared as described by Arnold *et al.*[253] by dissolving the thiol in a 10/90 volume mixture of acetic acid (AcOH) and EtOH to reach the desired concentration of 20 µM. To prepare MHDA SAMs, a clean gold substrate was placed in this solution for 72 h and then rinsed with the EtOH *p.a.* and gently dried under nitrogen flux. Next to the ellipsometric and the contact angle measurement (Table 2) the MHDA SAMs were characterised by Infrared Reflection Absorption Spectroscopy (IRRAS) as shown in the supplementary Figure S12 (Appendix section 7.3.1).

For the preparation of Dodecane-1-thiol (DDT), 11-mercapto-1-undecanol (11-hydroxy-undecan-1-thiol, HUDT) and HDT SAMs the clean gold substrates were immersed in 1 mM ethanolic thiol solutions. After 24 h the substrates were removed from the thiol solution and rinsed with EtOH *p.a.*, treated in an ultrasonic bath for 3 min to remove non chemisorbed thiols and rinsed again. The samples were blown dry in a nitrogen stream and were either used instantly or kept under argon atmosphere until use. The samples were characterised by contact angle measurement and spectral ellipsometry (Table 2).

Table 2: Properties of the different SAMs after self-assembly. The table gives the film thickness as determined by spectral ellipsometry and the contact angle as measured by contact angle goniometry. The error is the standard deviation (SD).

Surface Type	Film Thickness [Å]	Contact Angle [°]
30 nm gold slides	---	65 ± 2
MHDA SAM	14 ± 2	26 ± 3
HDT SAM	15 ± 2	98 ± 5
HUDT SAM	12 ± 2	36 ± 4
DDT	11 ± 2	101 ± 5

The preparation of patterned Cu^{2+} based SURMOF 2 substrates for the cell attachment studies was accomplished by micro-contact printing (µCP) of two different SAMs on a gold substrate.[254] A polydimethylsiloxane (PDMS) stamp with elevated 50 µm x 50 µm squares was inked with a 5 mM ethanolic solution of MHDA, dried and gently pressed against the gold substrate for 120 s. The bare areas (stripes) between the squares were coated with HDT SAMs as described above. The characterisation was done by ellipsometric and contact angle measurement (Table 2).

3.2.4 PREPARATION OF SURMOF SUBSTRATES

Metal-organic frameworks (MOFs) are a class of highly porous coordination polymers which presently attract enormous interest with regard to a broad variety of rather different applications ranging from storage of small molecules to nanotechnology and applications in drug release.[198,255-256] In this study the stability of different surface-anchored MOFs (SURMOF) as well as the biocompatibility of the respective SURMOF was studied. The spray method, one of the preparation techniques used in this study, is shown in Figure 26. Synthesis of the different SURMOF substrates was done by Hasan K. Arslan and Zhengbang Wang form the workgroup of Prof. Christof Wöll (IFG, KIT, Karlsruhe, Germany).

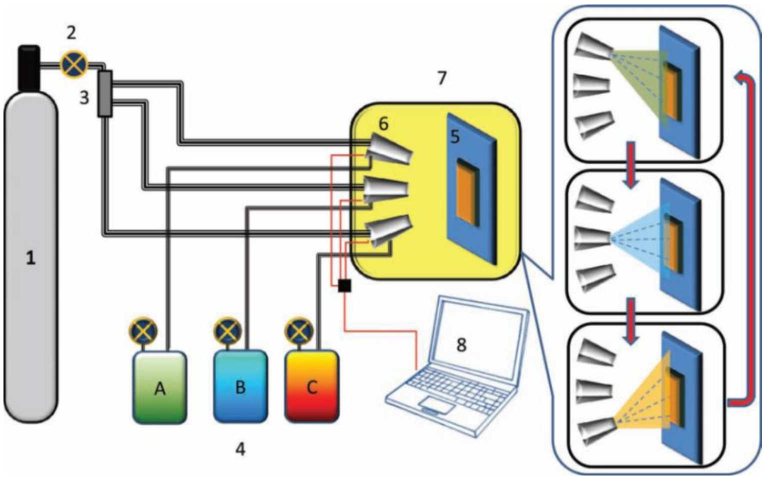

Figure 26: Setup of a spry coater as used for the preparation of SURMOF 2 substrates in this study. The two building units of the SURMOF (B and C) and EtOH *p.a.* (A) are in turns sprayed on the substrate (5). A computer (8) controls the spraying sequence. Image taken from Arslan *et al.*, 2011.[208]

HKUST-1

To grow the HKUST-1 SURMOF, MHDA SAM substrates were immersed in a 1 mM ethanolic solution of Cu(II)$Ac_2 \cdot 2H_2O$ for 15 min and subsequently in a 0.1 mM ethanolic solution of benzene-1,3,5-tricarboxylic acid (btc) for 30 min at 50 °C. The samples were rinsed with ethanol containing 0.5 % (by volume) of water for 2 min and dried under a flow of nitrogen between each step. The cycles were repeated 40 times, thus obtaining a 40 layer HKUST-1 SURMOF.[257]

SURMOF 2 / spray method

Cu-SURMOF 2 layers were grown on MHDA SAMs on Au substrates by employing the spray-method shown in Figure 26[208] with (a) a 1 mM ethanolic solution of Cu(II)$Ac_2 \cdot 2H_2O$ respectively for 10 seconds and then (b) with a 0.2 mM ethanolic solution of benzene-1,4-dicarboxylic acid (bdc) for 20 s at RT. Between each step the substrates were rinsed with ethanol for 3 s.

SURMOF 2 / pump system

Cu-SURMOF 2 layers were grown on MHDA SAMs on Au substrates. The freshly prepared substrates were then immersed subsequently (a) in a 1 mM ethanolic solution of Cu(II)$Ac_2 \cdot 2H_2O$ for 30 min and (b) in a 0.2 mM of bdc ethanol solution for 1 h at RT. Between each step the substrates were rinsed with ethanol for 2 min and dried under a flow of nitrogen between each step.

All SURMOFs were characterised by XRD in a Θ-2Θ geometry using Cu K_α radiation before all subsequent measurements were carried out. Characterisation of the SURMOFs shall be discussed in the context of the stability analysis in section 5.1.

3.3 MEDIA STABILITY ANALYSIS OF SURMOFS

To investigate the stability of Cu-/Zn-SURMOF 2 against MilliQ® water, artificial sea water (ASW, type: Instant Ocean®), phosphate buffered saline buffer (PBS), 1 mg/mL fibrinogen in PBS and the cell culture medium Dubelcco´s modified eagle medium (DMEM) supplemented with 10 % FCS and 5 % L-Glutamine, the Cu-/Zn-SURMOF 2 substrates were incubated in the different media in a beaker and shaken for (1-2) h on a vibrational table at 90 rpm. Then the samples were removed from the solution and carefully rinsed with MilliQ® water before they were used for surface characterisation. The stability of the HKUST-1 SURMOF in water was studied analogously but with shorter incubation times as the MOF was highly unstable in water.

3.4 PROTEIN ADHESION ASSAY

Protein resistance of different SAMs and the Cu-SURMOF 2s was characterised following established protocols.[220] The proteins were dissolved in PBS (filtered once with a 0.45 µm syringe filter; protein concentration: 2 mg/mL) under constant stirring at RT. Sample surfaces were preincubated in PBS buffer (10 mL, filtered once) in a 50 mL-beaker for 20 min. The clear protein solution was added to the PBS buffer solution, in which the samples were incubated, diluting the protein concentration to 1 mg/mL. After 30 min of incubation at RT the adsorption was stopped by careful flooding with 1 l deionised-water. The samples were then carefully rinsed with MilliQ® water and dried in a nitrogen stream.

3.5 CULTURE OF MODEL CELL LINES

While the interaction of primary human cell material with surfaces is generally of more interest than that of cell lines, the cell lines represent the only sensible way of undergoing broad mechanistic studies with large amounts of comparable cell material. In this study the cell lines were used as model systems for the interaction of cells with HA and as references for the analysis of the biocompatibility of SURMOF substrates.

3.5.1 CULTURE OF SUSPENSION CELL LINES

The suspension cell lines KG-1a, Jurkat and Kasumi-1 were cultured in 75 cm² culture flasks in 10 mL of RPMI 1640 (PAA Laboratories GmbH, Engelsbach, Germany) supplemented with 10 % FCS, 1 % penicillin/streptomycin and 1 % L-glutamine. The cells were split every 3-4 days in the range of 1:5 to 1:10. Therefore the cell suspension was diluted in PBS buffer and centrifuged for 5 min at 1200 rpm. The solution was then removed from the pellet, which was subsequently resuspended in fresh medium and stored in in a humidified incubator with ~ 5 % CO_2 at 37 °C.

For experiments, the cell concentration was determined with a Neubauer haemocytometer for cell counting before the cells were washed and adjusted to a cell concentration of 10^6 cells/mL.

3.5.2 CULTURE OF ADHERENT CELL LINES

REF52WT Cells

REF52WT were cultured in Dubelcco´s modified eagle medium (DMEM) supplemented with 10 % FCS, 1 % penicillin/streptomycin and 1 % L-glutamine. They were harvested at full confluence from T-25 tissue culture flasks by rinsing with 10 mL PBS buffer and subsequent incubation with 2.5 mL 0.05 % trypsin–EDTA solution for 3 min at 37 °C in an incubator. Then the suspension was diluted with 10 mL culture medium and centrifuged for 3 min at 800 rpm. The cell pellet was resuspended with fresh medium and used for experiments instantly. For continuous cultivation the cells were split 1:10 and seeded in T-25 tissue culture flasks. Confluent passages were obtained every 2-3 days.

For experiments, the cell concentration was determined with a Neubauer haemocytometer for cell counting before the cells were washed and adjusted to a cell concentration of 10^6 cells/mL.

HepG2 and HepG2Iso Cells

Culture and preparation for microfluidic experiments of HepG2 and HepG2Iso were performed by Katharina Fuchs (workgroup of Dr. Véronique Orian-Rousseau, ITG, KIT, Karlsruhe, Germany). For culture the cells were grown in either tissue culture flasks or plates in DMEM supplemented with 10 % FCS. To passage the cells the old growth medium was removed by aspiration. The cells were then washed with PBS. To detach the cells from the plate trypsin containing solution (Trypsin 0.25% (w/v) EDTA) was added and incubated at 37 °C for approximately 3-10 min. Trypsin-dependent digestion was then stopped with serum containing medium, the cells were collected by centrifugation at 1.200 rpm, resuspended in fresh DMEM and distributed in new tissue culture flasks or plates.

For experiments $3 \cdot 10^6$ cells were seeded in 10 cm plates and cultured for 24 h. After 24 h of starvation, the cells were washed 3 times with PBS. The following steps were performed on ice. The cells were harvested by 5 mM EDTA in PBS and afterwards washed three times with PBS. After that, the cells were counted and diluted to a concentration of $1 \cdot 10^6$ cells/mL in DMEM without FCS. They were stored on ice and used within a few hours.

An overview over all cell lines used in this work is given in Table 3.

Table 3: Overview over the cell lines used in this work.

Cell line	Organism	Tissue	Description	Reference
KG-1a (CCL-246.1)	Human	Bone marrow	Myeloblast, suspension	[258-259]
Jurkat (TIB-152)	Human	T-cell leukaemia	Lymphoblast, suspension	[260]
Kasumi-1 (CRL-2724)	Human	Peripheral blood	Myeloblast, suspension	[261]
REF52WT	Rat	Embryo	Fibroblast, adherent	[262]
HepG2Iso	Human	Liver	hepatocellular carcinoma, adherent	[263]
HepG2	Human	Liver	hepatocellular carcinoma, adherent	[263]

3.6 ISOLATION AND CULTURE OF HEALTHY AND LEUKAEMIC HAEMATOPOIETIC CELLS

The progression from the model cell line interaction with HA under flow conditions was the analysis of primary material under identical conditions. For this written informed consent was obtained according to the guidelines approved by the Ethics Committee of the Medical Faculty of Heidelberg for the collection of fresh umbilical cord blood (CB), bone marrow from healthy donors (BM), peripheral blood from healthy donors (PB) or G-CSF-mobilised peripheral blood from healthy donors (mPB) and bone marrow and peripheral blood from patients with newly diagnosed AML (PB blasts or BM blasts). Collection and purification was conducted by the group of Prof. Anthony D. Ho (Department of Medicine V, University of Heidelberg) following established protocols.[264-265]

Mononuclear cells (MNC) from healthy donors were isolated by density gradient centrifugation on Ficoll-Hypaque from healthy PB. Leukocytes (lymphocytes, monocytes and granulocytes) from healthy PB were sorted by FACS (FACSAria, Becton Dickinson) based on CD45 expression and SSC characteristics after red blood cell lysis with BD Pharm Lyse™.

$CD34^+$ cells from CB, mPB or BM were selected by magnetic-activated cell sorting (MACS) using a monoclonal anti-CD34 antibody labelled with magnetic beads on an affinity column (MiltenyiBiotec, Bergisch-Gladbach, Germany).

Leukaemia blast samples from patients with AML were sorted by fluorescence-activated cell sorting (FACS) (FACSAria, Becton Dickinson) based on CD45 expression and SSC characteristics ($CD45^{dim}SSC^{low}$). Between acquisition and use in this study, the AML samples were stored in liquid nitrogen at -196 °C. Most samples were isolated from the bone marrow of the respective patient. Samples isolated from the peripheral blood are marked appropriately in the text.

Both healthy and leukaemic cells were cultivated in Stemline™ II Haematopoietic Cell Expansion Medium supplemented with 100 ng/mL TPO, 100 ng/mL G-CSF, 100 ng/mL SCF, 500 ng/mL Flt-3L, 2 mmol/L L-glutamine, 1,000 U/mL penicillin and 100 U/mL streptomycin for 24 h.[266] The cell density was adjusted to 10^6 cells/mL, and the cells were analysed in the microfluidic cell detachment assay.

3.7 CELL TREATMENT AND MODIFICATION

To characterise the interaction of cells it is often necessary to modulate their binding properties. This for example offers the opportunity to determine dependencies on certain receptors or on the amount in which these are available for interaction. In this study the interaction of both model cell lines and human haematopoietic cells with HA was characterised in detail. To achieve this, the cell surface receptor CD44, responsible for a flow-induced interaction with HA, was modified and the effects of this modification were analysed in a microfluidic shear force device. The treatment with antibodies and siRNA is described in this section. It is also described how cells were prepared for SEM imaging.

3.7.1 ANTIBODY TREATMENT

The cell surface expression of CD44 in different HPC subpopulations, leukaemic blasts, leukocytes and KG-1a cells was investigated by staining with anti-CD44-phycoerythrin or anti-CD44-allophycocyanin (clone G44-26, Becton Dickinson) and subsequent FACS measurement.

For antibody blocking experiments, the cells were pre-incubated with different concentrations of the monoclonal CD44 antibody clone BU52 (hereafter referred to as BU52) or the isotype control anti-IgG1 (hereafter referred to as IgG1) for 30 min. The effectiveness of the binding of both BU52 and the isotype control IgG1 was verified by FACS measurement using FITC-marked BU52 (hereafter referred to as BU52-FITC, using the same protocol as for BU52) or by staining the cells previously incubated with IgG1 for 20 min with a FITC-marked anti-IgG1 antibody (hereafter referred to as FITC-IgG1).

3.7.2 SIRNA OLIGONUCLEOTIDES AND TRANSFECTION

Transfection of HepG2Iso cells with siRNA oligonucleotides were done by Katharina Fuchs from the workgroup of Dr. Véronique Orian-Rousseau (ITG, KIT, Karlsruhe, Germany). Aliquots of HepG2Iso cells ($2 \cdot 10^6$) were seeded in 10 cm plates 24 h before transfection. The cells were transfected with Lipofectamin 2000, according to the manufacturer's protocol. Per plate, 18 µl of Lipofectamin 2000 was diluted in 547 µl of the corresponding serum free cell culture medium (DMEM) and incubated for 10 min at RT. 5 nmol/L of CD44pan siRNA (5'-CTGAAATTAGGGCCCAATT-3'; 5'-AATGGTGCATTTGGTGAAC-3'; 5'-CAGAAACTCCAGACCAGTT-3'), CD44v3 siRNA (5'-TGAAGATGAAAGAGACAGA-3'; 5'-AGGCATTGATGATGATGAA-3'), CD44v6 siRNA (5'-AGTAGTACAACGGAAGAAA-3'; 5'-GGATATCGCCAAACACCCA-3') or control siRNA (5'-UAAUGUAUUGGAACGCAUAUU-3'; 5'-

AGGUAGUGUAAUCGCCUUGUU-3’; 5’-UGCGCUAGGCCUCGGUUGCUU-3’) was diluted with medium reaching a total volume of 547 µl. The two solutions were gently mixed together and incubated for 20 min at RT. In the meantime, the cell medium was replaced with 4.5 mL of fresh serum-containing medium. 1 mL of the siRNA-transfection reagent mixture was then applied to the cells. The cells were subsequently incubated with the siRNA mixture for 48 to 72 h.

3.7.3 TRANSWELL MIGRATION ASSAYS

Transwell migration assays were conducted in cooperation with Rainer Saffrich from the workgroup of Prof. Anthony D. Ho (Med.V, Universitätsklinikum Heidelberg). 24-well plates with transwell inlets of 3 µm pore size were used in this work. 700 µl of LTBMC medium were added to the well plate together with the SDF-1α (100 ng/mL) if required. HPC (80,000 cells to 150,000 cells in 200 µl) were either directly added to the transwell inlet or first mixed with the Plerixafor® solution (500 ng/mL) and then added to the transwell. All concentrations are given as final concentrations in the volume (900 µl) of the entire setup. The assay was run for 4 h in an incubator and terminated by fixing of the cells with 4 % PFA solution in PBS. The nuclei were marked with Hoechst 33342. The fixed HPC were washed into a 96-well plate and images were taken of each fraction. The number of migrated cells was then measured by object counting with ImageJ (National Institutes of Health, Bethesda, MD, USA).

3.7.4 SAMPLE PREPARATION FOR SEM IMAGING

REF52WT were incubated on the surfaces for at least 5 h. The cell culture medium was removed and the cells were carefully washed three times with PBS buffer. The PBS buffer was then also removed and the cells were incubated with 2 % paraformaldehyde (PFA) in PBS buffer for 30 min at RT. After the incubation the cells were washed three times with PBS buffer, which was then substituted by MilliQ® water in three dilution steps. The water was exchanged every 10 min with water/ethanol mixtures; the amount of ethanol increasing by 10 % each step beginning with 50 %. The washing with 100 % ethanol was repeated three times. The critical point drying with a CPD 030 (Bal-Tec, Schalksmühle, Germany) followed a well-established protocol.[267] The exchange of ethanol to liquid carbon dioxide was repeated 10 - 15 times at 10 °C. The temperature was then raised to 40 °C. By heating the solution the pressure rose from 50 bar up to 70 - 80 bar. The system was kept in the critical phase for 10 min before the gas was slowly released. The dried samples were then directly sputtered twice with graphite to avoid surface charging artefacts in the SEM.

HepG2Iso and KG-1a were fixed with 10 % PFA in PBS buffer under flow (approximately 1 dyn/cm²) in the microfluidic shear force setup. Therefore, the cells were injected in cell culture medium and the PFA/PBS solution was then sucked through the channel system gradually bringing the cells into contact with the solution. The cells remained in the PFA/PBS solution for 10 min. The following washing and drying steps were analogous to the procedure for REF52WT.

3.8 MICROFLUIDIC SHEAR FORCE MEASUREMENT

The microfluidic shear force setup used in this study was built and developed in our workgroup by Christof Christophis.[11-12] It allows the exact application of liquid flow speeds to defined channel systems containing modifiable sample surfaces, thereby allowing the quantification of the adhesion of objects to a surface and the observation of the interaction of cells with these surfaces under flow conditions.

3.8.1 GENERAL SETUP

The general setup consists of an inverted TE2000-U microscope (Nikon, Tokyo, Japan) housed in a self-built incubator (Figure 27), which allows the adjustment of the temperature to cell culture compatible conditions (37 °C). The incubator is further equipped with CO_2 regulation making long-term cell experiment not only possible, but presenting ideal conditions for these (5 % CO_2 in the atmosphere).

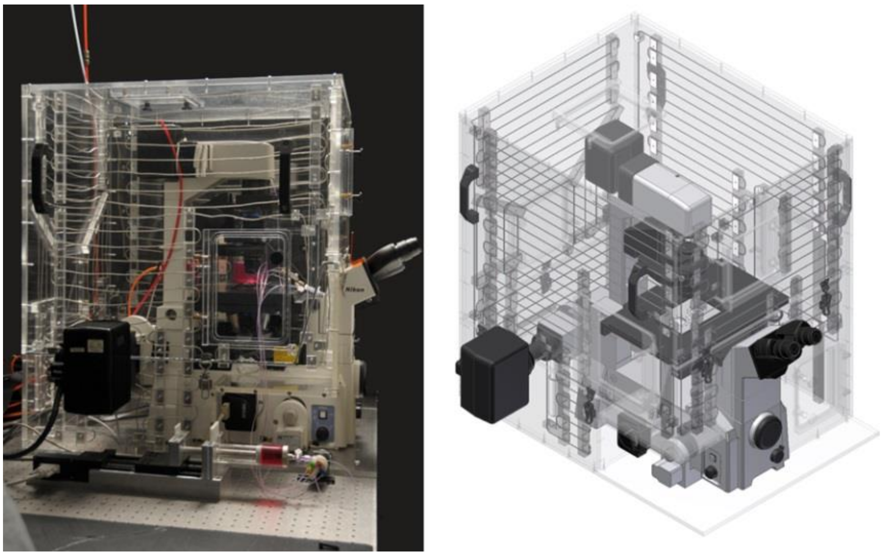

Figure 27: Photograph (left) and schematic image (right) of the incubator housed microscope TE2000-U. Image taken from Christophis, PhD thesis, 2011.[12]

The microfluidic setup consists of a liquid reservoir from which the carrier liquid is sucked through the assembled channel system to the syringe pump (Figure 28).[11-12] In detail, the liquid is distributed to all channels equally via a manifold. The samples are also directly injected into the manifold. Which channel is active is controlled by the selector located between the channel holder and the syringe pump. This form of setup allows a parallel incubation of *e.g.* epithelial cells inside of all four channels simultaneously. Friction in the tubings leads to a pressure drop, which is compensated by application of an overpressure applied to the liquid reservoir. To enable an equilibration of the pressure between the syringe pump and the liquid reservoir without requiring the opening of any of the channels a by-pass tubing directly connects the syringe pump to the manifold and thereby to the liquid reservoir.

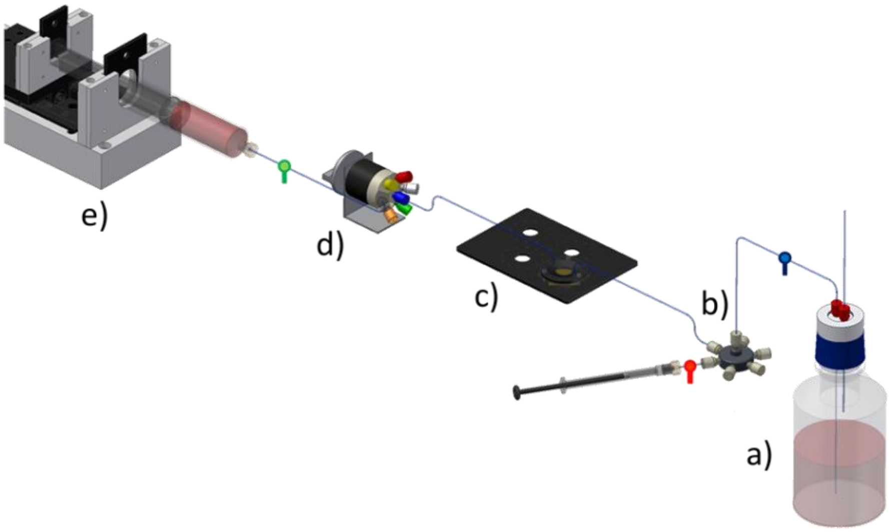

Figure 28: Flow path used for the microfluidic shear force experiments. The liquid is sucked from the liquid reservoir (a) through the manifold (b) that connects all channels to the reservoir through the channels (c) and the selector (d) that allows selection of each channel to which the flow is applied into the syringe pump (e) that controls the flow rate. Image taken from Christophis, PhD thesis, 2011.[12]

3.8.2 CHANNEL SETUP AND ASSEMBLY

The above mentioned channel system is a self-built 'sandwich-like' assembly. This allows the easy exchange of the substrate, which in itself presents the bottom of the assembled channel (Figure 29). The channel walls are a PDMS ring (overall height 130 µm with a 140 µm high inner ring; 2.5 cm long and 1.5 mm wide, hereafter referred to as '25 mm channel') that is cast from a brass mould. The lid is a glass slide (20 × 30 × 2 mm) into which 2 holes were drilled (distance = 2.4 mm) with a diamond tip drill. The holes in the glass lid were aligned to the beginning and end of the PDMS channel walls and to the inlet and outlet tubings fixed in the PDMS seal connecting the assembled channel system to the liquid flow path.

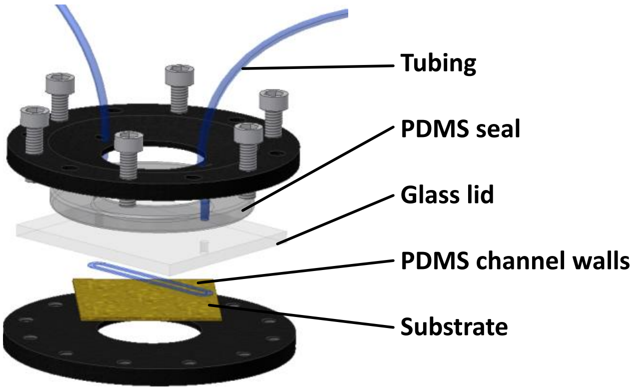

Figure 29: Scheme of the parts required for the assembly of a microfluidic channel. The in- and outlet tubings are held and sealed by the PDMS seal. This is stuck to the glass lid into which 2 holes are drilled. The holes are directly aligned to the in- and outlet tubing and to the beginning and end of the PDMS channel walls. The substrate completes the channel system as the bottom of the channel assembly. Image taken from [12].

The assembly of the system is simple as all elements are stacked and fixed with screws. Solely the fixation of the PDMS channel walls requires a defined protocol. As previously described[12] and shown in Figure 30, the PDMS channel walls were rinsed with MilliQ® water and iso-propanol after each disassembly of the system. The channels were then immersed in 2 % Extran solution for 1 h, kept in MilliQ® water over night and immersed in iso-propanol for ~ 30 min (at least 5 min). Before channel alignment the glass lid was cleaned with 2 % Extran, MilliQ® water and iso-propanol using dust free wipes. A droplet of EtOH *p.a.* on the lid on which the PDMS channel 'swam' and two blunt cannulas were used to align the PDMS channel to the holes of the glass lid. When the ethanol evaporated the channels stuck to the glass lid and were finally rinsed with MilliQ® water.

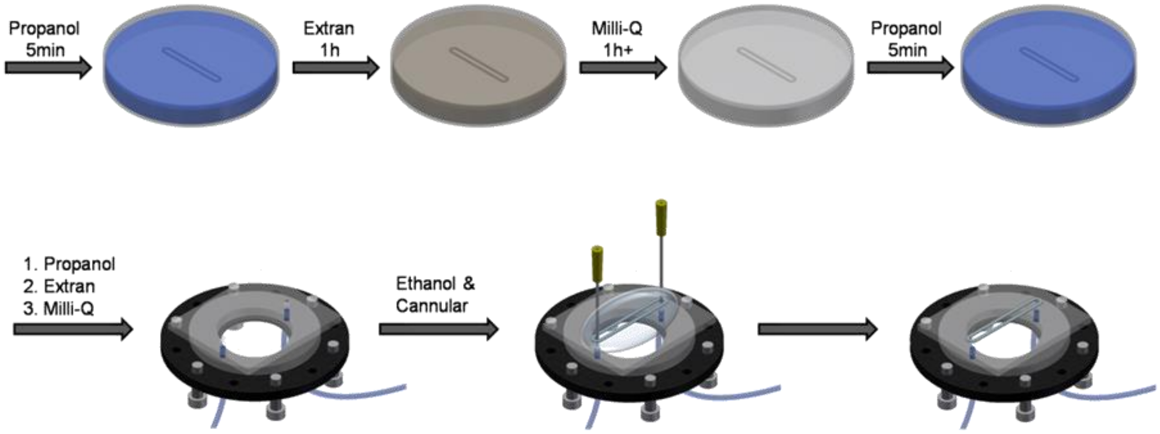

Figure 30: Cleaning and assembly process of the microfluidic channel. Image taken from [12].

3.8.3 MICROFLUIDIC DETACHMENT ASSAY

The microfluidic shear force setup can be used for the observation of the interaction of cells or objects with different surfaces under shear force conditions or for the measurement of the shear force required for the detachment of cells or objects from a variety of surfaces. In this study both types of utilisation were applied.

While the outcome of the two applications was of completely different nature (observation of cell/object-surface interaction under flow and comparison of shear stress required for detachment), the mode of measurement applied in the microfluidic shear force setup was the same. In both cases the detachment assay can be used (Figure 31).[11-12] For measurement of such an assay the channel system was assembled as described in the previous section. The test objects or cells were then injected into the channel system via a 2-way valve connected to the manifold. Here, alteration of the selector controlled which channels were loaded with test objects. After injection the selector was switched to the bypass tubing and the 2-way valve connecting the manifold to the liquid reservoir was opened applying an overpressure of 0.6 bar to the entire system. As elaborated in detail in the Appendix (section 7.1.1.1), among other things, frictional forces led to a pressure loss in the microfluidic setup. This was dependent on the average flow velocity of the liquid, meaning that faster liquid flow increased the pressure loss. Too far reduction of the overall pressure by the pressure loss led to the formation of gas bubbles in the system. As this in essence meant the actual flow differed from the theoretically applied flow making an estimation of the shear stress impossible, the overpressure was applied in order to avoid this scenario. The timespan for which the system remained in this bypass-opened state depended on the type of measurement. In the case of the observation of cell-surface interactions and for measurement of shear forces required to detach particles from surfaces approximately 5 min were required for the cells/particles to sink to the surface and for the pressure to equilibrate between the syringe pump and the liquid reservoir. For measurement of the shear force required to detach cells that actively adhere to a surface such as *e.g.* epithelial cells a longer incubation time was required. For fibroblasts Christophis *et al.* demonstrated that 5 h are sufficient to allow reproducible adhesion while not risking detachment of the cells due to proliferation.[11] After the appropriate incubation time the program controlling the movement speed of the syringe pump was started. For nearly all measurements in this study the movement speed of the syringe pump and thereby the shear stress was increased by 2.33 % every 0.5 s, resulting in a logarithmic increase of the shear stress over time (Figure 31 A). The only exception to this experimental procedure was necessary for the characterisation of the epithelial cell lines HepG2Iso and HepG2 (results shown in section 4.1). Here a pulse of approximately 10 dyn/cm² lasting 0.5 s preceded the stepwise increase of the shear stress (Figure 31 B). This pulse was necessary as the cells sometimes spontaneously adhered to the HA surface after injection and this ensured that all cells were detached from the surface at the beginning of the measurement.

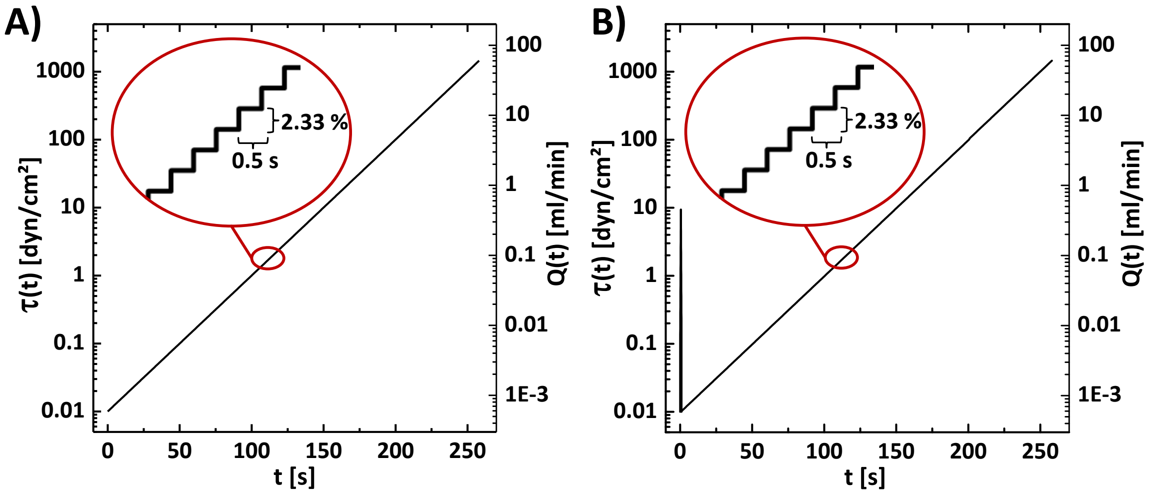

Figure 31: Scheme of the two types of detachment assay applied in this study. A) The regular detachment assay. The shear stress was stepwise increased from ~ 0.01 dyn/cm² to ~ 1,000 dyn/cm² every 0.5 s. B) Modified detachment assay with an initial 10 dyn/cm² pulse for 0.5 s used to detach spontaneously adhering cells.

The wall shear stress τ_n applied in each step can generally be described by

$$\tau_n = \tau_i * GC^n \tag{17}$$

With τ_i being the initially applied shear stress, GC the growth coefficient, by which the shear stress was increased in each step (*e.g.* 1.0233 for a 2.33 % increase), and n the step number. However, the growth coefficient was related to the step duration Δt (*e.g.* long steps with large GC could have the same overall shear stress increase as short steps with small GC). This made the comparison of the overall increase between different constellations (GC and Δt) difficult. As shown in Equation (18), substitution of GC by the step duration independent growth rate of the shear stress R_τ led to a more general description of the wall shear stress τ_{t_n}. For further elaboration see also the Appendix (section 7.1.1.3).

$$\tau_n = \tau_i * GC^n * \tau_{t_n} = \tau_i * GC^{\frac{\mathrm{n}*\Delta t}{\Delta t}} = \tau_i * \left(GC^{\frac{1}{\Delta t}}\right)^{\mathrm{n}*\Delta t} = \tau_i * (R_\tau)^{\mathrm{t}_n} = \tau_{t_n} \tag{18}$$

τ_{t_n} is the wall shear stress (hereafter referred to simply as 'shear stress') applied in a given step, t_n is the duration for which the experiment had proceeded (multiple of the step duration; $t_n = n * \Delta t$, $n = 0,1,2,3\ldots$), R_τ (growth rate of the shear stress) is the step duration independent factor by which the shear stress was increased each step and τ_i the initial shear stress applied to the channel system. The liquid flow rate, which was generated by the syringe pump, is directly correlated to the shear stress applied to the surface. In fact, τ_i can be calculated from the liquid flow rate (Q), the channel dimensions (width w and height h) and the viscosity of the liquid (μ) according to Equation (19).

$$\tau_i = \frac{6Q\mu}{h^2 w} \tag{19}$$

This calculation follows the Poiseuille model for parallel plate flow channels (Figure 32) using the Purday approximation and the fact that the ratio between the channel height and the channel width was large.[185-188] The derivation of the formula can be found in the Appendix (section 7.1.1.3). A prerequisite for the application of the approximations made there is the existence of a fully developed laminar flow. Here, a defined velocity gradient along the y-axis (orthogonal to the channel bottom/top) can be anticipated. In such a setting the flow can simply be viewed as a stack of non-mixing layers parallel to the wall. In the case of turbulent flow the calculation is more complicated. It relies on the modelling of the viscosity-affected inner region (the near-wall region) for solving the velocity gradient along the y-axis. This is possible by either applying semi-empirical formulas called ‘wall functions’ (the near-wall region is bridged) or by ‘near-wall modelling’ (the near-wall region is resolved by modifying turbulence models with a mesh all the way to the wall). The dimensionless Reynold´s number Re can be applied to predict if a laminar or a turbulent flow profile develops. At Reynold´s numbers below 2300 the flow is laminar and a parabolic flow profile as indicated by the grey arrows in Figure 32 can be observed. As shown in the Appendix (section 7.1.1.2) the Reynold´s number Re can be estimated for a flat rectangular channel (height << width) by Equation (20).

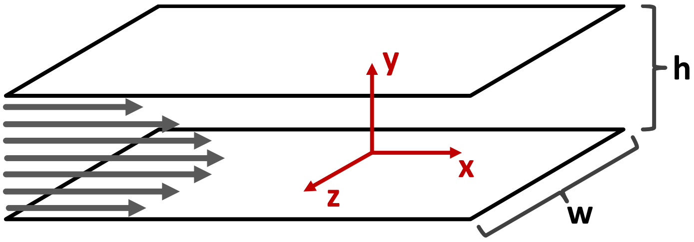

Figure 32: Parallel plate model for unidirectional flow. A parabolic flow profile between two immobile parallel plates is shown. The height is so much smaller than the width of the channel that the shear at the channel sides can be neglected.

$$Re \approx \frac{2Q\mu}{\eta w} \tag{20}$$

With Q being the liquid flow rate, ρ the liquid density, η the liquid viscosity and w the channel width. The maximum flow rate theoretically applicable by the syringe pump was ~ 81 mL/min. Due to the pressure drop in the tubings and the channel system, the practically applicable maximum flow rate was roughly 40 mL/min. Beyond this flow rate the formation of bubbles in the setup was observable. As the viscosity η is in the denominator the calculation of the maximum Reynold´s number presented here was done for the relatively low viscosity of cell culture medium at 37 °C (0.72×10^{-3} kg $m^{-1}s^{-1}$).[187] The viscosity of buffer solutions such as PBS buffer at lower temperatures is always larger than this leading to lower Reynold’s numbers. The liquid density ρ is ~ 1kg/L. The channel dimensions can be estimated as h = 135 µm and w = 1500 µm (which is neglectable due to the ratio w/h being so large). From this the Reynold's number calculates to ~ 830 (~ 1670 for the theoretically applicable 81 mL/min). This is well below the threshold Reynold´s number of 2300 for laminar flow.[177]

By expressing τ from Equation (19) with the Reynold´s number as given by Equation (20) the shear stress may also be estimated as

$$\tau \approx \frac{Re}{h^2} \tag{21}$$

This correlation emphasise the importance of maintaining small channel heights, as at a constant Reynold´s numbers the maximum applicable shear stress is correlated to the square of the channel height.

3.8.4 DATA ANALYSIS OF ADHESION STRENGTH EXPERIMENTS

The critical shear stress τ_{50} required to detach 50 % of the adhered organisms or particles (both hereafter referred to as objects) was an ideal variable to compare the adhesion strength of objects to different surfaces.

To determine the critical shear stress τ_{50} the number of objects adherent to the surface at a given time $N(t)$ was normalised to the number of objects initially adherent to the surface in the field of view (FOV) N_{ad} as shown in equation (22).

$$N(\tau) * N_{ad}^{-1} * 100\% \tag{22}$$

τ_{50} was, therefore, defined as

$$\tau_{50} = N(\tau_{50}) * N_{ad}^{-1} * 100\% \tag{23}$$

with

$$N(\tau_{50}) = \frac{1}{2} N_{ad} \tag{24}$$

The critical shear stress τ_{50} could easily be derived from the plot by magnification of the detachment area of the curve and utilisation of the 'Screen-Coordinates'-tool provided by OriginPro 9.1G©. For y = 0.5 the x-coordinate was equal to the τ_{50} value of the given object and surface (Figure 33).

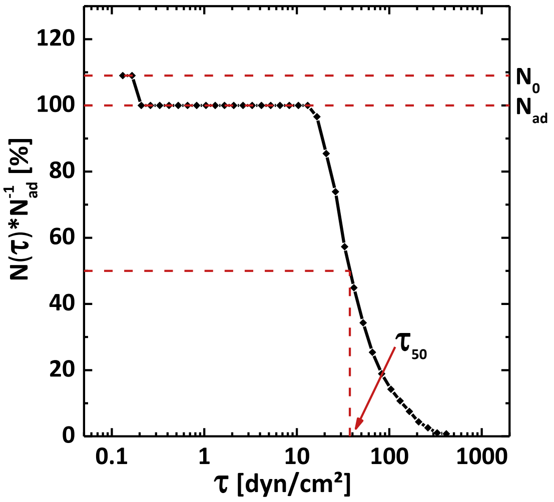

Figure 33: Explanatory graph showing the evaluation of the detachment of adherent cells or particles from surfaces in the microfluidic shear force setup. After normalisation of the adherent objects $N(t)$ to the initially adherent objects N_{ad} the τ_{50} value could easily be determined from the plot visually.

3.8.5 DATA ANALYSIS OF CELL-SURFACE INTERACTION EXPERIMENTS

The cell concentration of the cell line suspensions injected into the channel system was adjusted to 10^6 cells/mL. In the case of primary material this was not always possible, as counting and resuspension of the cells directly before the experiments was avoided to prevent stress to the cells or the amount of cells was simply not sufficient. For this reason and to ensure ideal comparability between all experiments the number of cells $N(\tau)$ interacting with the surface at a given time (the time elapsed in the measurement was directly correlated to the shear stress) was normalised to the number of cells initially visible in the FOV N_0 as shown in Equation (25). By doing so adhesion curves as shown in Figure 34 were measured.

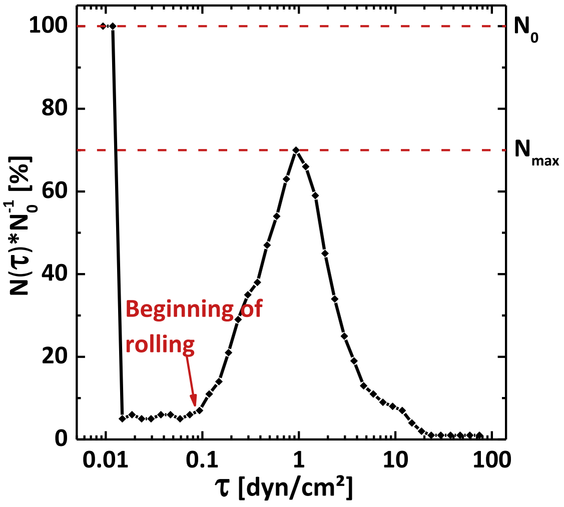

Figure 34: Explanatory graph showing the evaluation of the interaction of suspension cells with surfaces under flow in the microfluidic shear force setup. The number of interacting cells was normalised by the number of cells initially visible in the FOV N_0.

$$N(\tau) * N_0^{-1} * 100\% \tag{25}$$

The supplementary Video S3 found in the Appendix (description found in section 7.1.2.1, video provided on the supplementary CD) demonstrates the direct correlation between the video recorded during measurement and the interaction curve obtained after analysis. From the interaction curve values such as a threshold shear stress, beyond which a flow-induced rolling on the surface took place, and the shear stress, at which the maximum fraction of interacting cells N_{max} was observed, could be derived visually.

In contrast to the various types of suspension cells used in this study, which all showed reproducible tendencies to interact with the test surfaces (mainly HA-coated substrates), the two related epithelial cell lines HepG2 and HepG2Iso showed a highly heterogeneous tendency to interact with the surfaces. Depending on unidentified factors, which may involve cellular age, culture density or storage duration on ice, this ranged from cells spontaneously adhering to the substrate directly after injection into the channel system yielding no chance of observing any interaction under flow, over slow adhesion and a strong tendency interact with the HA-coated surface under flow, to a generally weak cell-surface interaction.

To mitigate this issue and to allow comparison of different experiments, an additional normalisation was applied for this specific cell type. As for the suspension cells, each experiment was normalised to the number of initially visible cells (normalisation to N_0), yielding the fraction of interacting cells in per cent. In addition, the fraction of interacting cells of the corresponding control group (untreated cells or cells treated with siRNA, respectively) was defined as full interaction, with the fractions of interacting modified cells corresponding to this value. This value was used to compare the influence of *e.g.* antibody blocking or siRNA treatment.

An example for this normalisation is shown in Figure 35. The two control measurements were averaged to the mean curve (black line, Figure 35 B). Due to the correction process the values were no longer given in per cent but rather in arbitrary units (a.u.). Furthermore, as the initial fraction of cells visible in the FOV was no longer of relevance it is not shown in the following graphs depicting the HepG2Iso-surface interaction.

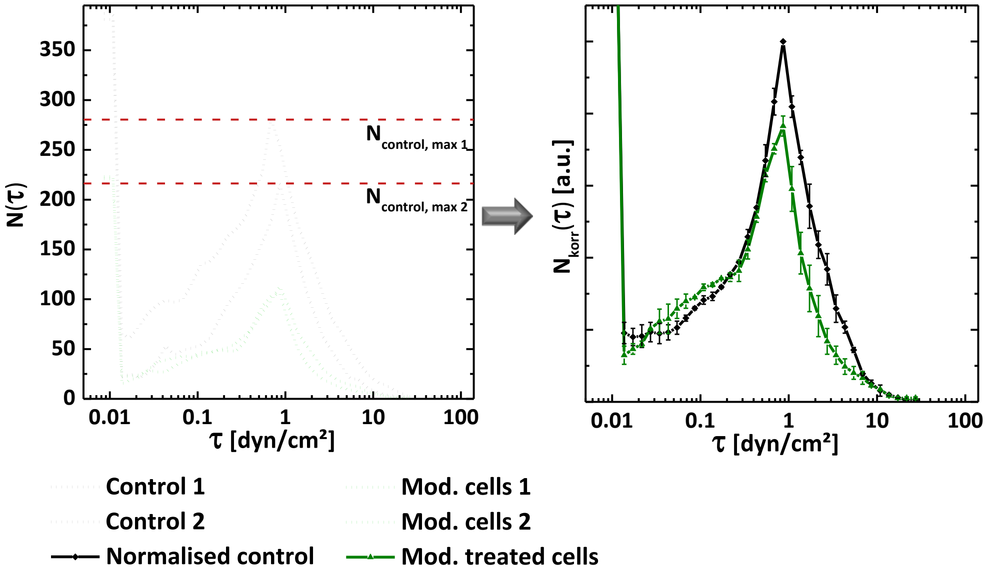

Figure 35: Exemplary graph showing the evaluation of the interaction of epithelial cells with surfaces under flow in the microfluidic shear force setup. The number of interacting cells was normalised to the respective control.

3.8.6 OPTIMISATION AND PROOF OF APPLICABILITY OF THE MICROFLUIDIC SHEAR FORCE DEVICE

Earlier studies in our workgroup experienced certain short comings concerning the precision and reproducibility of measurements of the shear stress required to detach objects or cells from a given surface in the microfluidic shear force device.[268-269] The studies focussed on the interaction of marine bacteria and of diatoms with potentially adhesion-resistant surfaces. While the recent studies clearly revealed the potential of the microfluidic assay to differentiate adhesion strength on different surfaces, the complexity of a microfluidic experiment becomes obvious when small effects cannot be distinguished due to the variations between experiments. To further optimise the microfluidic setup and more importantly to prove the applicability of the same for the use in the context of this work, calibration measurements were conducted. The work of Maria Alles demonstrated that the position of measurement inside the channel system, the concentration of adherent objects, the channel dimensions and the possibility of pressure fluctuations due to the pressure reducer were not responsible for the varying critical shear stresses τ_{50} measured for one object-surface type combination.[269] She could show that with a different channel assembly as used in this work (13 mm x 0.9 mm x 140 µm, hereafter referred to as ‘13 mm channel’) the application of an aluminium spacer could increase the reproducibility in one channel while only marginally improving the reproducibility between different assemblies of a channel system.[269]

In this work the effect of aluminium spacers (height 130 ± 5 µm) on the reproducibility of the channel dimensions after reassembly, on the stability of the channel dimensions during the experiments and on the inter- and intra-channel reproducibility after reassembly was studied. The effect of the maximum flow rate applied to the channel system during measurements was also analysed. Therefore, the τ_{50} values derived from successive measurements in a single channel and the corresponding channel dimensions were obtained. The progression of these variables and the relation between the same was then correlated to the presence or absence of a spacer. Finally, the applicability of the microfluidic shear force device for cell-surface interaction studies was demonstrated.

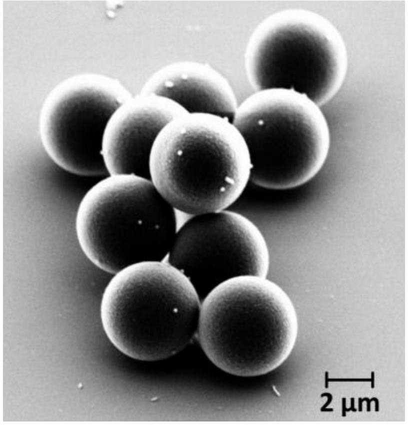

Figure 36: SEM image of the 4.5 µm carboxy terminated polystyrene microspheres used in this study.

As in the study of M. Alles, carboxy-terminated polystyrene microspheres with a mean size of 4.5 µm (later referred to as particles, Figure 36) were used. 40 µl of the particle stock solution were diluted in 1 mL PBS buffer (pH = 7.4) resulting in a concentration of approximately $20 \cdot 10^6$ particles/mL. The particles were washed thrice in PBS buffer by centrifugation (13,000 rpm, 4 min). The prepared particle suspension was stored at RT until use and was always used the day of preparation. SAMs were chosen as control surface as they present a flat surface with reproducible defined properties. If not mentioned otherwise the sample surface used in this study was a HUDT SAM on which the particles were incubated for 5 min prior to detachment.

3.8.6.1 INFLUENCE OF THE CHANNEL DIMENSIONS

Table 4 gives the mean channel dimensions observed throughout the particle measurements. In contrast to the improvement in the channel height fluctuation during assembly with a spacer found by M. Alles, no pronounced differences between the channel dimensions with and without a spacer were observed for the 25 mm channels. If differences between the measurements with and without a spacer occurred it was not due to the channel dimensions after assembly. This was in accordance with the findings of M. Alles that showed a general independence of the τ_{50} value measured from the channel dimensions after reassembly.[269]

Table 4: Mean values measured for the channel dimensions. The table gives the values for the channel height and width averaged over all measurements conducted in this section. 17 independently assembled channels without a spacer and 13 independently assembled channels with a spacer.

	Channel height [µm]	SD [µm]	Error [%]	Channel width [µm]	SD [µm]	Error [%]
Without spacer	136.5	3.8	2.8	1484.0	73.9	5.0
With spacer	137.0	2.4	1.8	1477.2	60.3	4.1

Figure 37 shows the correlation between the progression of the τ_{50} value and the channel dimensions in a channel lacking a spacer. It clearly shows that while the τ_{50} value initially decreased reaching a plateau at the third run, the channel dimensions did not noticeably change in the relaxed state (measured between experiments, but with the overpressure applied). A similar but inverted approach to a plateau is shown in Figure S3 (Appendix section 7.1.3.1). This means that the channel dimensions were not only independent of the assembly but they were also not permanently changed by running measurements, even though the τ_{50} value changed. This finding presents an expansion of the findings of M. Alles that demonstrated the independence of the dimensions after initial assembly.[269]

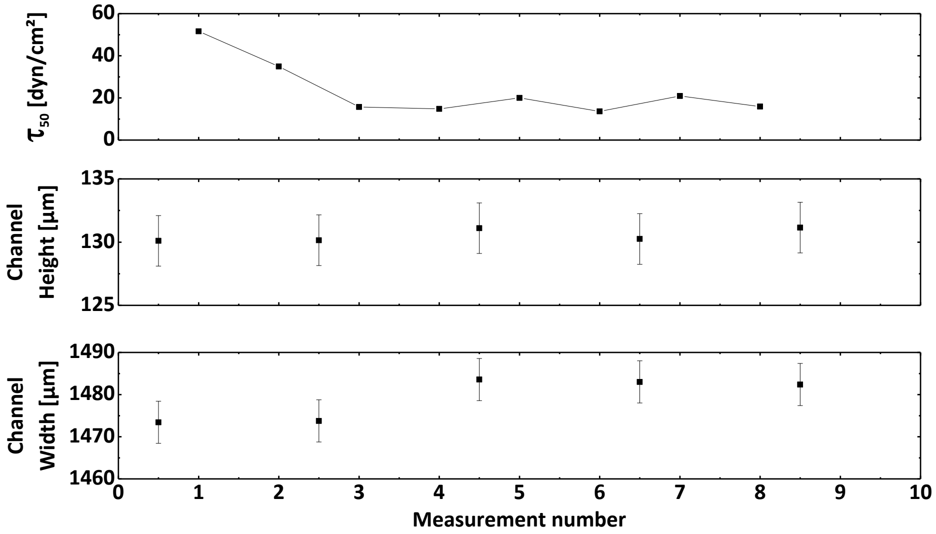

Figure 37: Correlation between the τ_{50} values measured in succession in one single channel without application of a spacer and the channel dimensions. The τ_{50} value increased over the first three measurements before reaching a plateau. The channel dimensions were measured between the experimental runs, thereby only representing the dimensions if no flow is applied. The errors given for the channel dimensions are estimated measuring errors.

3.8.6.2 EFFECT OF CHANNEL-REASSEMBLY AND APPLICATION OF SPACERS

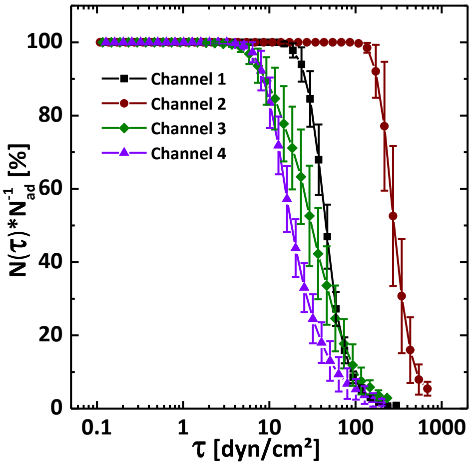

Figure 38: Detachment curves measured in 4 different channels assembled in parallel with a spacer. The data stems from one experimental setup with at least 3 repeats per channel. The error bars represent the SD.

Figure 38 shows the mean detachment curves measured in four channel systems assembled in parallel. It is easily seen that not only did the mean curves greatly differ from each other but the fluctuation in one channel was also apparent. It need not be mentioned that the τ_{50} values greatly differed (ranging from ~ 16 dyn/cm² to 300 dyn/cm²). This figure demonstrates not only that was the fluctuation between the channels large without application of a spacer but so was the fluctuation in the measurements in one single assembled channel system. For this reason the fluctuations in one channel were analysed by repeatedly assembling the channel and conducting measurement series in each assembly. This was then compared to the same channel repeatedly assembled with a spacer. The results are shown in Figure 39. The overviews over all detachment curves measured with and without a spacer give an impression of the fluctuations observed in the one channel (Figure 39 A). The graphs depicting the succession of the corresponding τ_{50} values (Figure 39 B) indicate that the fluctuation of the initial τ_{50} value measured with a spacer was larger than that without a spacer. As this is true for this set of measurements it shall be mentioned here that strong fluctuations were observed in other channels without a spacer. This is indicated in Figure 38, which shows that the τ_{50} value of channel 2 by far exceeded the τ_{50} values otherwise discussed in this section both with and without a spacer. The fact that the application of a spacer did not increase the reproducibility of the initially measured τ_{50} value was in line with the findings of M. Alles who also could not observe any improvement of the inter-channel reproducibility when applying a spacer.[269]

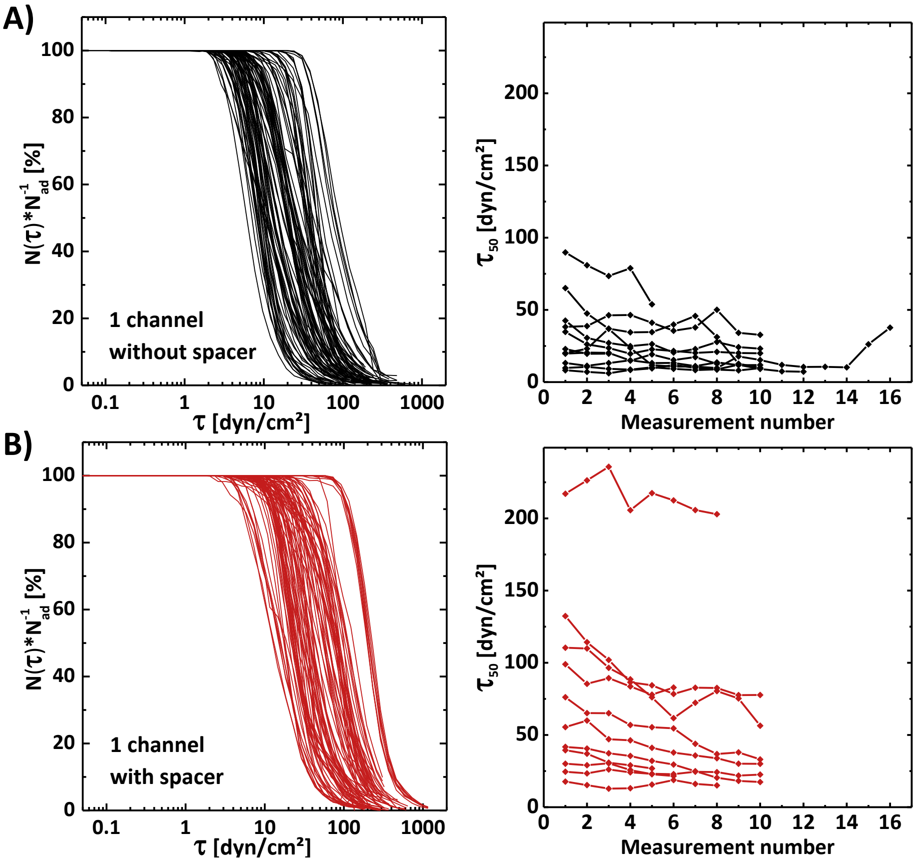

Figure 39: Comparison between the fluctuation in measurements in one repeatedly assembled channel with and without a spacer. The left graph shows all detachment curves measured and the right graph shows the progression of the τ_{50} values in each experimental series. The overviews are shown for measurements without (A) and with (B) a spacer.

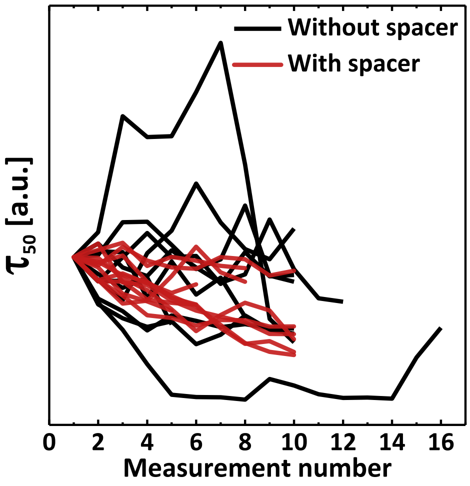

Figure 40: Progression of the τ_{50} value of each measurement series.

Next to the initially measured shear stress the reproducibility in each single assembly was a factor that needed to be considered. This tendency to of variation in one channel assembly was directly correlated to the percentage error of the measurement. This error should have been larger in a system prone to fluctuation of the measured values than in one which was not. Figure 40 shows the course of each measurement series. The τ_{50} values were divided by the first value measured in the corresponding series, resulting in each series beginning at the same value. This allowed the direct comparison of the course of the different measurement series. Not only did the general trend appear broader in the channel lacking a spacer, but outliers concerning the inter-channel reproducibility were also only apparent if no spacer was present.

This observation becomes even more apparent in Figure 41. The figure shows the mean τ_{50} values plotted against the percentage error of the respective measurement series. The centre scatter plot is surrounded by box plots of the τ_{50} values on the abscissa and the percentage errors on the ordinate. The box plots give the 1st (lower box margin), 2nd (middle line; median) and 3rd (upper box margin) quartile of the data and the whiskers represent the standard deviation of the data. A detailed explanation of box plots and what they show is given in the Appendix (section 7.1.2.3). To ensure ideal comparability only the first five τ_{50} values of each of the experimental series (ensuring the same number of measurements in each series) shown in Figure 39 were used for the calculation of the mean τ_{50} values and the percentage errors. This way lasting trends, such as a continuous reduction of the τ_{50} values in one series, always had the same influence on the overall percentage error. The graph clearly shows that, while the τ_{50} values tended to be slightly higher if a spacer was applied, the percentage error and its fluctuation (represented in the SD) were lower in the presence of a spacer. The overall mean percentage error of the τ_{50} values without a spacer was 18.1 ± 12.0 % and with that the mean value was roughly twice as high and the SD approximately thrice as high as that measured for the channel with a spacer (10.9 ± 3.9 %). The complete set of τ_{50} values and the corresponding SD and percentage errors are shown in Table S1 (Appendix section 7.1.3.2). These findings demonstrate that the application of a spacer helped improve the reproducibility in one assembled channel, while having nearly no effect on the reproducibility between independently assembled channels. Again this correlated well with the findings M. Alles, who also observed an improvement of the intra-channel reproducibility.[269]

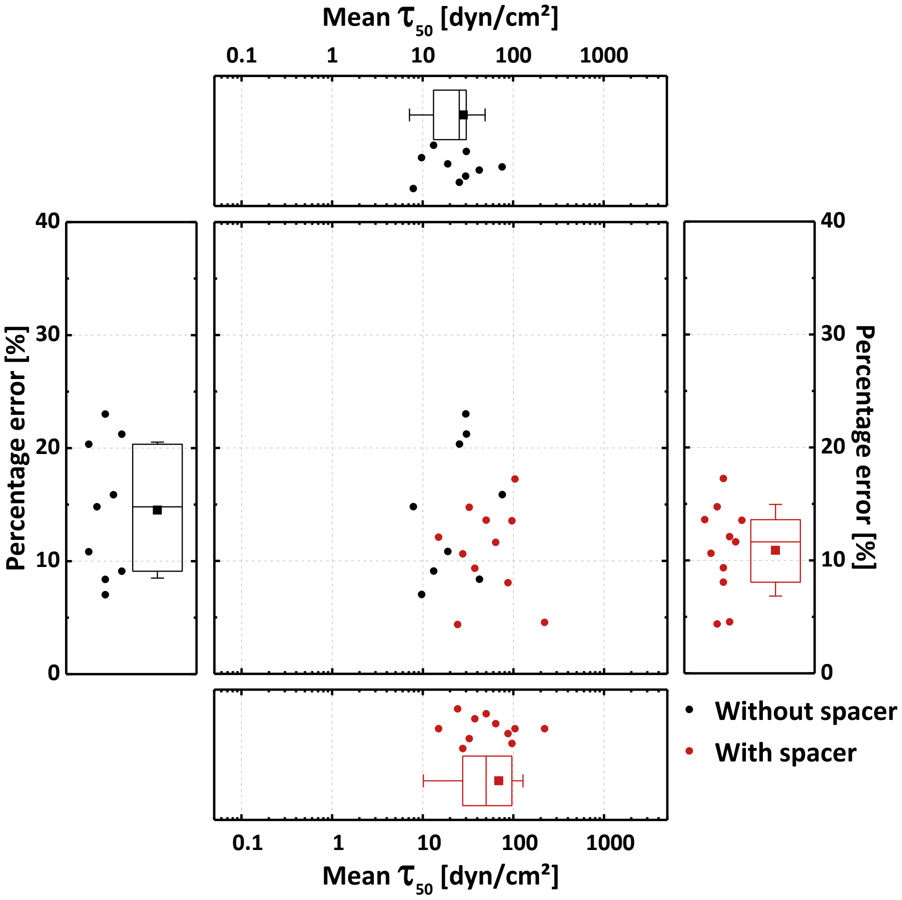

Figure 41: Correlation between the mean critical shear stress τ_{50} and the percentage error of the measurement in dependency of the application of a spacer. The centre graph shows the direct comparison of the percentage error for each set of measurements and the corresponding τ_{50} value for the detachment of particles with and without application of a spacer. The left and right box plots show the distribution of the percentage errors, while the top and bottom box plots show the distribution of the corresponding mean τ_{50} values. The box plots give the 1st (lower box margin), 2nd (middle line; median) and 3rd (upper box margin) quartile of the data and the whiskers represent the standard deviation of the data. ● gives the τ_{50} values, ■ is the mean percentage error (left, right) or the mean τ_{50} value (top, bottom). The whiskers represent the SD. The length of each experimental series was the same (n = 5).

3.8.6.3 DEPENDENCY ON THE EXPERIMENTAL PARAMETERS AND ON THE CHANNEL SYSTEM USED

The experimental parameters (the step duration Δt and the initial shear stress τ_i) and the channel setup used (13 mm channel or 25 mm channel) were another set of parameters studied towards their influence on the reproducibility of the measurements of the critical shear stress τ_{50}. The step duration Δt represents the time span for which a given shear stress was applied and R_τ is the step duration independent factor by which the shear stress was increased in each step. Equation (18), first introduced in section 3.8.3, demonstrates the calculation of the shear stress τ_{t_n} applied to the system after a given time t_n (= $n * \Delta t$, n = 0,1,2,3…) in dependence of the channel dimension dependent initial shear stress τ_i.

$$\tau_{t_n} = \tau_i * (R_\tau)^{t_n} \tag{18}$$

The influence of the experimental parameters is illuminated first. To determine this influence, combinations of two step durations (Δt = 0.5°s and Δt = 5°s) and two initial shear stresses (τ_i = 0.01 dyn/cm² and τ_i = 0.1 dyn/cm²) were tested in a successive series of measurements in a single channel. The overall increase of the shear stress was the same in all measurements (R_τ = 1.047). These parameters were chosen as they corresponded to those used in this work for cell-surface interaction measurements (Δt = 0.5°s, τ_i = 0.01 dyn/cm²) or to those used by M. Alles and M.P. Arpa Sancet from our workgroup for the detachment of marine organisms from various surfaces (Δt = 5°s, both τ_i = 0.01 dyn/cm² and τ_i = 0.1 dyn/cm²).[268-269] The channel dimensions in the relaxed state (between two measurements, with the overpressure applied) were recorded between the measurements and compared to the τ_{50} values obtained from analysing the detachment curves. From Figure 42 it can be seen that the τ_{50} values and the channel dimensions were completely independent of both the step duration and the initial shear stress applied. Comparable results are also shown in Figure S4 (Appendix section 7.1.3.3) demonstrating the reproducibility of this finding.

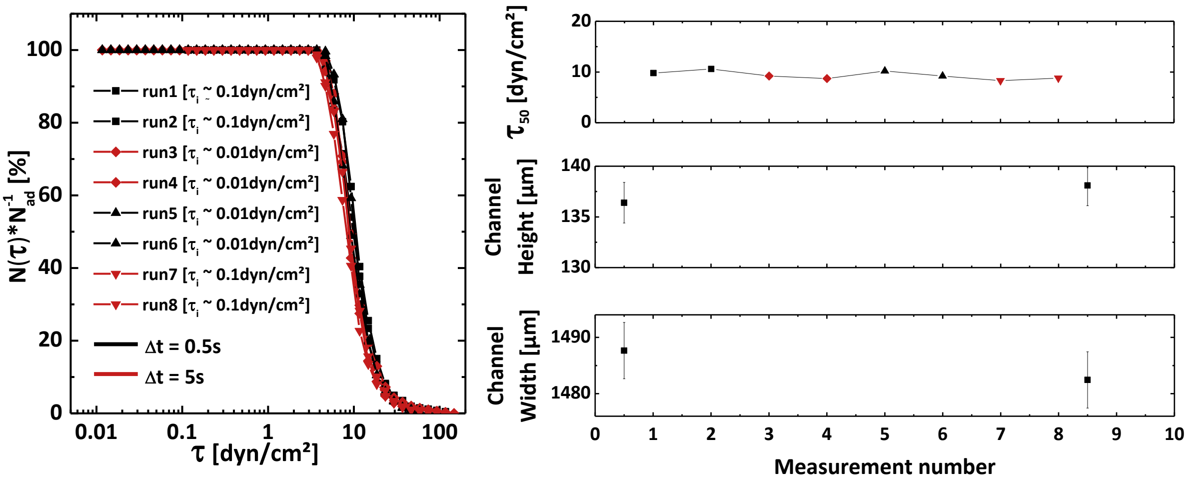

Figure 42: Effect of the experimental procedure on the τ_{50} values. The step duration Δt and the initial shear stress τ_i were varied. A spacer was used. The τ_{50} values remained nearly constant throughout the measurement, as did the channel dimensions. The errors given for the channel dimensions are estimated measuring errors.

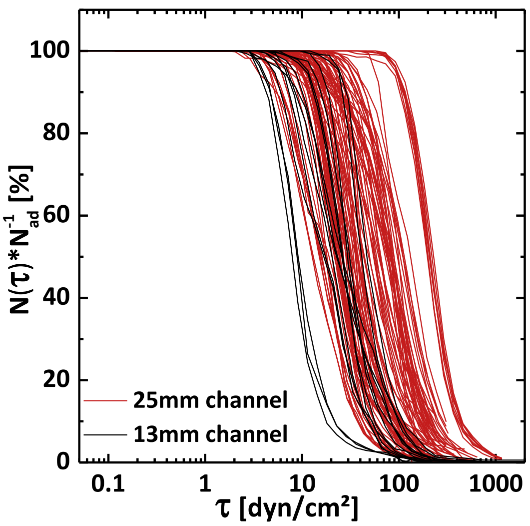

Figure 43: Comparison between the detachment curves obtained in a 13 mm channel by M. Alles and those obtained in a 25 mm channel. The results were all obtained in one channel of each setup that was repeatedly reassembled with a spacer. n = 15 in the 13 mm channel in 5 independent reassemblies. n = 93 in the 25 mm channel in 11 independent reassemblies.

The influence of the setup size was investigated by comparing the results for the detachment of particles from HUDT SAMs obtained by M. Alles in a 13 mm setup with those obtained in this study with a 25 mm setup. All detachment curves obtained this way are shown in Figure 43. All in all the detachment curves overlapped well, with a shift to higher shear stresses in the 25 mm setup. A more detailed view of the data is given in Figure 44. This graph shows the correlation between the mean τ_{50} values and the corresponding percentage error in each of the two setups. In accordance to the detachment curves shown in Figure 43 the centre scatter plot and the box plots at the abscissa clearly show that the mean τ_{50} values measured fluctuated in both setups. As each mean τ_{50} value was calculated from an individual experimental series (successive experiments in one fully assembled channel system), it can be seen as a measure for the reproducibility of the τ_{50} values measured after the reassembly of the channel (for each channel size the same channel was repeatedly reassembly). The fluctuation of the τ_{50} values, therefore, demonstrates the large fluctuation upon reassembly of the channel in both channel systems tested. The fact that the fluctuation appears to be bigger for the 25 mm setup may be ascribed to the larger number of experimental repeats. Bearing in mind that the dimensions of the two setups were so different and that both setups were prone to the just discussed strong fluctuations of the τ_{50} values measured, it was remarkable to see such a good correlation between the data obtained. Still, a small statistical indifference between the sample cohorts was determined (Student´s t-test; $p = 0.09 > 0.05$), even though the SD of the two sample cohorts fully overlapped. While the distribution of the mean τ_{50} values gives an impression on the reproducibility after reassembly, the mean percentage errors and their distribution represent the reproducibility in each experimental series and how this deviated between reassemblies. The distributions of the percentage error of the individual measurement series were similar, with the mean lying in the range of 5-10 % and a clear statistical indifference between the data sets (Student´s t-test; $p = 0.36 > 0.05$). This demonstrated that the reproducibility in each experimental series was roughly the same for all measurements independent of the channel system tested.

Overall, these findings demonstrate that the error of the measurement should be sought for elsewhere than in the channel dimensions. The fluctuation in each of the experimental series in both setups was comparable and the largest deviations were observed upon reassembly of the channels.

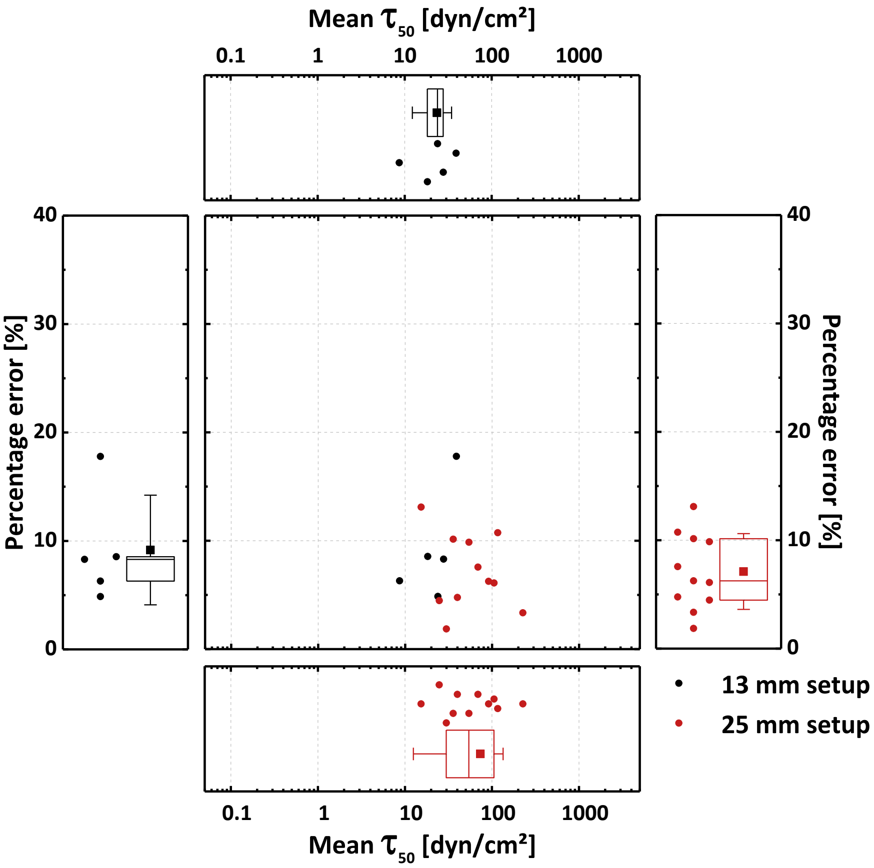

Figure 44: Correlation between the mean critical shear stress τ_{50} and the percentage error of the measurement in dependency of the channel setup used. A spacer was used for all measurements presented in this plot. The centre graph shows the direct comparison of the percentage error for each set of measurements and the corresponding τ_{50} value for the detachment of particles from a HUDT SAM in either a 13 or 25 mm channel setup. The left and right box plots show the distribution of the percentage errors of the mean τ_{50} values. ● gives the τ_{50} values, ■ is the mean percentage error (left, right) or the mean τ_{50} value (top, bottom). The whiskers represent the SD. The length of each experimental series was the same (n = 3).

3.8.6.4 DEPENDENCY ON THE MAXIMUM SHEAR STRESS APPLIED

As can be seen from the particle detachment data discussed so far, the τ_{50} values measured were small in comparison to the maximum shear stress that could have been applied with the 25 mm channel setup (~ 1,000 dyn/cm², see section 3.8.3). Therefore, an analysis of the effect of applying different maximum shear stresses during the experimental procedure was undergone (experiment aborted at ~ 200 dyn/cm² or at ~ 1,000 dyn/cm²). The measurement procedure is shown in Figure 45. Ten measurements were conducted in succession in each channel assembly. The first six measurements were aborted at approximately 200 dyn/cm², while the last four were ramped up to 1,000 dyn/cm². Of these ten data points the first four were compared to the last four to ensure ideal comparability between the data sets.

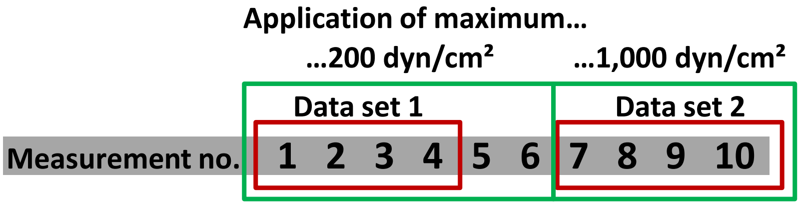

Figure 45: Measurement procedure for the analysis of the effect of the maximal applied shear stress on the τ_{50} values. Ten measurements were conducted in succession in one single channel assembly. Of these measurements the first 6 were aborted when the shear stress at the channel floor reached approximately 200 dyn/cm². The last 4 measurements were aborted only at approximately 1,000 dyn/cm². Of the obtained τ_{50} values the first 4 were combined as ‘data set 1’ (experiment aborted at 200 dyn/cm²) and the last 4 as ‘data set 2’ (experiment aborted at 1,000 dyn/cm²). This was done to ensure ideal comparability between the two data sets.

The effect of the different maximum shear stresses applied was analysed for channels with and lacking a spacer. As shown in Figure 46 the percentage error was larger for channels lacking a spacer than it was for those with a spacer if the experiment was aborted when a shear stress of approximately 200 dyn/cm² was reached. This undergirds the findings discussed in section 3.8.6.2 as nearly the same trend was observed. The final measurements (application approximately 1,000 dyn/cm²) of each series exhibited a surprisingly low percentage error. It was not only comparable for channel with and without a spacer, but it was also lower than that observed during the first measurements. A possible explanation for this behaviour could be that the channels somehow adjusted themselves during the measurements enabling lower deviations after a sufficient amount of experimental runs. Interestingly, the channel dimensions in the relaxed state, meaning the state of the channel between experiments when the over-pressure was applied but no suction was created by the syringe pump, did not change throughout the measurement. As shown in the Appendix section 7.1.3.4 this was regardless of whether a spacer was applied or not.

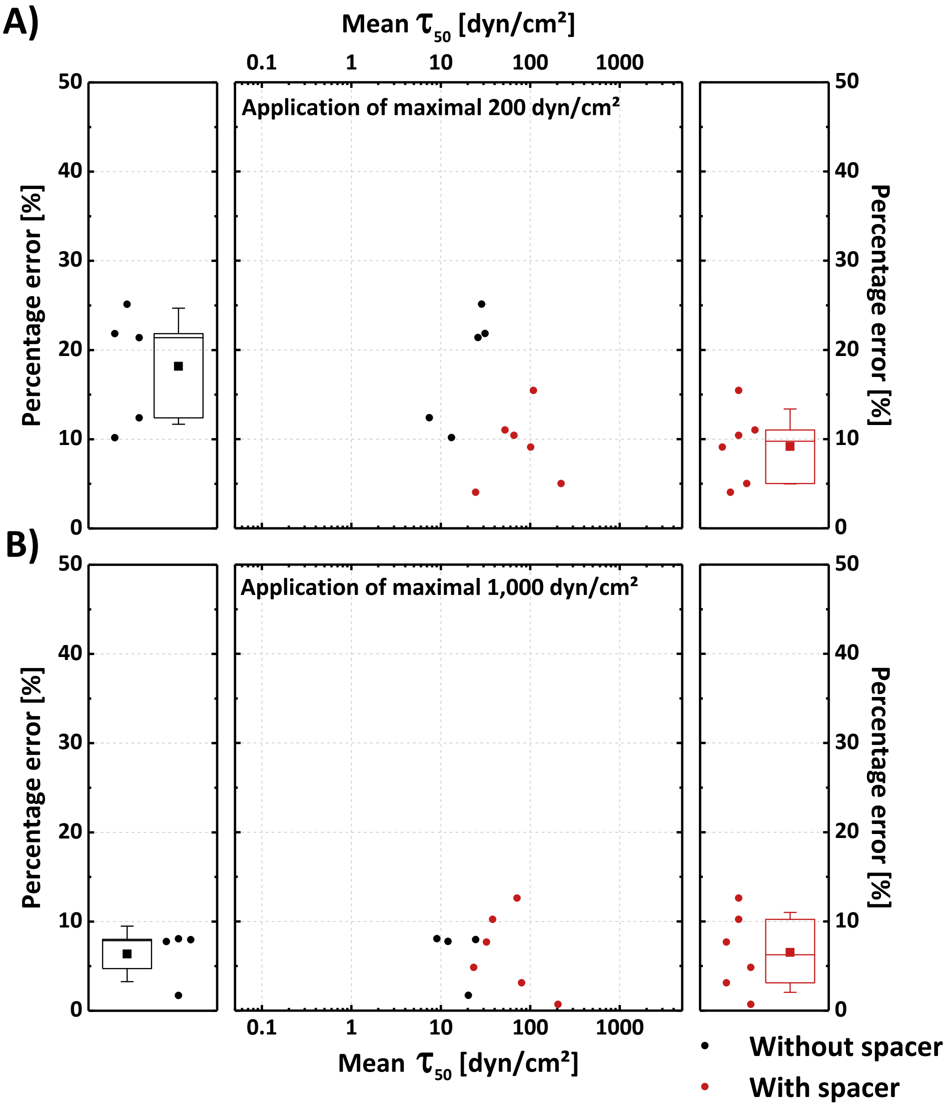

Figure 46: Correlation between the mean critical shear stress τ_{50} and the percentage error of the measurement in dependency of the maximal shear stress applied. The mean values and errors for measurements with maximal 200 dyn/cm² applied are the mean of the first 6 values of the series, while a maximal application of 1,000 dyn/cm² is given by the following 4 values. The centre graphs shows the direct comparison of the percentage error for each set of measurements and the corresponding τ_{50} value for the detachment of particles with either a maximum shear stress of 200 dyn/cm² or of 1,000 dyn/cm² applied. Each is shown with and without the application of a spacer. The box plots of the percentage errors shown on the outside better demonstrate the differences in the mean percentage error and the distribution of the same. ● gives the τ_{50} values, ■ is mean percentage error and the whiskers represent the SD.

3.8.6.5 SYSTEM APPLICABILITY FOR THE CHARACTERISATION OF CELL-SURFACE INTERACTIONS AT LOW SHEAR STRESSES

For this entire work the information whether the microfluidic shear force setup was capable of measuring with sufficient accuracy and reproducibility at low shear stresses to analyse the interaction between cells and surfaces under shear flow was of great importance. To gain an impression of the dependency of the behaviour of the τ_{50} values and the percentage errors on the region of shear stress in which they were measured strongly adherent surfaces were compared to the moderately adherent HUDT SAMs discussed in this work so far. The highly attractive DDT SAM presents a surface type on which high shear stresses are required to detach the particles. Figure 47 shows a comparison between the distribution of the τ_{50} values and the percentage error obtained from measurements on HUDT and DDT SAMs. In both cases no spacer was applied to maximise the effect and to make a comparison to the cell-surface interaction experiments possible, as these too were conducted without spacers. From the centre scatter plot, but more clearly from the abscissa box plots, it can be seen that the two sets of mean τ_{50} values were clearly distinguishable from each other. This demonstrates that, although the measurements were prone to a certain fluctuation between measurements, the setup was obviously capable of differentiating between varying surface types.

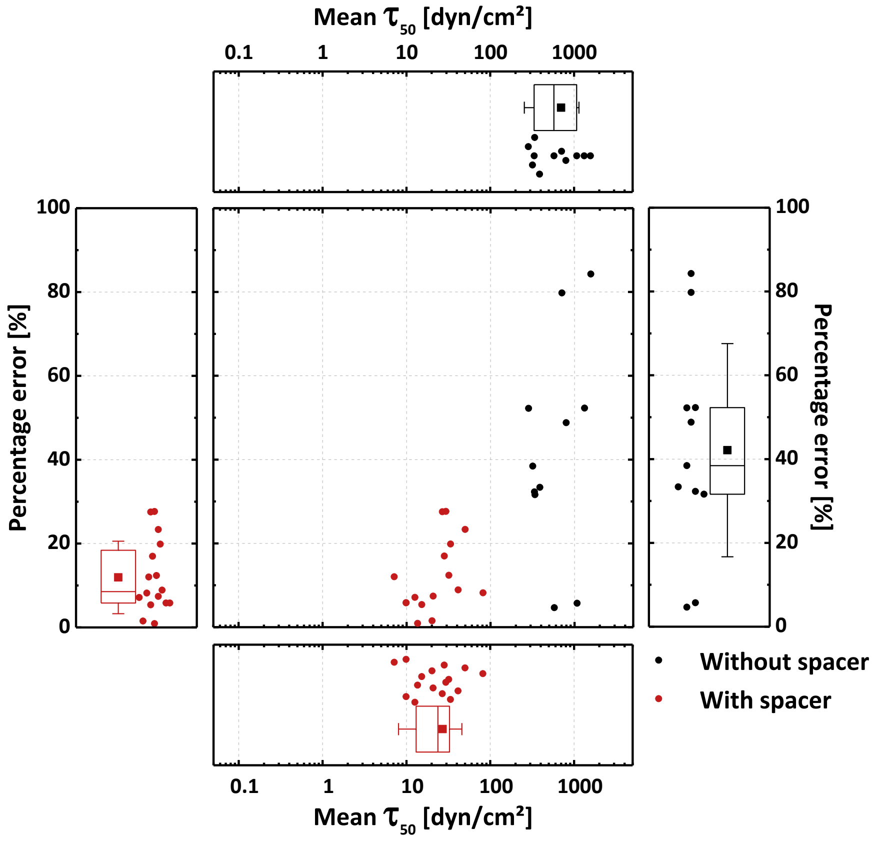

Figure 47: Correlation between the mean critical shear stress τ_{50} and the percentage error of the measurement on two different SAMs (HUDT and DDT). The centre graph shows the direct comparison of the percentage error for each set of measurements and the corresponding τ_{50} value for the detachment of particles from DDT or HUDT SAMs. The left and right box plots show the distribution of the values for the detachment from HUDT and DDT respectively. ● gives the τ_{50} values, ■ is the mean percentage error (left, right) or the mean τ_{50} value (top, bottom). The whiskers represent the SD. The length of each experimental series was the same (n = 3).

The ordinate box plots, in turn, demonstrate that the percentage errors were not only far greater in measurements conducted on highly attractive DDT SAMs, but they were also far more diverse than on HUDT SAMs. In fact the percentage error obtained on DDT SAMs of (42.1 ± 24.39 dyn/cm² was nearly four times as large as that measured on HUDT SAMs, which was (11.9 ± 8.4) dyn/cm². Furthermore, the SD of the percentage error on DDT SAMs, which was thrice more than that measured on HUDT SAMs, again demonstrated the high fluctuation of the measurements. The complete data set is shown in Table S2 (Appendix section 7.1.3.5). Concerning the dependency on shear stress applied to the system it can be said that the mean percentage error observed throughout the measurements was nearly quartered moving from τ_{50} values in the range of (100-1,000) dyn/cm² for DDT SAMs to values in the range of (10-100) dyn/cm² for HUDT SAMs. This shows that even without the application of a spacer the fluctuations within the measurements decreased with the shear stress applied to the system. The measurement of the interaction of cells and surfaces, such as they were studied in the context of this work, took place at shear stresses, which were another one to two orders of magnitude lower. It can, therefore, be assumed that the percentage error was quartered at least once more under the assumption of a nearly linear correlation. This good reproducibility was in fact observed. Figure 48 A shows the mean interaction curves with hyaluronic acid measured in this work for a model cell line (KG-1a). While the reason for this interaction as well as the cells and surfaces involved are beyond the scope of this section (theory in section 2.3-2.4, experimental results in section 4.1), the graph clearly shows a high reproducibility of the measurement. It shows that averaging of all measurements for this example model cell line that were conducted throughout this work yielded reproducible results. In fact the height variations observed in Figure 48 A were most probably related to deviations in the cell conditions (cell density during culture, cell culture passage) or to varying numbers of initially visible cells (the fraction of interacting cells was normalised to this value), rather than to imprecise measurements. Figure 48 B shows the first two as well as the 11th measurement of a series of measurements that were conducted with the model cell line in succession in one assembled channel system. The other measurements conducted are not of interest here as treatments of the cells modified their behaviour. The comparison shows how well the interaction of the cell line with the surface was reproducible in this channel assembly even after as many as ten measurements. Therefore Figure 48 in total demonstrates the high reproducibility not only between different channels but also after many repeated measurements in one channel. This not only supports the notion that fluctuation of the experimental deviation decreased with the shear stress applied, but also nicely demonstrates the applicability of this setup for the analysis of cell-surface interactions as they are presented in this work.

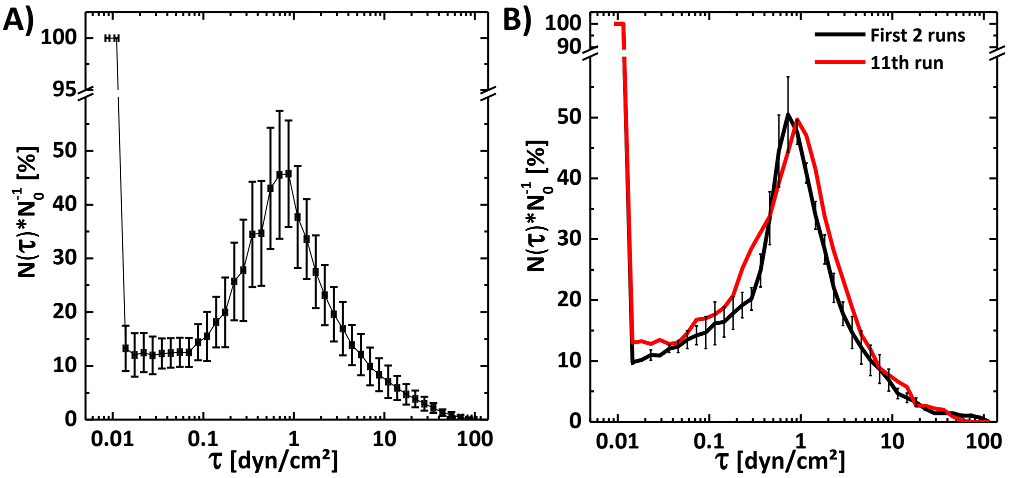

Figure 48: Reproducibility of cell-surface interaction experiments. A) Average of all measurements of the interaction of KG-1a cells with HA under shear stress conducted for this entire study (n = 9). B) Example of the reproducibility in one experimental setup. After the first two measurements other cell-surface interaction experiments were conducted. The 11th run was untreated KG-1a cells again. The interaction curve measured was nearly the same as that initially measured.

3.8.6.6 DISCUSSION

In this section the effect of different experimental parameters on the intra- and inter-channel reproducibility was analysed. Table 5 gives an overview over the parameters studied in this section and their effect on the reproducibility of the microfluidic shear force measurements. As the shear stress applied to the channel system was calculated from the liquid flow and the channel dimensions (discussed in section 3.8.3 resulting in Equation (19)) it is obvious that a change of the channel dimensions during the measurement would have affected the critical shear stress τ_{50} measured. It could be shown that in experiments conducted successively in a single channel assembly the channel dimensions in the relaxed state (between experimental runs, but with the overpressure applied to the channel) did not change even if a deviation of the τ_{50} values was observed. This was an expansion of the findings of M. Alles that showed that the channel height upon assembly was not related to fluctuations between different channel assemblies.[269]

Table 5: List of parameters studied concerning the optimisation of the microfluidic shear force system. ✓ indicates an effect of the listed parameter on the improvement of the mean τ_{50} value measured or on a reduction of the τ_{50} scattering in one experimental setup. ✗ indicates no improvement of the measurement.

Parameter studied	Effect on reproducibility of mean τ_{50} (Intra-channel reproducibility)	Effect on τ_{50} scattering during measurement (Inter-channel reproducibility)	Conclusion
Channel dimensions vs. τ_{50} progression	✗	✗	Fluctuation of τ_{50} values was independent of channel dimensions
Introduction of spacer	✗	✓	Stability of measurement in each assembly was increased, but each channel differed more
Comparison of sampling procedure	✗	✗	Measurement precision and result was independent of sampling procedure
Type of channel system used	✗	✗	Measurement precision and result was independent of channel system used
Maximum shear stress applied	✗	✗	Measurement precision and result was independent of maximal shear stress applied
Dependency of adhesion strength	✓	✓	Reproducibility was dependent on the range of interest in the shear stress spectrum

M. Alles could show that the application of a 130 µm high aluminium spacer to the 13 mm channel setup could increase both the reproducibility of the channel height after reassembly and the intra-channel reproducibility of the τ_{50} values. Here, in the 25 mm channel setup it could be shown that the usage of spacers had no noticeable effect on the channel dimensions after reassembly. This may be related to the by far larger area of the outer PDMS ring of the 25 mm channels compared to that of the 13 mm channels. This larger area was then less easily compressed and a reproducibility of the channel dimensions was internally given. In contrast to this differing observation, the observation that the application of a spacer increased the intra-channel reproducibility could be confirmed for the 25 mm channel setup.

Furthermore, it could be demonstrated that the quality of the measurement was independent of either the sampling protocol or even the channel setup itself. To determine the effect of the sampling protocol, the protocol was varied in successive measurements in a single channel assembly. It could be shown, that neither the step duration nor the beginning of the shear stress ramp resulted in a change of the τ_{50} values measured. For comparison of the influence of the channel setup, data acquired by M. Alles in the 13 mm channel setup was compared to that measured in this work with the 25 mm setup. Here, no differences were apparent between the different channel setups. It should be noted that the high comparability between the two setups, the dimensions of which were so different, may indicate that the origin of the error lay elsewhere than in the channel itself. A hint to this was an experiment in which the in- and outlet tubings were incorrectly aligned to the holes in the glass lid of the channel (Figure 49). Here the τ_{50} values greatly increased with each successive measurement. Such an error may be averted if the channel assembly were modified in such a manner that the tubings can no longer be misaligned to the holes in the glass lid. This could for example be achieved by countersinking the tubings into the holes of the glass and, thereby, ideally aligning them to these.

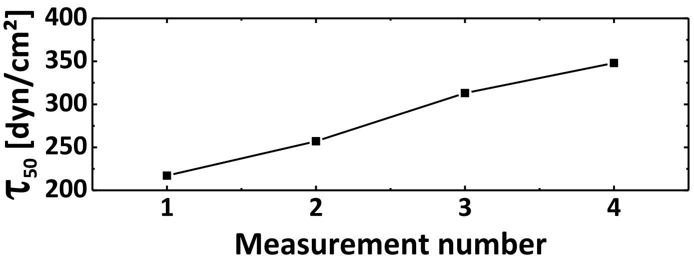

Figure 49: Progression of the τ_{50} values in a misaligned channel.

Another factor that needs to be taken into account when conducting microfluidic shear force measurements is the range of shear stress at which the observation of interest occurs. Here, this observation was the detachment of the particles from the surface, but as discussed later the interaction of cells with surfaces was the major focus of interest of this work. To determine the influence of the range of shear stress applied, first the effect of the maximum shear stress applied during measurements was evaluated. It could be shown that the maximum shear stress applied to the channel system during measurement did not affect the τ_{50} values measured independently of the application of a spacer. In fact, it seemed that high shear forces (approximately 1,000 dyn/cm²) could positively affect the fluctuations of the τ_{50} values. This may, however, have been due to the protocol of the measurements. This should originally ensure the comparability of the data as both different maximum shear stresses tested were applied in the same channel system, thereby eliminating the fluctuations due to reassembly of the channel setup. It is, possible though that this repeated measurement in one channel may have made an equilibration of the channel possible that could have been responsible for the compensation of the channel fluctuations. This should in further studies be addressed by comparing the percentage error of freshly assembled channels that were either ramped to 1,000 dyn/cm² or to only 200 dyn/cm². Furthermore, a comparison was made between the weakly attractive HUDT SAM and the highly attractive DDT SAM. It could be shown that the fluctuation of the percentage error was by far smaller for the detachment of the particles from the HUDT SAMs. This finding was further undergirded by averaging of all interaction curves of one of the model cell lines used in this study. Here, it could be shown that the interaction with the surface was highly reproducible. From these two observations it could be concluded that both the intra- and inter-channel fluctuations were reduced with decreasing the range of shear stress in which the observation of interest occurred. It is important to mention that although the fluctuations were present for the detachment of the particles from both the HUDT and the DDT SAMs, the two different chemistries were still clearly distinguishable from each other. This demonstrates that the microfluidic shear force setup was indeed applicable for the comparison of the shear stress required to detach objects from different surface chemistries.

In conclusion, it could be shown that although shifts in the τ_{50} values measured were not correlated to permanent changes of the channel dimensions the application of a spacer could improve the intra-channel reproducibility. It could also be shown that the measurement precision increased with decreasing shear stresses applied. Especially this last finding was highly relevant for this work as it clearly demonstrated the applicability of this setup for the analysis of cell-surface interactions at very low shear force conditions.

3.9 ROLLING VELOCITY ANALYSIS USING QUANTUMCAT

When analysing the rolling interaction of cells with a surface the velocity with which the cells roll was an interesting factor. Furthermore, the effect treatments with *e.g.* antibodies, which block the receptor responsible for rolling, had on the rolling velocity was also of great interest. To analyse this in detail the MatLab® (MathWorks, Natick, Massachusetts, USA) based analysis tool quantumCAT (quantitative analysis of two-dimensional undirected motion by computer assisted tracking) was developed by Stojan Maleschlijski in our workgroup implementing a tracking core algorithm by Prof. Bodo Rosenhahn (Leibniz-University of Hannover, Hannover, Germany).

3.9.1 MEASUREMENT PROCEDURE OF QUANTUMCAT

Videos of cells rolling on HA-coated surfaces were obtained using the microfluidic shear force device described in section 3.8. The cells were injected into the channel system and a flow rate of approximately 1 dyn/cm² was applied. The duration of the videos acquired was dependent only on the time for which the cells interacted with the surface. A frame rate of 5 fps was set for video acquisition in the imaging software NIS Elements AR 3.0 (Nikon, Tokyo, Japan). NIS Elements AR 3.0 provided the exact time spans between each frame as this was mostly not perfectly constant. These exact time spans were extracted from the video file for later use in the calculation of the rolling velocities. For analysis the videos were split up into the single frames. The distance between the cell positions was calculated between each of those frames and together with the time between the frames the rolling velocities were later calculated. The cohort of rolling velocities acquired was later used for the comparison between the rolling behaviour of cells.

A screenshot of the user interface of quantumCAT is shown in Figure 50. The main part of the screen is the video which was binarised by thresholding prior to investigation. The binarisation procedure was controlled by the parameter ‘Threshold max’ denoting the grey value used as threshold in relation to the maximum grey value available in the frame. Thus all values above the threshold (ideally only the objects of interest) were assigned the value 255 (white) and all values lower than the threshold a value of 0 (black).The image shows a set of traces (blue lines) and the scan window of each trace (red box at the end of a trace). The scan window defined the area in which the tracking algorithm searched for the object. The size of the scan window (in pixels), the number of windows scanned in each direction and the direction of search could be altered in the top right ‘Settings’ and in the centred ‘Direction’ input field. Examples for the resulting scanning pattern are shown in Figure 51. As the direction of rolling of cells was dictated by the direction of liquid flow the setting shown in Figure 51 B was used in this work. Scanning in other directions as that of the flow would have been a waste of resources.

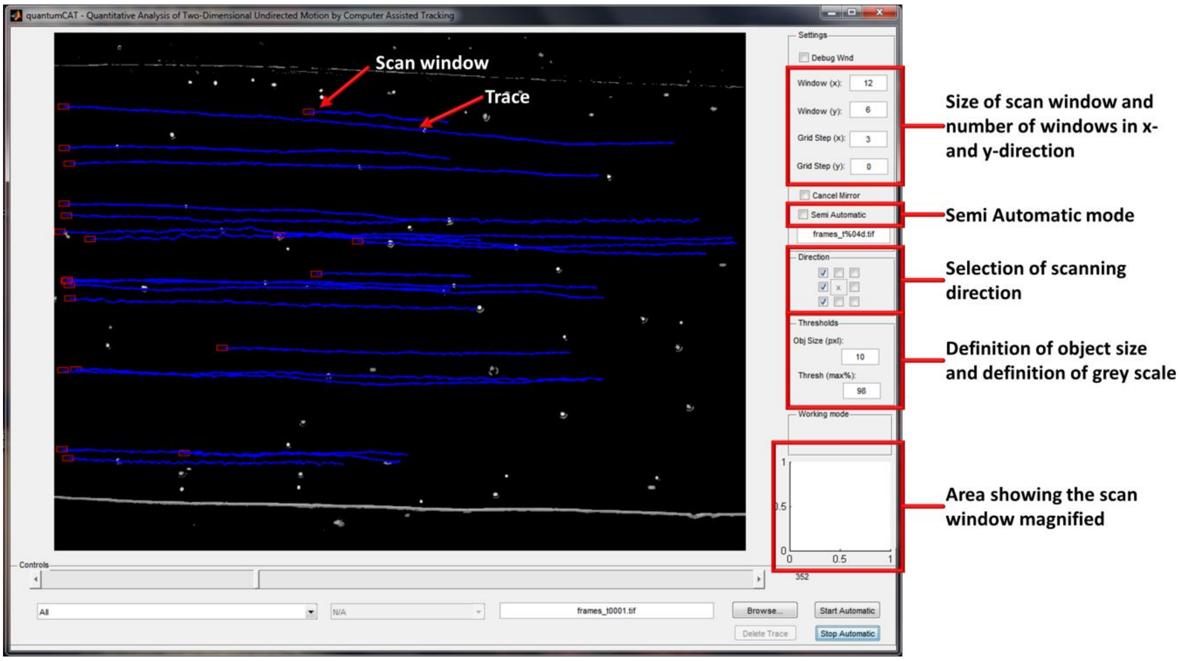

☐ Debug Wnd
Window (x): 12
Window (y): 6
Grid Step (x): 3
Grid Step (y): 0
☐ Cancel Mirror
☐ Semi Automatic
frames_t%04d.tif
Direction
☑ ☐ ☐
☑ x ☐
☑ ☐ ☐
Thresholds
Obj Size (pxl): 10
Thresh (max%): 98
frames_t0001.tif

Size of scan window and number of windows in x- and y-direction

Semi Automatic mode

Selection of scanning direction

Definition of object size and definition of grey scale

Area showing the scan window magnified

Figure 50: Image of quantumCAT with the most relevant functions marked. The picture shows a view of quantumCAT with a video loaded. The blue lines represent the traces recorded. At the end of each line is a red window, the scanning window. As indicated on the right, the size of the scanning window can be adjusted to the type of cells measured. This is also true for the number of steps measured, the direction of measurement and the size of the cells tracked.

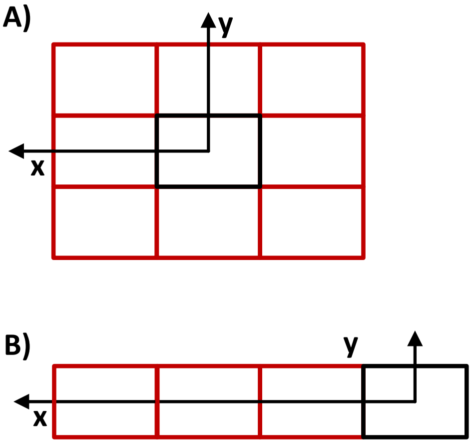

Figure 51: Examples of the orientation of the scan window. The black rectangle is the origin in which the cell was located in the last frame. A) Scanning of 1 scan window in all 8 directions. B) Scanning for 3 scan windows only in the x direction. The setting shown in B was used for the analysis of the rolling velocity of cells in this work.

The minimal area of the cells (number of pixels) could be defined in the ’Thresholds’ input field. This allowed the elimination of objects with lower areas as potential errors. QuantumCAT also allowed the choice of different tracking modes. The standard mode was a fully automatic mode in which tracking continued until the cell left the field of view. For cases in which cells crossed their path in the scan window and the software could not perform an unambiguous differentiation a semi-automatic mode was available. Here, the user must manually place the centroid position on the cell in a magnified scan window in the bottom right of the screen. For each tracked cell, the software created a ‘.txt’ file, where the positions of the cell in each frame of the observation period were recorded, thus representing the trajectories of the rolling movement. From the traces (the coordinates) and the time spans between each frame the rolling velocities, but theoretically also *e.g.* the direction or the acceleration, could be deducted.

3.9.2 ANALYSIS OF QUANTUMCAT DATA

From the distance between the coordinates of a cell centroid in two frames and the time span between these two frames a single momentary rolling velocity was calculated as shown in Equation (26). The velocity v_i between the frame i and the following frame $i + 1$was calculated by dividing the distance s between the two points by the time $t_{(i+1)-i}$ elapsed between the frames. The distance, in turn, was calculated from the x,y-coordinates of the respective point. As the data was acquired in pixels a conversion factor k_{korr} must be applied to convert the pixels to a metric distance. For the 4x PhL objective used for the acquisition of the videos this was k_{korr} = 1.58 µm/pixel.

$$v_i = \frac{s}{t_{(i+1)-i}} = k_{korr} \frac{\sqrt{(x_{i+1} - x_i)^2 - (y_{i+1} - y_i)^2}}{t_{i+1} - t_i} \tag{26}$$

This led to a velocity for each cell tracked for each pair of frames. Rolling was defined as an interaction with the surface, which was slower than the movement of the non-interacting cells. A threshold of maximal 100 µm/s was set beyond which the velocity was defined as too fast for rolling and ignored as a ‘jump’ in the later analysis.

The velocities in their entirety were used for comparison of the effects of different cell treatments on the rolling velocity. The simplest approach to do so would have been to compare the mean values and the SD of the measurements. This would have given an oversimplified view of the data with very large SD indicating an imprecise measurement. The SD, however, was due to the natural inhomogeneities of the interaction between cells and a surface (CD44 expressing cells and HA-coated surfaces in the specific case of this study) and should not be confused with an inaccurate measurement. The large amount of data points (typically at least 250 for very weakly interacting cells up to 25,000 for readily interacting cells) collected for a given treatment allowed the reliable creation of distribution plots such as histograms or box plots. A detailed elaboration of the values found in such a box plot is given in the appendix (section 7.1.2.3).

4 CD44: HOW STEM CELLS ROLL

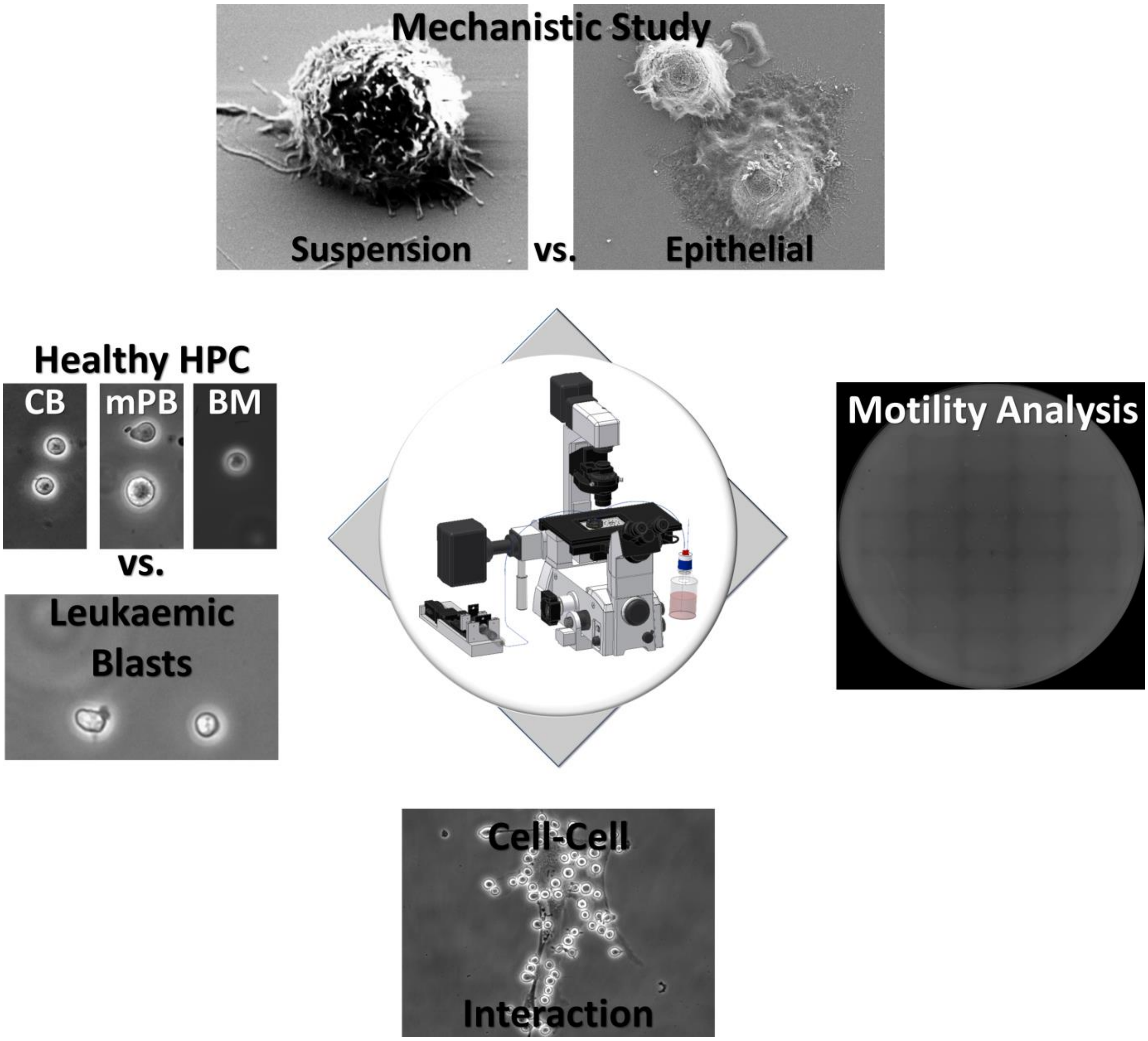

Figure 52: Scheme depicting the aims of this chapter. In this chapter the CD44 mediated interaction of cells with HA and other cells is addressed. In this context suspension and epithelial cell lines are utilised to gain a detailed understanding of this interaction. This knowledge is then applied in the comparison of the interaction of healthy HPC and leukaemic blasts with surfaces artificially coated with HA. The next step is the establishment of an experimental procedure to study cell-cell interaction under flow. Finally, the effect of the cytokine SDF-1α and its antagonist Plerixafor® on migration and the interaction with HA under flow is investigated.

As presented in chapter 1 the first aim of this work was to characterise the CD44 mediated interaction of healthy and leukaemic cells with HA in order to reveal differences between these cells types. Ideally, these can later be exploited for the targeted mobilisation of leukaemic stem cells (LSC) from the niche, thereby, making them more susceptible to chemotherapy. In the first section of this chapter the characterisation of the interaction of CD44 positive cell lines with hyaluronic acid (HA) is presented. For this a comparison was made between the interaction of a leukaemic suspension model cell line (KG-1a) and an epithelial liver carcinoma model cell line (HepG2Iso) with HA-coated surfaces under flow. In this system the dependence of the interaction with HA on CD44 was verified and it was studied whether these fundamentally different cell types exhibited different interact patterns with HA. In the following section some light is shed on the interaction of both healthy haematopoietic progenitor cells (HPC) and leukaemic blasts with HA, demonstrating the pronounced differences between healthy and leukaemic cells. Furthermore, the establishment of a method to study cell-cell interactions under flow is presented. In this context the interaction of both healthy and leukaemic cells with mesenchymal stromal cells (MSC) was investigated. Finally, the effect of the cytokine SDF-1α and its antagonist Plerixafor® on migration of HPC and on their interaction with HA under flow is discussed.

4.1 ANALYSIS OF THE INTERACTION OF CD44 WITH HYALURONIC ACID

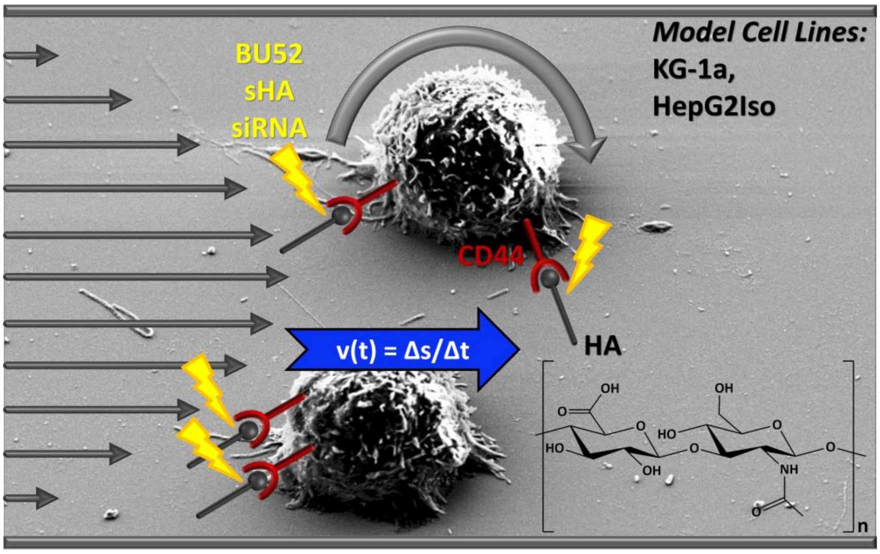

Figure 53: Overview over the aims of this section. The flow-induced interaction of CD44 with HA shall be studied by analysis of the binding motive, the requirement of CD44 or its isoforms and the rolling velocity.

Before the valuable and rare primary material could be studied, a detailed understanding of the underlying interaction motive was necessary. As mentioned above this was the flow-induced interaction between the cell surface receptor CD44 and the glycosaminoglycan HA. An overview over the findings that are presented in this section is given in Figure 53. Next to a comparison between two fundamentally different cell types, suspension cells and epithelial cells, the specificity of this interaction was verified. For this a comparison was made between the interaction of the two model cell lines KG-1a and HepG2Iso (Figure 54) with different GAGs and between biologically similar CD44 negative cells with HA. Furthermore, the expression of CD44 in general (CD44pan) or different CD44variant isoforms was down-regulated to determine the relevance again of CD44 generally and of the two isoforms. The possibility of blocking the flow-induced interaction with HA by a monoclonal antibody and short chain length HA fragments (sHA) was also analysed. In this context the rolling velocity of cells was studied using the analysis software quantumCAT. All experiments with liver carcinoma cell lines were conducted in cooperation with Katharina Fuchs from the workgroup of Dr. Véronique Orian-Rousseau (ITG, KIT, Karlsruhe, Germany).

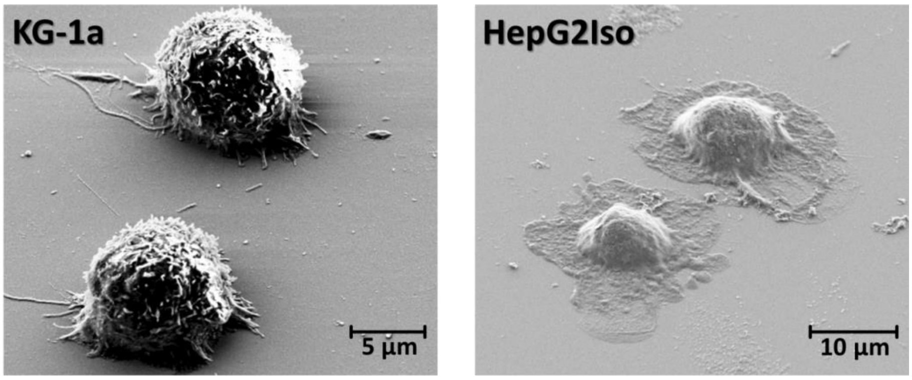

Figure 54: SEM images of the leukaemic suspension cell line KG-1a and the epithelial liver cancer cell line HepG2Iso.

4.1.1 ANALYSIS OF THE BINDING PARTNER NECESSARY FOR ROLLING

To validate that the rolling interaction with the surface was specific for HA both model cell lines were tested on HA- and chondroitin sulphate (CS)-coated surfaces. The chemical structure of HA and CS is shown in Figure 55. The only difference between the two molecules is the sulphated hydroxyl-group of CS, the location of which is dependent on the tissue it originates from and the conditions of synthesis.[270] The hypothesis was that if the interaction was specific for either of the two this would point towards a high binding partner specificity, due to the only marginal chemical differences exhibited by the molecules.

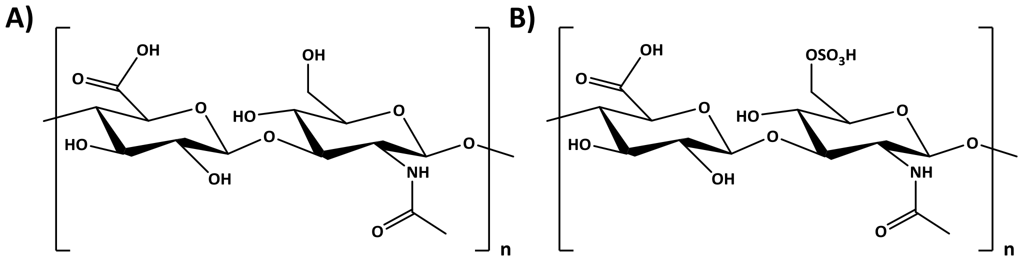

Figure 55: Chemical structures of HA (A) and CS (B). HA is composed of N-acetyl-D-glucosamine and D-glucuronate, connected by β-1,4 and β-1,3 linkages and CS consists of N-acetyl-D-galactosamine and glucuronic acid that are in turn connected by β-1,3 and β-1,4 linkages.

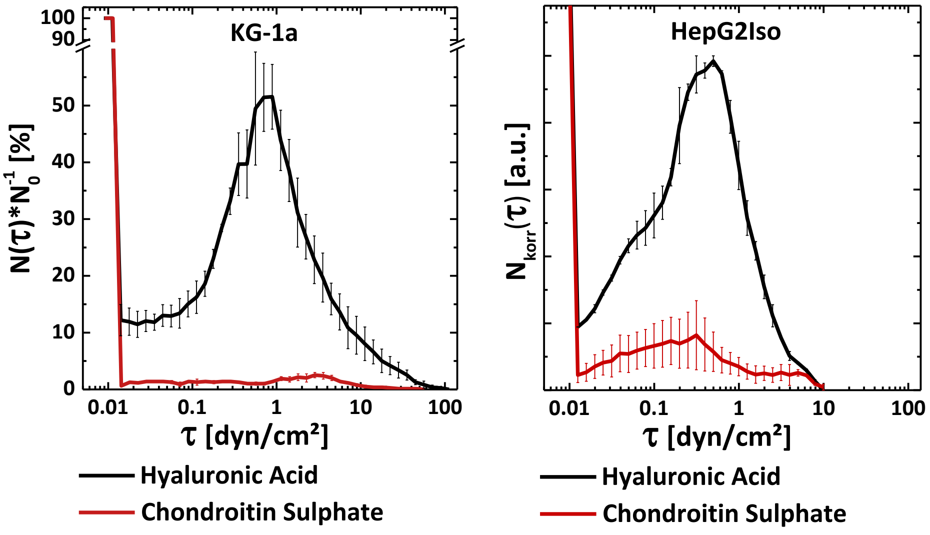

Figure 56: Comparison of the interaction between two different chemically similar GAGs. Both the KG-1a (A) and the HepG2Iso cells (B) showed a pronounced flow-induced interaction with HA while hardly any interaction with the CS-coated surface was observable (n = 4; ≥ 130 cells/FOV). For the HepG2Iso cells the fraction of interacting cells ranged from 72-92 % for the cells interacting with HA and from 4-22 % for the cells interacting with CS.

As shown in Figure 56 the flow-induced interaction could be observed on HA for both model cell lines, while nearly no interaction was observable with CS. The supplementary Video S1 (description found in the Appendix section 7.1.2.1, video provided on the supplementary CD) shows an exemplary HepG2Iso cell rolling on HA. The flow-induced interaction showed the same characteristics as previously described by Christophis *et al.*[10] At very low flow speeds hardly any cells interacted with HA. Beyond a threshold shear stress level the fraction of cells interacting with the surface increased. The fraction of interacting cells reached its maximum at approximately (0.7-1) dyn/cm². The threshold of interaction was more pronounced for the epithelial cell line HepG2Iso, which was surely due to the adherent nature of the cells as well as the flow pulse at the beginning of the experiment. The system required a certain time to slow down from the pulse, resulting in the actual flow speed being faster than that set in the program of the syringe pump. This led to the epithelial cells seeming to interact at flow rates at which the suspension cells showed no interaction. This phenomenon could not be avoided as the initial pulse was necessary to avoid crowding of the sample surface due to the omnipresent adherent nature of the cells.

4.1.2 NECESSITY OF CD44 FOR FLOW-INDUCED INTERACTION

After proving the necessity of the binding partner HA it was important to demonstrate that the interaction was solely mediated by CD44. One of the tests used to prove this fact was to analyse the interaction of different cell lines expressing and lacking CD44 with HA. As suspension cells the model cell line KG-1a (CD44$^+$) was compared to the cell line Jurkat (CD44$^-$). For the epithelial cells the model cell line HepG2Iso (CD44$^+$) was compared to the related cell line HepG2 (CD44$^-$). As shown in Figure 57 only the CD44 positive cell lines KG-1a and HepG2Iso showed the flow-induced interaction with HA. Thus, it could be concluded that, at least for these cell lines, CD44 was the only receptor mediating the flow-induced interaction with HA.

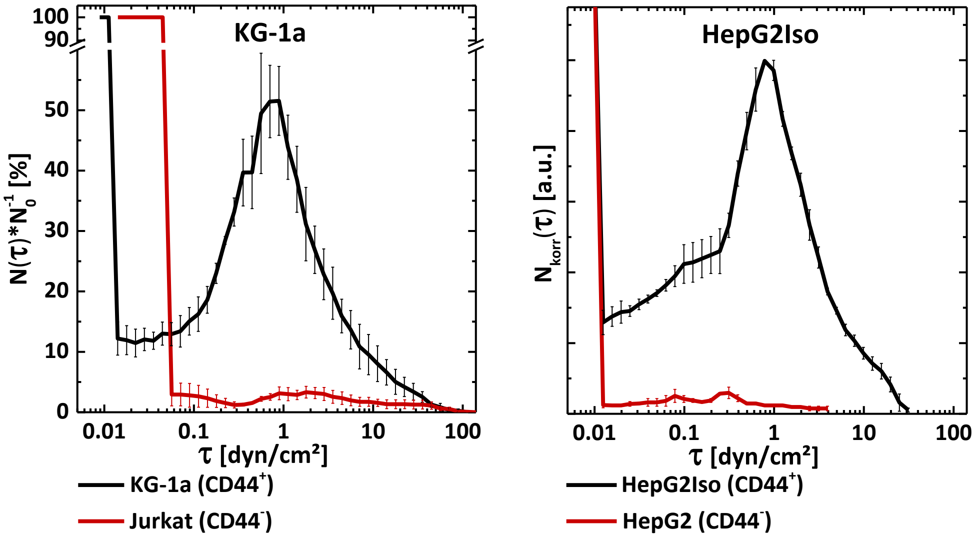

Figure 57: CD44 required for rolling. A) Comparison of the interaction of two suspension cell lines with HA. The CD44 positive cell lines (KG-1a, HepG2Iso; black line) showed a flow-induced interaction with HA, while the CD44 negative cell lines (Jurkat, HepG2; red line) did not (n = 4; ≥ 150 cells/FOV). For the HepG2Iso cells the fraction of interacting cells ranged from 71-79 % for the untreated HepG2Iso cells and from 4-9 % for the HepG2 cells.

In order to prove that the interaction with HA was mediated by the HA binding domain of CD44 an antibody specific for this binding domain was applied. The monoclonal CD44 antibody (clone BU52, hereafter referred to as BU52) was chosen. Figure 58 shows the FACS data for the incubation of KG-1a cells with 9 µg/mL BU52 for 30 min. Figure 58 A and D show the cell selection gate for the untreated control (A) and the cells treated with BU52 (D). The propydiumiodide (Pi) vs. FSC gate in B and E was used to gate out all dead cells for later analysis. From this gate it can also be seen that the treatment with the antibody did not harm the cells, as their cellular integrity remained intact. The fluorescence channel in Figure 58 C and F shows that no cells were marked in the autofluorescence control (C), while all cells were marked by the antibody.

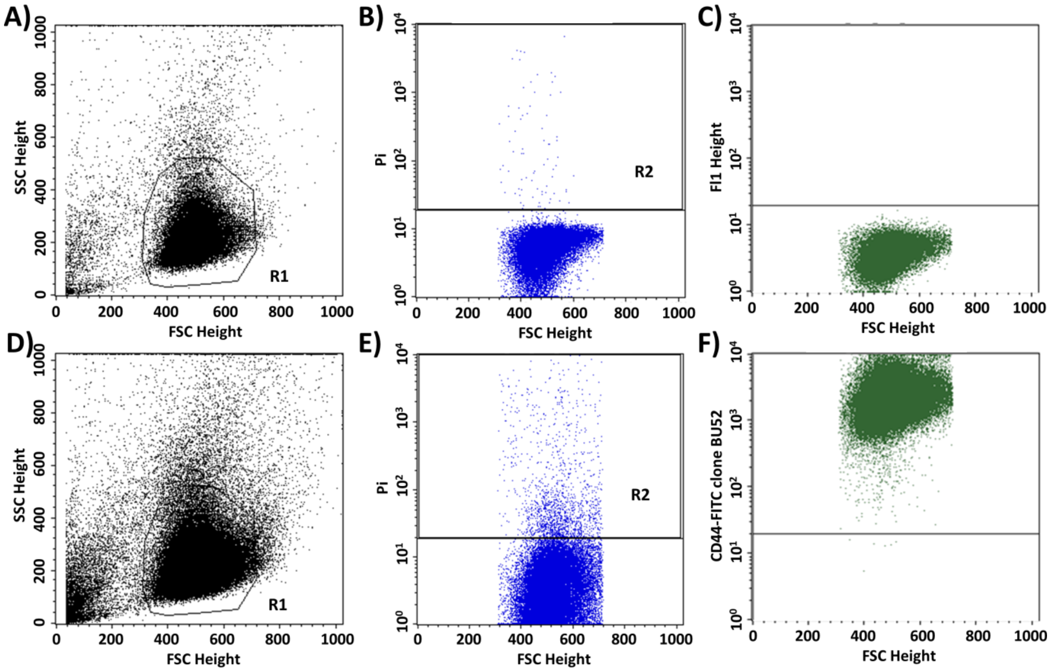

Figure 58: FACS analysis of the binding efficiency of BU52 to KG-1a. The auto fluorescence (A-C) is compared to the cells incubated with FITC-marked BU52 (D-F). The graphs show: SSC vs. FSC with the gate selecting only the healthy cells marked by the black line (R1; A, D); Pi vs. FSC to evaluate the amount of dead cells in the sample (R2; B, E) and the fluorescence channel for the FITC marked antibody BU52 vs. FSC (C, F). It is clearly shown that while nearly all cells were unaffected by the BU52 treatment, all were marked by the antibody.

As shown in Figure 59 A the flow-induced interaction of KG-1a with HA could be inhibited in a concentration dependent manner by BU52. While an incubation with 1 µg/mL BU52 already caused a significant reduction ($p < 0.05$; Figure 59 B) in the fraction of interacting cells (from $N(\tau)/N_0 \approx 60$ % of the initially visible cells to ~ 35 %), a nearly complete suppression of the flow-induced interaction required the application of ≥ 9 µg/mL BU52. In all subsequent experiments, 9 µg/mL BU52 was used to block the CD44 mediated interaction with HA. This concentration of BU52 could for example suppress the interaction of the model cell line HepG2Iso (Figure 60) with HA. The concentration dependency with a complete suppression at 9 µg/mL BU52 of the interaction was also undergirded by BU52 concentration dependent measurements of the accumulation of KG-1a on HA as shown in Figure S7 (Appendix section 7.2.2).

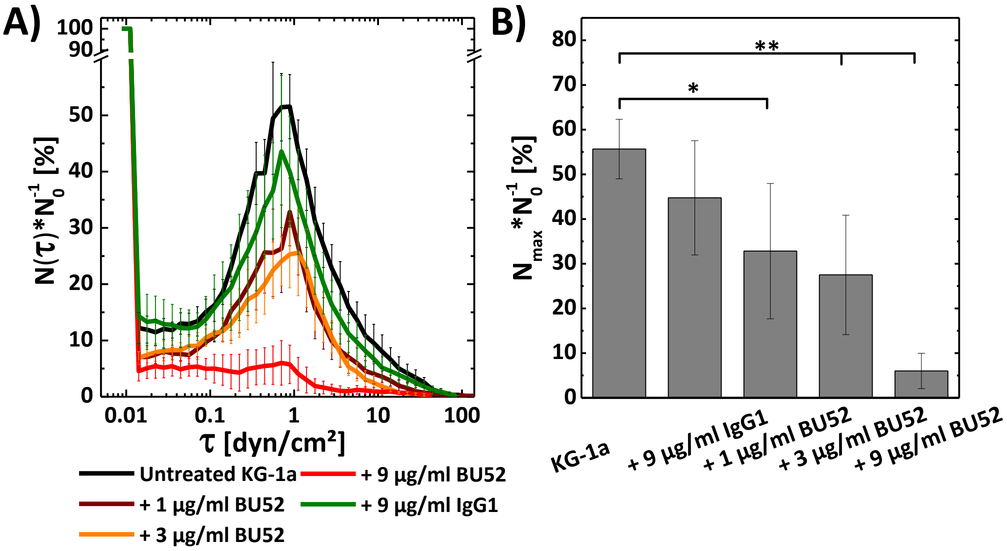

Figure 59: Dependency of the interaction of KG-1a cells with HA on the concentration of BU52. Interaction curves (A) and the corresponding maximum peak heights (B) measured for the reference cell line KG-1a (n ≥ 4 for each treatment with > 300 cells/FOV). Treatment with increasing concentrations of BU52 led to a decrease in the fraction of cells interacting with HA. Full suppression of all interactions was achieved with 9 µg/mL BU52, while the same concentration of the isotype control IgG1 hardly reduced the interaction. * indicates a significance of $p < 0.05$, ** indicates a significance of $p < 0.01$ in a two-sided Student´s *t*-test. All error bars shown in this figure represent the SD.[266]

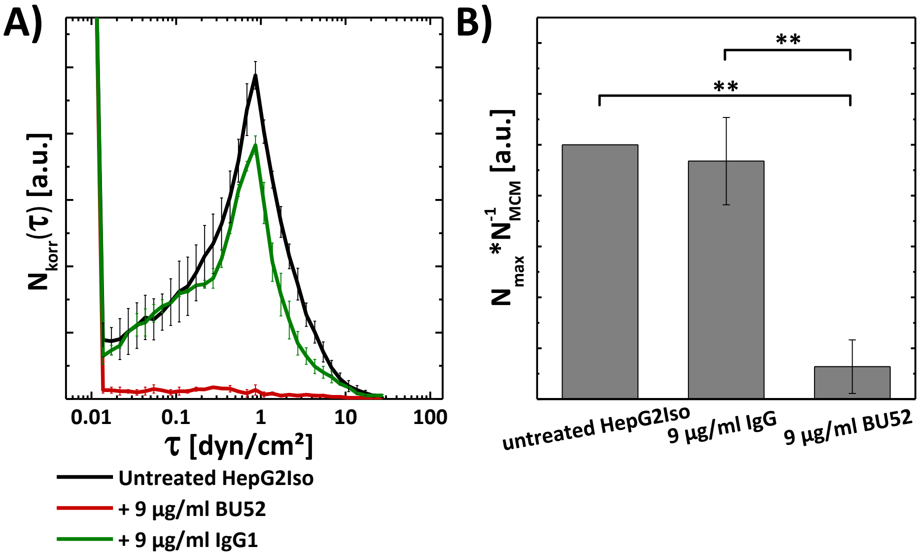

Figure 60: Suppression of the interaction of HepG2Iso with HA by BU52. Exemplary interaction curves (A) and the overall maximum peak heights (B) measured for the reference cell line HepG2Iso (untreated: n = 9; with BU52: n = 7; with IgG1: n = 4; each treatment with > 200 cells/FOV). Full suppression of all interactions was achieved with 9 µg/mL BU52, while the same concentration of the isotype control IgG1 hardly had any effect. ** indicates a significance of $p < 0.01$ in a two-sided Student´s *t*-test. The error bars represent the SD. The fraction of interacting cells in the interaction curve shown ranged from 56-72 % for the untreated HepG2Iso cells, from 47-51 % for the HepG2 cells incubated with the IgG1 control antibody and from 1-3 % for the HepG2 cells incubated with BU52.

Another possibility to determine the necessity of the receptor CD44 for the interaction was the knock down of the same by means of siRNA (CD44pan siRNA knocked down all CD44variant isoforms as well as the standard form). This methodology also rendered it possible to knock down specific CD44variant isoforms on the cells. The relevance of these isoforms for the interaction with HA could then also be tested. In this study the two isoforms CD44v3 and CD44v6 were knocked down. These isoforms were chosen as a high expression of the CD44v3 isoform is correlated with tumour growth and metastasis[271] and CD44v6 is a co-receptor for the activation of the receptor tyrosine kinase (RTK) Met and their collaboration is reported to be important in tumour progression and metastasis.[272] Figure 61 shows the Western Blots acquired by Katharina Fuchs from workgroup of Dr. Véronique Orian-Rousseau (ITG, KIT, Karlsruhe, Germany) after the treatment of HepG2Iso cells with control siRNA and the either CD44pan, CD44v3 or CD44v6 siRNA. The Western Blots reveal a clear repression of the respective receptor expression in all cases.

The results of the microfluidic shear force analysis, shown in Figure 62, reveal that treatment of HepG2Iso cells with CD44pan siRNA led to a nearly complete reduction of the interaction with HA. This was not the case for the two CD44variant isoforms. In both cases no reduction of the fraction of interacting cells was observed compared to the siRNA control. This demonstrated that the flow induced interaction with HA was not solely mediated or significantly influenced by either of the two isoforms alone, but that suppression was only achieved by full knock-down of the CD44 receptor (CD44pan).

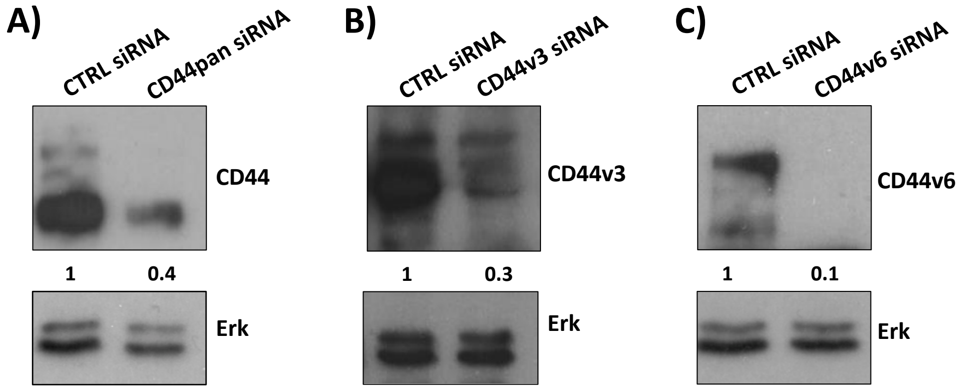

Figure 61: Western Blot analysis of the siRNA treatment of HepG2Iso cells. The membrane was probed with an anti-CD44 antibody that recognises all isoforms (CD44pan) or one of the two CD44variant isoforms. An extracellular signal-regulated kinase (Erk)-antibody was used as a loading control. The numbers between the panels indicate the fold induction of the respective treatment.

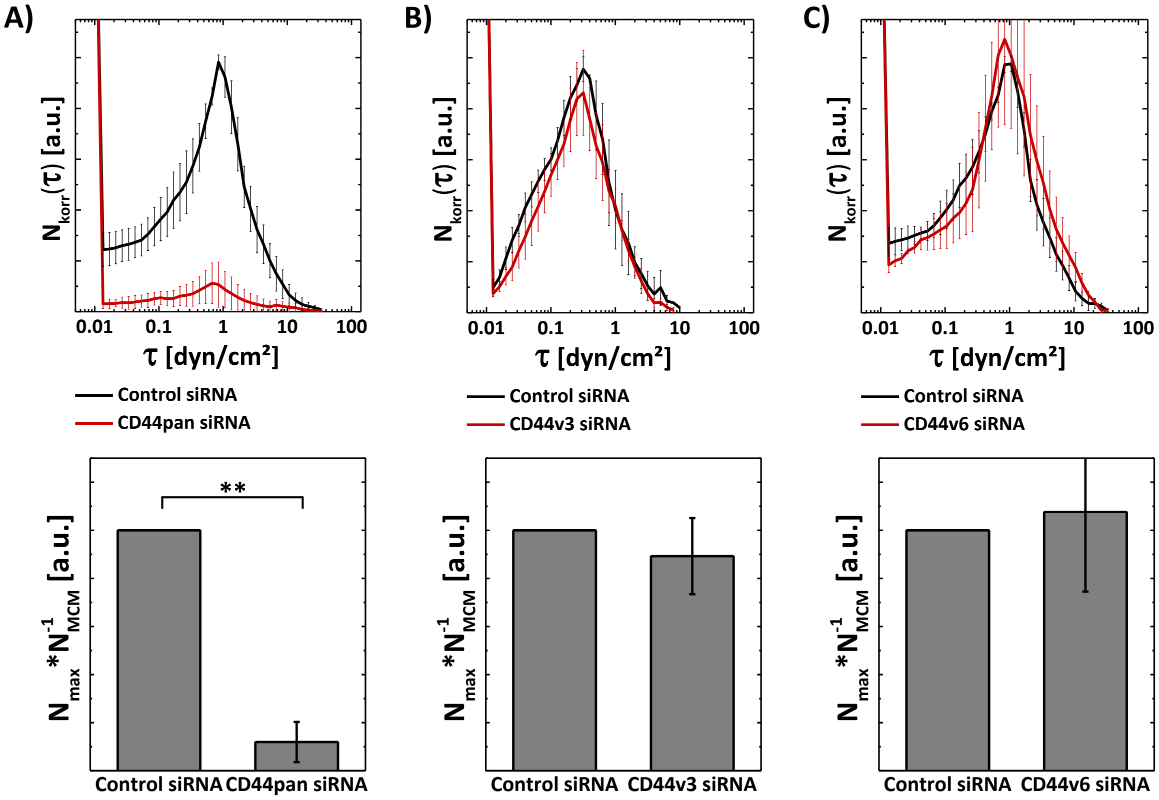

Figure 62: Knock down of different CD44 isoforms on HepG2Is. The top graphs show the detachment curves of HepG2Iso cells transfected with control siRNA and CD44pan (A), CD44v3 (B) and CD44v6 siRNA (C) (n ≥ 4 for each treatment with > 250 cells/FOV). The fraction of interacting cells ranged as followed: A) From 54-76 % for the HepG2Iso cells treated with control siRNA and from 2-20 % for the HepG2 cells treated with the CD44pan siRNA; B) From 21-87 % for the HepG2Iso cells treated with control siRNA and from 34-82 % for the HepG2 cells treated with the CD44v3 siRNA; C) From 57-74 % for the HepG2Iso cells treated with control siRNA and from 52-90 % for the HepG2 cells treated with the CD44v6 siRNA. The bottom bar graphs give the maximum peak heights with significant differences marked. ** indicates a significance of $p < 0.01$ in a two-sided Student´s *t*-test. All error bars shown represent the SD.

4.1.3 ROLLING SUPPRESSION BY SOLUBLE GLYCOSAMINOGLYCANS

As the rolling interaction occurred between CD44 and the surface bound HA the question arose if it could be suppressed by soluble macromolecular glycosaminoglycans (GAGs) or by the corresponding polysaccharide fragments. To test for this HepG2Iso cells were preincubated with 50 µg/ml of four different GAGs. The macromolecular GAGs used were HA, CS, heparin sulphate (HS) and keratane sulphate (KS). Figure 63 shows the results obtained from the microfluidic shear force experiments obtained with the preincubated cells. While a small but not significant reduction of interaction was observed for most macromolecular GAGs, only the incubation with HA led to a significant decrease of cells interacting with the HA-surface.

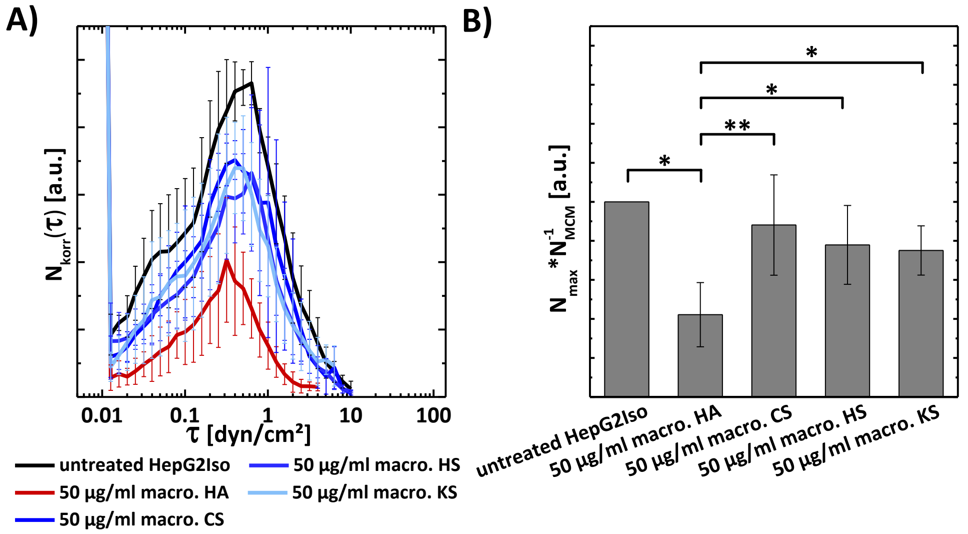

Figure 63: Effect of macromolecular GAGs on the flow-induced rolling interaction of HepG2Iso with HA. HepG2Iso incubated with 50 µg/ml of macromolecular HA, CS, HS and KS (n = 4 with > 150/FOV). While most macromolecular GAGs led to an insignificant reduction of the fraction of interacting cells, only the reduction by HA was significant. The bar graph (B) shows the maximum fraction of rolling cells $\boldsymbol{N_{max}(\tau)} * \boldsymbol{N_{MCM}}$ measured. * indicates a significance of $p < 0.05$, ** indicates a significance of $p < 0.01$ in a two-sided Student´s t-test t. All error bars shown represent the SD. The fraction of interacting cells ranged from 15-92 % for the untreated HepG2Iso cells, from 4-62 % for the HepG2 cells incubated with HA, from 15-72 % for the HepG2Iso cells incubated with CS, from 15-76 % for the HepG2Iso cells incubated with HS and from 12-76 % for the HepG2Iso cells incubated with KS.

The blocking capabilities of HA were further studied by pre-incubation with short chain length HA (sHA; 6-10 DS). Prior to measurements in the microfluidic shear force system it was tested whether the incubation with sHA was toxic for the cells. For this the cells were incubated with the sHA (6-10 DS) for 1 h under culture conditions before they were imaged by light microscopy. The treatment did not lead to any morphological changes in the cells as shown in Figure S8 (Appendix section 7.2.3). This compatibility with large amounts of sHA allowed the study of the effect of the same on the interaction of the cells with HA-coated surfaces under flow conditions. The results of a representative set of measurements are shown in Figure 63. While the treatment with 10 µg/mL sHA did not lead to a significant reduction of the fraction of interacting cells, larger concentrations did. Both the preincubation with either 30 µg/mL or 50 µg/mL sHA led to a significant reduction of the fraction of interacting cells compared to the respective lower concentration. These findings demonstrated a concentration dependent reduction of the fraction of interacting cells similar to the observed for the treatment with BU52. Comparable results were obtained in two further independent experimental series.

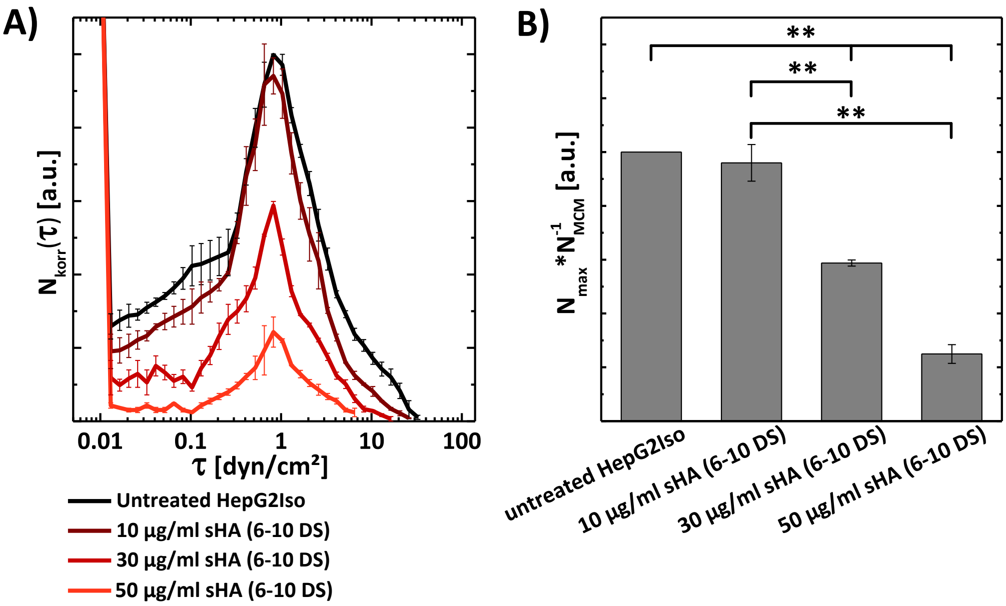

Figure 64: Dependency of the rolling interaction of the concentration of sHA (6-10 DS). The graph shows a representative data set for the sHA concentration dependent reduction of the interaction of HepG2Iso cells with HA (n = 2, ≥ 150 cell/FOV). Treatment with sHA concentrations ranging from 10 µg/mL to 50 µg/mL gradually decreased the maximum fraction of HepG2Iso cells rolling on the HA-surface. * indicates a significance of $p < 0.05$, ** indicates a significance of $p < 0.01$ in a two-sided Student´s *t*-test. All error bars shown in this figure represent the SD. The fraction of interacting cells ranged from 71-80 % for the untreated HepG2Iso cells, from 66-74 % for the HepG2 cells incubated with 10 µg/ml sHA, from 43-45 % for the HepG2Iso cells incubated with 30 µg/ml sHA and from 16-18 % for the HepG2Iso cells incubated with 50 µg/ml sHA.

4.1.4 EFFECT OF BLOCKING REAGENTS ON THE ROLLING VELOCITY

Next to the amount of cells that interact with HA following a given treatment with a blocking reagent (BU52, sHA), the effect of the treatment on the rolling velocity was analysed using the analysing MatLab© based software quantumCAT designed by S. Maleschijski in our workgroup.

The effect of different concentrations of BU52 and the corresponding isotype control IgG1 on the rolling velocity of HepG2Iso cells is shown in Figure 65. A wall shear stress of approximately 1 dyn/cm² was applied during the measurements. From the BU52 concentration series conducted with KG-1a cells (section 4.1.2, Figure 59) three concentrations were chosen that covered the whole range from only weak blocking (2 µg/mL) over medium blocking capability (4.5 µg/mL) to nearly complete blocking (9 µg/mL). In the box plot (Figure 65, top) each box gives the 1st (lower box margin), 2nd (middle line; median) and 3rd (upper box margin) quartile of the data. The diamond symbol (◇) gives the mean rolling velocity and the whiskers represent the standard deviation. Further information about the values depicted in the box plot can be found in section 7.1.2.3. It can be seen that both the median and the mean rolling velocity were hardly influenced by the treatment with IgG1. Treatment with BU52, however, led to an increased rolling velocity with increasing amounts of BU52. The median rolling velocity of the untreated HepG2Iso cells was approximately 23 µm/s. For cells treated with 2 µg/mL BU52 the median was roughly 32 µm/s and increased to approximately 43 µm/s for cells treated with 9 µg/mL BU52. This trend can also be seen in the histograms of the rolling velocity (Figure 65, bottom). Here, the black arrows indicate the progression of the most frequent rolling velocity. Although the comparably low number of data points for the treatment with 9 µg/mL BU52 (280, compared to ~ 11,000 for the untreated cells; interaction with HA was suppressed with BU52, making rolling cells rare) yielded a crooked histogram, the trend was still clear. While the most frequent rolling velocity was approximately 20 µm/s for the untreated cells and for all concentrations of IgG1, it increased from approximately 25 µm/s for cells treated with 2 µg/mL BU52 to roughly 40 µm/s for cells treated with 9 µg/mL BU52.

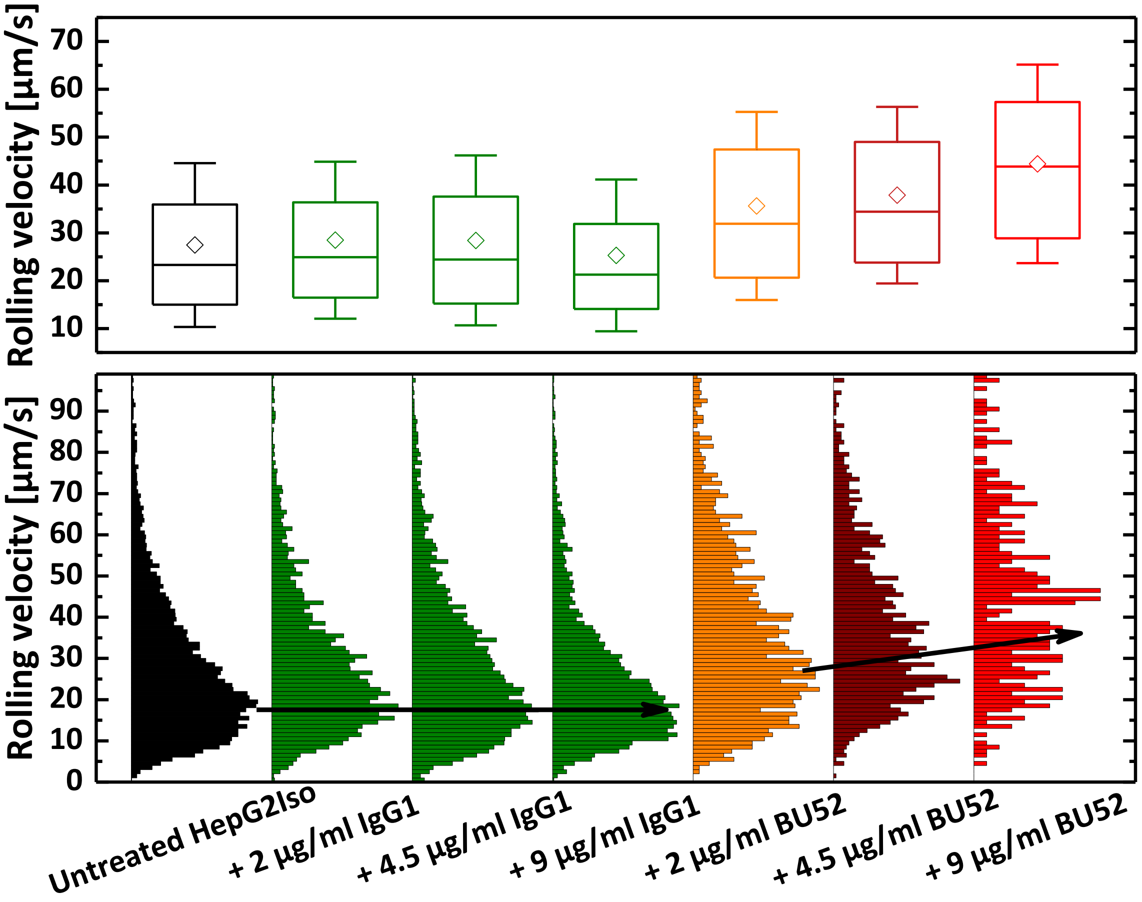

Figure 65: Rolling velocity analysis of HepG2Iso cells after treatment with BU52 at a shear rate of 1 dyn/cm². Box plots (top) and histograms (bottom) depicting the rolling velocity distribution for HepG2Iso cells treated with BU52 and the isotype control IgG1. At least 7 traces with 280 data points (for 9 µg/ml BU52) to ~11,000 data points (untreated cells) were recorded for each type of treatment. ◇ is the mean rolling velocity. The box plots give the 1st (lower box margin), 2nd (middle line; median) and 3rd (upper box margin) quartile of the data. The whiskers represent the standard deviation.

Analogous measurements of the dependency of rolling velocity of HepG2Iso cells on the blocking of the CD44 receptor with sHA (6-10 DS) were also conducted. Again the rolling velocity was measured with a wall shear stress of approximately 1 dyn/cm² applied. Figure 66 shows the rolling velocities measured in dependency of the concentration of sHA. Both from the box plots (Figure 66, top) it can be seen that the mean rolling velocity continuously increased with increasing amounts of sHA. The only exception to this trend was the treatment with 60 µg/mL sHA. Here, a stagnation of the mean rolling velocity was observed. The median rolling velocity followed the same trend as the mean velocity, but showed a slight decrease for the highest concentration. It increased from approximately 10 µm/s for the untreated cells to roughly 30 µm/s for cells treated with 50 µg/mL sHA. The same observation could be made for the most frequent rolling velocity seen in the histograms (Figure 66, bottom). This, too, increased with the sHA concentration and stagnated for the last increase of concentration.

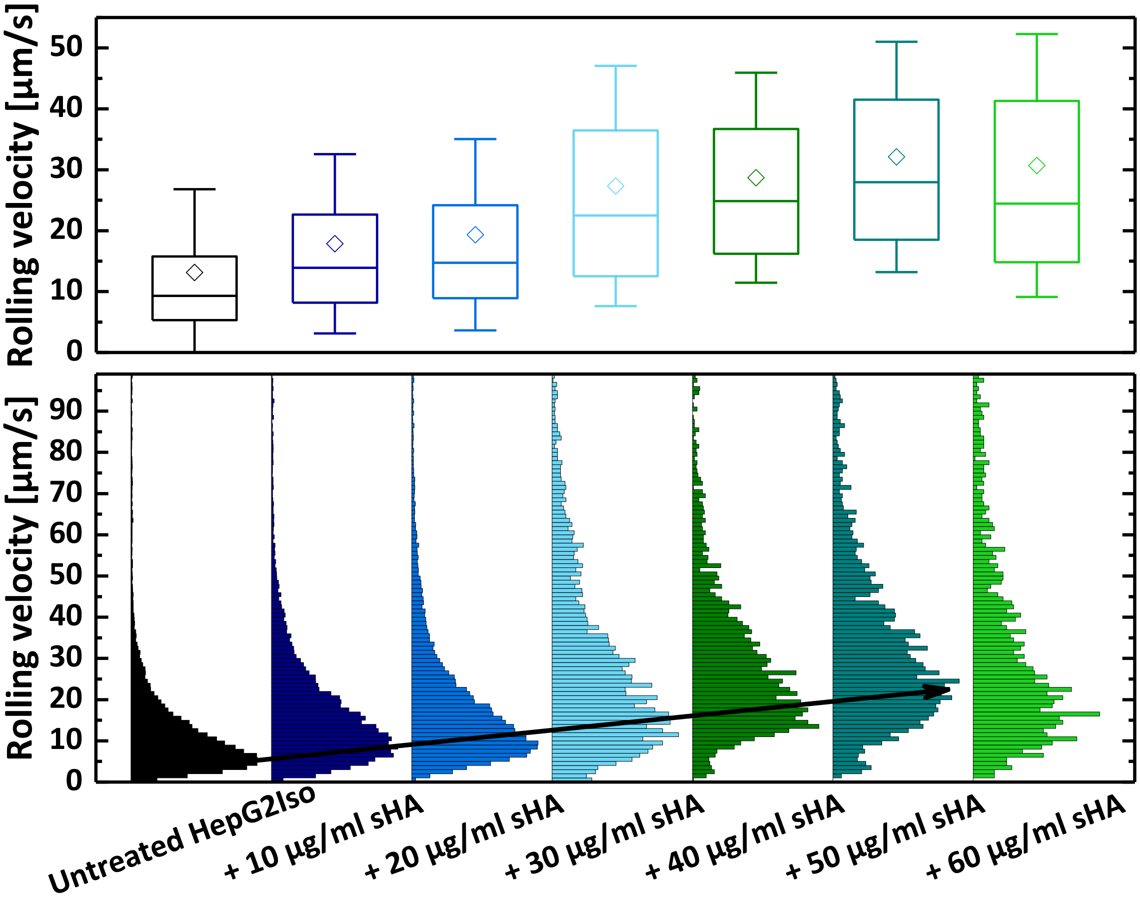

Figure 66: Analysis of the rolling velocity of HepG2Iso on HA after treatment with sHA (6-10 DS). Box plots (top) and histograms (bottom) depicting the rolling velocity distribution for HepG2Iso cells treated with different concentrations of sHA (6-10 DS). At least 13 traces with 800 data points (for 60 µg/ml) to 25,000 data points (untreated cells) were recorded for each sHA concentration. ◇ is the mean rolling velocity. The box plots give the 1st (lower box margin), 2nd (middle line; median) and 3rd (upper box margin) quartile of the data. The whiskers represent the standard deviation.

4.1.5 DISCUSSION

In this section the flow induced interaction of the suspension cell line KG-1a and that of the epithelial cell line HepG2Iso with HA was studied towards its CD44 dependence, while comparing these two fundamentally different cell types.

For suspension cells the basic principal of such a flow-induced interaction is well known in literature. A good and probably the most prominent example is the selectin- and integrin-mediated extravasation of lymphocytes at sites of inflammation which has been extensively studied.[63-64,273-275] In this context it was shown that fluid shear promotes the P-, E-, or L-selectin mediated rolling of lymphocytes on the endothelium.[116-117] Recently, the capability of CD44 to mediate such a flow-induced interaction was demonstrated for KG-1a in our workgroup.[10] For epithelial cells this has not been shown so far.

As different modes of glycosylation of CD44 influence the binding to HA,[159,166-167] the expression of CD44 alone does not directly correlate with HA binding. As this is the case, the first focus was to determine whether CD44 solely mediated the observed interaction with HA and whether this was specific for HA. This was achieved by applying the analysis matrix shown in Table 6 to the two model cell lines KG-1a and HepG2Iso.

Table 6: Matrix of tests demonstrating the relevance of CD44 for the rolling interaction on HA. If the criteria given in the left column was fulfilled the corresponding cell line is marked by ✓. If it was not it is marked by ✗.

Criteria	Leukaemic suspension cell line KG-1a	Liver cancer epithelial cell line HepG2Iso
Rolling on HA	✓	✓
Rolling on CS	✗	✗
Rolling while CD44$^-$ cell line does not	✓	✓
Effective blocking by BU52	✓	✓
Effective suppression by CD44pan siRNA	n.a.	✓

For both cells lines the HA specificity could be demonstrated by comparing the interaction with HA to that with CS. While the two GAGs are structurally very similar the interaction was highly specific for HA. Furthermore, it could be shown that the interaction with HA could only be observed for CD44 positive cell lines, while CD44 negative cell lines lacked any form of interaction with the HA-coated surfaces under flow. These findings could clearly validate that the flow induced interaction observed on the HA-coated surfaces was not only dependent on CD44 but also specific for HA. The necessity of the HA binding domain for this interaction was investigated by treating the cells with the CD44 antibody BU52. A concentration dependent blocking of the interaction with the HA-coated surfaces was observed. As BU52 specifically blocks the HA binding domain of the CD44 receptor this proved its necessity for the flow induced interaction with HA. The concentration series conducted in this context also served to establish a protocol for later experiments with primary human cells. This sort of material was not accessible in the quantities a cell line was and the concentration series allowed the identification of an antibody concentration at which blocking could completely and reproducibly be suppressed. This concentration was found to be 9 µg/mL.

The similarity of the interaction of the two model cell lines, KG-1a and HepG2Iso, concerning the interaction with HA was remarkable. The interaction characteristics found for the two cell types were highly comparable and in good accordance to earlier findings.[10] A threshold shear stress of approximately 0.2 dyn/cm² could be identified above which the interaction was observed. In the case of the HepG2Iso cells this threshold could not always be observed or in some cases it was shifted to apparently lower shear stresses. This impression may be appointed to the adhesive nature of the HepG2iso cells, which made an initial flow pulse necessary, slightly altering the flow applied in the initial phase of the experiment. This was extensively discussed in section 3.8.3. Again in good correlation to the first observation of the CD44-HA interaction[10] the maximum fraction of interacting cells was reached at roughly (0.7-1) dyn/cm² for both cell types, before it gradually decreased. This comparison clearly demonstrated the independence of the CD44-HA interaction from the model cell type. This prompts the conclusion that the CD44-HA interaction may generally be independent from the type of cell, be it suspension or epithelial. As this was deemed sufficient other experiments concerning the characterisation of the CD44-HA interaction were conducted with only one cell type, HepG2Iso.

To undergird the finding that CD44 must be present on the cell surface for an interaction to take place, the effect of its down regulation was studied. It could be shown that knock down of CD44 in general (CD44pan) resulted in a complete suppression of the flow-induced interaction with HA. This was not the case for the down regulation of the two CD44variant isoforms CD44v3 and CD44v6. As all CD44 isoforms share the same HA binding domain each isoform would have the possibility to compensate for the loss of another isoform.[276]

As nicely reviewed by B. Toole HA has different functions depending on its chain length.[277] Indeed, rolling of HepG2iso cells was induced on substrates coated with macromolecular HA. Incubation of HepG2Iso cells with macromolecular GAGs in solution led to no significant reduction of the fraction of interacting cells for the treatment with CS, HS and KS, while a significant reduction was observed for macromolecular HA. The blocking by HA was further analysed by treatment with sHA (6-10 DS). It could be shown that this reagent could impair the process of flow-induced rolling on HA in a concentration dependent manner. Furthermore, it could be shown that while the number of rolling cells was reduced with an increasing concentration of sHA, the rolling velocity of the cells was increased. The reduction of rolling by sHA may be due to competitive binding of sHA to CD44.[162] For example, sHA treatment might have led to a displacement of macromolecular HA bound to CD44,[278] thereby preventing CD44 clustering which was required for the binding of HA.[279] The reduced CD44 clustering would then result in weaker binding of CD44 to the HA surface.[280] Also, macromolecular HA may be able to stabilise complexes between CD44 and itself or other cell surface receptors that might be required for rolling.[281] The treatment with sHA might prevent these complexes, thereby inhibiting the rolling on HA.

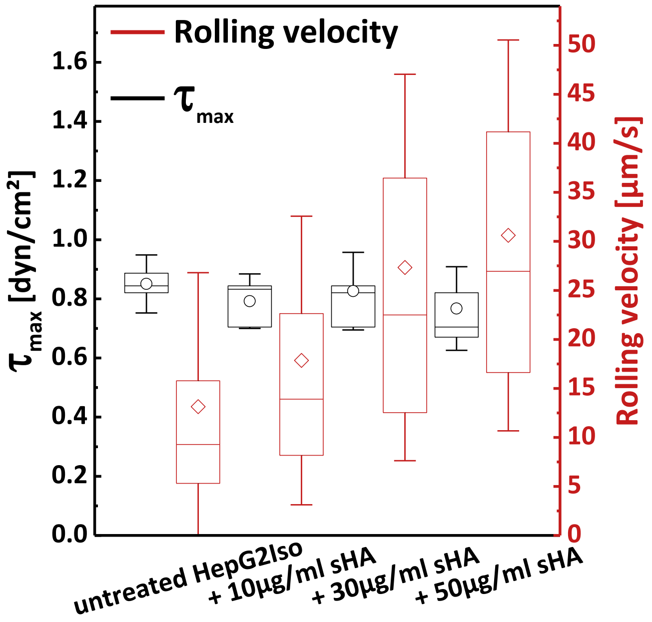

Figure 67: Comparison of the shear stress at which the maximum fraction of interacting cells is reached τ_{max} and the rolling velocity at approximately 1 dyn/cm². The data for τ_{max} originates from 3 independent experiments with 2 repeats each. The rolling velocities were calculated from at least 13 traces per treatment with a total of 800 data points (for 60 µg/ml) to 25,000 data points (untreated cells). ○ is the mean τ_{max}, ◇ is the mean rolling velocity. The box plots give the 1st (lower box margin), 2nd (middle line; median) and 3rd (upper box margin) quartile of the data. The whiskers represent the standard deviation.

As for the rolling velocity, the density of accessible CD44 on the cell surface may have been reduced by the sHA. This in turn would have led to larger distances between the individual receptors and, therefore, to a longer 'step' a cell took with each detachment-adhesion cycle. An interesting aspect of the effect of the treatment of HepG2Iso cells with sHA was that, while increasing amounts of sHA (6-10 DS) led to a reduction of the fraction of interacting cells and to an increase of the rolling velocity of the cells at a shear stress of approximately 1 dyn/cm², the shear stress at which the maximum fraction of interacting cells was reached (τ_{max}) did not noticeably change. Figure 67 gives a comparison between the mean rolling velocity and τ_{max} for HepG2Iso cells treated with a given concentration of sHA (6-10 DS). This finding was remarkable, as it demonstrated that both the probability of binding to the HA surface from flow (maximum fraction of rolling cells) as well as the rolling velocity of the cells (representing the detachment-attachment rate of a cell to the surface) interacting with HA, were strongly dependent on the density of the receptor available on the cell surface.

In contrast to this, the τ_{max}, which can be interpreted as the strength of the CD44-HA interaction, was independent of the number of receptor molecules available for interaction. It seems that as long as the interaction could take place, the strength with which CD44 bound to HA was the same.

So far it is not fully understood why metastatic cancer cells only extravagate at organs like the lung or the liver. As these organs are perfused by small blood capillaries, two explanations why the cancer cells extravagate only at these sites present themselves. Firstly, cancer cells may aggregate in the blood stream. These cancer cell aggregates may get stuck in the small capillaries and then attach to the endothelium of these capillaries as an initial step for extravasation.[282] Secondly, rolling, as a first step to extravasation, of the cancer cells on the endothelium might be induced by specific shear stress thresholds. As the shear stress on the blood vessel walls increases with a reduction of the capillary diameter, the smaller capillaries of the organs may offer a sufficient shear stress to induce rolling of the metastatic cells. The CD44-HA interaction pattern discussed in this study offers such a shear stress induced rolling, thus presenting a possibility for the cells to extravagate from the blood stream under sufficient shear conditions with HA present.

Summarising, the analysis of the role of CD44 in the rolling of leukaemic suspension cells and epithelial cancer cells on HA-coated surfaces revealed that CD44 was essential for this process. Blocking experiments using a CD44 antibody (BU52) and knock down experiments using panCD44 siRNA resulted in inhibition of the flow-induced rolling interaction, suggesting a decisive role of CD44 in the rolling process. Furthermore, sHA fragments with a size of 6-10 DS were able to prevent the rolling of HepG2iso cells on HA-coated surfaces. Both BU52 and sHA led to an increase in rolling velocity with increasing concentration. The findings presented in this section gave deep insight into the interaction with HA mediated by CD44.

4.2 INTERACTION OF HAEMATOPOIETIC PROGENITOR CELLS AND LEUKAEMIC BLASTS WITH HYALURONIC ACID

CD44 has been reported to be relevant both for the homing and engraftment of haematopoietic progenitor cells (HPC)[9] and of leukaemic stem cells[6-7] into the bone marrow (BM) and spleen of non-obese diabetic/severe combined immunodeficiency (NOD/SCID) mice. Furthermore, it could be shown that an activating monoclonal CD44 antibody could reduce the leukaemic repopulation of human acute myeloid leukaemia (AML) cells transplanted in NOD/SCID mice.[6] The mechanism underlying this effect is not yet understood. Thus, after unravelling the nuances of the interaction with HA mediated by CD44 as presented in the previous section it was of great interest to further understand its role both for healthy haematopoietic cells and for leukaemic cells.

4.2.1 INTERACTION OF HEALTHY HAEMATOPOIETIC PROGENITOR CELLS WITH HYALURONIC ACID

The results of the characterisation of the interaction of CD34 positive HPC with hyaluronic acid (HA) under flow conditions are described in this section. The HPC were derived from three different sources: cord blood (CB), mobilised peripheral blood (mPB) and the BM directly. This selection allowed the comparison between different cell sources. The HPC were kindly provided by the group of Prof. Anthony D. Ho from the Universitätsklinikum Heidelberg.

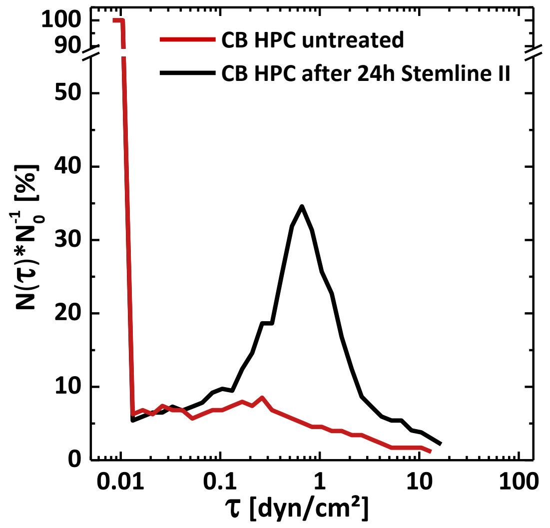

Figure 68: Effect of Stemline II pre-incubation of CD34$^+$ HPC from CB. Only the cells incubated in Stemline II medium supplemented with TPO, G-CSF, SCF and Flt-3L showed the flow-induced interaction with HA known from the model cell lines KG-1a and HepG2Iso.

First interaction experiments with freshly isolated HPC from CB on HA (Figure 68) yielded only negative results. Consistent with the findings of Legras *et al.*, Figure 68 demonstrates that incubation of HPC samples in cytokine-rich medium for 24 h prior to measurement of rolling on HA-coated surfaces was necessary.[283] As described in section 3.6, the cells were incubated in Stemline^{TM} II Haematopoietic Cell Expansion Medium supplemented with 100 ng/mL TPO, 100 ng/mL G-CSF, 100 ng/mL SCF, 500 ng/mL Flt-3L, 2 mmol/L L-glutamine, 1,000 U/mL penicillin and 100 U/mL streptomycin (hereafter referred to as Stemline II medium) for 24 h prior to measurement in the microfluidic shear force setup. Flow cytometry measurements (examples shown in Figure 69 for CB, in Figure 70 for mPB and in Figure 71 for BM) showed that the incubation in Stemline II medium did not lead to a differentiation of the cells. The graphs not only show that nearly all cells remained CD34 positive after the 24 h in Stemline II medium, but also that most were CD44 positive. Further data concerning the fractions of cells remaining CD34 after incubation in Stemline II medium for 24 h and on the CD44 expression are shown in Table S6 (Appendix section 7.2.4.1)

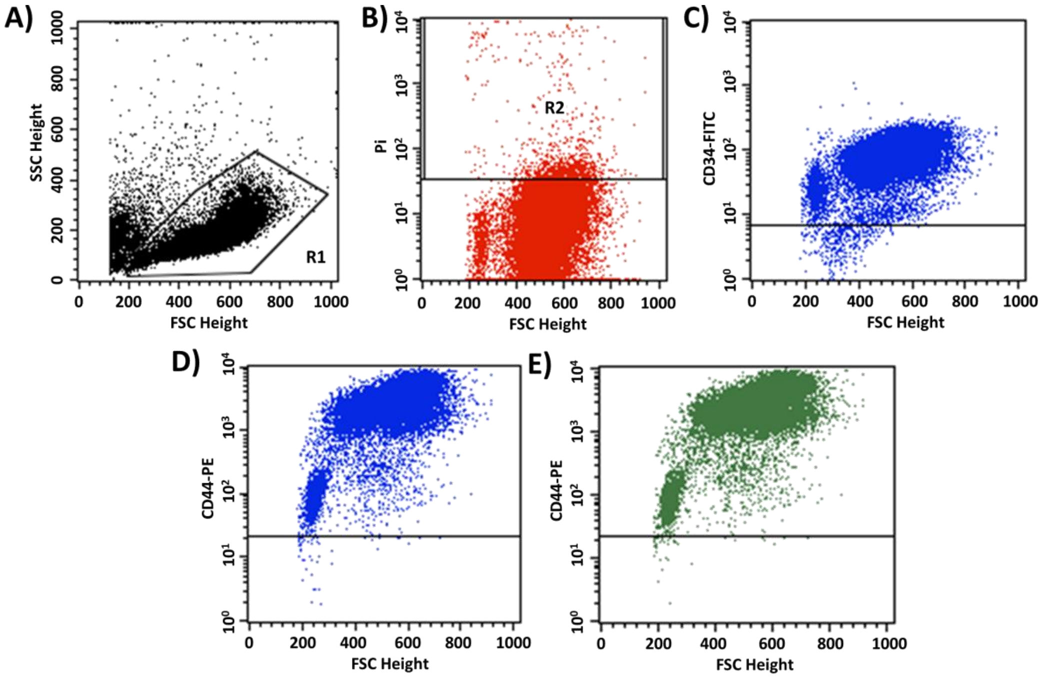

Figure 69: Flow cytometry measurement of CB HPC after 24 h incubation in Stemline II. Based on their SSC- and FSC-properties the cell population was gated (R1 in A). These cells were then tested for their integrity by Pi-staining and dead cells were excluded (R2 in B). In the example depicted here from the live cells nearly all were CD34 (98.82 % in C) and CD44 (99.85 % in D) positive. From the CD34 positive cells also nearly all were CD44 positive (99.88 % in E). Other measurements yielded comparable results.

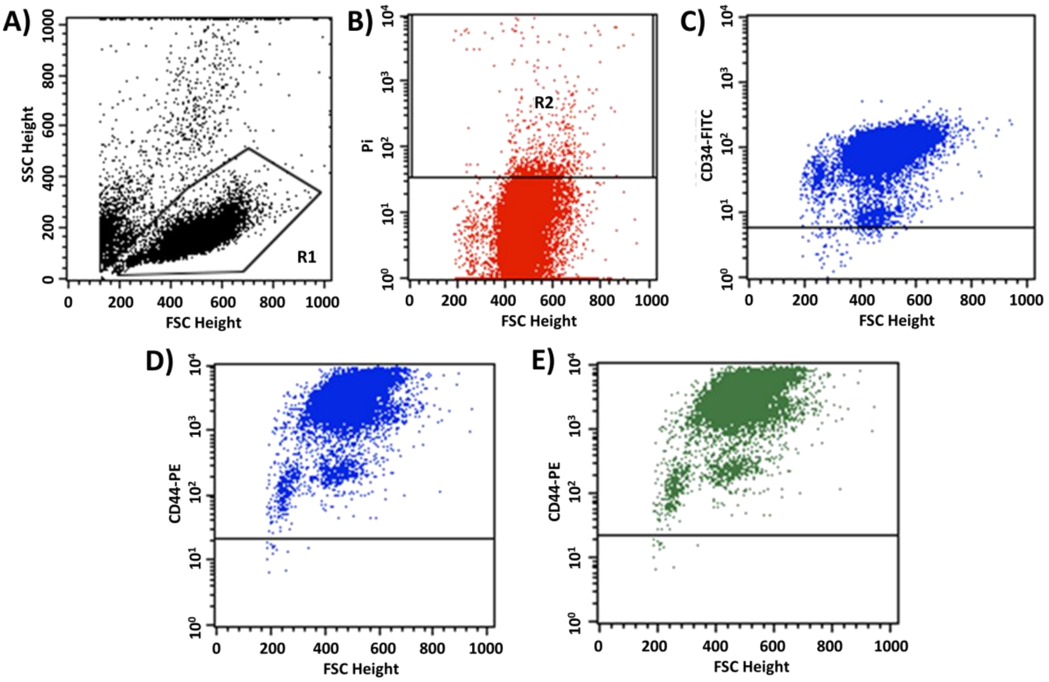

Figure 70: Flow cytometry measurement of mPB HPC after 24 h incubation in Stemline II. Based on their SSC- and FSC-properties the cell population was gated (R1; A). These were also tested for their integrity by Pi-staining and dead cells were excluded (R2; B). In the example depicted here from the live cells nearly all were CD34 (99.66 %; C) and CD44 (99.96 %; D) positive. From the CD34 positive cells also nearly all were CD44 positive (99.96 %; E). Other measurements yielded comparable results.

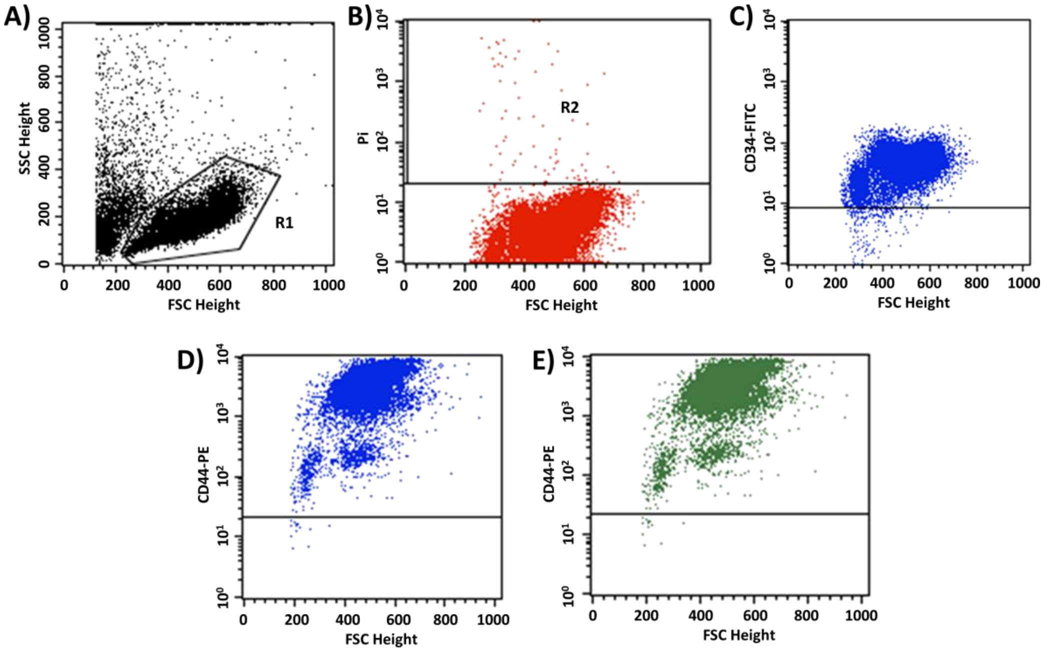

Figure 71: Flow cytometry measurement of BM HPC after 24 h incubation in Stemline II. Based on their SSC- and FSC-properties the cell population was gated (R1; A). These were also tested for their integrity by Pi-staining and dead cells were excluded (R2; B). In the example depicted here from the live cells nearly all were CD34 (98.32 %; C) and CD44 (97.27 %; D) positive. From the CD34 positive cells also nearly all were CD44 positive (97.40 %; E). Other measurements yielded comparable results.

As shown in Figure 72 the interaction curves of KG-1a cells with HA were composed of two forms of interaction: rolling and immobile adherence (the supplementary Video S2 shows rolling and immobile adherent cells in comparison; the description can be found in section 7.1.2.1, the video is provided on the supplementary CD). Next to the pre-incubation, this discrimination between the two forms of interaction was the second aspect important for the analysis of the HPC interaction data. This discrimination was not made for the interaction of the cell lines with HA, as it was of no great importance to the analysis or the findings. In Figure 72 the discrimination is made for untreated KG-1a cells and for cells treated with 3 µg/mL and 9 µg/mL BU52. It can be seen that the fraction of rolling cells increased after a critical shear stress of approximately 0.2 dyn/cm² was reached. In contrast to this flow-induced behaviour of the rolling cells, the immobile adherent cells only marginally increased and then detached from the surface with increasing shear stress applied. This behaviour could be observed not only for the untreated KG-1a cells, but also for the cells incubated with BU52.

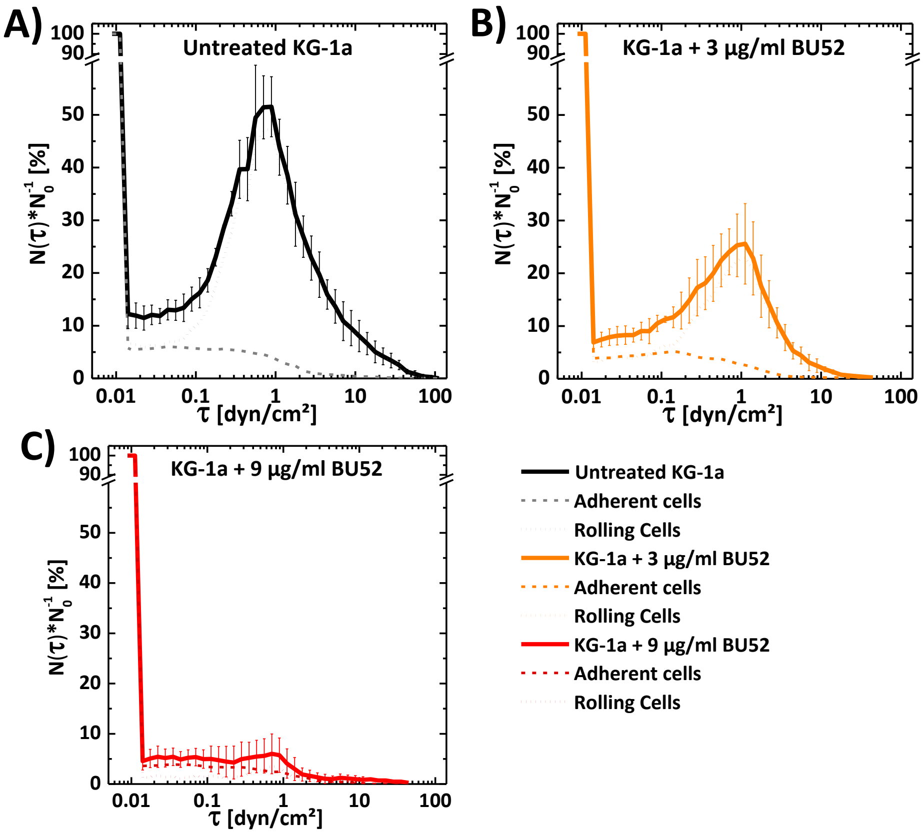

Figure 72: Discrimination between immobile adherent and rolling cells. A comparison is shown between untreated KG-1a cells and KG-1a cells treated with 3 and 9 µg/mL BU52 (n ≥ 4 for each treatment with > 300 cells/FOV). All error bars represent the SD. For clarity, no error bars are shown for the discrimination curves (dotted and dashed lines).[266]

Following the establishment of the experimental protocol (antibody concentration: 9 µg/mL, pre-incubation in cytokine-rich Stemline II medium, discrimination between rolling and immobile adherent cells), the interaction curves for HPC shown in Figure 73 were measured. A critical shear stress of approximately 0.2 dyn/cm² was required to induce rolling in HPC derived from healthy donors, irrespective of the source, *i.e.* CB, mPB or BM. The maximum fraction of rolling cells was also observed in the same region as previously described for KG-1a for all types of HPC (approximately (0.7-1) dyn/cm²; Figure 73). While the maximum fraction of rolling cells was very similar between HPC from different sources, it was significantly lower (approximately (15-25) %) than that found for KG-1a (approximately 60 %, see section 4.1) Due to the limited number of HPC that could be isolated from the blood and bone marrow samples, BU52 and anti-IgG1 blocking studies were not performed for all samples. Overall, the addition of 9 µg/mL BU52 suppressed the rolling and partially also the immobile adhesion, while the anti-IgG1 isotype control did not affect the interaction between the HPC and HA. While the rolling interaction was comparable for all types of HPC measured, the immobile adhesion was not. Relatively higher percentages of immobile adherent cells were observed in BM HPC than in CB or mPB (< 5 % for CB and mPB HPC and ~ 10 % for BM HPC). Furthermore, BM HPC generally showed a lower tendency to interact with HA. Only 1 of 4 BM HPC samples showed a prominent flow-induced rolling at a comparable level as observed for the CB or mPB HPC samples.

In contrast to the homogeneous interaction of the HPC with HA under shear stress, flow experiments with leukocytes from the PB of healthy donors showed no rolling on HA. The data is shown in Figure S9 (Appendix section 7.2.4.1).

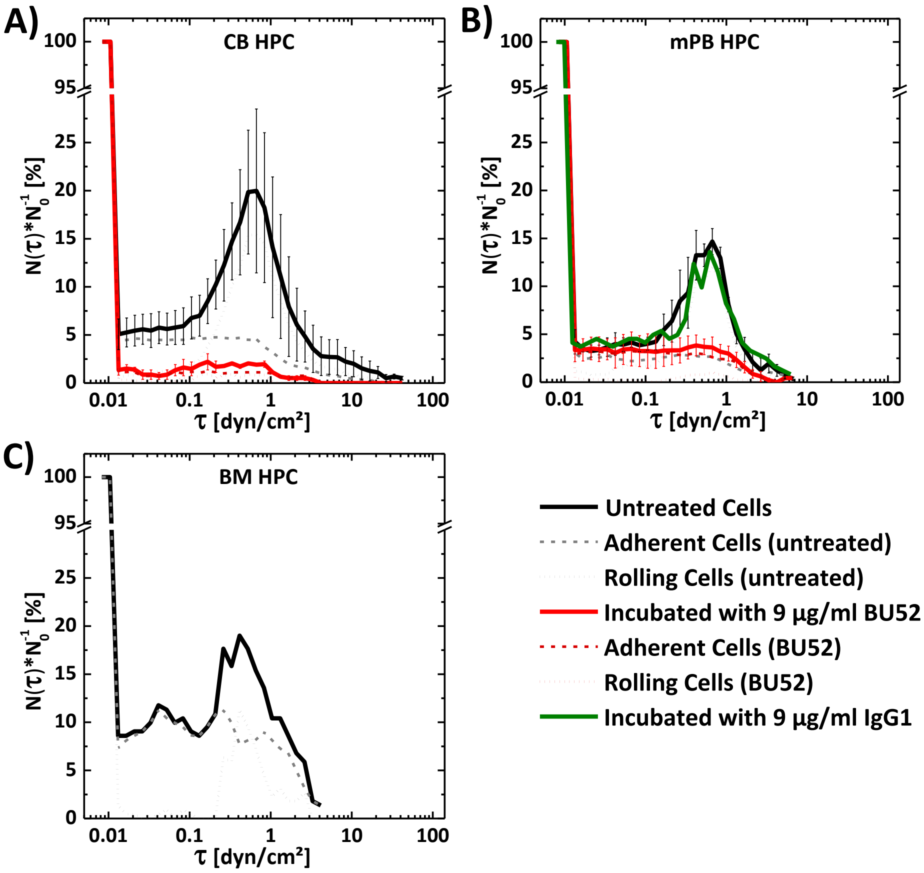

Figure 73: Comparison of the interaction of HPC from different sources with HA. Interaction measured in untreated HPC from CB (n = 6 from 5 groups of donors; > 200 cells/FOV), mPB (n = 4 from 3 donors; > 250 cells/FOV) and BM (n = 1 from 1 donor; 221 cells/FOV) and in HPC treated with 9 µg/mL BU52 (CB: n = 2 from 2 groups of donors; > 260 cells/FOV; mPB: n = 3 from 3 donors; > 230 cells/FOV) or with 9 µg/mL anti-IgG1 control (mPB: n = 1; 234 cells/FOV). In all cases, the interaction curve is comprised of immobile adherent and rolling cells, similar to KG-1a. Error bars represent the SD. For clarity, no error bars are shown for the discrimination curves (dotted and dashed lines).[266]

4.2.2 INTERACTION OF BLASTS FROM PATIENTS WITH ACUTE MYELOID LEUKAEMIA WITH HYALURONIC ACID

The leukaemic cell material used in this study was kindly provided by the group of Prof. Anthony D. Ho from the Universitätsklinikum Heidelberg. The blasts from patients with freshly diagnosed AML were isolated from the raw cell material by FAC sorting and stored in liquid nitrogen until use. In this study the blasts from 11 individual patients (named AML 1-11) were used. If not mentioned otherwise the leukaemic blasts were isolated from the BM of the respective patient. Cells isolated from samples from the PB are marked appropriately. As shown in the exemplary overviews (Figure 74, Figure 75) the cells were sorted based on their side scatter (SSC) and CD45 characteristics (SSC^{low}, CD45^{dim}). The cells were then incubated in Stemline II medium for 24 h, as established for the HPC, to ensure equivalent treatment of all cell types allowing later comparison.

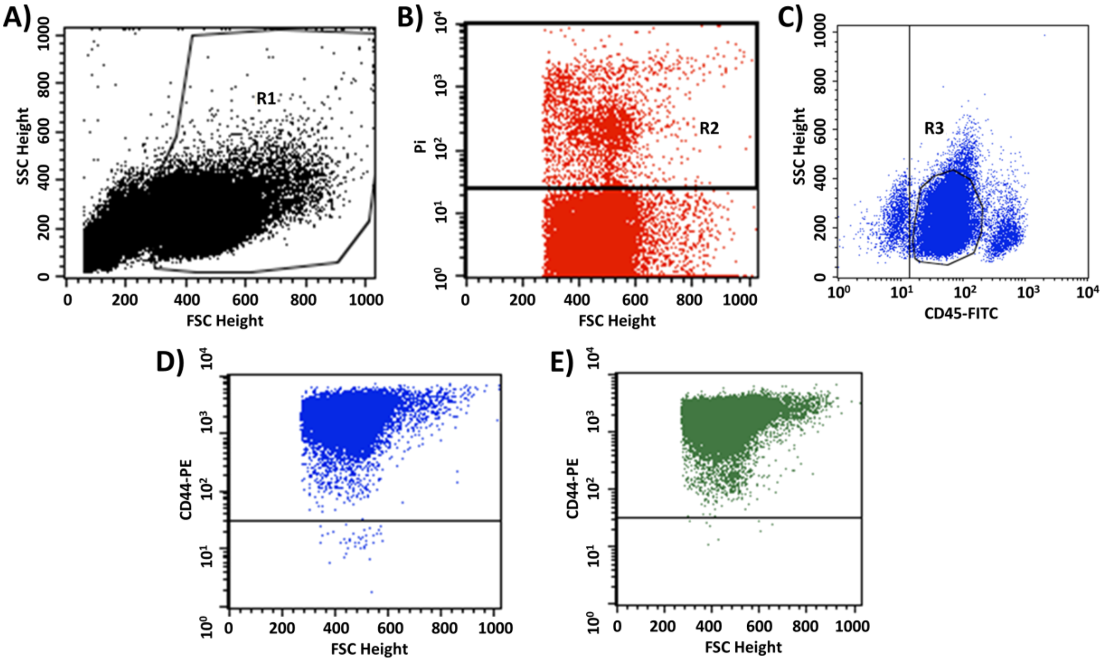

Figure 74: FAC sorting of the blasts from AML 1. Based on their SSC- and FSC-properties the cell population was gated (R1; A). These were also tested for their integrity by Pi-staining and dead cells were excluded (R2; B). From the live cells the blasts were selected by their SSC and CD45 characteristics (SSC^{low}, $CD45^{dim}$, C). The CD44 expression was measured for the live cells (99.82 %; D) and for the leukaemic blasts (99.99 %; E).

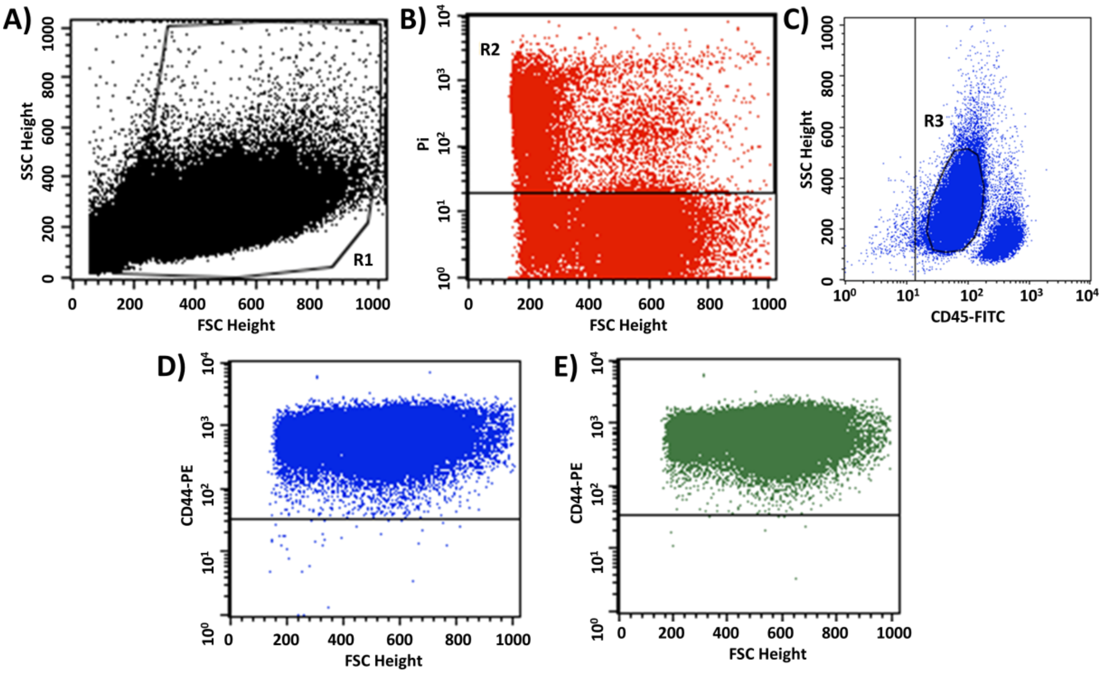

Figure 75: FAC sorting of the blasts from AML 2. Based on their SSC- and FSC-properties the cell population was gated (R1; A). These were also tested for their integrity by Pi-staining and dead cells were excluded (R2; B). From the live cells the blasts were selected by their SSC and CD45 characteristics (SSC^{low}, $CD45^{dim}$, C). The CD44 expression was measured for the live cells (99.95 %; D) and for the leukaemic blasts (99.98 %; E).

Microfluidic shear force measurements revealed a remarkably variable behaviour in terms of rolling and immobile adhesion of leukemic blasts. This was surprising as the CD44 expression was high in all 11 samples (CD44pan expression of ≥ 95.7 %, Table S7 in the Appendix section 7.2.4.2). In contrast to HPC from healthy donors which all showed basically the same interaction pattern, the rolling interactions of leukaemic blasts could be divided into 3 patterns (Figure 76): (A) pronounced rolling interaction, with most of the rolling cells detaching from the surface prior to (5-10) dyn/cm²; (B) rolling interaction persistent beyond (5-10) dyn/cm²; and (C) no rolling observed at all. An overview of all samples is shown in the supplementary Figure S10 (Appendix section 7.2.4.2). In all cases, flow-induced rolling was observed only beyond a critical shear stress of approximately 0.2 dyn/cm² and reached the maximum at approximately (0.7-1) dyn/cm², in analogy to healthy HPC and KG-1a cells. The amount of immobile adherent cells varied, however, greatly among the AML samples (from < 5 % to approximately 20 % of the initially visible cells N_0). No direct relation between the two different interactions, *i.e.* rolling versus immobile adhesion, could be observed in the sample cohort.

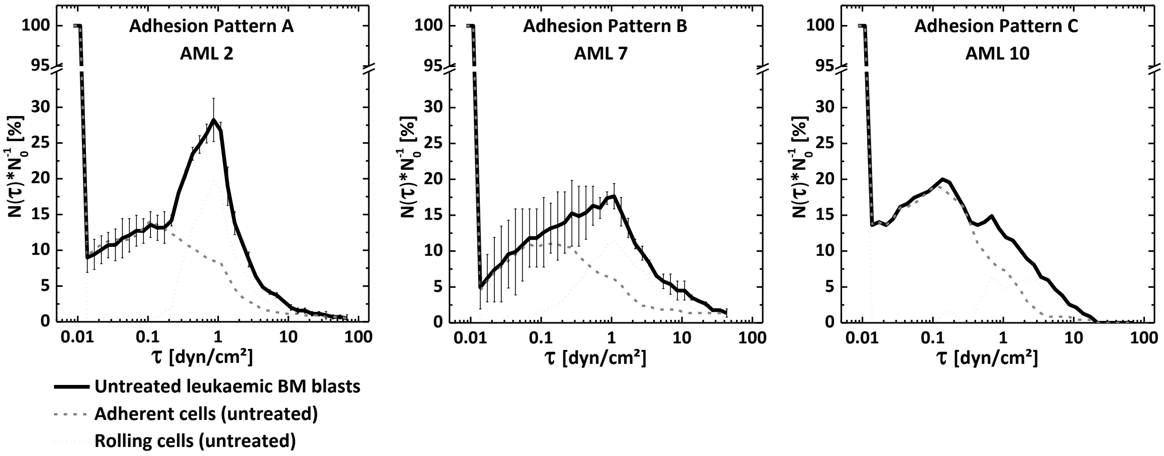

Figure 76: Adhesion patterns found for the interaction of leukaemic blasts with HA. The blasts ($CD45^{dim}SSC^{low}$) were isolated from 11 different frozen AML samples. Despite the heterogeneity of the samples, 3 subclasses were characterised. Pattern A: High numbers of rolling cells that detach prior to a shear stress of (5-10) dyn/cm². Pattern B: High numbers of rolling cells that remain adherent beyond a shear stress of (5-10) dyn/cm². The A and B adhesion patterns show varying numbers of immobile adherent cells. Pattern C: Very few rolling cells and high numbers of immobile adherent cells. Each experiment was conducted with > 160 cells/FOV. If error bars are given they represent the SD from two measurements. If none are shown the sample material was not sufficient for more than one measurement. For clarity, no error bars are shown for the discrimination curves (dotted and dashed lines).[266]

Treatment with BU52 completely inhibited rolling in all samples, while suppression of the immobile adhesion to HA was at best achieved partially. In three cases, no effect was observed at all. Whether the immobile adhesion could be blocked by BU52 or not, was not related to the rolling pattern as shown in Figure 77. Here, an example for both an effective and en ineffective suppression of the immobile adhesion by BU52 is presented for each of the three rolling patterns found for the leukaemic blasts. For two samples of leukaemic blasts isolated from the BM and in which the treatment with BU52 was ineffective concerning the suppression of the immobile adhesion, a comparison was made to the blasts isolated from the PB of the same patient (Figure 78 and Figure S11 in the Appendix section 7.2.4.2). Remarkably, although blocking of the immobile adhesion with BU52 was ineffective for the BM blasts an effective suppression was observed for the corresponding PB blasts. The rolling interaction in turn was completely suppressed in both cases.

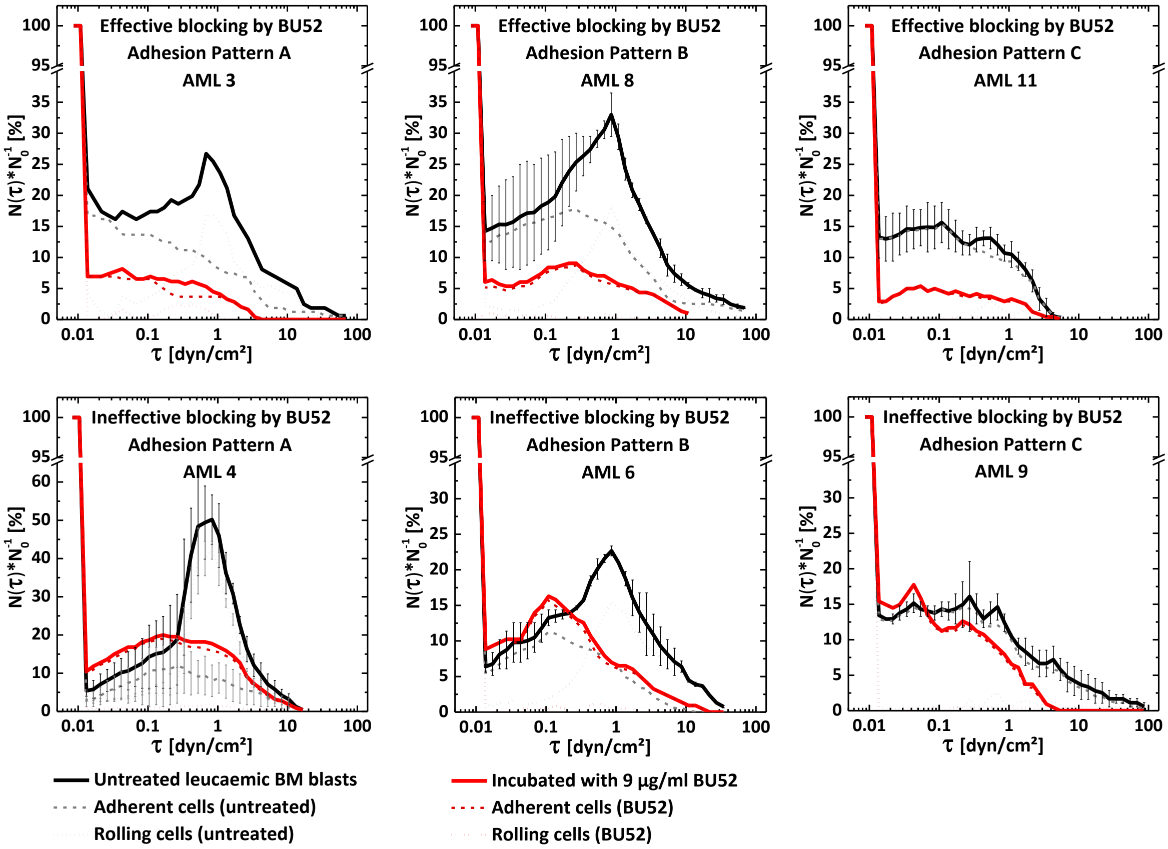

Figure 77: Effectiveness of BU52 on the suppression of interaction with HA. An exemplary comparison of samples for which treatment with BU52 was either effective or ineffective is shown in this graph. Each experiment was conducted with > 160 cells/FOV and error bars are the SD. For clarity, no error bars are shown for the discrimination curves (dotted and dashed lines).[266]

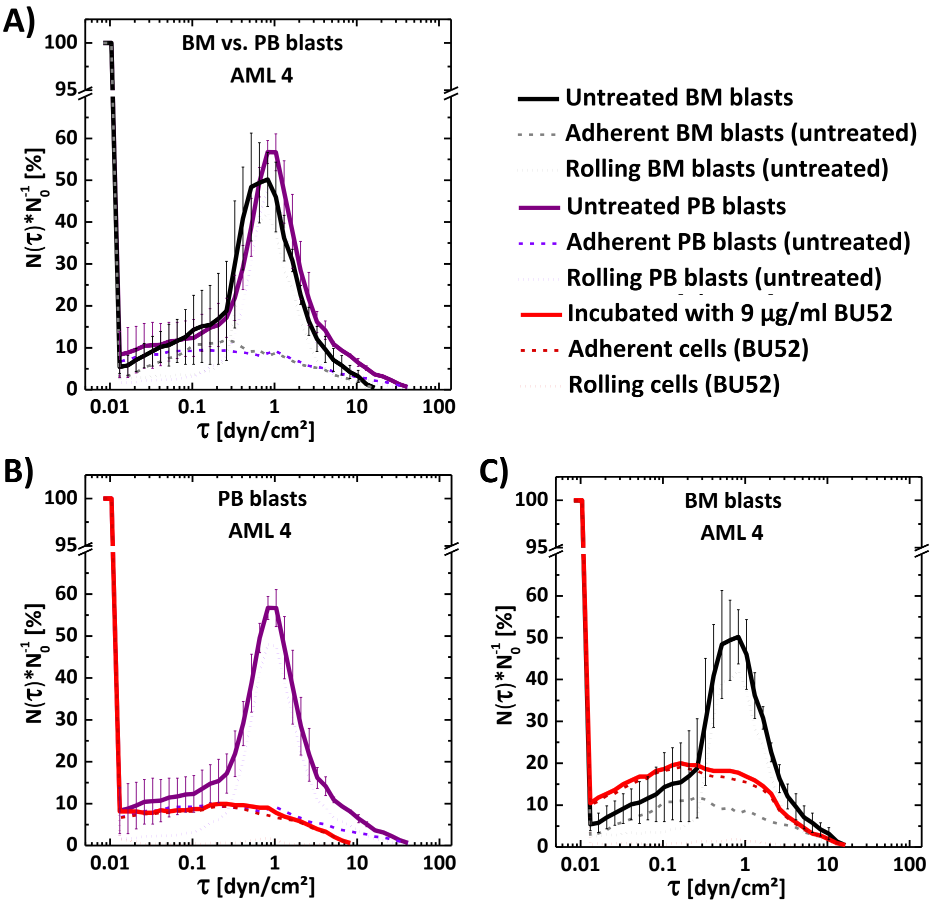

Figure 78: Comparison between leukemic blasts from BM and PB. No significant difference in the interaction curves for leukemic blasts was observed between PB and BM (A). Treatment with BU52 was highly effective in blasts from PB (B), while large numbers of blasts from the BM remained capable of adhering to HA (C). Each experiment was conducted with > 160 cells/FOV and error bars are the SD. For clarity, no error bars are shown for the discrimination curves (dotted and dashed lines).[266]

The AML samples with immobile blast adhesion to HA of greater than 10 % upon BU52 treatment were clinically associated with poor response to induction chemotherapy compared to the other patients in which the blast interaction to HA could be inhibited by BU52 (Table 7). In the group in which BU52 was ineffective, only one of five patients achieved complete remission (CR) after induction chemotherapy. Whereas in the group of six patients, in whom the adhesion of the leukemic cells to the HA-surface could be inhibited by BU52, three of them achieved CR. Furthermore, the overall survival for the latter group of patients (mean: 375.5 days, 95 % confidence interval: 265.5-485.5) was also significantly longer than that for the former group (mean: 100.6 days, 95 % confidence interval: 0-219.2), in which BU52 did not show any effect (log-rank test: $p = 0.016$, Figure 79). Further comparisons in terms of cytogenetic and molecular genetic risk factors did not show a significant difference between the two groups, but it was remarkable that all patients with favourable risk factors belonged to the group in which BU52 was effective (Table S8, Appendix section 7.2.4.2).

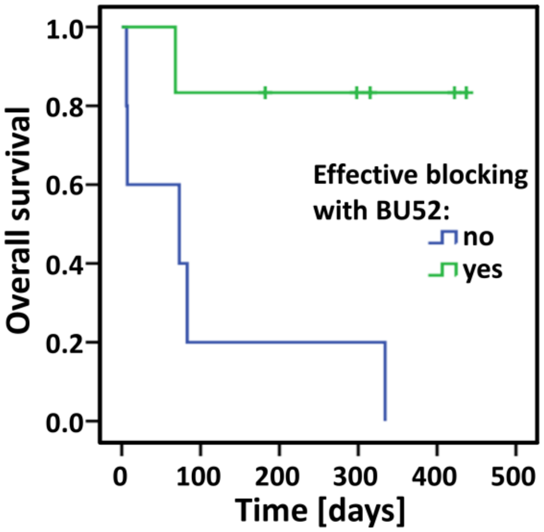

Figure 79: Kaplan-Meier curve showing the patients' overall survival for the two subclasses of BU52 blocking efficiency. It is evident that efficient blocking of the immobile adhesion to HA by BU52 was directly correlated to a longer overall survival.[266]

Table 7: BU52 blocking efficiency for each blast sample and the associated patient's outcome. The efficiency of the suppression of the immobile adhesion to HA by BU52 is shown. Light grey marks the samples for which efficient blocking could be observed. Dark grey marks the inefficient samples.[266]

Sample No.	BU52 blocking efficiency (remaining % of N_0)		State after induction chemotherapy	Deceased
	< 10 %	> 10 %		
1	░		Persistence	No
2	░		CR	No
3	░		Persistence	Yes
4		▓	Persistence	Yes
5		▓	Deceased during chemotherapy	Yes
6		▓	Persistence	Yes
7	░		CR	No
8	░		CR	No
9		▓	CR	Yes
10		▓	No chemotherapy	Yes
11	░		Persistence	No

4.2.3 DISCUSSION

In this section the ability of CD44 to mediate rolling and immobile adhesion of HPC and leukaemic blasts to HA-coated surfaces under physiological shear stress conditions was analysed. Using a microfluidic shear force device, it was possible to precisely quantify the shear stress required to induce rolling and to overcome adhesion for HPC versus leukaemic cells on HA-coated surfaces. Whereas HPC from healthy donors behaved relative homogeneously on HA-coated surface, there was a much broader range of behavioural patterns concerning the rolling and immobile adhesion for leukaemic cells under identical conditions. The monoclonal CD44 antibody BU52 was able to completely abrogate the shear stress-induced rolling of HPC from healthy donors and leukaemic cells from patients with AML in contrast to the incomplete inhibition of the immobile adhesion exhibited by the leukaemic blasts. Another remarkable finding was that those patients, in whom the immobile adhesion of the leukaemic blasts was not affected by BU52, were associated with poor response to induction chemotherapy and an adverse long-term clinical outcome.

It was shown that expression of CD44 was not the only prerequisite for an interaction with HA. Consistent with the findings of Legras *et al.,* the necessity to pre-incubate HPC in cytokine-rich medium for 24 h prior to measurement of rolling on HA-coated surfaces was established.[283] In the case of healthy leukocytes even this incubation could not initiate the interaction, suggesting that the mechanism controlling the interaction of CD44 with HA was highly complex or may have become redundant in the highly differentiated cell types.

Whereas all types of HPC analysed displayed a high expression of CD44pan, the expression of CD44variant isoforms was mostly low.[265-266] Two forms of interaction were of interest throughout the healthy HPC and the leukaemic blasts; the flow induced rolling interaction and the immobile adherence. If rolling was observed the shear stress at which the maximum interaction was observed was always in the range of approximately (0.7-1) dyn/cm². This corresponds well with the shear stress observed in post-capillary venules. In the latter venular system, the shear stress has been estimated to be in the range of (1-4) dyn/cm², which is consistent with the parameters reported for the selectin-dependent leukocyte rolling.[116-117,284] Though the interaction of HPC with HA-coated surfaces was significantly weaker (a smaller maximum fraction of interacting cells) than that of KG-1a, the maximum fraction of cells undergoing the rolling interaction was comparable throughout all HPC samples from CB, mPB and BM. Furthermore, the threshold shear stress of approximately 0.2 dyn/cm², beyond which rolling was induced, was also observed throughout all cell types if rolling was observed at all. While KG-1a and

HPC isolated from the blood stream (CB, mPB) hardly showed immobile adherence to HA, a significant fraction of HPC from the BM exhibited this form of interaction. A possible explanation for this result could be the inactive, dormant state of the HPC derived from the BM niche, in contrast to cells that had been mobilised out of the niche into the peripheral blood. Wilson *et al.* demonstrated that dormant BM haematopoietic stem cells were activated to self-renewal upon exposure to stress to the BM, *e.g.* blood loss, infection, or G-SCF stimulation.[285] Accordingly, the activation status probably alters the adhesion mechanisms, either rolling or immobile adherence, of HPC to the marrow niche.

In leukemic blasts the immobile adherence to HA was a remarkable finding. The fraction of immobile adherent cells varied greatly among the 11 leukemic blast samples and no correlation between the rolling patterns and the fraction of immobile adherent cells was found. Moreover, the CD44 antibody BU52 in some cases had little or no effect on this adhesion, whereas rolling of the leukemic blasts was completely abrogated by the same antibody. In addition, a correlation between an ineffective blocking of the immobile adherence and a poor long-term outcome of the respective patients could be demonstrated. This trend was independent of the risk stratification according to the cytogenetic and molecular genetic risk factors. Furthermore, the suppression of the immobile adhesion by BU52 was less effective for AML blasts isolated from the BM than it was for those isolated from the PB, although the fractions of rolling and adherent cells were nearly identical for the untreated cells. This again strengthened the notion that the immobile adhesion to HA could be associated with the vicinity to the BM niche. Saito *et al.* reported that leukemic stem cells in the stem cell niche were more chemotherapy resistant and that mobilisation enhanced the induction of apoptosis and elimination of these cells.[22] As the immobile adhesion is linked to the niche it may be involved in the retention of the leukaemic stem cells in the niche and could present a valid target for mobilisation of leukaemic stem cells in the future.

Similar to the observations reported by Bendall *et al.*,[286] the expression of CD44variant isoforms in AML was more divergent than that found for the normal HPC from the marrow.[265-266] This might explain the more heterogeneous adhesion patterns and the BU52 blocking efficiency in AML. Assuming that the leukaemic blasts show a behaviour similar to that of the LSC it is possible that a special CD44variant isoforms, which BU52 is not able to neutralise, might be involved in the retention of leukemic cells in the BM niche, rendering them invulnerable to chemotherapy. In line with this, Jin *et al.* demonstrated that blocking of CD44 reduced leukemic repopulation of human AML transplanted in NOD/SCID mice.[6] This indicates that CD44 somehow contributes to the homing and engraftment of LSC. All in all the occurrence of the CD44 mediated rolling and immobile adhesion on HA was highly diverse. Similarly the heterogeneity of the leukaemia initiating cells in AML might be highly diverse as well, such that an antibody against CD44pan might not be effective for different patients with differing over-expressions of CD44variant isoforms.

4.3 CELL INTERACTION WITH LAYERS OF MESENCHYMAL STROMAL CELLS

The study of the interaction of cells with HA artificially immobilised on a surface presents an ideal scenario for the characterisation of interactions specific for HA, as it was described in the previous sections. *In vivo*, however, a far broader spectrum of ligands and, therefore, of ligand-receptor interactions is possible. In the context of homing the most important cell-cell contacts are between the homing HSC, of course, and either the endothelial cells, forming the blood vessels, or the mesenchymal stromal cells (MSC), found abundantly in the BM niche.[57,71] To gain an impression of the relevance of the CD44-HA interaction, discussed so far in this work, in a more realistic environment, the interaction with surfaces covered with MSC was analysed. In this section the establishment of the procedure to conduct such analysis in the microfluidic shear force setup is described. Subsequently, first cell-cell interaction curves of the model cell line KG-1a and HPC with MSC are presented.

4.3.1 EXPERIMENTAL DETAILS FOR THE ESTABLISHMENT OF MSC FEEDER LAYERS

To analyse the interactions between suspension cells, as previously used in this work, and MSC under flow conditions it was necessary to prepare surfaces completely covered with convergent MSC, the so-called feeder layers. As the MSC were harvested from the BM, they were, like other primary cell materials, only available in relatively low quantities. It was, therefore, desirable to require as few MSC as possible to develop a feeder layer. For this reason the glass sample holder, on which the feeder layer was to grow, was not pre-coated with MSC, but the MSC were rather directly injected into the fully assembled channel system and allowed to settle there. In principle the procedure was adapted from experiments concerning the detachment of fibroblast cells from different sample surfaces.[11-12] It was important for the cells to be fully adhered and in a healthy state, as impairment of the cells may lead to modified interaction behaviour by *e.g.* differing receptor expression. The most easily analysable parameters that are determined by the condition of the MSC were the morphology and shear stress required for detachment. Both were studied for MSC cultured in the microfluidic shear force system. Due to the limited amount of cell culture medium in the channel system the most critical factor influencing the condition of the MSC was the amount of nutrients available to the cells.

Figure 80 and the corresponding supplementary Video S4 (description found in the Appendix section 7.2.5, video provided on the supplementary CD) show the adhesion of MSC to a glass substrate in the microfluidic channel system. With the MSC density used for this experiment the best cell morphology was observed after approximately 5 h of incubation. Figure 81 A shows such well spread healthy cells. Longer incubation led to unhealthy, elongated cells (Figure 81 B).

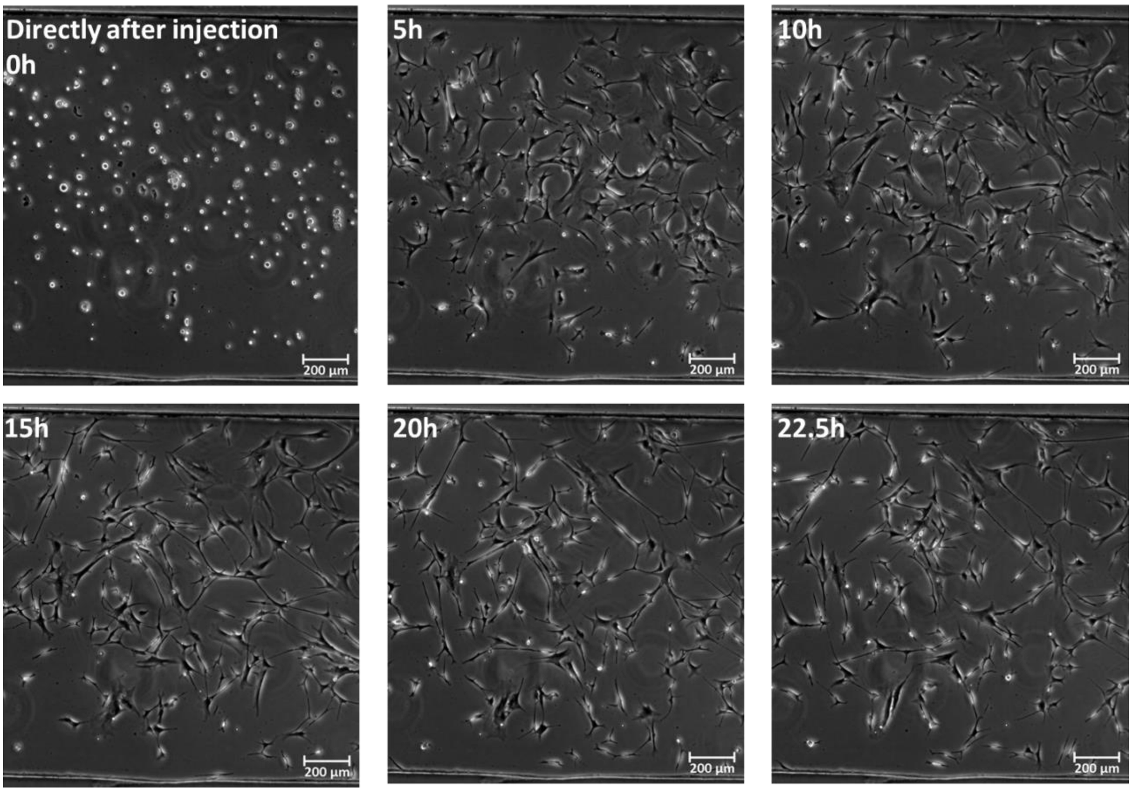

Figure 80: Incubation of MSC in an assembled microfluidic channel setup. The images show different time points of the incubation of MSC inside an assembled microfluidic channel setup. It can be seen that while the cells spread broadly initially the cells appear thin and elongated after longer period of incubation.

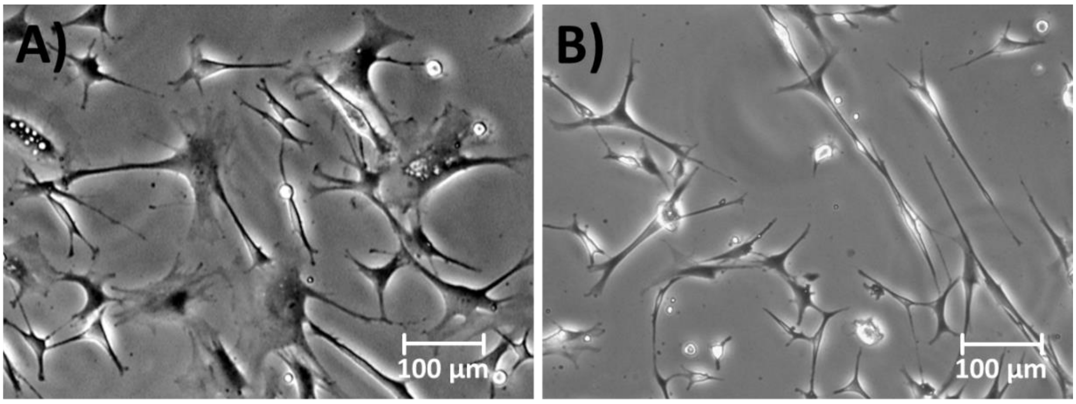

Figure 81: Images of well spread MSC (A) and unhealthy, elongated MSC (B).

To determine whether cell-feeder layer interaction experiments could repeatedly be conducted without detaching the MSC and to evaluate the effect such experiments had on the MSC, the interaction with the model suspension cell line KG-1a was investigated. As seen in Figure 82 A the shear stress required to detach all KG-1a cells from the MSC was approximately one order of magnitude below that required to detach the MSC from the glass surface. This was the prerequisite for being able to use an MSC feeder layer for repeated measurement of the interaction with other cells, such as KG-1a cells, under flow. This meant that the MSC could be used far more efficiently, than if the feeder layer had been a single-use surface. As shown in Figure 82 B the interaction with the KG-1a cells had no noticeable effect on the shear stress required to detach the MSC from the glass substrate on which they were adhered. This, like the cell morphology, can be seen as a measure for the viability of the MSC. It required at least 1,000 dyn/cm² to detach 50 % of the MSC independent of the number of interaction experiments conducted prior to their detachment. Exact numbers could not be determined in all measurements as the maximum flow rate applicable in the microfluidic system was not always sufficient to detach the MSC. That the viability of the MSC was directly correlated to the shear stress required to detach them could well be seen in channels with strongly elongated MSC, which could not even be brought into contact with other cells as they were so weakly adhered that they detached even during injection of the KG-1a cells.

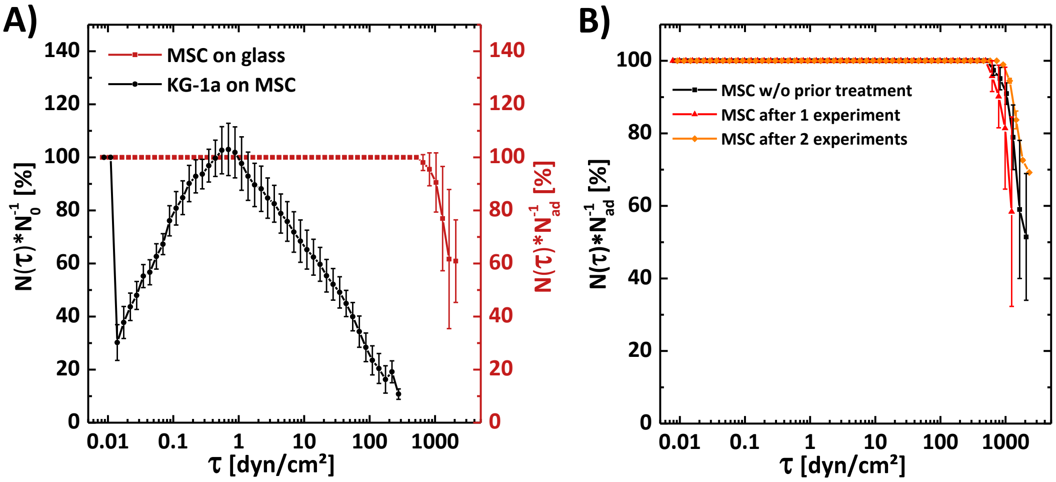

Figure 82: Demonstration of the strong adhesion of healthy MSC to glass. A) The adhesion strength of MSC on glass is compared to the interaction strength of KG-1a cells (n = 4, > 68 cells/FOV, reduced number of cells visible because video microscopy was conducted with 10x Ph1 objective to better determine between the different cells types) with the MSC. B) Shear stress required to detach MSC from glass (n = 2, > 130 cells/FOV). Prior interaction of KG-1a cells with the MSC had no effect on the shear stress required to detach the MSC. The error bars represent the SD.

4.3.2 INTERACTION OF SUSPENSION CELLS WITH MSC FEEDER LAYERS UNDER FLOW

This section goes into more detail on the interaction of KG-1a cells with MSC, introduced in the last section, and presents how HPC from different sources behaved in this system. As shown in Figure 83 for the untreated cells an interaction curve similar to that of KG-1a cells with HA was measured. A nearly identical interaction curve was observed for KG-1a cells preincubated with 9 µg/mL BU52. As this concentration of BU52 was sufficient to fully suppress the interaction with HA, this observation indicated that the interaction with MSC was independent of CD44. Although altogether weaker the same interaction pattern and, by treating the cells with BU52, the same independence of CD44 was observed for HPC from both CB and mPB (Figure 84). In all cases the number of interacting cells increased directly after a flow was applied. The maximum fraction of interacting cells reached was approximately 100 % for KG-1a, 60 % for CB HPC and 40 % for mPB HPC. After the maximum was reached the cells were continuously detached from the surface. In contrast to the flow induced interaction discussed in the previous sections (sections 4.1 and 4.2) the interaction here was not of a rolling, but more of an immobile nature. As can be seen in the supplementary Video S5 (description found in the Appendix section 7.2.5, video provided on the supplementary CD) the practically ‘stuck’ to the surface from the flow, similar to the immobile interaction observed mostly for leukaemic blasts (section 4.2). However, such a distinctive increase of the fraction of immobile adherent cells was not observed on HA-coated surfaces.

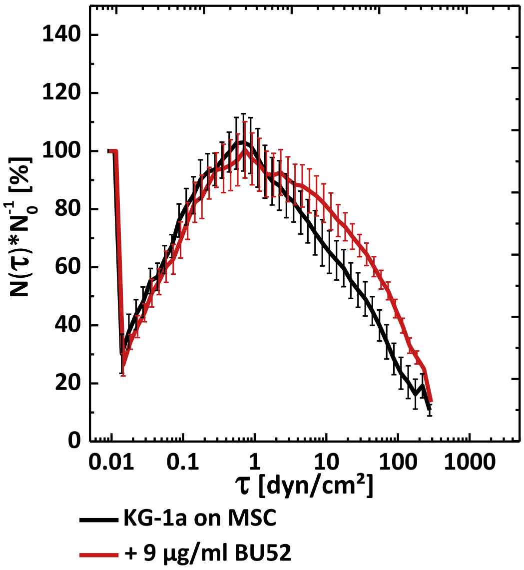

Figure 83: Interaction of KG-1a cells with MSC under flow conditions. The fraction of KG-1a cells interacting with the MSC increased until a maximum was reached at ~ 1 dyn/cm² (n = 4, > 68 cells/FOV, video microscopy with 10x Ph1 objective to better determine between the different cells types). After this the cells detached from the MSC. Treatment of the KG-1a cells with 9 µg/mL BU52 did not lead to an abrogation of the interaction. The error bars represent the SD.

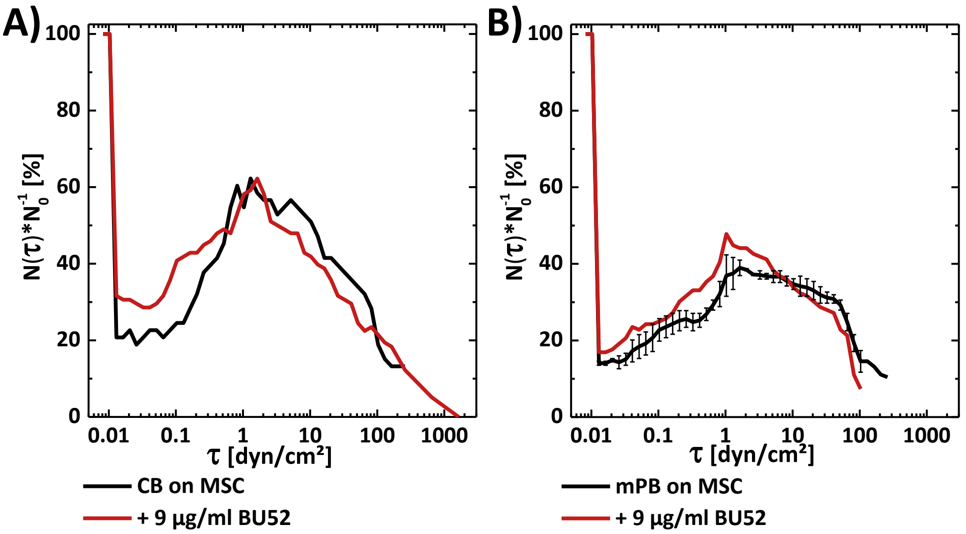

Figure 84: Interaction of HPC from CB (A) and mPB (B) with MSC under flow conditions. The HPC from both sources show nearly the same interaction with the MSC (n ≥ 1, > 53 cells/FOV, video microscopy with 10x Ph1 objective to better determine between the different cells types). The error bars represent the SD.

4.3.3 DISCUSSION

In this section the possibility to culture MSC inside the microfluidic shear force setup was demonstrated and the interaction of other cells with the MSC was analysed under flow conditions. The aim was to prepare a closed layer of convergent MSC. It could be shown that, if the correct conditions were upheld, the culture of MSC inside a fully assembled channel system was possible and well spread, strongly adherent MSC could be cultured. Albeit no full confluence was reached, successful experiments concerning the interaction of other cells with the MSC could be undergone. By analysing the repeated interaction with KG-1a cells it could be demonstrated that the shear stress at which the KG-1a detachment and the MSC detachment occurred were sufficiently wide apart so that the MSC were not detached. Furthermore, this analysis showed that the shear stress required to detach the MSC did not change due such repeated interaction analysis. These findings demonstrated that the MSC cultured directly in the channel system presented a robust system for the analysis of the interaction of suspension cells with the MSC under flow conditions. Concerning the interaction of the KG-1a cells with the MSC it could be shown that dependent on the flow rate the cells accumulated on the MSC. The same behaviour was also observed for HPC from CB and mPB. For all three cell types tested accumulation commenced as soon as a flow was applied. The maximum fraction of interacting cells was observed in the range of approximately 1 dyn/cm². Beyond this shear the cells were detached from the surface by the flow. Pre-treatment of the cells with 9 µg/mL BU52 had no effect on the interaction of the cells with the MSC. This concentration of BU52 was sufficient to fully suppress the flow induced interaction with HA as shown in the sections 4.1 and 4.2. However, the number of receptor-ligand interactions was limited in that setup, as only immobilised HA was available for interaction. When investigating the interaction with MSC a vast variety of interactions were possible.[27] Amongst others possible receptors mediating interaction between the cells and MSC were integrins and cadherins. These typically mediate a firm adhesion and are the first obvious candidates for mediating the firm interaction observed in the experiments. It is possible that the catch-bond mediated capture of the cells directly resulted in a firm adhesion, possibly mediated by the above mentioned receptors. Future experiments should surely address the questions which receptors mediate this ‘sticking’ of the cells and whether the CD44 mediated flow induced rolling can be observed if the appropriate other receptors are blocked.

4.4 THE EFFECT OF SDF-1α AND PLERIXAFOR® ON CELL MOTILITY

The flow induced rolling of cells, which can be mediated by CD44, as described in the previous sections, or by selectins, as discussed in section 2.3, is an important step in the extravasation of cells from the blood stream. This in turn is a crucial step in the process of HSC homing to the BM niche.[99-101] That the CD44-HA interaction is in fact relevant in this context has been described in literature.[9] As both HA[237] and CD44[130-132] are ubiquitously expressed in the mammalian cells a regulation of this interaction is required. It was shown for example that proinflammatory stimuli could upregulate the expression of HA on endothelial cells to induce CD44 mediated binding.[287] In the context of HSC homing another regulation is possible. The homing process is directed by a gradient of the cytokine stem-cell-derived factor-1 alpha (SDF-1α).[9,16,69-70] Fuchs *et al.* recently described a molecular link between SDF-1α and CD44 via the SDF-1α receptor CXCR4,[288] raising the question whether SDF-1α could regulate the CD44 mediated flow induced interaction with HA. The investigation of the possibility of this form of regulation is presented in this section.

4.4.1 THE EFFECT OF SDF-1A ON THE MIGRATION OF HPC

It is well known that SDF-1α induces migration.[16-19,289] To determine whether, in the *in vitro* environment used in this work, the HPC reacted to SDF-1α as expected by migrating, transwell assays were applied. Plerixafor® (syn.: AMD3100; 1,1-[1,4-phenylene-bis(methylene)]-bis-1,4,8,11-tetra-azacyclo-tetradecane) was used as a control reagent. In the clinical environment this is used to mobilise HSC from the BM niche.[93-95] While the mechanism of action is not yet understood in detail,[96-97] it has been shown to block the CXCR4 receptor,[98] and, therefore, functions as SDF-1α antagonist.

For the analysis HPC derived from CB were seeded in the top compartment of a transwell setup and the migration through a membrane with a pore size of 3 µm was analysed by fixing the cells after 4 h and counting the number of cells that had migrated through the membrane into the lower compartment. First the effect of the isolated cytokine and of Plerixafor® was studied. As baseline-level, only HPC were added to the upper compartment and migration through the membrane into the lower compartment was measured (Figure 85 A). The migration rate was significantly increased upon addition of SDF-1α into the lower compartment ($p < 0.01$, 2-sided Student´s *t*-test). This migration inducing effect of SDF-1α could be abrogated almost fully by the addition of Plerixafor® ($p < 0.01$, 2-sided Student´s *t*-test). This clearly demonstrated that the HPC used in this work were susceptible to SDF-1α and that Plerixafor® could successfully be applied to suppress this effect.

As MSC secrete the chemokine SDF-1α and also express the corresponding receptor CXCR4 themselves[15] the migration towards these cells and, therefore, towards natural SDF-1α, was also analysed (Figure 85 B). For this MSC were seeded into the lower compartment of the transwell setup. Directly prior to the experiments the medium in which the MSC were cultured was removed and replaced by SDF-1α free medium. This ensured that the induction of migration was solely due to cytokines (presumably SDF-1α) secreted by the MSC. The bar graph in Figure 85 B shows a clear while not significant increase of the migration rate when comparing the CB HPC control to those migrating towards the MSC. The migration rate could be further increased by addition of synthetic SDF-1α to the lower compartment. Again this effect could be nearly fully antagonised by the addition of Plerixafor® to the upper compartment.

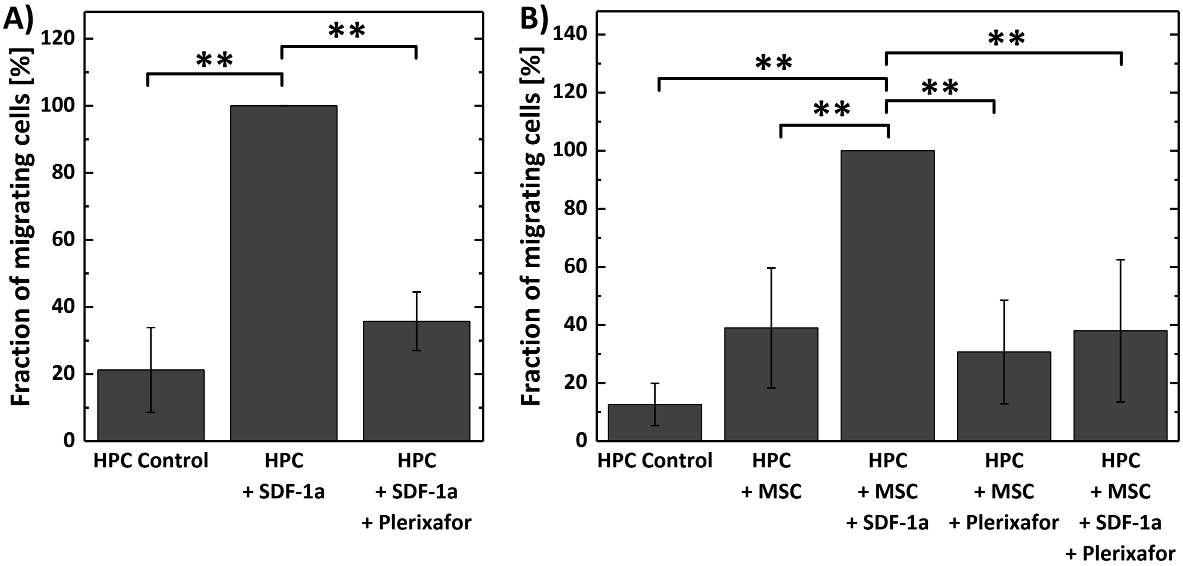

Figure 85: Transwell assay to determine the effect of SDF-1α and Plerixafor® on the migration of HPC. A) Effect of synthetic SDF-1α on the migration of CB HPC. The unspecific migration through the transwell membrane (HPC control) is compared to the addition of either 100 ng/mL SDF-1α alone or in combination with 500 ng/mL Plerixafor® to the lower compartment ($n = 6$).[289] B) Effect of presence of MSC on the migration of CB HPC. The lower compartment was seeded with MSC and the effect of 100 ng/mL SDF-1α and/or 500 ng/mL Plerixafor® was studied ($n = 4$). The error bars represent the SD.

4.4.2 THE EFFECT OF SDF-1A ON THE CD44-HA INTERACTION

After validation of the effectiveness of both SDF-1α and of Plerixafor® in an *in vitro* environment as used in this work, the influence of both on the interaction of cells under flow was analysed. As presented in section 4.2.1 the HPC were preincubated in Stemline II medium for 24 h prior to microfluidic measurement. Prior to measurement the cells were pre-incubated with SDF-1α or a combination of SDF-1α and Plerixafor® for (20-30) min to determine whether either of the two has an effect on the flow-induced rolling interaction with HA. HPC from CB and mPB were used for this analysis. As shown in Figure 86 the HPC from both sources exhibited the flow-induced rolling on HA previously discussed. Rolling was observed beyond a critical shear stress of approximately 0.2 dyn/cm² and reached the maximum at approximately (0.7-1) dyn/cm². Also as previously described the fraction of immobile adherent cells was low. Interestingly, for all treatments no change in the rolling interaction or the immobile adherence could be observed.

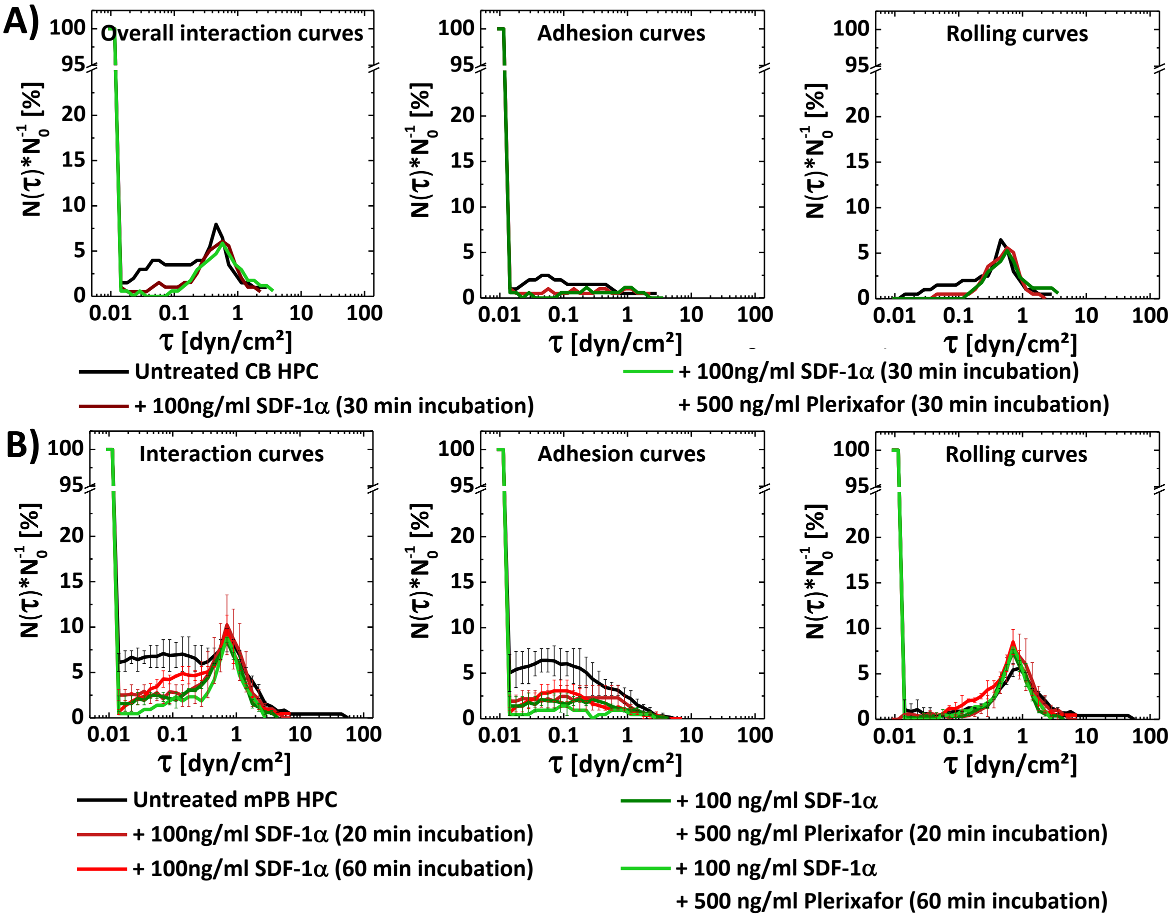

Figure 86: Effect of SDF-1α and Plerixafor® on the interaction of HPC with HA under flow. Interaction of HPC from CB (A; n = 1) and mPB (B; n = 2) with HA under flow. The cells were preincubated with SDF-1α or SDF-1α and Plerixafor® prior to measurement for varying lengths of time. The error bars represent the SD.

4.4.3 DISCUSSION

This chapter focussed on determining the relevance of SDF-1α as regulating agent for the CD44 mediated flow induced interaction with HA. To determine the viability of the *in vitro* environment in which the experiments were conducted, the effect of both SDF-1α and Plerixafor® on the HPC used in this work was evaluated using a transwell migration assay. It could be shown that in accordance to the findings of Kim and Broxmeyer SDF-1α was a very potent trigger for HPC migration.[18] This effect was best observed upon addition of synthetic SDF-1α. A certain increase, however, was also observed for HPC seeded in a transwell with MSC grown in the lower compartment as only source of natural SDF-1α. Of course, *in vivo* there may be other systems involved as well inducing chemotaxis as MSC produce more chemokines than merely SDF-1α.[27] Both with and without MSC it could be shown that addition of Plerixafor® reduced the interaction to the levels of the respective control group. This clearly showed that the HPC were susceptible to SDF-1α and Plerixafor® in the *in vitro* environment used in this work and that both reagents were highly effective.

Based on this validation of the effectiveness of SDF-1α and Plerixafor® the possible role of SDF-1α as regulatory agent for the CD44 mediated rolling interaction with HA was investigated. The CXCR4 antagonist Plerixafor® is a mobilisation reagent for HSC commonly used in the clinical environment.[93-95,98] Next to that of SDF-1α, the effect of this drug on the rolling on HA was also determined. The analysis was conducted with HPC originating from both CB and mPB. It could be shown that neither a pre-treatment with SDF-1α, Plerixafor® or a combination of both affected the interaction with a HA-coated surface under flow. This was the case both for the CD44 mediated flow induced rolling and for the immobile adhesion of the cells to HA. This new insight suggested that although some aspects of the function of the two receptors were linked[288] others, such as the CD44 mediated flow induced rolling on HA, were not. It should be noted that the absence of an effect of SDF-1α or Plerixafor® may be related to the pre-treatment of the cells in Stemline II medium (Table S5, Appendix section 7.2.1). Amongst others this medium contained the cytokine 'granulocyte colony-stimulating factor' (G-CSF), which is known for its stem cell mobilising abilities. In a clinical environment G-CSF is often used in combination with Plerixafor® as this is more effective than the standard procedure with G-CSF alone.[290-292] Possibly this cytokine negated the effect of SDF-1α or Plerixafor®. Another possibility is that the mechanistic determination between migration, where the molecular link between CD44 and CXCR4 was observed,[288] and the flow induced rolling is so sophisticated that the two forms of interaction are under certain circumstances strictly separated. Further experiments concerning this dependency would be desirable.

5 STABILITY AND BIOCOMPATIBILITY OF SURMOF 2 AS CANDIDATE FOR A DRUG RELEASE SYSTEM

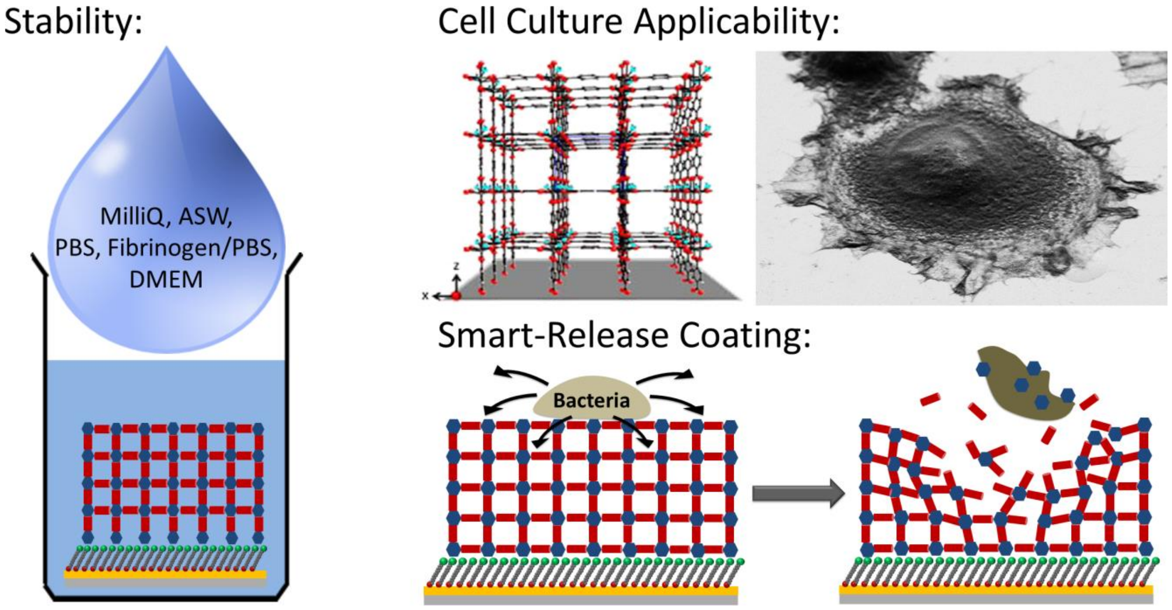

Figure 87: Overview over the work presented in this chapter. In the first section of this chapter the stability of Cu-/Zn-SURMOF 2 in different media is analysed. It was tested whether SURMOF 2 was generally applicable for cell culture and whether it could function as smart-release coating under the right conditions.

As elaborated in the introduction to this work (section 1) there are two major pathways in the improvement of the therapy of acute myeloid leukaemia (AML). The first is the selective mobilisation of leukaemic stem cells (LSC) out of their niche. As this requires a detailed understanding of the interactions between the LSC and their niche and the CD44-HA interaction was reported to be such an interaction,[6-7,9] this was characterised in this study. The second pathway is to improve the culture of haematopoietic stem cells (HSC) *in vitro* to make sufficient amounts of HSC for successful haematopoietic stem cell transplantation (HSCT) more easily accessible.[27-28] The HSCT are required to rescue the haematopoietic system after failure due to intensive chemotherapy.[24] Mimicking the *in vivo* conditions of a slow and continuous release of cytokines and growth factors to the HSC is a key step in doing so. Porous materials such as zeolites, porous metals or porous silicon are widely used in many applications involving the incorporation of small molecules, *e.g.* gas purification.[35-42,293-294] The pore size, the stability and of course the biocompatibility are three major aspects of a material that shall be used for drug delivery *in vivo*. A relatively new class of porous materials, the metal-organic frameworks (MOF), are due to their building blocks, chemically and structurally highly flexible.[43-45] The synthesis of such frameworks on surfaces (surface-anchored MOF; SURMOF) is straightforward[191,201,204] and allows the coating of devices, such as stents, or cell culture dishes. A novel 2-D structured SURMOF, namely SURMOF 2, was recently developed in the group of Prof. Christof Wöll at the Karlsruhe Institute of Technology (IFG, KIT, Karlsruhe, Germany).[209,295] Figure 87 gives an overview over the work conducted with this type of SURMOF. The stability of SURMOF 2 in different media, the compatibility of the same with cell culture and its potential as a drug release system were studied in corporation with the group of Prof. Christof Wöll.

5.1 STABILITY OF SURMOF 2

In this study a copper ($[Cu_2(bdc)_2]_n$; Cu-SURMOF 2; bdc = benzene-1,4-dicarboxylic acid) and a zinc ($[Zn_2(bdc)_2]_n$; Zn-SURMOF 2) based derivative of SURMOF 2 were studied. Both were assembled from solutions of the precursors of the divalent cations (Cu^{2+} and Zn^{2+}) and the linker molecule bdc. In contrast to most 3-D crystalline MOF structures this type of SURMOF exhibited a 2-D layer structure as shown in Figure 88.

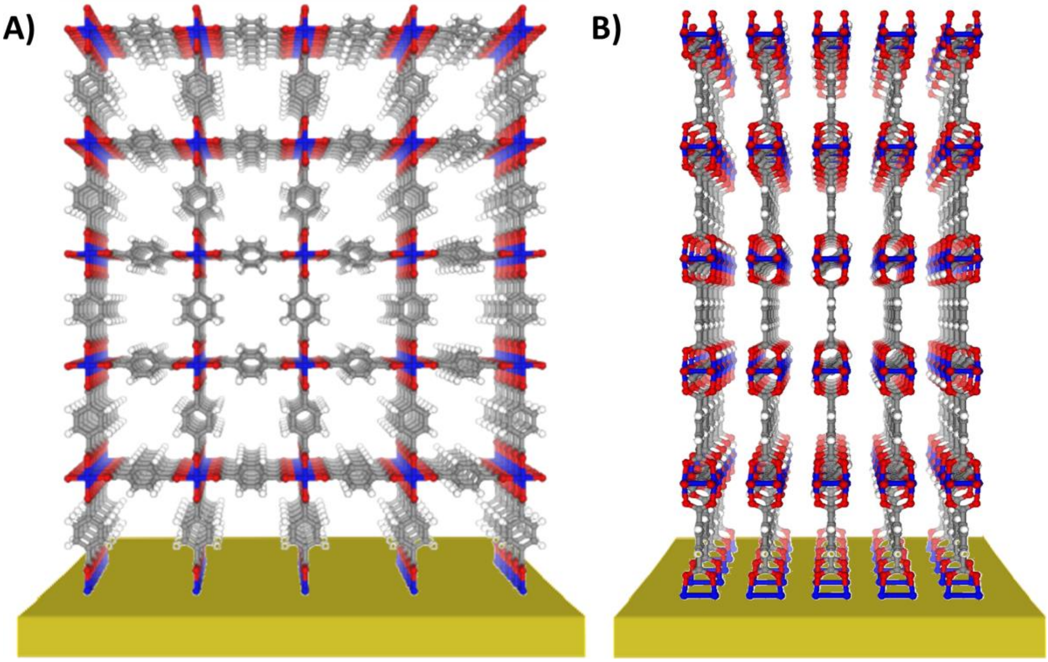

Figure 88: Schematic representation of the proposed structure of SURMOF 2. The structure of SURMOF 2 $[Zn_2(bdc)_2(H_2O)_2]$ and $[Cu_2(bdc)_2(H_2O)_2]$ is proposed to be 2-D; A) front view and B) side view. Image taken from Arslan *et al.*, 2011.[209]

In order to study the stability of Cu- and Zn-SURMOF 2 towards different media the respective SURMOF 2 was incubated in MilliQ® water, artificial sea water (ASW, type: Instant Ocean®), phosphate buffers saline (PBS buffer), 1 mg/mL fibrinogen in PBS and the cell culture medium Dubelcco´s modified eagle medium (DMEM, relevant media for a range of biological applications) supplemented with 10 % FBS and 5 % L-Glutamine for 1 h. After the incubation the SURMOF was carefully rinsed with MilliQ® water, dried in a nitrogen stream and analysed by XRD (by Hasan K. Arslan or Zhengbang Wang from the group of Prof. Christof Wöll, IFG, KIT, Karlsruhe, Germany), XPS (by Stella Bauer from our workgroup) and spectral ellipsometry.

Figure 89 A shows the XRD data obtained after the incubation of the Zn-SURMOF 2 in the above mentioned media. It is clearly visible that the crystallinity of the Zn-SURMOF 2 was lost after the incubation for 1 h in every of the tested media. The instability of the Zn-SURMOF 2 could be underlined by XPS measurements (Figure 89 B, C) which showed an increase of the Zn 3p peak together with a decrease of the C 1s peak for both the incubation with MilliQ® water and ASW. The increase of the Zn 3p peak can be explained by the exposure of zinc by removal of the outer bdc layers. This is in line with the decrease of the C 1s peak which can only originate from a loss of the bdc linker. Incubation in the remaining media also led to a disassembly of the SURMOF 2 (data not shown as no peaks were visible).

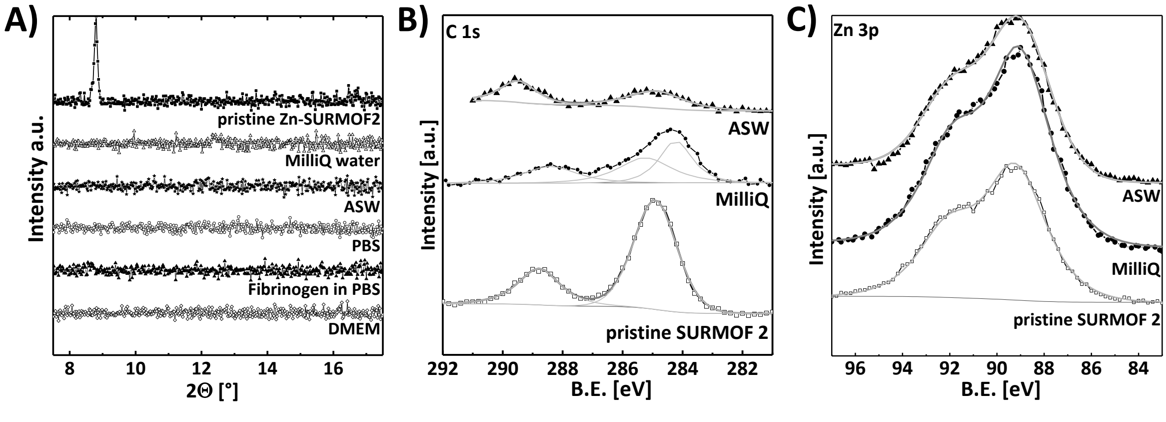

Figure 89: Spectroscopic analysis of the stability of Zn-SURMOF 2 in aqueous media. XRD spectra (A) of pristine Zn-SURMOF 2 and of the same after incubation in MilliQ® water, ASW, PBS buffer, PBS buffered fibrinogen solution and the cell culture medium DMEM (supplemented with 10 % FCS and 1 % L-Glutamine) for 1 h. All tested media led to a loss of crystallinity. The corresponding C 1s (B) and Zn 3p (C) XP spectra of the samples shown in A are also given. For clarity only the spectra for MilliQ® water and ASW are shown. Both the C 1s and Zn 3p spectra clearly show the disassembly of the Zn-SURMOF 2.

While the XRD data revealed the instability of Zn-SURMOF 2 in all media it also showed that immersion in MilliQ® water and ASW for times of up to 1 h had no detectable effect on the crystalline nature of the copper based SURMOF 2 (Cu-SURMOF 2). After incubation of the same with PBS buffer, PBS buffered fibrinogen solution and DMEM a loss of crystallinity was detectable (Figure 90 A), however.

XPS was used to gain a more detailed insight into the chemical composition of the surface after immersion of the Cu-SURMOF 2s into the different media (Figure 90 B-E). No change of the Cu 2p signal could be observed for the samples incubated in MilliQ® water and ASW, while the sample incubated in PBS showed a slight increase of the Cu 2p signal. For the samples containing proteins (PBS buffered fibrinogen solution and DMEM supplemented with 10 % FCS and 5 % L-Glutamine) a complete disappearance of the Cu 2p signal was observed. Evaluation of the C 1s XPS signals in Figure 91 C, D allowed similar conclusions. In the case of the incubation in MilliQ® water and ASW no change in the signal intensity or shape could be observed which was in good agreement with the unchanged crystallinity found by XRD. Incubation in PBS led to a strong decrease of the C 1s signal. This was in accordance with the loss of crystallinity indicated by the XRD data. After immersion of the Cu-SURMOF 2 films into buffered solutions of fibrinogen or cell culture medium DMEM (supplemented with 10 % FCS and 5 % L-Glutamine), a pronounced change of the C 1s peak shape was observed. This indicated changes in the chemical composition of the organic components after immersion into the protein containing media as expected due to the deposition of proteins on the surface. Since at the same time the Cu-SURMOF 2 diffraction peak intensities decreased it could be concluded that the protein deposition was accompanied by dissolution of the SURMOF 2 coating. The N 1s spectra recorded before and after immersion into the different aqueous solutions is shown in Figure 90 E. As it could be anticipated from the compositions of the different building units for the Cu-SURMOF 2, the pristine surfaces did not contain any nitrogen. After incubation in the protein rich (and thus nitrogen rich solutions) a distinct N 1s signal appeared. This underlined the conclusion from the C 1s spectra that macromolecules such as proteins adsorbed from solution.

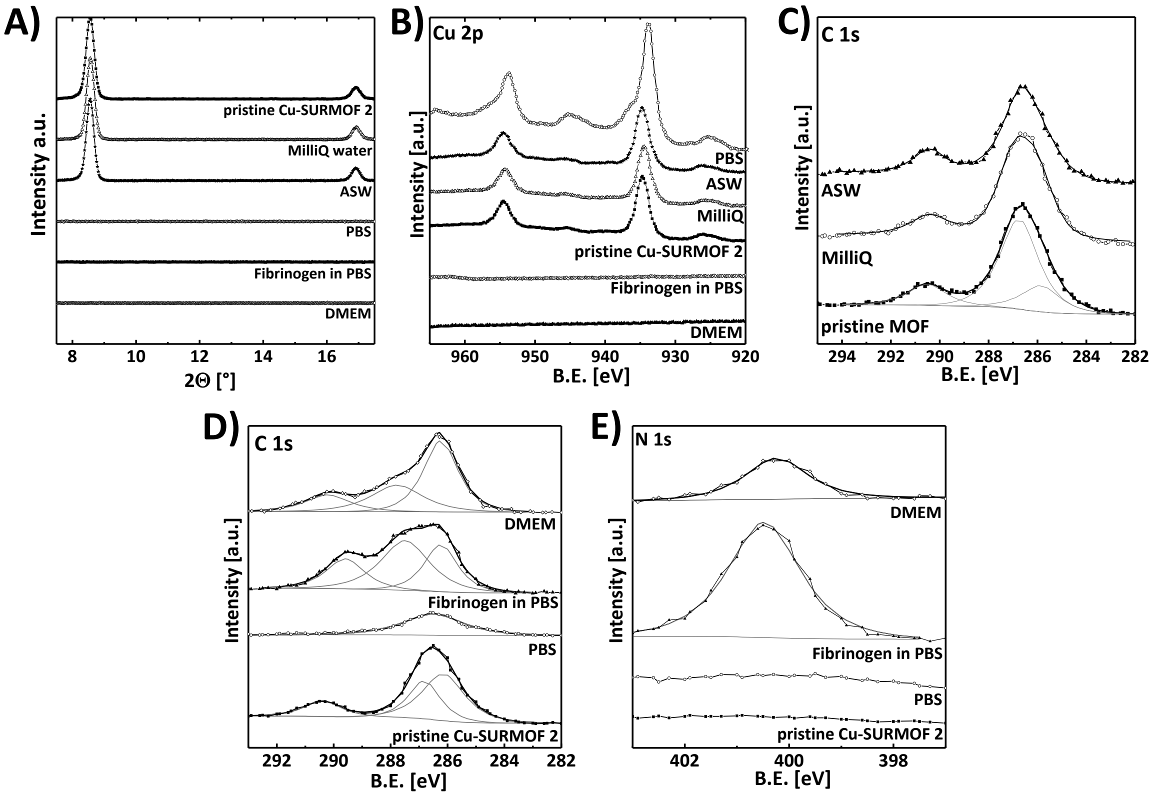

Figure 90: Spectroscopic analysis of the stability of Cu-SURMOF 2 in aqueous media. XRD spectra (A) of Cu-SURMOF 2 before and after incubation in MilliQ® water, ASW, PBS buffer, PBS buffered fibrinogen solution and the cell culture medium DMEM (supplemented with 10 % FCS and 1 % L-Glutamine) for 1 h. Crystallinity was retained during the incubation in MilliQ® water and ASW. The Cu 2p spectra (B) and the C 1s spectra (C, D) show nearly no changes in MilliQ® water and ASW, while obvious changes are visible in the other media. Nitrogenous species were deposited on the surface from the proteinacous media as seen in the N 1s spectra (E).[296]

Additionally, spectral ellipsometry was used to investigate the effect of the incubation in the different media on the film thickness. As shown in Figure 91 A Cu-SURMOF 2 was stable with regard to MilliQ® water and ASW for at least 1 h. This was in agreement with the XRD and XPS data. In case of the analysis of the film thickness after the PBS incubation problems fitting the ellipsometric data to the theoretical model were encountered. The mean square error (MSE) of the corresponding fit (numbers above the bar graph in Figure 91 A) was much larger for the PBS incubated surface (142) than for the other surfaces (less than 70). This finding could be explained by a very high roughness, for which the Cauchy layer model[214] was not adequate any more. A high degree of roughness was also consistent with the XRD data showing that the remaining overlayer was non-crystalline. As reference the film thickness of a HKUST-1 (Hong Kong University of Science & Technology-1) SURMOF after different times of incubation in MilliQ® water is shown in Figure 91 B. The rapid decrease of the film thickness stood in strong contrast to the high stability observed for Cu-SURMOF 2 after even 1 h. For incubation of the Cu-SURMOF 2 in fibrinogen solution and the protein rich medium DMEM an increase in thickness would have been expectable due to absorption of a protein overlayer. Table 8 shows the protein thicknesses typically obtained on the SAMs onto which the Cu-SURMOF 2 was deposited. Both, spectral ellipsometry and XPS show a similar increase in thickness by approximately 4 nm, which is in agreement with literature values for a single layer of proteins.[220,297] In contrast, incubation of the Cu-SURMOF 2 led to a rapid decrease of the thickness of the MOF overlayer (Figure 91 A).

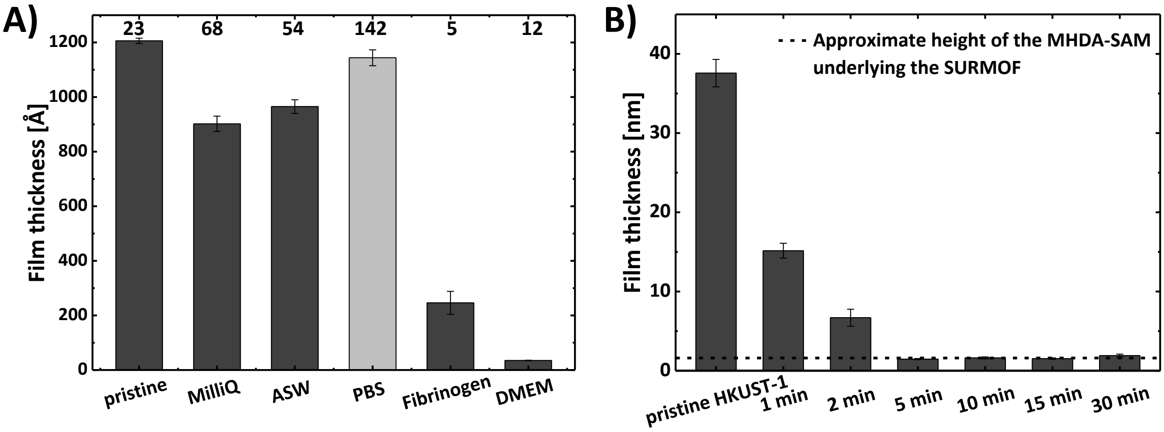

Figure 91: Ellipsometric measurements of SURMOF film thicknesses. A) Film thickness of the pristine Cu-SURMOF 2 before and after incubation in different media for 1 h. The size of the error bars corresponds to the average film thickness errors as provided by the WVASE32 program for each measurement. The MSE of each fit is shown above the graph. In case of PBS problems were encountered in the fitting process, see text. B) Time-dependent reduction of the HKUST-1 film thickness in MilliQ® water.[296]

Table 8: Comparison of the fibrinogen film thickness on SAMs measured by ellipsometry and by XPS. Errors are the SD.[296]

Surface Type	Film Thickness Ellipsometry [Å]	Film Thickness XPS [Å]
Fibrinogen on MHDA	42.9 ± 0.6	39.2
Fibrinogen on HDT	49.1 ± 1.7	45.6

Figure 92 shows the overview XPS data comparing the elemental composition of the pristine Cu-SURMOF 2 and the Cu-SURMOF 2 after PBS and ASW incubation. For the PBS incubation one can see that both the O 1s and O KVV peaks increased and that P 2s and P $2p_{3/2}$ peaks appeared. The increase of oxygen and phosphorous was connected to the decrease of the C 1s peak and the increase of the Cu $2p_{3/2}$ peak (Figure 90 B-D), which pointed towards a substitution of the organic linker molecules, most likely by phosphate. This change in chemistry resulted in a loss of crystallinity as seen in the XRD measurement (Figure 90 A). Thus, it could be deduced that the incubation of the Cu-SURMOF 2 in PBS led to a transformation of the crystalline metal-organic framework into an amorphous thin film comprised of Cu-SURMOF 2 components and phosphate from the buffer solution. In the case of incubation with ASW no new peaks were seen in the XPS data (Figure 92), revealing that none of the non-copper metal ions contained in the ASW were stored in the Cu-SURMOF 2 material (*e.g.* by ion incorporation or exchange).

In order to explore whether and where proteins adhered on patterned Cu-SURMOF 2 adlayers, patterned Cu-SURMOF 2 surfaces were exposed to green fluorescent protein (GFP)-labelled fibrinogen for 30 min and subsequently investigated by fluorescence microscopy. Although it was known from the spectroscopy data that the Cu-SURMOF 2 was completely removed during this experiment, it was still interesting to investigate if protein affinity varied spatially, *i.e.* whether the adhesion of proteins was affected initially when the Cu-SURMOF 2 was still present. The corresponding fluorescence micrographs are shown in Figure 93 A. The fluorescence on top of the patterned areas was higher than on the HDT SAM, a material which was known to be very proteophilic.[220] The intensity was roughly 4 times larger on the MHDA structures compared to the HDT SAM. Interestingly, the largest fluorescence was observed directly at the borders between HDT SAM and the Cu-SURMOF 2 squares.

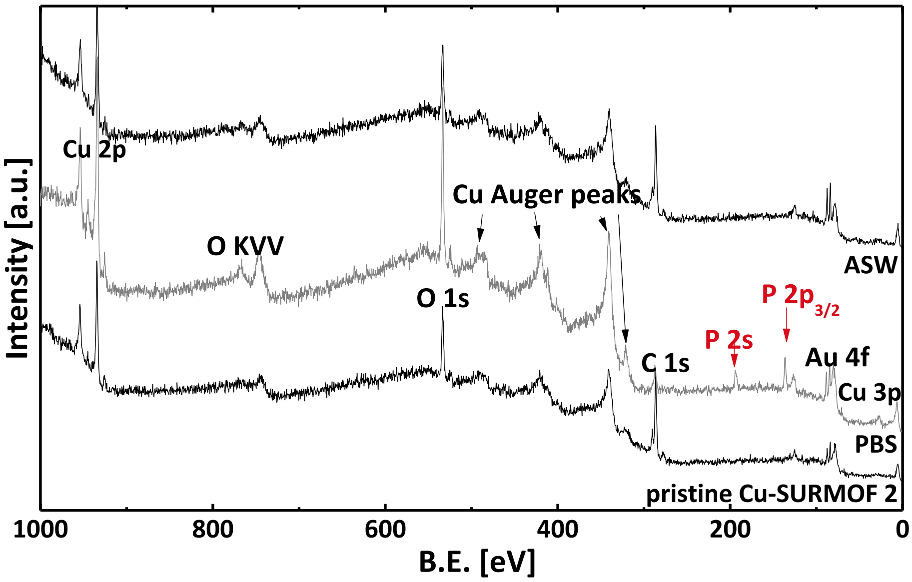

Figure 92: XPS spectra of pristine Cu-SURMOF 2 and of Cu-SURMOF 2 incubated in PBS and ASW for 1 h. The overview spectra shows phosphate peaks in the SURMOF.[296]

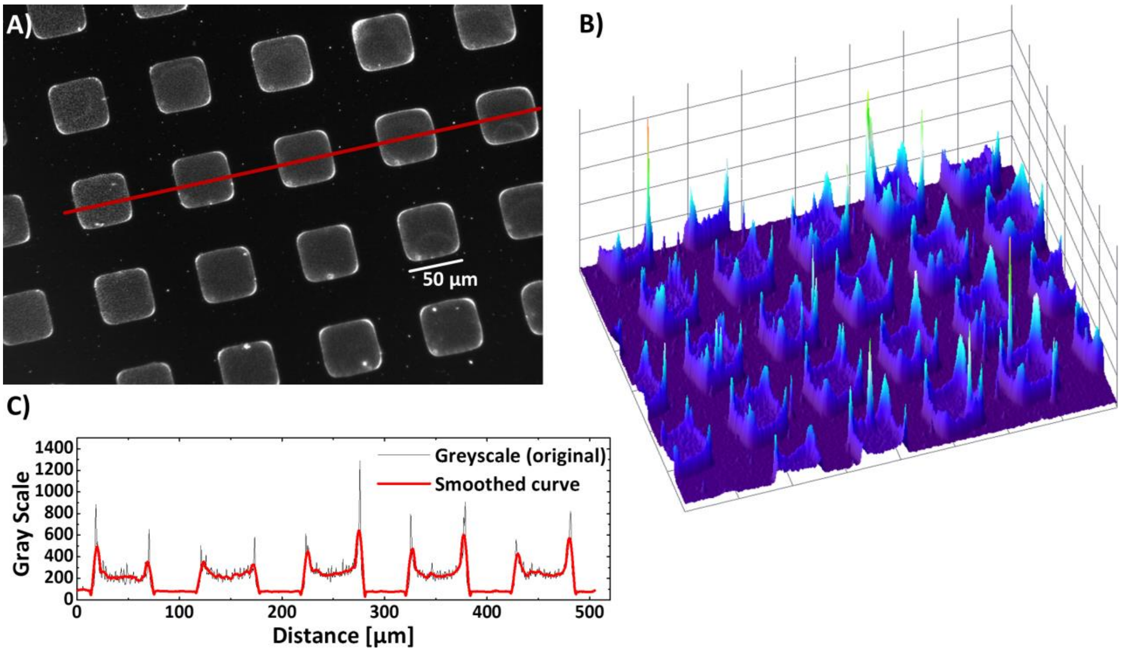

Figure 93: Adhesion of GFP-labelled fibrinogen to structured Cu-SURMOF 2 surfaces. The fluorescence image (A) of a structured Cu-SURMOF 2 substrate incubated for 30 min with GFP-labelled fibrinogen, the intensity profile (B) of the fluorescence signal detected and the greyscale (C) along the red line depicted in A show the preference of the protein to adhere to the borders of the MHDA squares.[296]

5.2 BIOCOMPATIBILITY AND CELL CULTURE APPLICATION

The fact that Cu-SURMOF 2 was stable in water at least for a limited duration made it interesting for the application in life and environmental sciences. The dissolution of the Cu-SURMOF 2 in cell culture media as described above might be the basis for using such coatings as slow release matrix for drugs or soluble control factors for cell differentiation and growth. In this section the general compliance of Cu-SURMOF 2 substrates with cell culture is investigated. For this wild type rat embryonic fibroblasts (REF52WT), a well characterised model cell line from the connective tissue frequently used for cell adhesion studies [298] and mechanistic studies on the formation of focal contacts and integrin clustering,[299] were used. For this prototype cell, time-lapse cell adhesion analysis and microfluidic detachment experiments were conducted *in vitro* on different substrates.

The optical micrograph images (Figure 94) obtained after 3 h of incubation show that the initial adhesion and spreading of REF52WT cells proceeded similarly on the homogeneous Cu-SURMOF 2 surfaces as it did on the MHDA SAM. This analysis was conducted in the cell culture medium DMEM in which REF52WT cells were typically cultured. As the stability studies presented in section 5.1 showed that the Cu-SURMOF 2 was dissolved upon immersion in DMEM, it could be concluded that the Cu^{2+}-ions liberated during this process into the solution did not harm the cells or delay their life cycle. Adhesion to both the patterned (Video S6, description found in the Appendix section 7.3.2, video provided on the supplementary CD) and the homogeneous Cu-SURMOF 2 took place immediately after the cells got in contact with the surface and spreading occurred on the same timescale as on the control substrate, the MHDA SAM. Proliferation of the cells took place after approximately 7 h on both surfaces, thus supporting the notion that the concentration of solvated Cu^{2+}-ions did not harm the cells (Figure 95). XRD data recorded after the coating with fibroblast cells (data not shown) showed no Cu-SURMOF 2 diffraction peaks, thus revealing that the dissolution of the SURMOF 2 into the cell culture medium was not substantially delayed by cell adhesion.

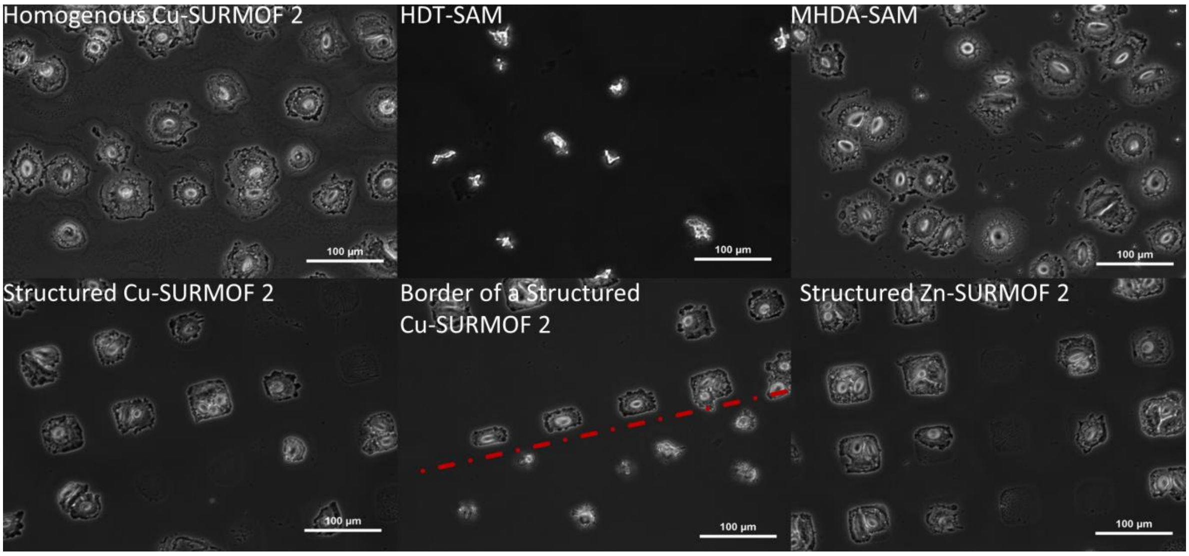

Figure 94: Microscopic images taken after incubating Cu-/Zn-SURMOF 2 with REF52WT for 3 h. The border of the structured SURMOF 2 area is indicated by the red dotted line.[296]

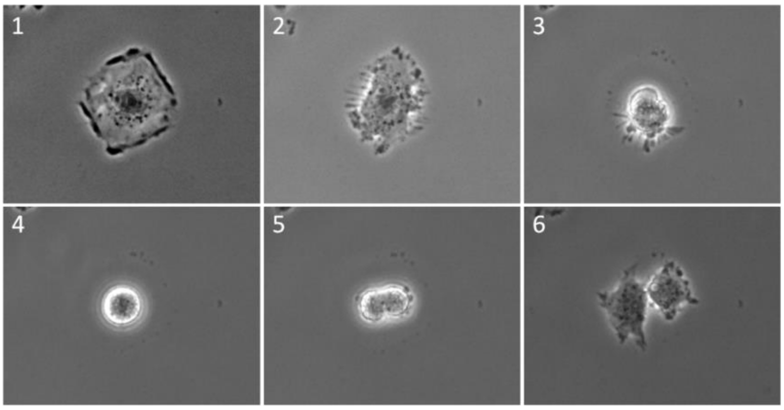

Figure 95: Microscopic images of a REF52WT cell proliferating on a homogeneous Cu-SURMOF 2 substrate. Six steps (1-6) in the proliferation process are shown. The images show the fully spread cell (1), which detached from the surface (2-4), divided into two daughter cells (5), which both adhered to the surface (6). Proliferation was observed after ~ 7 h. This time span corresponded well with that found on the SAM reference.

Besides cell adhesion dynamics and analysis of proliferation the critical shear stress required to detach 50 % of the REF52WT cells from Cu-SURMOF 2 was quantified. This aimed at providing further evidence for the normal adhesion behaviour of the cells and for the full integrity of the cell-surface contact. MHDA and HDT SAMs were measured as control surfaces. The REF52WT cells were incubated in the microfluidic channel system for 5 h according to a well-established protocol.[11] Figure 96 shows the adhesion curves in A) and τ_{50} values determined by microfluidic shear force measurement in B). The curves in Figure 96 A show the decrease in the fraction of adherent cells on a surface against the applied shear stress. It can be seen that the critical shear stress needed for removal of 50 % of the cells τ_{50} was nearly the same for the homogeneous Cu-SURMOF 2, the MHDA SAM and the structured Cu-SURMOF 2 (Figure 96 B). Only for the hydrophobic background, the HDT SAM, the adhesion strength was reduced. This was in agreement with the time-lapse microscopy images shown in Figure 94, in which the REF52WT cells hardly adhered to the HDT SAMs after 3 h, thus proving that the presence of the copper released from the dissolving Cu-SURMOF 2 did not affect the adhesion and allowed for a normal development of the fibroblasts.

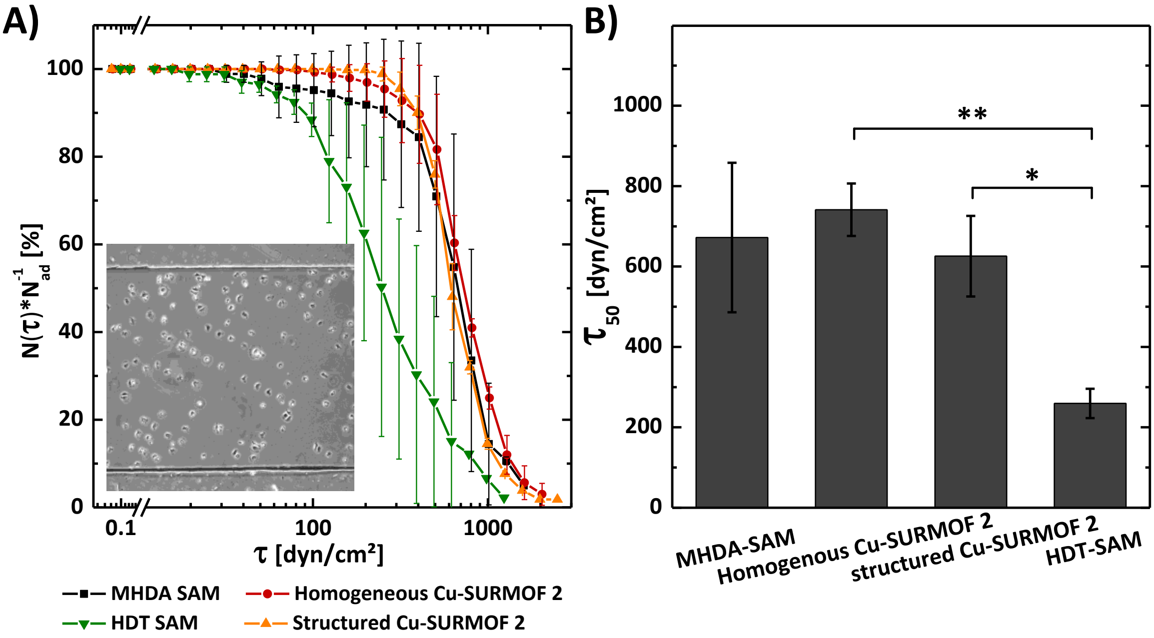

Figure 96: Microfluidic adhesion measurement of REF52WT cells on different sample surfaces. The measurements were conducted on the two reference SAMs, MHDA and HDT, as well as on homogeneous and structured Cu-SURMOF 2 samples. The mean detachment curves are shown in A, while B gives the corresponding mean τ_{50} values. The MHDA SAM and both Cu-SURMOF 2 samples yield the same mean τ_{50} values while adhesion to the HDT SAM is significantly weaker. Each measurement was repeated at least 3 times with > 60 cells/FOV. The error bars are the SD.[296]

5.3 APPLICATION AS SMART-RELEASE SURFACE

As the stability of Cu-SURMOF 2 in ASW for at least 1 h could be demonstrated in section 5.1 this medium offered the possibility to test the applicability of Cu-SURMOF 2 as smart-release surface. However, ASW was not adequate for cell culture. For this reason a substitutive organism, the marine bacterium *Cobetia marina* (*C. marina*), was chosen. *C. marina* is a model bacterium used in many adhesion studies due to its relevance in marine biofouling. [300-302] The studies with the bacterium were conducted in cooperation with Maria Pilar Arpa Sancet from our workgroup.

The stability of Cu-SURMOF 2 in ASW was again analysed by XPS and XRD. Figure S13 (Appendix section 7.3.2) shows virtually the same XP spectra of the Cu 2p (A) and the C 1s (B) peak for the pristine surfaces and after an incubation for 2 h in MilliQ® water. After an equally long incubation in ASW, minor peak changes became visible. The Cu 2p peak slightly increased, while the C 1s peak showed a marginal reduction. This indicated a disassembly of the top layers of the SURMOF structure resulting in better spectroscopic accessibility of the Cu^{2+} building units and a loss of some bdc linkers. The XRD measurements proved that all samples retained their crystallinity (Figure S13 C, D, Appendix section 7.3.2).

XPS analysis yields the elemental composition of the sample in dependency of the sample depth. Measurements of the SURMOF with bacteria present would have led to superimposed signals in which a differentiation between signals originating from the SURMOF and signals from the bacteria would have been near impossible. XRD in contrast only generates signals from regularly structured objects such as crystals. The overall amorphous structure of the bacteria did not contribute to the signal detected. Therefore, only XRD was applied for detecting changes in the SURMOF. It could be shown that incubation of Cu-SURMOF 2 with *C. marina* in ASW led to a significant reduction of the XRD signal intensity over the course of 2 h (Figure 97 A) hinting a disassembly of the Cu-SURMOF 2 initiated by the adhesion of the bacteria. On the basis of these observations the scenario depicted in Figure 97 B was proposed. After attaching to the SURMOF substrate (which was stable in ASW), the bacteria released biomolecules which diffused into the MOF and led to a structural rearrangement of the MOF material. This structural arrangement was likely to include an exchange of ions, which in turn led to a release of a small amount of Cu^{2+} ions that are toxic to microorganisms.[303]

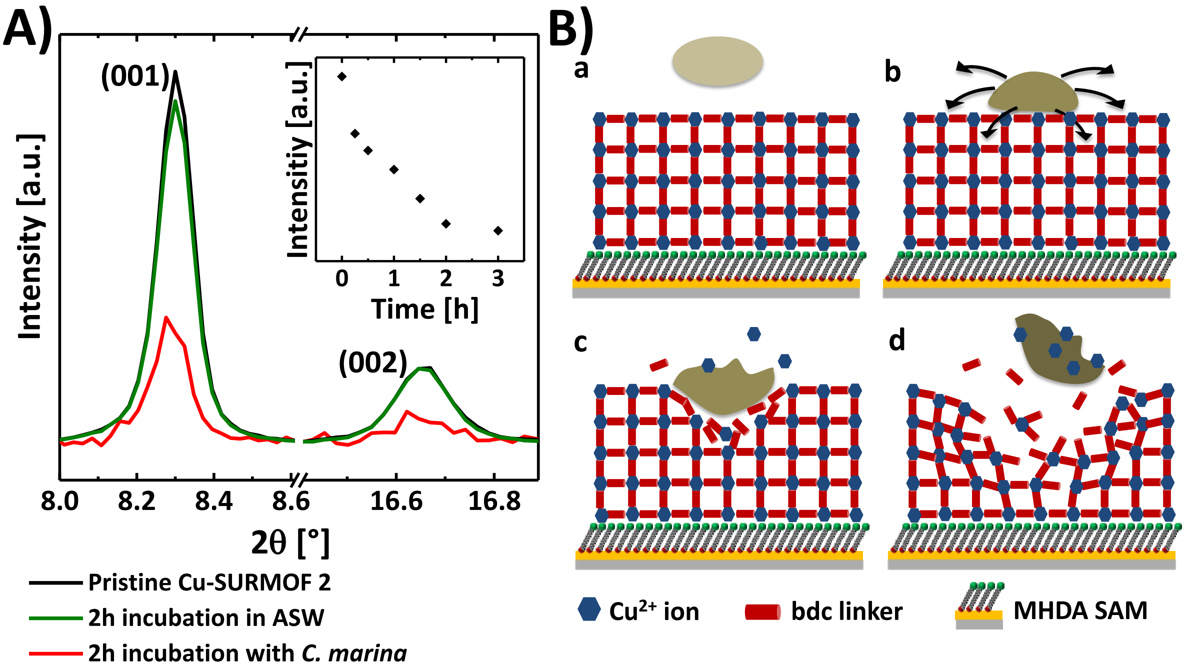

Figure 97: Stability analysis of Cu-SURMOF 2 in the presence of the marine bacterium *C. marina* and a proposed mechanism for the active degradation of the same by the bacterium. XRD spectra (A) of Cu-SURMOF 2 before and after incubation with ASW as reference and a suspension of the bacterium *C. marina* in ASW. The inlayed graph shows the decrease of the intensity of the (001) peak during the incubation with *C. marina*. A possible mechanism for this loss of crystallinity is shown in (B). (a) Healthy bacteria on initial contact with the SURMOF. (b) Bacteria settled on the intact SURMOF begin secretion of EPS and other molecules. (c) Disassembly of the SURMOF and release of Cu^{2+} ions. (d) Adverse effect on bacteria leading to reduced viability and adhesion strength.[304]

In the process of attaching to a surface the bacteria secrete extracellular polymeric substances (EPS) composed of macromolecules (mostly polysaccharides[305] such as alginic acid (AA)[306]). That such biomolecules can affect the metal-organic frameworks was demonstrated by incubation of test samples in a variety of solutions related to the bacterial physiology. These solutions were pure ASW as reference, a solution of 0.5 µg/mL AA in ASW, an EPS solution and the supernatant after the growth of bacteria in a glass vial for 2 h. Figure 98 A shows the XRD spectra obtained after the incubation of the Cu-SURMOF 2 substrates for 2 h in the test solutions. For both the AA solution and the EPS solution a dramatic decrease of the XRD peak intensities was observed. After immersion into the supernatant of a bacterial suspension, a complete loss of the crystalline order could be detected. Inductively coupled plasma optical emission spectrometry (ICP-OES) measurements of the test solutions after the incubation of Cu-SURMOF 2 samples in them, revealed significantly increased copper concentrations (Figure 98 B). The highest copper concentrations of approximately 2 mg/L were measured after 2 h exposure of the Cu-SURMOF 2 to the supernatant of a bacterial suspension and after incubation in suspensions of *C. marina*. These findings together with AFM measurements of the bacterial morphology (Figure S14 and Figure S15 in the Appendix section 7.3.3) and the Cu-SURMOF 2 height after incubation with the bacteria (Figure S16 in the Appendix section 7.3.3), SEM imaging of bacteria (Figure S17 in the Appendix section 7.3.3), viability assays (Figure S18 A in the Appendix section 7.3.3) and detachment experiments (Figure S18 B in the Appendix section 7.3.3) clearly underlined the hypothesis of the active degradation of the SURMOF by the bacteria.

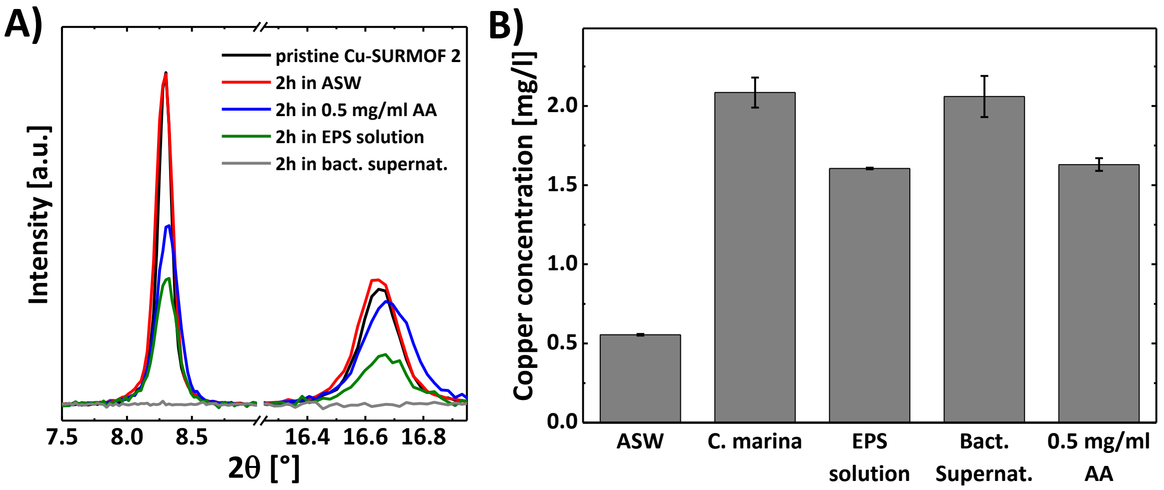

Figure 98: Stability analysis of Cu-SURMOF 2 in different media connected with the physiology of the bacteria *C. marina* and measurement of the corresponding copper release. A) XRD spectra of the SURMOF after the 2 h incubation. B) Copper concentration in the supernatant after the incubation as determined by ICP-OES.[304]

5.4 DISCUSSION

The development of viable methods for the *in vitro* culture of HSC to improve HSCT presents a second route to optimising the treatment of AML, next to selectively mobilising the LSC from their niche to make them more susceptible to chemotherapy. In the context of the latter approach the CD44-hyaluronic acid interaction was investigated and the results were presented in chapter 4. This chapter focussed on new matrix systems for the *in vitro* culture of HSC. One good approach when aiming at improving cell culture conditions, is to mimic the *in vivo* environment of the cells.[307-308] In the bone marrow niche, where the HSC dwell,[55-57] they undergo many different forms of interaction with their surroundings.[27] Some of these are the exhibition to soluble factors, such as cytokines or growth factors. In an *in vitro* approach such drugs should ideally be released continuously to the HSC as is the case *in vivo*. The material type predestined for use in such an application is a porous material. Of the various porous materials available the MOFs are by far the chemically and structurally most flexible. In this study the first fundamental investigations concerning the application of a novel 2-D surface-bound MOF, namely SURMOF 2, as drug release substrate in cell culture were undergone. Therefore, the stability of the structure and the biocompatibility of the building blocks were analysed. First tests as smart-release substrate were also undergone in a marine environment.

Stability analysis of Cu-SURMOF 2 demonstrated a pronounced stability with regard to the exposure to MilliQ® water. After immersion times of 2 h, the integrity of the Cu-SURMOF 2 was completely maintained, as evidenced by ellipsometry, XPS and XRD. This result was somewhat surprising, as HKUST-1,[309] a SURMOF which was also based on copper dinuclear carboxylate paddlewheel-units, and the structurally nearly identical Zn-SURMOF 2 were unstable even in MilliQ® water. Ellipsometric measurements showed that HKUST-1 was removed in less than 5 min. It could furthermore be demonstrated that while PBS buffer induced an amorphisation of the SURMOF, proteinacous media led to a complete disassembly of the same.

The stability of Cu-SURMOF 2 in water opened the possibility to test the suitability of these MOF thin films for environmental and life science applications. The Cu-SURMOF 2 substrates showed an overall compliance with eukaryotic cell culture (culture of REF52WT cells in DMEM), even though the dissolution of the Cu-SURMOF 2 substrates was accelerated in the cell culture media. No toxic or inhibitory effects on the proliferation or adhesion of fibroblast cells were observed on the Cu-SURMOF 2 coated substrates, despite the rapid release of Cu^{2+}-ions. Therefore, the experiments represented an extreme case in which cells were exposed to the maximum copper concentration possible in this setup. A smart-release system, similar to that aimed for in cell culture, could already be realised with the Cu-SURMOF 2 substrates and bacteria, which thrived in ASW. It could be demonstrated that Cu-SURMOF 2 was, next to MilliQ® water, also rather stable in this salt based medium for up to 2 h. Based on this stability it could be shown that incubation with the marine bacterium *Cobetia marina* led to a localised disassembly of the SURMOF. This disassembly, which presumably was induced by chemicals secreted by the bacteria, locally released the copper ions incorporated in the SURMOF matrix, which in turn led to most bacteria dying and detaching from the surface.

Overall the major requirements for the application of a structure as drug release surface are the possibility to incorporate the drug (pores of the appropriate size), a mode of slow and continuous drug release (diffusion, disassembly of the framework) and if used in contact with biological material the biocompatibility of the structure and its building blocks. Considering these prerequisites the findings presented in this section demonstrated the high potential of Cu-SURMOF 2 for the future application in this field. The release of the incorporated drug, cytokine or growth factor by a slow disassembly of the framework could be the means of choice. For this the foundations were laid by the pronounced stability in water. Slight structural modifications of the organic linker molecules should be sufficient to increase the stability so far that a slow release should be possible. The biocompatibility of the building units, most specifically the Cu^{2+} ions, was demonstrated by the unimpaired adhesion and proliferation of eukaryotic fibroblast cells to Cu-SURMOF 2 substrates. Finally, based on the stability of Cu-SURMOF 2 in marine conditions, experiments with marine bacteria could demonstrate the principal applicability of Cu-SURMOF 2 substrates as smart-release matrix. The mechanism of localised disassembly induced by the bacteria may possibly be transferred to cell culture, where the presence of the cells could trigger the release of the drug, cytokine or growth factor. The refinement of the framework structure and the application as drug release structure are currently successfully being pursued by the workgroup around Prof. Christof Wöll at the Karlsruhe Institute of Technology (IFG, KIT, Karlsruhe, Germany).[310]

6 SUMMARY AND OUTLOOK

Acute myeloid leukaemia (AML) is the most common form of acute leukaemia in adults. Although most patients reach complete remission after initial chemotherapy the overall survival rate is as low as 30-40 % over 4 years. This is ascribed to leukaemic stem cells (LSC) which survive the chemotherapy in the bone marrow (BM) niche and later cause the relapse.[2-3] Therefore, two aspects of the treatment need to be improved. The first is the efficiency of the apoptosis induction in LSC by chemotherapeutic agents whilst ideally sparing the haematopoietic stem cells (HSC). The second is the efficiency of the haematopoietic stem cell transplantation, as this currently presents the only method of rescuing the haematopoietic system after failure due to intensive, potentially LSC-eradicating chemotherapy. An overview over the analysis conducted in this work is shown in Figure 99.

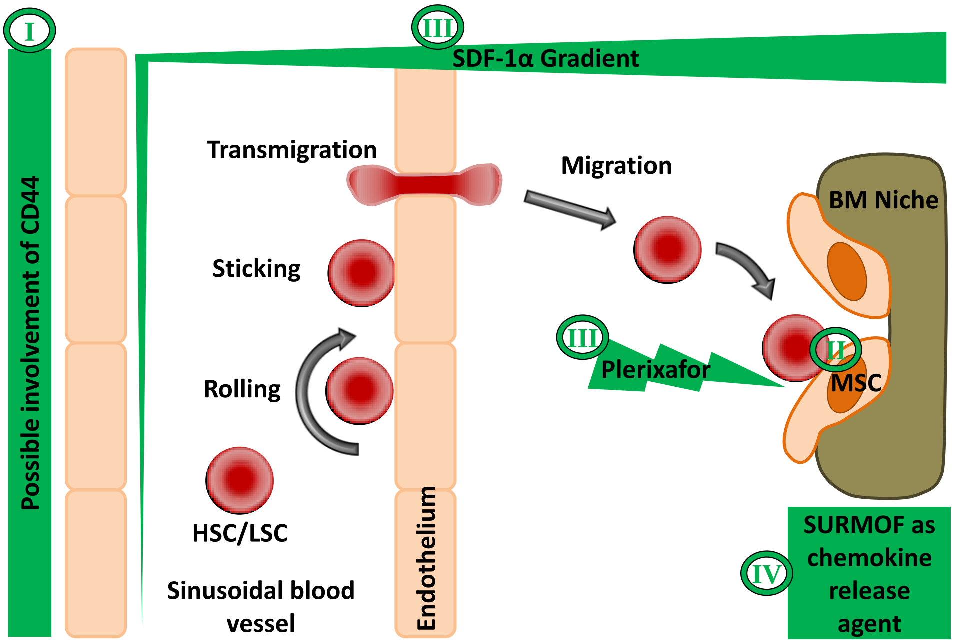

Figure 99: Overview over the aspects of the HSC/LSC-niche interaction studied in this work. The interaction of the cell surface receptor CD44 with HA under flow (I; section 4.1 and 4.2), the interaction of $CD44^+$ cells with MSC under flow (II; section 4.3), the effect of the cytokine SDF-1α and the mobilisation reagent Plerixafor® (III; section 4.4) and the first analysis of the possibility to utilise a novel 2-D surface bound metal-organic framework structure as release matrix for future applications in cell culture (IV; section 5) were studied. Image inspired by Barrett *et al.*, 2008.[68]

The cell surface receptor CD44 has been reported to be involved in the retention of LSC in their niche[6-7] and in the homing and engraftment of healthy HPC to the bone marrow (BM) niche.[9] The exact step, though, where this involvement occurs is still unclear, as indicated in Figure 99 (I). It has been hypothesised that CD44, similar to selectins,[63-67] is involved in the primary adhesion of leukocytes under flow during extravasation.[119] As the receptor is the same there is no apparent reason why this role should not be upheld in HSC or leukaemic cells. In fact C. Christophis *et al.* identified a flow induced interaction of CD44 positive leukaemic cells and haematopoietic progenitor cells (HPC) isolated from umbilical cord blood (CB) with hyaluronic acid (HA). The first step of this study was to fully characterise the interaction of this receptor with its major ligand HA. To do so a microfluidic shear force device, established in our group,[10,12] was utilised. With this the flow conditions found *in vivo* were mimicked and the interaction of two cell lines, namely the leukaemic suspension cell line (KG-1a) and the epithelial liver cancer cell line (HepG2Iso), was characterised and compared. It could be demonstrated that the flow-induced rolling interaction observed on HA was specific for HA, could only be observed if CD44 was expressed by the cells and that it was dependent on the HA binding domain of CD44. This analysis matrix clearly proved that the flow-induced rolling interaction was mediated by the cell surface receptor CD44. Interestingly, the CD44 mediated rolling interaction observed on HA was independent of the cell type. For the leukaemic suspension cell line and the epithelial liver cancer cell line, but also for healthy HPC and to a certain extent leukaemic blasts, the characteristics of the flow-induced interaction were nearly identical. In all cases rolling was induced beyond a critical shear stress of approximately 0.2 dyn/cm², reaching the maximum fraction of rolling cells at roughly (0.7-1) dyn/cm². Beyond this region of shear stress the cells continuously detached from the surface. This was in good correlation with previous findings of C. Christophis *et al.* who first observed this flow induced rolling for KG-1a cells and HPC isolated from CB.[10] Analysis of the dependency on different CD44variant isoforms revealed that the rolling interaction could not be abrogated by suppression of either CD44v3 or CD44v6. The flow-induced rolling interaction could, however, be suppressed by CD44pan knock down or by treatment either with the monoclonal CD44 antibody (clone BU52) or with short chain length HA. In the context of the treatment of HepG2Iso cells with the two latter mentioned blocking agents a concentration dependency was observed. This demonstrated a clear correlation between on the one hand the probability of the cells to bind to the HA-coated surface from flow and the rolling velocity and on the other hand the density of the receptor available for binding. In contrast to this stood the independence of the strength of the CD44-HA binding which was similar throughout all experiments. This could be demonstrated by the independency of the shear stress at which the maximum interaction was observed from the treatment with different concentrations of the blocking reagents.

As hinted above the rolling interaction was independent of the cell type studied and, therefore, could not be identified as a possible therapeutic target distinguishing between the leukaemic and the healthy cells. It was, however, not the only interaction observed with the HA-coated surfaces. All cell types expressed a, in most cases low, tendency to immobily adhere to the HA-coated surfaces. This tendency was less pronounced for the model cell lines and the HPC isolated from CB or mobilised peripheral blood (mPB) for which typically a fraction of less than 5 % of immobile adherent cells was observed. For HPC isolated from the BM and leukaemic blasts values up to 20 % were not uncommon. Even more striking was the effectiveness of the treatment with the CD44 antibody BU52. While the rolling interaction of all cell types studied in this work could be suppressed with sufficient amounts of BU52, the immobile adhesion could not. In some samples of leukaemic blasts (each being isolated from a different patient) treatment with the antibody had no or only a marginal effect on the fraction of immobile adherent cells. Interestingly, a comparison between blast samples from a single patient originating either from the BM or the peripheral blood (PB) revealed that the suppression of the immobile adhesion was more effective in the samples originating from the PB. This indicated that the resistance towards the antibody may have been correlated to a vicinity to the BM niche prior to isolation of the cells. Furthermore, a comparison between patient data for the blast samples in which the antibody was effective with those where it was not, uncovered a link between the BU52 resistance and a poor long-term therapeutic outcome of the respective patients.

All cells, except for the HSC, the BM niche is comprised of can be derived from mesenchymal stromal cells (MSC).[13-14] For this reason and due to the fact that they play a significant role for maintaining the self-renewal potential of HSC and HPC, MSC are often used as model system for the BM niche.[57,71,73-75] In this work the analysis of the interaction of CD44 positive cells with HA-coated surfaces was expanded towards MSC feeder layers (Figure 99 (II)). Feeder layers were defined as surfaces completely covered with convergent MSC. For this a procedure where the MSC were seeded into and cultured in a fully assembled microfluidic channel was developed. Here, the morphology of the cells was correlated to the shear stress required to detach the cells and supposedly ideal culture conditions were identified. Preliminary experiments concerning the interaction of both the cell line KG-1a and HPC (from CB and mPB) were conducted. Rolling was hardly observable on the MSC. In contrast to this a high fraction of cells immobily attached to the MSC during the experiments. Furthermore, the interaction with MSC could not be suppressed by BU52 demonstrating that the overall interaction pattern was more complex in this system than the simple CD44-HA interaction observed on the HA-coated surfaces. For a more detailed understanding an antibody matrix suppressing a variety of receptors, *e.g.* integrins, selectins or cadherins would need to be applied, thus determining the receptors involved and the form of interaction they mediate with MSC.

Both CD44[130-132] and its ligand HA[237] are ubiquitously expressed in the mammalian cells. Therefore, regulation of the interaction between them is of great importance. One mode of regulation is controlling the expression of HA on endothelial cells. It was shown that proinflammatory stimuli could upregulate HA expression, thereby, inducing CD44 mediated interaction with the endothelial cells.[287] HSC homing, where the CD44-HA interaction is thought to be relevant (Figure 99 (III),[9] is directed by a gradient of the cytokine stem-cell-derived factor-1 alpha (SDF-1α).[9,16,69-70] It is, therefore, possible that this cytokine may also be involved in the regulation of the CD44 activity. This notion was further supported by the identification of a molecular link between SDF-1α and CD44 via the SDF-1α receptor CXCR4.[288] As control reagent the CXCR4 antagonist[98] Plerixafor®, which is clinically used for the mobilisation of HSC out of the BM niche,[93-95] was used. As SDF-1α is known to induce migration,[16-19,289] the effect of both SDF-1α and Plerixafor® on the migration of HPC was evaluated in a transwell assay to determine the effectiveness of the reagents in the *in vitro* environment of the assays applied in this work. It could be shown that SDF-1α strongly induced migration and that the effect could successfully be suppressed by Plerixafor®, demonstrating the validity of the system. The effect of the two reagents on the interaction of HPC with HA under flow was evaluated by pre-treating HPC isolated from CB and mPB and subsequently evaluating the interaction in the microfluidic shear force device. It could be shown that neither SDF-1α nor Plerixafor® influenced the interaction with HA under flow in the system used in this work. These findings demonstrated a clear mechanistic separation of the migration form the interaction under flow, despite the molecular link[288] between the involved receptors.

In the context of the evaluation of the interaction of HPC and leukaemic blasts with HA the identification of the immobile adhesion to HA, mainly exhibited by the leukaemic blasts, could be an important step towards the selective mobilisation of LSC. The fact that this immobile adhesion to HA was not only correlated to a vicinity to the niche, but also to an adverse therapeutic outcome suggested that it may have been involved in the retention of LSC in the BM niche. Under this hypothesis the questions why this interaction was stronger in leukaemic cells than in HPC and why it was found primarily in cells originating from the BM niche should urgently be addressed. Revealing the exact mechanism of this interaction and searching for drugs to selectively target this mechanism of LSC retention in the niche could lead to means of selectively mobilising LSC rendering them more susceptible to chemotherapy. This would make the use of lower dosages of chemotherapeutic drugs possible, thus reducing the need for stem cell transplantation after chemotherapy. Also the interaction with MSC should not be omitted as this cell type is found abundantly in the niche.[75] It is possible that while the role of the CD44 mediated interaction could not be demonstrated in this work, it may become apparent when other interactions such as those mediated by integrins or cadherins are preempted.

Next to analysing the interaction of HSC/LSC with their microenvironment in order to selectively target the LSC with mobilisation or chemotherapeutic reagents, a second approach is to find ways of improving the culture of HSC *in vitro*. A basis for this is finding suitable substrates that can be used to slowly and continuously release cytokines and growth factors into solution to mimic the *in vivo* environment. Today porous materials such as zeolites, porous metals or porous silicon are widely used in catalysis, in sensors or in filtering processes, *e.g.* gas or water purification.[35-42] An example is the application of porous stents loaded with drugs for the localised application of the same.[311] In the context of drug storage and delivery, however, the pore size (determining the size of the drug embedded in the structure), the stability of the material under the conditions of later use (*e.g. in vivo* use as a stent) and of course the biocompatibility of the material are of great importance. Here, a relatively new class of materials shines. The metal-organic frameworks (MOFs) are highly flexible in their structural and chemical properties due to framework being grown from a combination of metal precursors and organic linker molecules.[43-45] Furthermore, the growth of MOFs on functionalised surfaces, creating so-called SURMOFs (surface-anchored MOFs), is easily possible.[191,201,204] This enables the coating of devices, such as stents, or cell culture dishes. A novel 2-D structured SURMOF, namely SURMOF 2, which was recently developed in the group of Prof. Christof Wöll at the Karlsruhe Institute of Technology (IFG, KIT, Karlsruhe, Germany)[209,295] presented a good basis for such work. In this work first tests concerning the stability of the basic SURMOF 2 ($[M_2(bdc)_2]_n$; M = Cu, Zn) in different media and the biocompatibility of the building blocks were undergone (Figure 99 (IV)). Analysis by XPS, XRD and spectral ellipsometry could show that Zn-SURMOF 2 was instable in all media tested and that while Cu-SURMOF 2 was stable in MilliQ® water and ASW it was rapidly disassembled in proteinacous solutions such as cell culture medium. Still, the effect of the building units of Cu-SURMOF 2 (Cu^{2+} ions and the bdc linker) on the adhesion and growth of fibroblasts (REF52WT) was analysed. Measurement of the shear stress required to detach the fibroblasts from a matrix of test surfaces as well as time-lapse observations of the proliferation rate and cell morphology revealed no impairment of proliferation or adhesion. Due to the demonstrated stability in ASW and the instability in cell culture conditions smart-release tests were conducted in a marine environment. Here, it could be demonstrated that incubation with the marine bacterium *Cobetia marina* led to a locally induced disassembly of the SURMOF. The copper ions released thereby were toxic for the bacteria resulting in bacterial death after adhesion. The biocompatibility and the ability to tune the system as smart-release matrix, indicate the principal applicability of

Cu-SURMOF 2 as drug delivering substrate in future cell culture applications. The further development of the stability of SURMOFs is thereby of great interest. Under the premise that the disassembly can be slowed down sufficiently and that the pores can be designed such that loading with *e.g.* cytokines or growth factors is possible, continuous release of these reagents to the cells should be achievable.

Concluding, this work presents new insights in the interaction between CD44 and its major ligand hyaluronic acid and elaborates the importance of differences in this interaction for the treatment of acute myeloid leukaemia. Additionally, the principal applicability of a novel 2-D framework structure as drug release system was demonstrated.

7 APPENDIX

7.1 SUPPORTING INFORMATION CONCERNING THE MICROFLUIDIC SHEAR FORCE MEASUREMENT

This section gives further insight into the theory underlying the microfluidic shear force setup and presents alternative modes of measurement not presented in the main chapters, but relevant for the supplementary material. Finally, data supporting the observations and conclusions made in section 3.8.6 is presented.

7.1.1 CALCULATION OF THE VARIABLES RELEVANT FOR THE MICROFLUIDIC SHEAR FORCE SYSTEM

7.1.1.1 PRESSURE DROP IN THE MICROFLUIDIC CHANNEL SYSTEM

With liquid flowing through a pipe as in any other system the laws of conservation of energy are upheld. This section elaborates the origin of the pressure loss between two points of a channel through which liquid flows. Finally, the implications for the microfluidic shear force measurements are also discussed.

Equation (S1) shows the comparison of the liquid energy at two points (indexed as '1' and '2'). For a steady average velocity flow of incompressible fluids the total energy can be summarised as elevation energy, velocity energy and pressure energy.[312] The energy equation can then be expressed as

$$p_1 + \alpha_1 \frac{1}{2} \rho \bar{v}_1^2 + \rho g h_1 = p_2 + \alpha_2 \frac{1}{2} \rho \bar{v}_2^2 + \rho g h_2 + p_{loss} \tag{S1}$$

Here, p_i is the pressure of the fluid at the different points i = 1 and i = 2, p_{loss} is the pressure loss between the two points, ρ is the density of the fluid, $\bar{v}_n$ is the average flow velocity, g is the acceleration of gravity and h is the elevation. α_n is the kinetic energy parameter, which corrects for the use of an average velocity in case the velocity profile is not uniform. Under the assumption of a uniform fully developed flow throughout the tubing, both α_n are the same and neglectable. Taking this into account the kinetic energy terms of the fluid flow

$$\alpha_n \frac{1}{2} \rho \bar{v}_n^2 \tag{S2}$$

as well as the potential energy terms

$$\rho g h_n \tag{S3}$$

are easily calculable, given that the variables such as $\bar{v}_n$, ρ or the elevation h are known. The remaining term describing the pressure loss p_{loss} between the two points can be divided into two terms. The first is the ‘major loss’ term, which for a fully developed, steady state and incompressible flow can be described by Equation (S4), which is also known as the Darcy-Weisbach equation. The no-slip clause between a viscous fluid and a solid, states that the flow velocity of the fluid is zero relative to the boundary of the solid. Therefore, the wall shear stress results in an energy loss of the fluid making the surface roughness and flow profile (given by the Reynold´s number which is described in section 7.1.1.2) highly important factors for the amount of energy lost due to friction. The ‘minor losses’ described by Equation (S5) arise from changes in velocity due to bends, fittings, valves, elevation *etc*.

$$\Delta p_{major} = f_D \frac{l}{2d} \rho \bar{v}_n^2 \tag{S4}$$

$$\Delta p_{minor} = \sum K_L \frac{1}{2} \rho \bar{v}_n^2 \tag{S5}$$

With f_D being the Darcy friction factor, d the diameter of the pipe, and K_L the loss coefficient. The Darcy friction factor f_D can be graphically derived from the Moody diagram or may be calculated using *e.g.* the Colebrook equation[313] or the Haaland equation.[314] For laminar flow f_D can be calculated from the Reynold´s number Re according to Equation (S6).[177,312]

$$f_D = \frac{64}{Re} \tag{S6}$$

It should be noted that all formulas calculating the friction factor are approximations based on extensive experimental data. Similarly, the dimensionless loss coefficient K_L is well documented for various pipe geometries and can be looked up in the appropriate tables.

In the microfluidic shear force setup used in this work the pressure loss was a variable that needed to be considered. The pressure loss was mainly due to the energy loss mainly originating from frictional forces and velocity changes, both of which are velocity dependent. Therefore, increasing the flow velocity led to an increased pressure loss over the system. Reduction of the overall pressure in the system led to the formation of gas bubbles in the system. This had could have various reasons. If the overall pressure in the system was reduced below the vapour pressure of the fluid (water based in all applications used in this work), this would have resulted in the formation of bubbles of aqueous vapour. It is also possible that the low pressure in the system led to the leakage of air into the system through *e.g.* fittings and valves or to the release of gas from the liquid. This would have made the calculation of the shear stress at the channel bottom impossible as the exact liquid flow would no longer have been known. To avoid this, an overpressure of approximately 0.6 bar was applied to the system in all measurements.

7.1.1.2 DERIVATION OF THE REYNOLDS NUMBER IN THE MICROFLUIDIC CHANNEL SYSTEM

The Reynold´s number Re is a dimensionless number that helps characterise different flow profiles. Calculation of the Reynold´s number can be used to predict whether a flow will be laminar or turbulent. Typically flow with a Reynold´s number below 2300 is defined as laminar.[177] For the calculations of the wall shear stress inside the microfluidic channels system the establishment of a laminar flow is mandatory as only then a defined velocity gradient along the y-axis (orthogonal to the channel bottom/top) can be anticipated. This will be further discussed in section 7.1.1.3.

For circular pipes the Reynold´s number Re[177,312] is given as

$$Re = \frac{dv\rho}{\mu} \tag{S7}$$

With the viscosity μ and the density ρ of the liquid, die diameter d and the flow speed v. For non-circular channels the diameter is substituted by the hydraulic radius r_h

$$r_h = \frac{A}{C} = \frac{cross\ sectional\ area\ of\ the\ pipe}{circumference\ of\ the\ pipe} \tag{S8}$$

In order to substitute d in Equation (S7) one must calculate r_h for a circular tube:

$$r_h = \frac{A(of\ a\ round\ pipe)}{C(of\ a\ round\ pipe)} = \frac{\pi d^2/4}{\pi d} = \frac{d}{4} \rightarrow d = 4r_h \tag{S9}$$

Insertion of this into Equation (S7) results in

$$Re = \frac{4r_h v\rho}{\mu} \tag{S10}$$

r_h can now be calculated for a rectangular cross sectional area of the width w and the height h as

$$r_h = \frac{wh}{2(w+h)} \tag{S11}$$

Knowing that $v = Q/wh$ the Reynold´s number may be calculated by

$$Re = \frac{4\frac{wh}{2(w+h)}\frac{Q}{wh}\rho}{\mu} = \frac{2Q\rho}{\mu(w+h)} \tag{S12}$$

Under the premise that the width w of the channel by far exceeds the height h (with $h \approx 135$ µm and $w \approx 1500$ µm this is the case in the microfluidic channel system), Equation (S12) can be simplified to

$$Re \approx \frac{2Q\rho}{\mu w} \tag{S13}$$

For the most extreme conditions applied in the microfluidic shear force setup throughout this work (Q = 81 mL/min maximum applicable flow, $\eta = 0.72 \times 10^{-3}$ kg m^{-1}s^{-1} cell culture medium at 37 °C[187], ρ = 1kg/L, h = 135 µm) the Reynold’s number calculates to ~ 1670 (or to ~ 830 if it is considered that $Q \approx 40$ mL/min is the maximum practically applicable flow rate). This is well below the threshold Reynold´s number of 2300 for laminar flow.[177]

7.1.1.3 DERIVATION OF THE WALL SHEAR STRESS IN THE MICROFLUIDIC CHANNEL SYSTEM

The calculation of the wall shear stress τ_w was a central aspect of the work with the microfluidic shear force setup as it gave a value to easily compare between experiments. τ_w does, in contrast to *e.g.* the flow rate, take variables such as the channel dimensions into account and, thereby, provided a mean of comparison independent of the variables specific for each assembly.

Shah and London presented both the exact solution, involving Fourier series expansions, as well as a simple approximation of the velocity profile originally proposed by Purday.[186] Because this approximation is in excellent agreement with classical experimental results, and is much easier to compute, it was used to estimate the maximum velocity at the midplane of the microchannels, and the shear stress on the microchannel surface.

The Purday approximation for rectangular channels (shown in Figure 32 in section 3.8.3 is repeated here for convenience), as used in the microfluidic shear force setup, gives the axial velocity as shown in Equation (S14).[186]

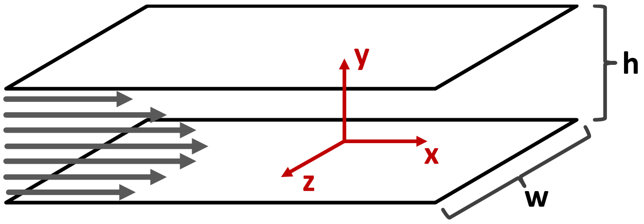

Figure 32: Parallel plate model for unidirectional flow. A parabolic flow profile between two immobile parallel plates is shown. The height is so much smaller than the width of the channel that the shear at the channel sides can be neglected.

$$u(y,z) = u_m \left(\frac{m+1}{m}\right)\left(\frac{n+1}{n}\right)\left[1-\left(\frac{2y}{h}\right)^n\right]\left[1-\left(\frac{2z}{w}\right)^m\right] \tag{S14}$$

and

$$\frac{u_{max}}{u_m} = \left(\frac{m+1}{m}\right)\left(\frac{n+1}{n}\right) \tag{S15}$$

u, u_m, u_{max} are the axial, mean and maximum velocities, respectively and m, n are empirical parameters dependent on the aspect ratio $\alpha = h/w$ (height/width). For an aspect ratio α smaller than 1/3, $m = 1.7 + 0.5 \cdot \alpha^{-1.4}$ and $n = 2$. In the channel system used in this work $\alpha \approx 1/10$. For all Newtonian fluids in laminar flow the shear stress τ is proportional to the strain rate in the fluid with the viscosity μ being the constant of proportionality. This correlation is shown in Equation (S16).[177] The laminarity of the flow in the microfluidic shear force setup was described both in section 3.8.3 and in more detail in the previous section.

$$\tau(y) = \mu \frac{\partial u}{\partial y} \tag{S16}$$

The wall shear stress τ_w is defines as

$$\tau_w = \tau(y=0) = \mu \left.\frac{\partial u}{\partial y}\right|_{y=0} \tag{S17}$$

Differentiation of $u(y,z)$ (Equation (S14)) with respect to y, as part of Equation (S17), yields

$$u = u_m \left(\frac{m+1}{m}\right)\left(\frac{n+1}{n}\right)\left(\frac{2n}{h}\right)\left[1-\left(\frac{2z}{w}\right)^m\right] \tag{S18}$$

With $u_m = Q/wh$ with Q being the flow rate, and calculating at the centre of the channel width ($z = 0$)

$$\tau_w = \frac{2\mu Q}{wh^2}\left(\frac{m+1}{m}\right)(n+1) \tag{S19}$$

Bearing in mind that n = 2 in the setup used in this work this can further be simplified to

$$\tau_w = \frac{6\mu Q}{wh^2}\left(\frac{m+1}{m}\right) \tag{S20}$$

Note that Equation (S20) has the familiar form of the parallel plate approximation

$$\tau_w = \frac{6\mu Q}{wh^2} \tag{6}$$

with the addition of the $(m+1)/m$ term to account for side wall effects. This term is neglectable in cases were the width is much larger than the height of the channel system, as is the case in the microfluidic channel system applied in this work. This demonstrates that the parallel plate approximation of Equation (6) could be applied in this work.

It should be mentioned that by insertion of Equation (S13) into Equation (6) the shear stress may also be estimated from the Reynold´s number as

$$\tau \approx \frac{Re}{h^2} \tag{S21}$$

As elaborated in section 3.8.3 the wall shear stress was increased stepwise during the commonly applied detachment assay. In principal the wall shear stress applied in each step could be calculated from the initially applied shear stress τ_i, the growth coefficient GC, by which the shear stress was increased in each step, and by the step number x.

$$\tau_x = \tau_i * GC^x \tag{17}$$

In this context Equation (6) was used to calculate the dimension dependent initial shear stress τ_i of each experiment.

$$\tau_x = \frac{6\mu Q}{wh^2} * GC^x = \tau_i * GC^x \tag{S22}$$

As different step durations were used in this work and in related studies using the same microfluidic setup with different channel dimensions[268-269] a substitution of GC by a factor, independent of the step duration, was desirable. This was achieved by introducing the growth rate of the shear stress R_τ allowing a more straightforward description of experiments with different step durations, but the same overall increase of the shear stress. To do so the exponent x was substituted by the duration t_n for which the experiment had been conducted (≙ how many steps had been taken). As the shear stress was increased stepwise it must be mentioned that t_n was a multiple of the duration of a step Δt.

$$t_n = n * \Delta t \tag{S23}$$

With this Equation (S22) could be rewritten as the universal equation for the calculation of the wall shear stress (Equation (18)) in each step as follows

$$\tau_{t_n} = \tau_i * GC^{\frac{\mathrm{n}*\Delta t}{\Delta t}} = \tau_i * \left(GC^{\frac{1}{\Delta t}}\right)^{\mathrm{n}*\Delta t} = \tau_i * (R_\tau)^{\mathrm{t}_n} \tag{18}$$

An example for the practicality of R_τ can be given when comparing the two forms of the detachment assay, that were both used in this work. The first was a stepwise increase by approximately 26 % (GC = 1.2589) every 5 s. The second was a stepwise increase by 2.33 % (GC = 1.0233) every 0.5 s. From these values it is not apparent that the overall increase was the same. For both cases R_τ = 1.047. This common value nicely illustrates the common slope of both shear stress curves.

7.1.2 MICROFLUIDIC DATA ACQUISITION AND ANALYSIS

7.1.2.1 DATA ACQUISITION IN CELL-SURFACE INTERACTION EXPERIMENTS

The main focus of the microfluidic cell-surface interaction experiments was the flow induced rolling interaction of CD44 positive cells with hyaluronic acid (HA). Video S1 shows an exemplary HepG2Iso cell (a CD44 positive model cell line) rolling on a HA-coated substrate with a shear stress of approximately 1 dyn/cm² applied. The full video can be found on the CD provided with the printed edition of this thesis. Next to this rolling interaction an immobile adherent interaction of some cell types was also observed in the cell-surface interaction experiments. These two behaviours of the cells are shown in Video S2. Here, the interaction of KG-1a cells, another CD44 positive model cell line used in this work, with HA again with approximately 1 dyn/cm² applied is shown. The immobile adherent cells are marked in green, while rolling cells are labelled in red. The full video can be found on the CD provided with the printed edition of this thesis.

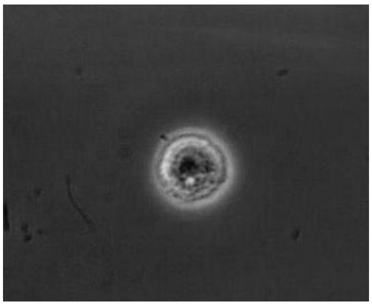

Video S1: HepG2Iso cell rolling on a HA surface.

As discussed in section 3.8.5 the number of cells in contact with the sample surface at a given time was normalised either to the number of cells initially visible in the field of view (FOV) N_0 or by the mean maximum number of interacting cells. The procedure chosen depended on the type of cells analysed. All cell types (the model cell lines KG-1a, Jurkat and Kasumi-1, the HPC from cord blood, mobilised peripheral blood and the bone marrow as well as the leukaemic blasts) except for the HepG2Iso and HepG2 cells were normalised all normalised by N_0. Video S3 shows the correlation between the cells counted in the FOV in the microfluidic channel and the interaction curve generated after normalisation. This is shown for the first analysis method (correction to N_0) as this was the standard procedure in this work. This video is presented to help the reader visualise the procedure of analysing the videos recorded during measurement. The number of cells interacting with the sample surface was counted by hand in a 5 s interval. This number was then corrected appropriately and plotted as shown in the graph on the right in Video S3. For labelling the cells in the FOV a differentiation is made between rolling (marked in red) and immobile adherent cells (marked in green). The evaluation is, however, only shown for the overall interaction of the cells with the surface (the sum of all cells interacting with the surface at a given time is plotted) as this should only give an example. The full video can be found on the CD provided with the printed edition of this thesis.

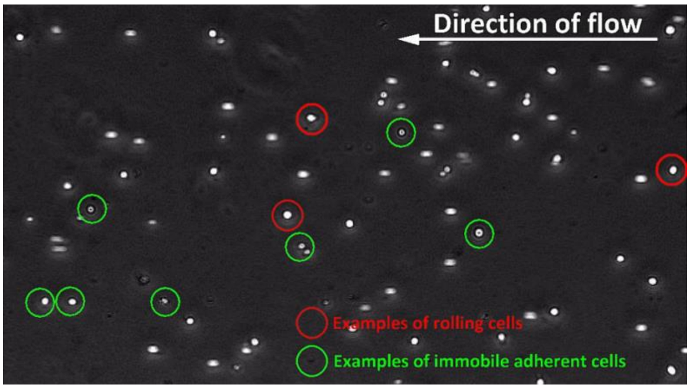

Video S2: Video demonstrating the difference between rolling and immobile adherent cells. Rolling cells are marked in green. The immobile adherent cells are marked in red.[266]

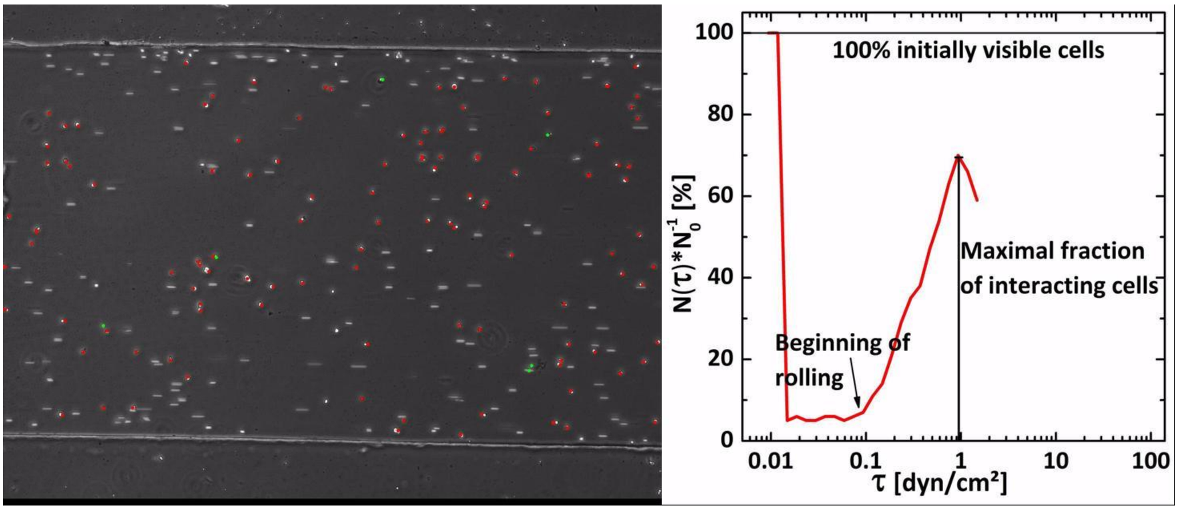

Video S3: Video demonstrating the creation of a detachment curve by counting the cells interacting with a surface at a given time. The rolling cells (marked in red) and the immobile adherent cells (marked in green) are summed and divided by the number of cells initially visible in the FOV. Plotting this against the shear stress applied at the time of counting yields the detachment curve shown on the right.[266]

7.1.2.2 ACCUMULATION ASSAY

The accumulation assay was a second method next to the detachment assay to compare the effects of different treatments on the interaction of cells with surfaces under shear flow. For this assay the cells were not injected into the channel system directly but were rather flushed through the channel during the entire assay. The channel was initially flooded with the cell suspension (typically $1 \cdot 10^6$ cells/mL). A strong flow pulse of approximately 1,200 dyn/cm² was then applied. This not only ensured a sufficient amount of cells in the channel but also detached all cells interacting with the surface after injection. The flow was then reduced to approximately 7.8 µL/min (≈ 0.2 dyn/cm²) and kept constant. This flow rate was sufficient to trigger the flow induced interaction of the cells with the surface, while remaining slow enough to allow the initial contact with the surface from flow. Analysis of this form of experiment was straightforward as the number of cells interacting with the surface at a given time simply was counted and plotted against the time.

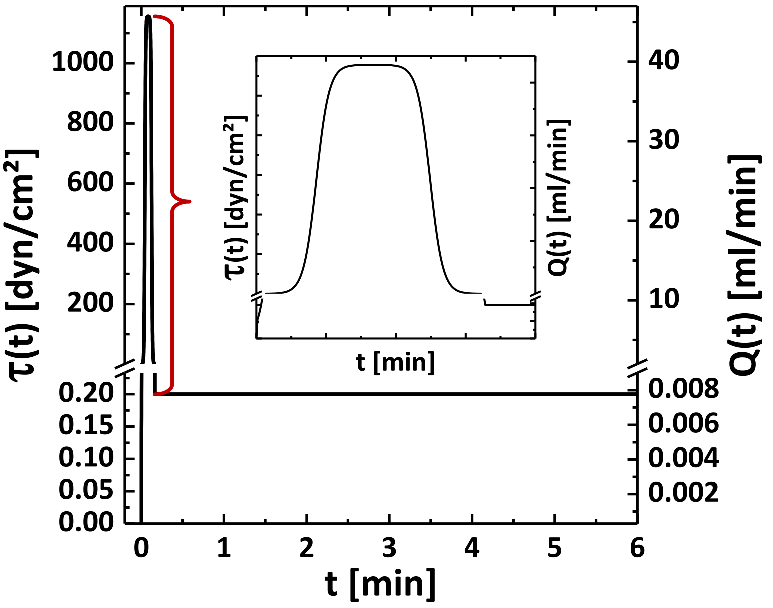

Figure S1: Flow profile of an accumulation assay. A first high pulse detached all cells from the surface. The flow was then reduced and kept constant at approximately 7.8 mL/min.

7.1.2.3 EVALUATION OF DATA WITH HISTOGRAMS AND BOX PLOTS

Histograms and box plots present the most straightforward method of graphically depicting distributions of large numbers of data points, while giving clear information about the distribution of the data and allowing an easy determination of trends. The histogram (Figure S2) gives a nice visualisation of the distribution of the data points. Here, a bar is plotted for each interval. An interval is a region of data points.[315] It the specific case of the rolling velocities measured in this work it may for example be the range of

(5-10) µm/s. From the histogram the range of the most frequent value (*e.g.* rolling velocity) is easily deducible.

Figure S2 presents a typical box plot. As shown in the figure the box plot in this example is comprised of three values (five are also typical). Mostly these represent the 1st (lower box margin), 2nd (middle line) and 3rd (upper box margin) quartile of the data.[315] The 1st quartile is also known as the 25th or the 25 % percentile. Equally, the 2nd quartile is the 50th or the 50 % percentile and the 3rd quartile is the 75th or 75 % percentile. These are all specific forms of quantiles, commonly used in descriptive statistics. Quantiles are defined as values, which divide the distribution of a random variable into data subsets of equal size. Accordingly, a percentile represents a per cent of the data points and a quartile represents a quarter of the data points. Therefore, the 1st quartile is defined as the value below which 25 % of the values can be found. The 2nd quartile (50 % percentile) is more commonly known as the median of the values. As the median value is defined as the value which halves the data set, it is clear that this value corresponds to the 2nd quartile (50th percentile, 50 % percentile). The mean value $\bar{x}$ is the average value of all values and is given by ◇ in the box plot. It can be calculated by

$$\bar{x} = \frac{\sum x_i f_i}{n} \tag{S24}$$

Where x_i is each value of the data set, f_i is the frequency of x_i and n is the sample size.[315] The whiskers represent the standard deviation SD of the data, which is calculated as follows

$$SD = \sqrt{\frac{\sum (x_i - \bar{x}) f_i}{n - 1}} \tag{S25}$$

Where x_i is each value of the data set, $\bar{x}$ is the mean value, f_i is the frequency of x_i and n is the sample size.[315]

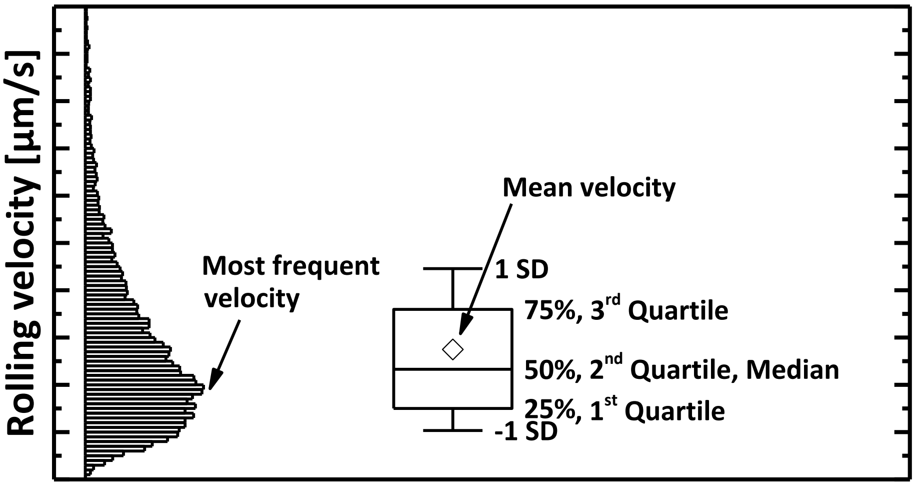

Figure S2: Exemplary analysis of rolling velocity data with a histogram and a box plot. The histogram best shows the most frequent velocity. The boxplots gives statistical values such as the mean velocity, the median velocity or the 1st and 3rd quartile.

7.1.3 OPTIMISATION AND PROOF OF APPLICABILITY OF THE MICROFLUIDIC SHEAR FORCE DEVICE

Section 3.8.6 focussed on understanding the origin of the inaccuracy, concerning the measurement of the critical shear stress τ_{50} required to detach 50 % of the objects of interest from a sample surface, recently observed by M.P. Arpa Sancet and M. Alles in our workgroup. This section provides data either undergirding the findings presented in that section or giving the full data set given there in short.

7.1.3.1 INFLUENCE OF THE CHANNEL DIMENSIONS

As M. Alles demonstrated an improvement of the intra-channel reproducibility by application of a 130 µm thick aluminium spacer in the 13 mm channels used by her, this was also investigated in this work. By analysing the detachment of carboxy-terminated polystyrene microspheres (diameter d ≈ 4.5 µm, hereafter referred to as particles) from HUDT SAMs, an independence of the initial channel dimensions (before an experiment was conducted) of the application of a spacer was demonstrated in section 3.8.6.1. It was, furthermore, shown that in an experimental series conducted in one channel (without reassembly between the measurements) a change of the τ_{50} value was independent of the channel dimensions in the relaxed state (no experiment run, but with the overpressure applied). In the experimental series presented in section 3.8.6.1 the τ_{50} values decreased before reaching a plateau. Figure S3 presents the reverse trend. The τ_{50} values increased over the first three measurements and then reached a plateau. This was in no correlation to the channel dimensions in the relaxed state of the system, which remained the same throughout the experimental series.

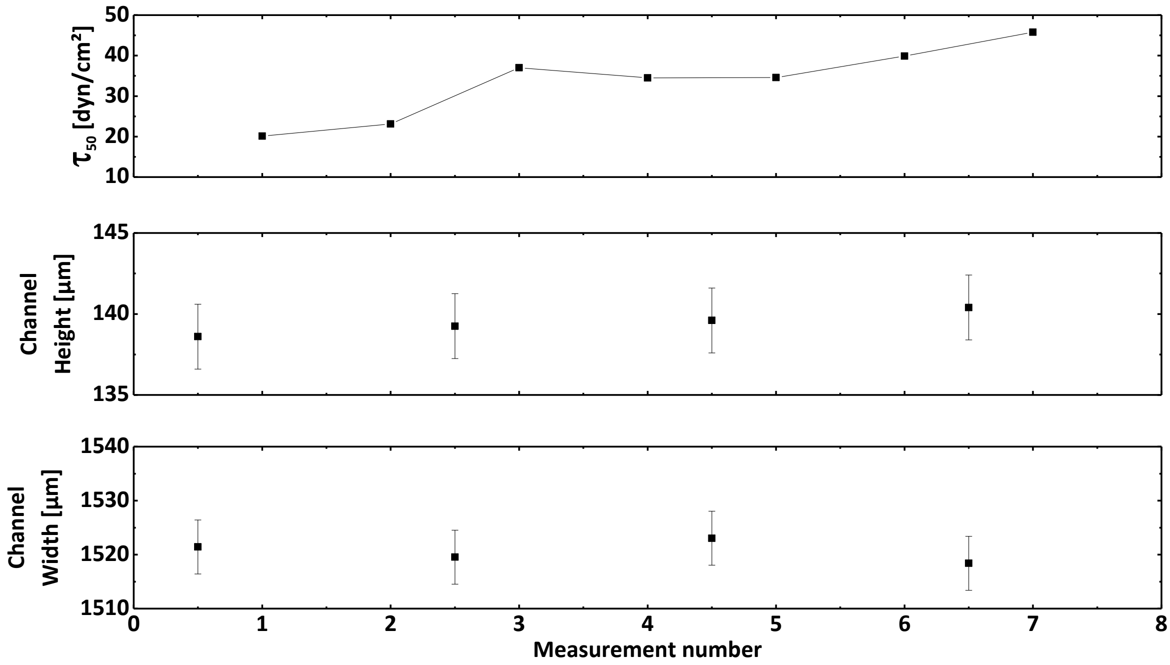

Figure S3: τ_{50} values measured in succession in one single channel without application of a spacer. The τ_{50} value increased over the first three measurements before reaching a plateau. The channel dimensions were measured between the experimental runs, thereby only representing the dimensions if no flow was applied. The errors given for the channel dimensions are estimated measuring errors.

7.1.3.2 EFFECT OF THE APPLICATION OF SPACERS ON THE REPRODUCIBILITY OF THE MEASUREMENT

The influence of the application of a spacer on the inter-channel reproducibility was presented in section 3.8.6.2. Table S1 gives an overview over all mean τ_{50} values and the corresponding errors determined in the cause of the investigation. The number of repeats conducted in each experimental run ranged from at least 5 to up to 16 repeats. The data was homogenised by only considering the first five repeats. From the data it can be seen that the mean percentage error and the SD of the same were reduced by application of a spacer. Without spacer the mean percentage error was 18.1 ± 12.0 %. This was reduced to 10.9± 3.9 % by use of a spacer, meaning that the use of a spacer increased the reproducibility in each series of measurements.

Table S1: Overview over the τ_{50} values measured in one channel either with or without application of a spacer. Only the first 5 repeats of each experimental series were taken into account for the calculation of the mean τ_{50} values and the corresponding errors.

	1 Channel without spacer			1 Channel with spacer		
Exp. number	**Mean τ_{50} [dyn/cm²]**	**SD [dyn/cm²]**	**Error [%]**	**Mean τ_{50} [dyn/cm²]**	**SD [dyn/cm²]**	**Error [%]**
1	75.4	12.0	15.9	14.9	1.8	12.1
2	42.2	3.5	8.4	220.5	10.0	4.6
3	18.9	2.0	10.8	37.5	3.5	9.3
4	29.9	6.9	23.0	32.6	4.8	14.7
5	9.7	0.7	7.0	24.3	1.1	4.4
6	25.4	5.2	20.3	87.1	7.0	8.1
7	30.3	6.4	21.2	27.6	2.9	10.6
8	7.9	1.2	14.8	63.8	7.4	11.6
9	13.2	1.2	9.1	103.9	17.9	17.3
10				96.3	13.0	13.5
11				50	6.8	13.6
Mean error [%]	18.1 ± 12.0			10.9 ± 3.9		

7.1.3.3 DEPENDENCY ON THE STEP DURATION AT A CONSTANT OVERALL INCREASE

To evaluate the effect of different sampling procedures on the reproducibility of successive measurements two different sampling procedures were applied in the microfluidic shear force device. Both procedures followed the same overall increase with one procedure being sampled every Δt = 0.5 s (growth rate R_τ = 1. 047) and one being sampled every 5 s (R_τ = 1. 047). As shown in Figure S4 and in contrast to the example discussed in section 3.8.6.3 the fluctuations were slightly higher in the measurement series presented here. This may be due to the fact that this measurement was conducted without a spacer. However, the conclusion that the results obtained were independent of the sampling procedure can be drawn from this data set as well as the detachment curves on the one hand and the τ_{50} values on the other hand clearly overlapped. This undergirds the findings presented in section 3.8.6.3.

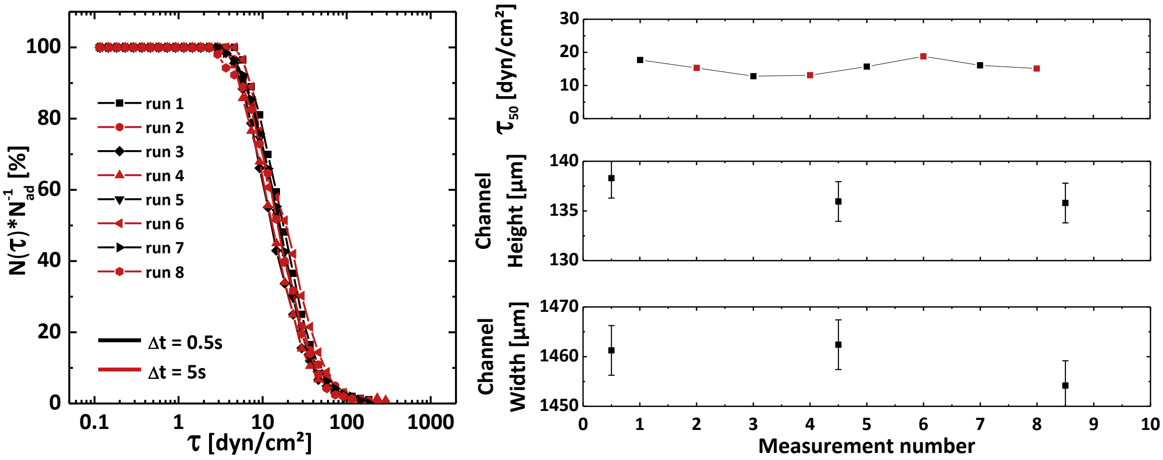

Figure S4: Evaluation of the effect of the experimental procedure on the τ_{50} values measured. The step duration Δt was varied while the growth rate R_τ was constant. No spacer was used. The τ_{50} values remained nearly constant throughout the measurement. The errors given for the channel dimensions are estimated measuring errors.

7.1.3.4 Dependency on the Maximum Shear Stress Applied

The effect of the maximum shear stress applied to the channel system was discussed in section 3.8.6.4. Here, it was demonstrated that while the application of a spacer improved the intra-channel fluctuation at low shear stresses, it had no effect if high shear stresses were applied. In this case the fluctuation was not only generally smaller, but it was also independent of the application of a spacer. As deviations of the channel dimensions were one possible explanation for the shifts of the τ_{50} values, the progression of the τ_{50} values in dependence of the channel dimensions and the maximum shear stress applied is shown here. Figure S5 and Figure S6 each present a successive series of measurements in a channel without and with application of a spacer, respectively. Figure S5 demonstrates that while the τ_{50} values changed during the measurement, especially after the application of high shear stresses of approximately 1,000 dyn/cm², the channel dimensions did not. This behaviour was not typical for channels lacking a spacer under high shear stress, but it does nicely demonstrate the independency of the channel dimensions from the τ_{50} values observed in this setup. The same conclusion can be drawn from Figure S6 that shows both stagnating channel dimensions and τ_{50} values. These findings indicate that any errors observed during the measurements were not correlated with the channel dimensions in the relaxed state (over pressure applied, but no suction generated by the syringe pump).

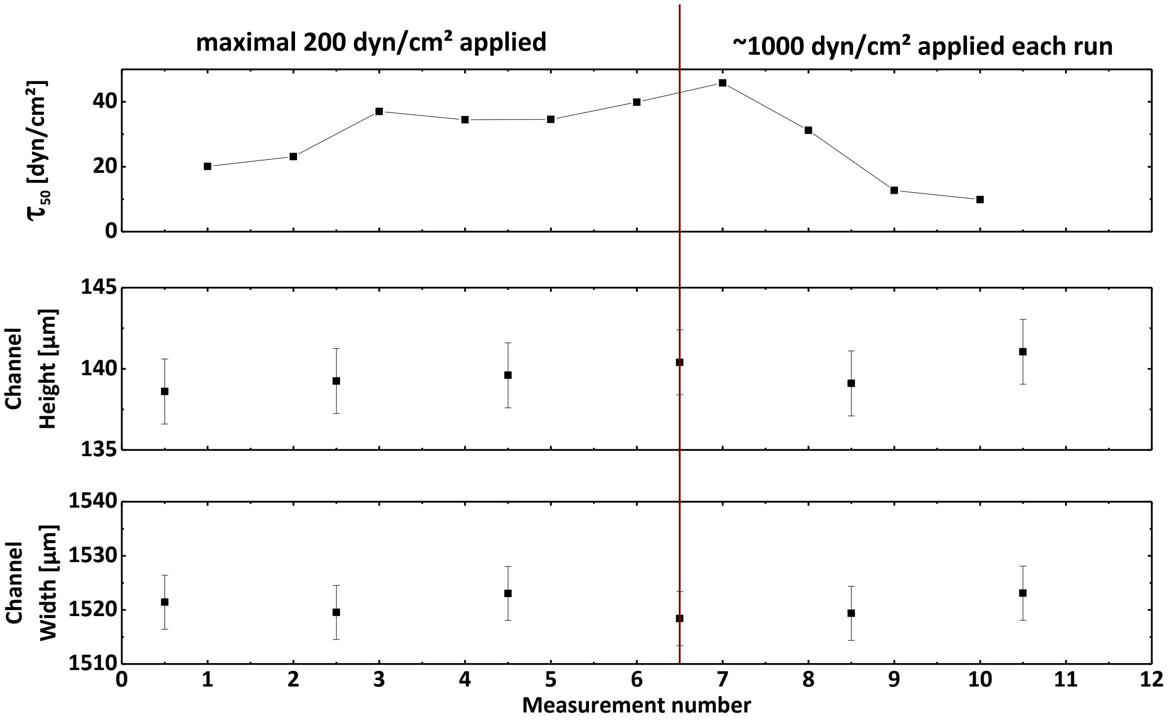

Figure S5: Dependency of the τ_{50} value measured on the maximum shear stress applied to the system without a spacer applied. The measurements were conducted in succession in one single channel. The channel dimensions were measured between the experimental runs, thereby only representing the dimensions if no flow was applied. The errors given for the channel dimensions are estimated measuring errors.

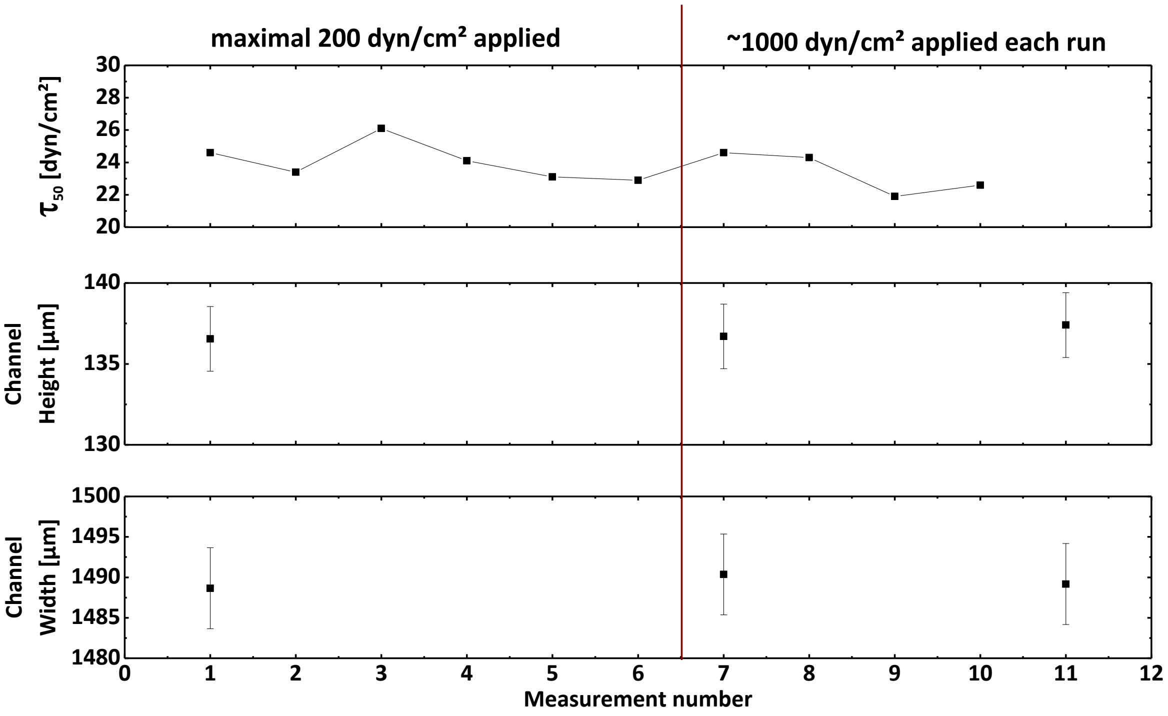

Figure S6: Dependency of the τ_{50} value measured on the maximum shear stress applied to the system with a spacer applied. The measurements were conducted in succession in one single channel. The channel dimensions were measured between the experimental runs, thereby only representing the dimensions if no flow was applied. The errors given for the channel dimensions are estimated measuring errors.

7.1.3.5 DEPENDENCY ON THE ATTRACTIVENESS OF THE SAMPLE SURFACE

In section 3.8.6.5 the dependency of the errors of the measurement was correlated with the region of shear stress in which the objects of interest detached from the surface. For this the detachment of particles from DDT SAMs (highly attractive) was compared to that from HUDT SAMs (moderately attractive). While the main text provides the direct comparison of the data obtained during the measurements the full data is presented in Table S2. The mean τ_{50} values and the corresponding errors (SD and percentage error, PE) obtained in all measurement series conducted on DDT or HUDT SAMs without a spacer are given. While the overall deviation was large in all experimental series, the mean PE was far larger of the measurements on DDT, the SAM which required higher shear rates to detach the particles from. This hinted that measurements at even lower shear stresses should provide an even higher accuracy.

Table S2: Overview over the τ_{50} values measured on HUDT and DDT without application of a spacer.

	Measurements on HUDT without spacer			Measurements on DDT without spacer		
Exp. number	**Mean τ_{50} [dyn/cm²]**	**SD [dyn/cm²]**	**PE [%]**	**Mean τ_{50} [dyn/cm²]**	**SD [dyn/cm²]**	**PE [%]**
1	29.4	8.1	27.6	333.2	107.6	32.3
2	31.9	4.0	12.4	797.7	389.3	48.8
3	13.6	0.1	0.9	1318.2	689.1	52.3
4	15.2	0.8	5.4	1562.6	1317	84.3
5	20.7	1.5	7.4	283.8	148.2	52.2
6	81.4	6.7	8.2	318.3	122.4	38.4
7	41.1	3.7	8.9	337.8	106.8	31.6
8	20.1	0.3	1.5	708.2	565.1	79.8
9	26.7	7.4	27.5	1733.4	1095.5	63.2
10	49.8	11.6	23.3	574.2	26.8	4.7
11	9.9	0.6	5.8	387.1	129.2	33.4
12	28.2	4.8	17.0			
13	33.4	6.6	19.9			
14	7.1	0.9	12.0			
15	12.6	0.9	7.1			
16	9.9	0.6	5.8			
Mean PE [%]	11.9 ± 8.4			42.1 ± 24.3		

7.2 SUPPORTING INFORMATION CONCERNING THE ANALYSIS OF THE INTERACTION OF CD44 WITH HYALURONIC ACID

This section provides background information concerning the investigation of the interaction of the cell surface receptor CD44 with its major ligand hyaluronic acid (HA) under shear flow conditions presented in section 4.

7.2.1 OVERVIEW OVER THE CELL CULTURE MEDIA COMPOSITIONS USED IN THIS WORK

As always when handling cells the culture conditions were of great importance. Therefore, this section presents the compositions of the cell culture media in which the different cell types used in this work were cultured.

Table S3: Cell culture medium used for the model cell lines KG-1a, Jurkat and Kasumi-1.

Component	Concentration	Company
RPMI 1640	88 %	Invitrogen
FCS	10 %	Invitrogen
L-Glutamine	1 %	PAA Laboratories GmbH
Penicillin/Streptomycin	1 %	PAA Laboratories GmbH

Table S4: Cell culture medium used for REF52WT and HepG2Iso.

Component	Concentration	Company
DMEM	88 %	Invitrogen
FCS	10 %	Invitrogen
L-Glutamine	1 %	PAA Laboratories GmbH

Table S5: Cell culture medium used for healthy human cells from the PB, for human HPC from CB, mPB and BM and for leukaemic blasts.

Component	Concentration	Company
Stemline^{TM} II Haematopoietic Cell Expansion Medium	95.4 %	Sigma-Aldrich
L-Glutamine (2 mmol/L)	1 %	PAA Laboratories GmbH
TPO (100 ng/mL)	1 %	PAA Laboratories GmbH
SCF (100 ng/mL)	1 %	PAA Laboratories GmbH
G-CSF (10 µg/mL)	0.1 %	PAA Laboratories GmbH
FLT3-L (500 ng/mL)	0.5 %	R&D Systems
Penicillin 1,000 U/mL Streptomycin 100 U/mL	1 %	PAA Laboratories GmbH

7.2.2 EFFECT OF BU52 ON THE ACCUMULATION OF KG-1A CELLS ON HA

The accumulation assay was used to further strengthen the finding, presented in section 4.1.2, that the HA binding domain of the cell surface receptor CD44 was required for the interaction of the CD44 positive cells studied in this work with HA-coated surfaces under flow. For this the effect of the treatment of KG-1a cells with different amounts of the CD44 antibody BU52 was analysed. Figure S7 A shows the accumulation curves acquired. It can be seen that the number of untreated cells interacting with the surface steadily increased until a plateau was reached after approximately 3 min. Increasing amounts of BU52 led to decreasing numbers of cells interacting with the surface. Full suppression was achieved with 9 µg/mL BU52. The CD44 negative cell line Kasumi-1 served as negative reference for the experiment. The amount of BU52 required for a complete suppression of the interaction was is good accordance with that determined by measurement using the detachment assay as presented in section 4.1.2. Furthermore, the same concentration dependent reduction of the interaction potential with HA could be observed in these measurements.

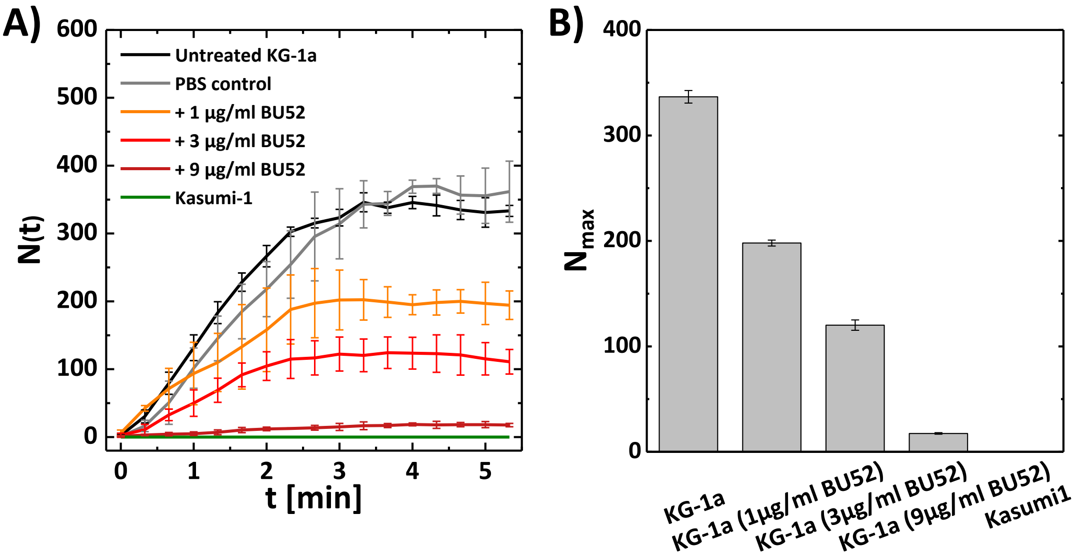

Figure S7: KG1a accumulation on HA in dependence of the BU52 concentration. KG-1a cells were incubated with varying amounts of BU52 prior to investigation of the interaction with HA under shear flow. The accumulation curves (A) and the bar graphs depicting the maximum number of cells interacting with the surface (B) show the reduction of the interaction by BU52. The graph shows the results of one set of measurements (n = 3). This was repeated thrice with comparable results. The maximum number of cells interacting with the surface was highly sensitive to experimental variations making an averaging of the data difficult. In all cases increasing amounts of BU52 led to a reduction of the interaction.

7.2.3 VIABILITY OF HEPG2ISO CELLS INCUBATED WITH SHA

In the course of the study of the characteristics and dependencies of the CD44-HA interaction the effect of the treatment of the cells with glycosaminoglycans (GAGs) such as the otherwise surface-bound HA was analysed. For this HepG2Iso cells were incubated with soluble macromolecular and oligomer GAGs. As high concentrations of the oligomer HA (short chain length; sHA; length: 6-10 disaccharide units, DS) were used for this study the viability of the model cell line HepG2Iso in such concentrations of sHA was tested. The analysis was conducted by Katharina Fuchs (group of Dr. Véronique Orian-Rousseau at ITG, KIT, Karlsruhe, Germany). HepG2Iso cells were incubated with 50 µg/mL sHA (6-10 DS) for 1 h in cell culture conditions before imaging the cells by light microscopy. The cellular shape, the area of adhesion and the overall appearance of the cells was then compared to untreated cells to estimate whether the incubation had an impairing effect on the cells. As shown in Figure S8 the incubation had no negative effects on the HepG2Iso cells after 1 h. This time span was longer than the incubation time before microfluidic shear force measurements (30 min) plus the duration of the measurement (5 min per measurement with 2 measurements per incubated vial, resulting in 40 min in total) and, therefore, safely covered the necessary time span of exposure.

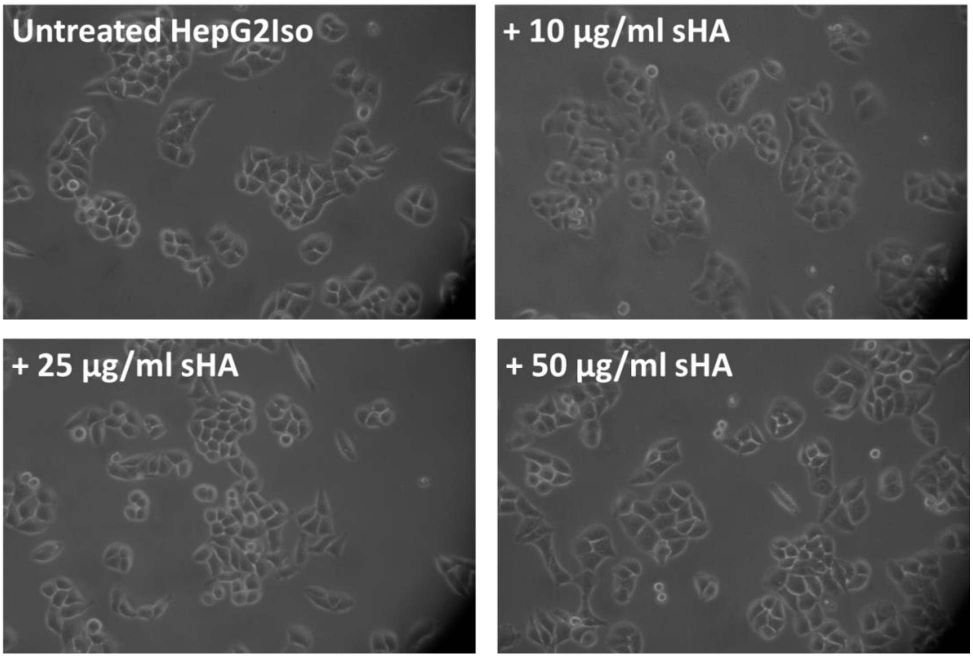

Figure S8: Treatment of HepG2Iso cells with sHA for 1 h. HepG2Iso cells were incubated with sHA (6-10 DS) for 1 h before they were imaged using a Canon Power Shot S620 digital camera connected to an Axiovert 40c Zeiss microscope (10x objective). The cells showed no obvious change indicating no impairing effects resulting from the incubation.

7.2.4 Interaction of Primary Human Haematopoietic and Leukaemic Cells with HA

This section provides supporting or more extending information concerning the interaction of healthy haematopoietic and leukaemic cells with HA. This shall undergird or elaborate the findings presented in section 4.2.

7.2.4.1 Interaction of Healthy Blood Cells with HA

As demonstrated for haematopoietic progenitor cells (HPC) isolated form umbilical cord blood (CB) a preincubation of the cells in Stemline^{TM} II Haematopoietic Cell Expansion Medium supplemented with 100 ng/mL TPO, 100 ng/mL G-CSF, 100 ng/mL SCF, 500 ng/mL Flt-3L, 2 mmol/L L-glutamine, 1,000 U/mL penicillin and 100 U/mL streptomycin for 24 h (hereafter referred to as Stemline II medium) was required to enable the rolling interaction of the cells with HA. Table S6 depicts the results of the flow cytometry measurements for some of the HPC samples from CB, mobilised peripheral blood (mPB) and the bone marrow (BM) used in this work as measured by Isabel Hoffmann from the group of Prof. Anthony D. Ho at the Universitätsklinikum Heidelberg. Not all samples were analysed as the material was available only in small quantities and was needed for the microfluidic measurements. However, Table S6 clearly shows that after the incubation in Stemline II medium all HPC maintained their stemcellness marked by expression of the CD34 receptor. It was also shown that the cells expressed high levels of CD44pan.

Table S6: Flow cytometry measurements of HPC after Stemline II incubation for 24 h.

HPC source (sample number)	CD34 positive cells [%]	CD44pan positive cells [%]
CB (1)	98.88	99.64
CB (2)	99.39	99.94
CB (3)	98.82	99.85
mPB (1)	99.66	99.96
BM (1)	98.20	97.27

The interaction of the different HPC with HA under flow conditions was extensively discussed in the main text (section 4.2.1). Here, the interaction of blood cells isolated from the peripheral blood (PB) of healthy donors with HA is discussed. The data shown in Figure S9 represents one of two independent, but comparable sets of measurements. In each set of measurements the interaction of mononuclear cells (MNC; also known as peripheral blood mononuclear cells PBMC) with HA under flow was compared to that of granulocytes, monocytes and lymphocytes. Here, MNC present the totality of all cells isolated from the peripheral blood containing a round nucleus (rather than a lobed nucleus) with the granulocytes, monocytes and lymphocytes covering most of the other blood cells less the red blood cells. As shown in Figure S9 A there was hardly any interaction of the cells from the healthy PB observable with HA. Lymphocytes and monocytes did not roll or adhere to HA, despite expression of CD44. For MNC and granulocytes a certain amount of immobile adherent cells could be observed (B). In the case of the granulocytes firm adhesion to and spreading on the surface could be observed in the time-lapse videos obtained during measurement in the microfluidic channel system. This led to a strong, non-rolling adhesion to the surface. Pre-incubation of cells with cytokines in Stemline II medium did not increase the number of cells that interacted with HA. These findings demonstrated that rolling on HA-coated surfaces could not be observed for the highly differentiated cell types although all expressed CD44.

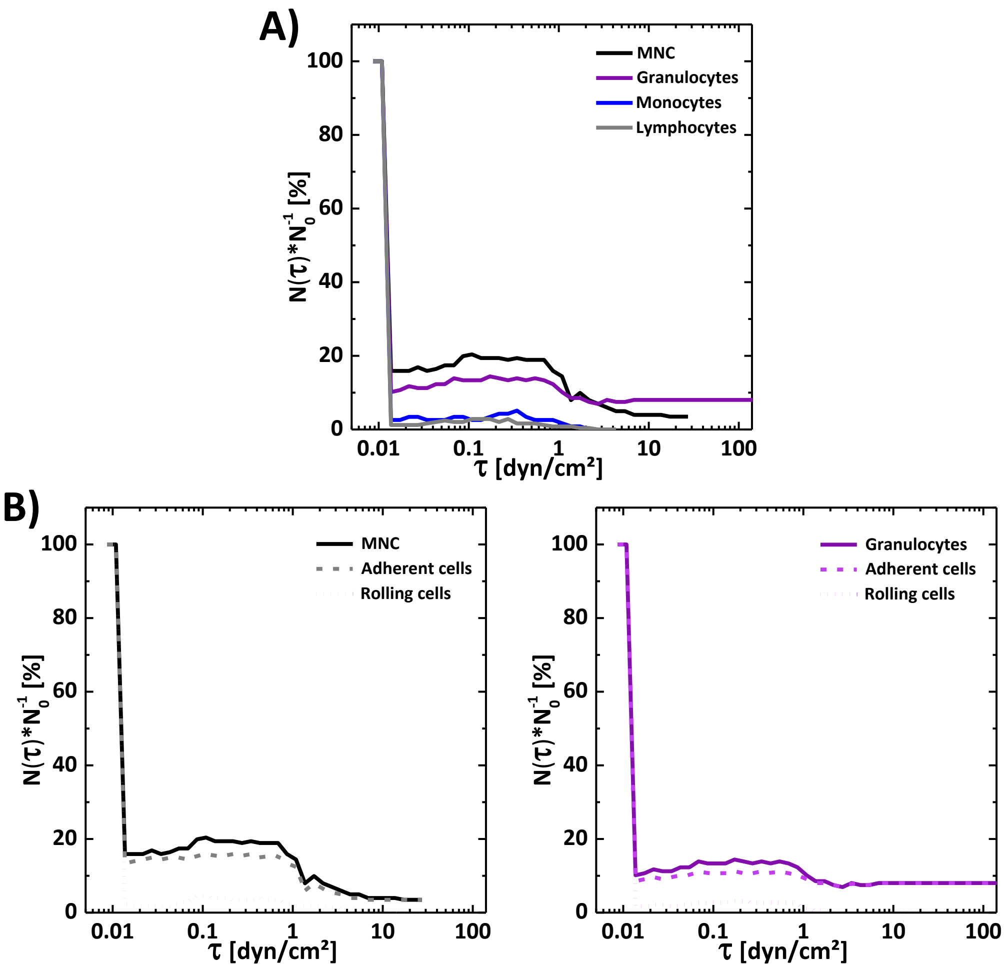

Figure S9: Interaction curves for healthy cells from the PB with HA. The interaction curves (A) show absence of interaction with HA for both monocytes and lymphocytes. MNC and granulocytes exhibit a weak interaction with HA that is only comprised of immobile adhesion (B).

7.2.4.2 INTERACTION OF LEUKAEMIC BLASTS WITH HA

The leukaemic blasts were isolated from frozen samples of patients freshly diagnosed with acute myeloid leukaemia (AML) by FAC sorting based on their SSC and CD45 characteristics (SSC^{low}, $CD45^{dim}$). The CD44 expression was also measured to determine whether an investigation in the context of this work was expedient. The percentage of blasts gated from the isolated cell material and the fraction of those cells expressing CD44 is shown in Table S7. If not mentioned specifically the blasts were isolated from the BM of the respective patient. At least 95.70 % of the blasts were CD44 positive. The data was obtained by the group of Prof. Anthony D. Ho at the Universitätsklinikum Heidelberg.

Table S7: Fraction of cells that were blasts isolated from the frozen patient material as sorted by FACS and the CD44 expression of the leukaemic blasts.

Leukaemic Blast Sample	Blasts gated from the cell material [%]	CD44pan positive cells [%]
AML 1	72.90	99.99
AML 2	86.30	99.98
AML 3	75.70	99.70
AML 4 BM	89.50	99.90
AML 4 PB	91.60	99.40
AML 5 BM	36.40	99.20
AML 5 PB	75.90	99.30
AML 6	72.50	98.20
AML 7	60.60	100.00
AML 8	83.90	99.30
AML 9	66.50	99.34
AML 10	66.50	100.00
AML 11	58.70	95.70

The interaction of the leukaemic blasts with HA-coated surfaces was later measured in the microfluidic shear force setup. During data evaluation a discrimination was made between the cells undergoing the CD44 mediated flow induced rolling (extensively described and characterised in the main text in section 4.1) and those demonstrating an immobile adhesion to the surface. Furthermore, the effect of a CD44 antibody (clone BU52, hereafter referred to as BU52) on both forms of interaction was studied. A concentration of 9 µg/mL BU52 was used for these experiments as this concentration had previously (section 4.1.2 in the main text and Figure S7 in the Appendix section 7.2.2) been shown to fully suppress the interaction with HA. An overview of the interaction patterns obtained from the microfluidic measurements for the untreated blasts and for those treated with 9 µg/mL BU52 is shown in Figure S10.

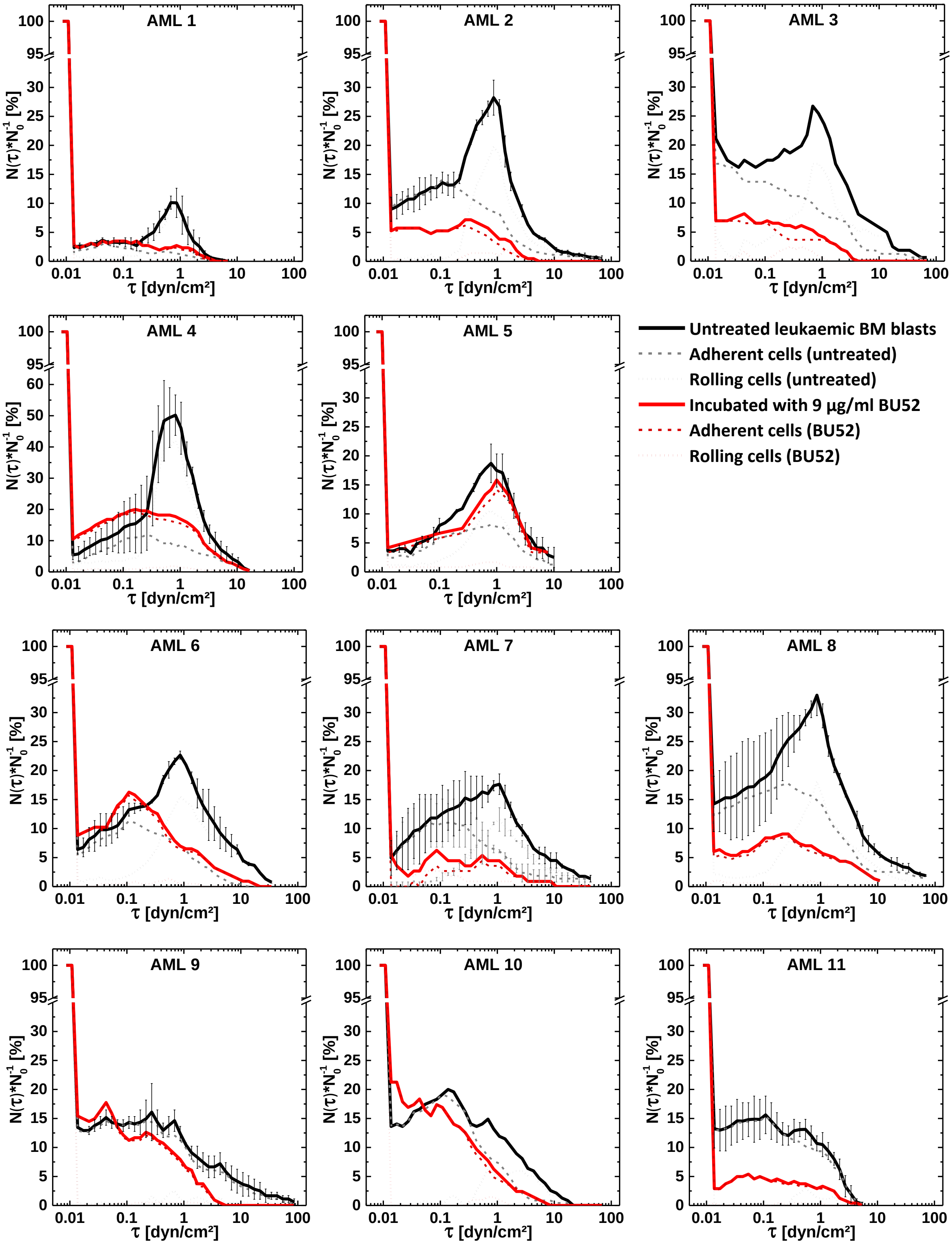

Figure S10: Overview of all 11 AML blast samples measured. AML samples 1-5 represent interaction pattern A with flow-induced rolling and detachment of the interacting cells from the surface prior to ~ 10 dyn/cm². AML samples 6-8 represent interaction pattern B with flow-induced rolling that persisted beyond ~ 10 dyn/cm². Both cases were accompanied by varying numbers of immobile adherent cells. AML samples 9-11 represent interaction pattern C with few rolling cells but large numbers of immobile adherent cells. [266]

From the interaction curves or more specifically from the curves after treatment with BU52 it can be seen that while the antibody effectively suppressed the flow induced rolling of the cells in all cases the effect on the immobile adhesion was always so pronounced. The samples AML4 and AML5 both showed an ineffective blocking of the immobile adhesion by BU52. For these patients a comparison was made between both the overall interaction and the effectiveness of the BU52 treatment for blasts isolated either from the BM or from the PB. As shown in Figure S11 the interaction patterns of the untreated cells were nearly identical in both cases. The effect of the treatment with 9 µg/mL BU52, however, differed. While the rolling interaction was fully supressed in all four samples the immobile adhesion was more effectively blocked in the samples isolated from the PB than in those isolated from the BM.

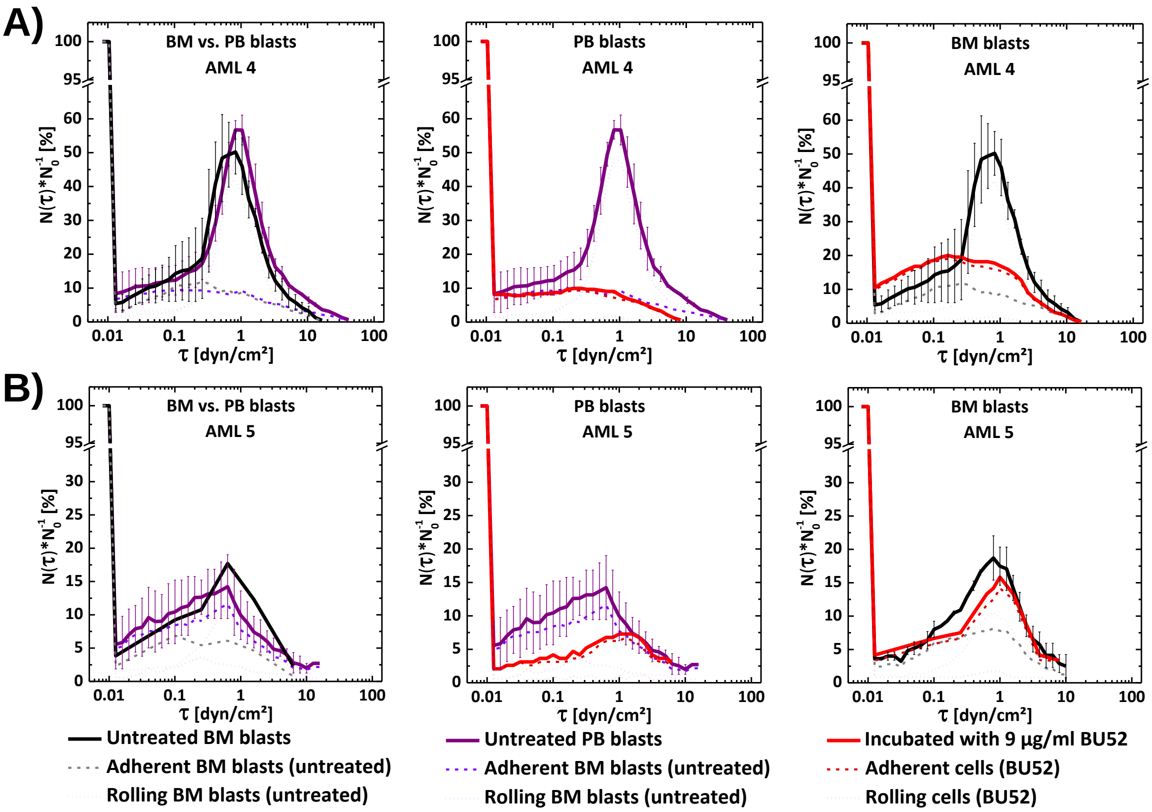

Figure S11: Comparison of the interaction patterns from blasts from BM and PB in AML 4 (A) and AML 5 (B).[266]

A fraction of at least 10 % immobile adherent cells after treatment with BU52 was defined as ineffective blocking. Table S8 gives an overview over the patient characteristics, the risk group stratification according to the European LeukaemiaNet[316] and Foran *et al.*,[317] the blocking efficiency of the immobile adhesion to HA by BU52 and the outcome of the induction chemotherapy. While a correlation of the blocking efficiency with the risk group stratification was not apparent, one with the overall survival of the patients was. In the group in which BU52 was ineffective, only one of five patients achieved CR after induction chemotherapy. Whereas in the group of six patients, in whom the adhesion of the leukaemic cells to the HA-surface could be inhibited by BU52, three achieved CR. A Kaplan-Meier plot (Figure 79), visualising the correlation between the blocking efficiency and the overall survival of the respective patient, is shown in section 4.2.2 in the main text.

Table S8: Patient characteristics, risk group stratification, efficiency of the blocking of the immobile adhesion to HA by BU52 and state after induction chemotherapy for all AML samples.[266]

Sample No.	Gender	Age	Abnormalities	Risk Group		BU52 efficiency			State after induction chemo-therapy	Deceased
				ELN[316]	Foran[317]	$N*N_0^{-1}$	>10 %	<10 %		
1	male	52	add(2)(q33), -7, del(7q22), del(7q36)	high	high	< 5		▒	Persistence	No
2	male	65	-Y ,t(8;21) (q22;q22), c-Kit mutation	high	high	~ 5		▒	CR	No
3	male	66	del(4)(q21),t(5;16)(q11.2;q11.2),t(6;12)(q13;p11.2),del(7)(q22q32),-17, -18,del(20)(q11.2),add(20)(q11.2) amplification of MLL-Gene +11q23	fav.	int.	~ 5		▒	Persistence	Yes
4	female	71	amplification of MLL-Gene +11q23	int.	int.	~ 20	▓		Persistence	Yes
5	female	56	none	int.	int.	~ 15	▓		Deceased during chemo-therapy	Yes
6	male	67	-Y,+13	int.	int.	~ 15	▓		Persistence	Yes
7	male	56	NPM1 positive	int.	fav.	~ 5		▒	CR	No
8	male	32	t(8;21)(q22; q22)	fav.	fav.	5-10		▒	CR	No
9	male	53	FLT3-ITD positive ratio 0,74	int.	high	~ 15	▓		CR	Yes
10	male	87	+8	int.	int.	~ 15	▓		No chemo-therapy	Yes
11	male	63	del(12)(p13)	int.	int.	< 5		▒	Persistence	No

7.2.5 VISUALISATION OF THE GROWTH OF MSC FEEDER LAYERS AND THE INTERACTION WITH KG-1A CELLS UNDER FLOW

This section presents two videos connected to the work with feeder layers (surfaces completely covered with convergent cells) of mesenchymal stromal cells (MSC). Video S4 gives an impression of how MSC grew inside a fully assembled microfluidic channel system over the course of ~ 23 h. It can be seen that during the first hours the MSC spread in the typical flat manner of epithelial cells reaching ideal spreading after roughly 5 h. Later the cells elongated until they appeared string-like. The video can be found on the CD provided with the printed edition of this thesis.

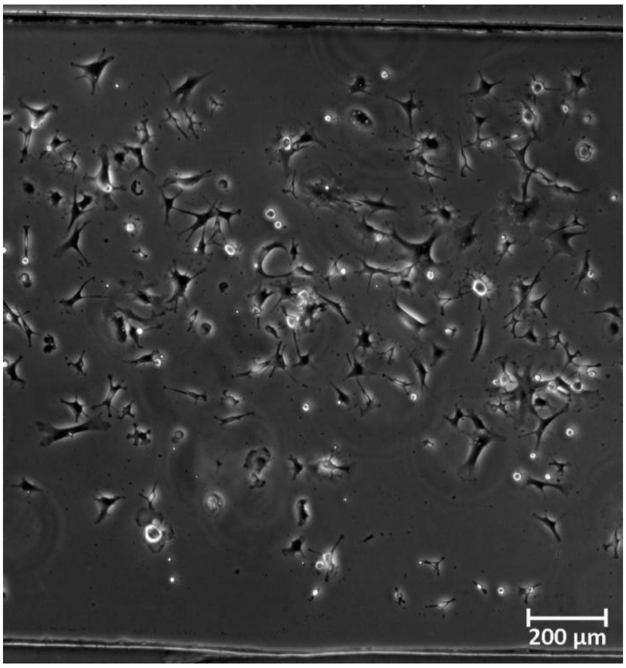

Video S4: Supplementary video demonstrating the growth of MSC inside a microfluidic channel. From the cell morphology alone it can be seen that an overnight incubation inside the channel was too long. Ideal spreading of the cells was reached after roughly 5 h.

Video S5 shows the interaction of the cells of the model cell line KG-1a with a reasonably good example of an MSC feeder layer. The KG-1a cells were not allowed to settle on the surface prior to measurement to minimise the number of cells ‘sticking’ to the MSC before the experiment was started. The video clearly shows that the KG-1a cells did not roll across the MSC as they did across the HA-coated surfaces. The KG-1a cells instead ‘stuck’ to the MSC. Detachment of the KG-1a cells then involved elongation of the cells before the force of the liquid detached the cells from the MSC. This too was an observation, which could not be made for KG-1a cells on HA. The video can be found on the CD provided with the printed edition of this thesis.

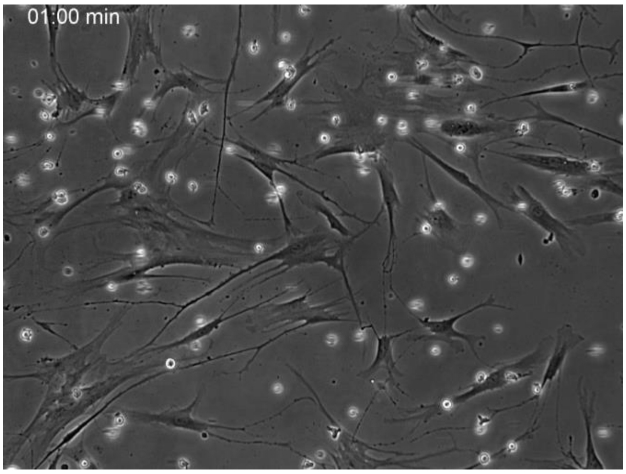

Video S5: Interaction of KG-1a cells with MSC under flow conditions.

7.3 SUPPORTING INFORMATION CONCERNING THE ANALYSIS OF THE STABILITY AND BIOCOMPATIBILITY OF SURMOF 2

This section provides supplementary information undergirding and expanding the studies presented in section 5 of the main text.

7.3.1 CHARACTERISATION OF THE MHDA SAMS USED FOR THE GROWTH OF THE SURMOFS

As mentioned in section 3.2.3 self-assembled monolayers (SAMs) of 16-Mercaptohexadecanoic acid (MHDA) were used as functional surfaces on which the surface anchored metal-organic frameworks (SURMOFs) were grown. If used for this purpose the SAMs were prepared either by Hasan K. Arslan or by Zhengbang Wang from the workgroup of Prof. Christof Wöll (IFG, KIT, Karlsruhe, Germany). The MHDA SAMs were characterised by infrared reflection adsorption spectroscopy (IRRAS) prior to use.

IRRAS grounds on the absorption of certain wavelengths of light (typically infrared light, hence the name) by molecules if the energy of the wave corresponds to the energy of a molecular rotation or vibration. The IRRAS surface selection rule states that only those molecular vibrations are visible of which a component is orthogonal to the surface. Such dynamic dipoles will be enhanced by the electric field induced by polarisation of the metal surface on which the measurement takes place.[318-319] A typical spectrum for a MHDA SAM used in this work was kindly provided by Zhengbang Wang and is shown in Figure S12. The spectrum shows the symmetric and the asymmetric vibrations of CH_2 groups at 2850 cm^{-1} and 2919 cm^{-1}, respectively. The C=O vibrations for monomeric carboxylic groups are observed at 1717 cm^{-1} and the C=O vibrations for acyclic dimeric carboxylic groups are observed at 1742 cm^{-1}. These values correspond well with those found by Arnold *et al.*[253] giving good evidence for the quality of the SAMs used.

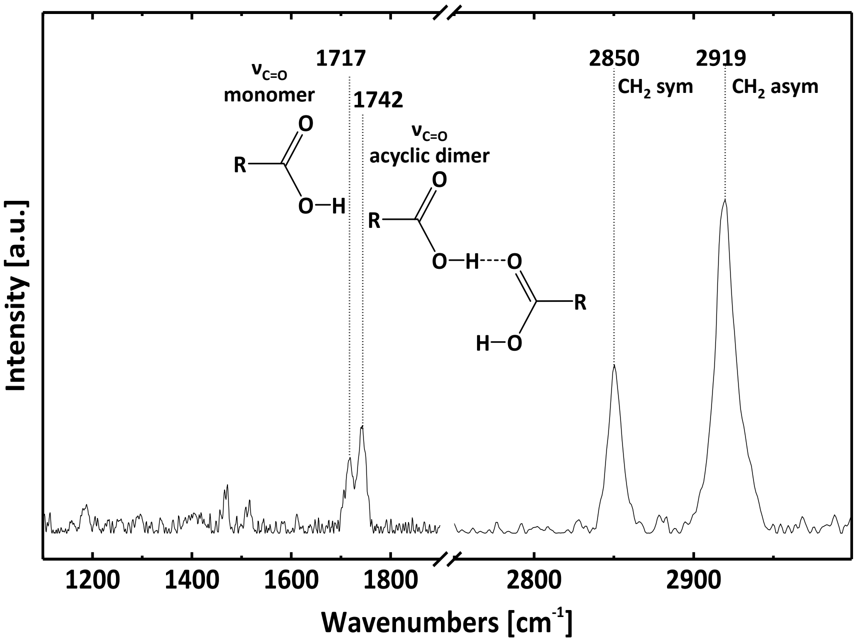

Figure S12: IRRA spectrum of an MHDA SAM. The spectrum shows the symmetric and asymmetric CH_2 vibrations as well as the stretching vibrations $\nu_{C=O}$ for monomeric and acyclic dimeric carboxylic groups.

7.3.2 EXTENDED STABILITY ANALYSIS OF CU-SURMOF 2 IN DIFFERENT MEDIA AND CELL SUSPENSIONS

The stability of Cu-SURMOF 2 in MilliQ® water, artificial sea water (ASW), phosphate buffered saline (PBS) with and without fibrinogen added and the cell culture medium DMEM (relevant media for the culture of wild type rat embryonic fibroblasts, REF52WT) supplemented with 10 % FCS and 5 % L-Glutamine over a period of 1 h was presented in section 5.1. In the following section (section 5.2) the compatibility to the culture of eukaryotic cells was studied using REF52WT cells. Although the instability of the Cu-SURMOF 2 samples in PBS or the proteinacous media resulted in a release of the building units (benzene-1,4-dicarboxylic acid, bdc and Cu^{2+} ions) to the solution no impairment of the adhesion or proliferation of the cells was observed. Video S6 shows the unimpaired adhesion and proliferation of REF52WT cells on a structured Cu-SURMOF 2 substrate over

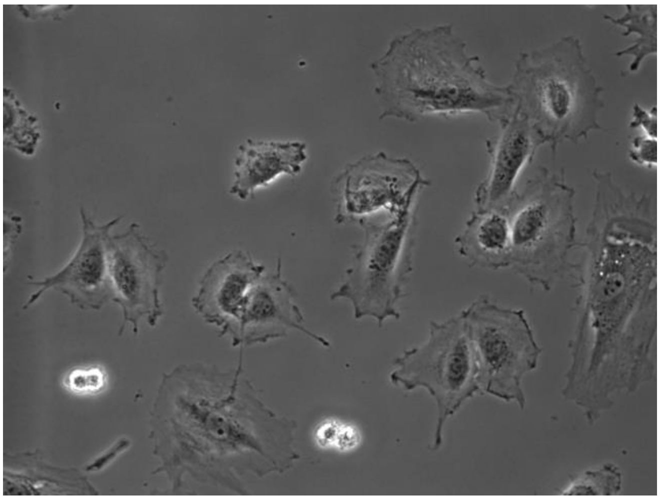

Video S6: Proliferation of REF52WT cells on a structured Cu-SURMOF 2.

the course of 22 h. The temperature in the incubator was set to 37 °C and 5 % CO_2 was in the atmosphere. Under these ideal conditions the cells were monitored by time-lapse microscopy in the TE2000-U microscope described in section 3.8.1. It can be seen that the cells adhered to and spread on the structured surface. Proliferation of the cells could also be observed. The video can be found on the CD provided with the printed edition of this thesis.

Testing of the SURMOF substrates towards their general applicability as smart-release substrates was one of the aims of this work. As a pronounced stability of Cu-SURMOF 2 was observed in ASW the substrate was tested with the marine bacterium *Cobetia marina*, which thrives in ASW. *C. marina* is a model bacterium used in many adhesion studies due to its relevance in marine biofouling.[300-302] The studies with the bacterium were conducted in cooperation with Maria Pilar Arpa Sancet from our workgroup. As a length of incubation of *C. marina* on sample surfaces of 2 h was typical for adhesion experiments[268,302] the stability analysis was expanded to this time span. Figure S13 A-C shows XP and XRD spectra clearly demonstrating the stability of Cu-SURMOF 2 in MilliQ® water for up to 2 h. The XP spectra were recorded by Stella Bauer from our workgroup and the XRD spectra were recorded by Hasan K. Arslan or Zhengbang Wang from the group of Prof. Christof Wöll (IFG, KIT, Karlsruhe, Germany). As seen in the same spectra the stability in ASW was nearly as pronounced as that of MilliQ® water. Here only a disassembly of the outermost layer(s) could be observed making the copper slightly more accessible by spectroscopy, seen by the increase of the Cu 2p peak and the decrease of the C 1s. The retention of the crystallinity during the incubation in ASW as measured by XRD is shown in Figure S13 D. Figure S13 E demonstrates that incubation with *C. marina* led to a gradual loss of crystallinity over time.

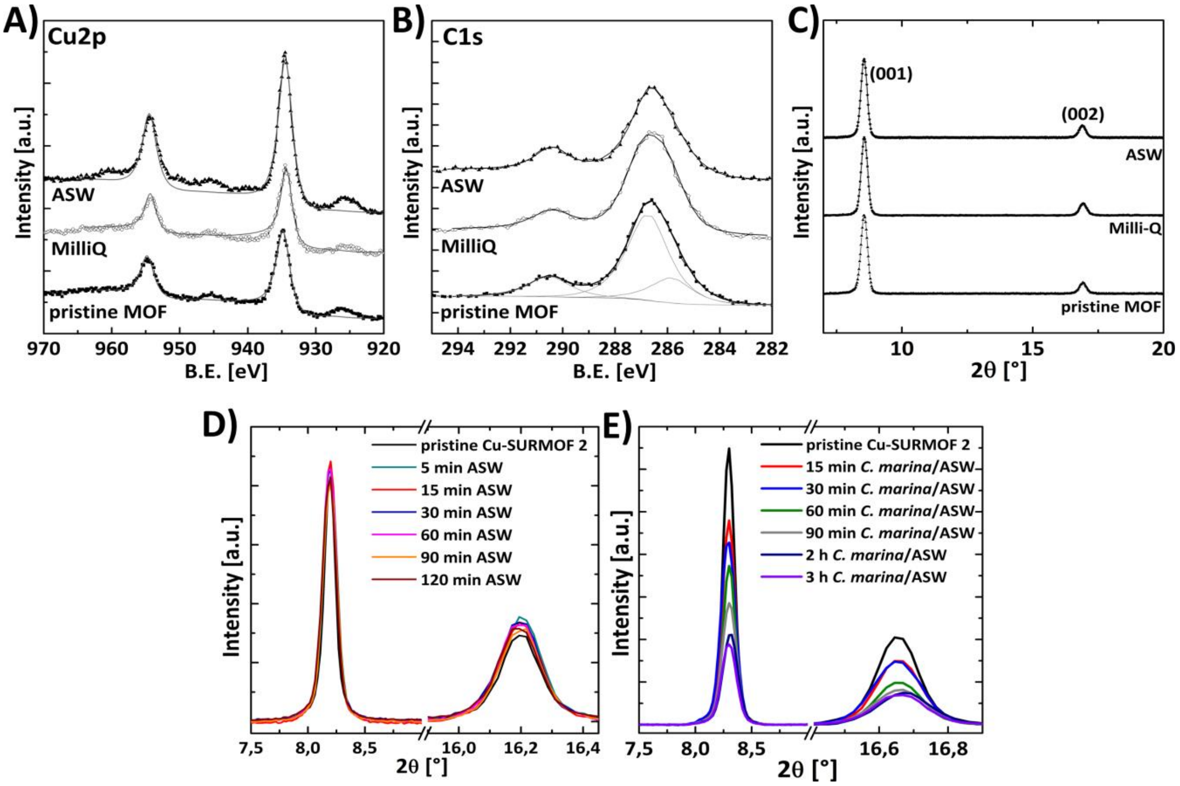

Figure S13: Stability analysis of Cu-SURMOF 2 in different media for 2 h. X-ray photoelectron spectra of (A) the Cu 2p and (B) the C 1s core level of Cu-SURMOF 2 for pristine samples and after incubation for 2 h in MilliQ® water and ASW. (C) X-ray diffraction data before and after immersion of the Cu-SURMOF 2. (D) XRD of Cu-SURMOF 2 after incubation in ASW and (E) XRD after exposure to C. marina in ASW for different times.[304]

7.3.3 CU-SURMOF 2 AS SMART-RELEASE SURFACE IN CONTACT WITH *C. MARINA*

This section presents the study of the effect the bacteria *C. marina* had on the Cu-SURMOF 2 substrates and *vice versa*. The main tools used for this analysis were atomic force microscopy (AFM), microfluidic shear force detachment assays measuring the shear stress required to detach *C. marina* from the sample surfaces and a viability assay. AFM images were recorded by Carlos Azucena from the group of Prof. Christof Wöll (IFG, KIT, Karlsruhe, Germany) and the bacteria samples were provided, measured and analysed by Maria Pilar Arpa Sancet from our workgroup. Before discussing the results the methods are briefly presented.

Atomic force microscopy (AFM) After 2 h incubation on the sample surface, the bacteria were air dried overnight following published protocols [320-321]. Bacteria were imaged using an Asylum Research Atomic Force Microscope, MFP-3D BIO. The AFM was operated at 25°C in an isolated chamber in alternating current mode (AC mode). AFM cantilevers were purchased from Ultrasharp™ MikroMasch. Three types of AFM-cantilevers were used, an NSC-35 (resonance frequency 315 kHz; spring constant 14 N/m), an NSC-36 (resonance frequency: 105 KHz; spring constant: 0.95 N/m) and an NSC-18 (resonance frequency: 75 kHz; spring constant: 3.5 N/m).

Bacterial viability assay The widely used[322-323] live/dead® BacLight™ bacterial viability kit was used to determine the viability of the bacteria after 2 h incubation on Cu-SURMOF 2 substrates (~120 nm thickness) and MHDA SAM as non-toxic control. The assay was performed following the manufacturer´s protocol. Prior to staining, the surfaces were incubated in a bacterial suspension in ASW with an optical density $OD_{600} = 0.1$ for 2 hours. Subsequently, 3 µl of a 1:1 mixture of both stains (red- and green-fluorescent nucleic stain) was added per millilitre of bacterial solution and incubated at RT in the dark for 15 min. The samples were removed from the solution and rinsed with MilliQ® water. All samples were analysed by florescence microscopy with an upright Nikon microscope 90i and suitable optical filters (BV-2A and Texas red HYQ, Nikon, Tokyo, Japan) using a 40x objective.

Microfluidic bacterial detachment assay The adhesion strength of the bacterium *Cobetia marina* on SURMOF 2 was quantified using a custom built microfluidic shear force setup[11] which has previously been utilised for the study of bacterial adhesion on surfaces.[302] Four fully assembled channel systems (dimensions: 13 mm x 1 mm x 140 µm) were mounted on an inverted microscope (Nikon TE2000-U). Bacteria suspensions with an $OD_{600} = 0.1$ were injected into all four channels and incubated for 2 h in parallel as established in previous protocols.[302] After the incubation phase, medium from a reservoir was sucked through the channels by a computer controlled syringe pump generating a flow which was increased stepwise by 26 % every 5 s. The detachment was followed via video microscopy with a 40x Ph2 objective and the fraction of adherent bacteria was determined every 5 s. The removal from all four channels was done sequentially. The wall shear stress τ_W created by the liquid flow was calculated as described in section 7.1.1.3. From the removal curves, the critical shear stress required to detach 50 % of the adherent bacteria (τ_{50}) was derived. Each measurement was repeated at least four times.

The first step in the evaluation of the influence the bacteria and the Cu-SURMOF 2 had each other was to record AFM images to determine the morphology of the bacteria after incubation on Cu-SURMOF 2. A HDT SAM served as reference substrate to compare the morphology of healthy well adhered bacteria. Figure S14 A shows the bacteria on a HDT SAM. In comparison to this the bacteria incubated on the Cu SURMOF 2 (Figure S14 B) were wrinkled and deformed. It could be shown that the roughness of the bacteria on the Cu-SURMOF 2 was approximately 50 % higher than that of those on the HDT SAM (Figure S14 C). Similarly, the mean width of the bacteria on the Cu-SURMOF 2 was approximately 25 % larger compared to that of those seeded on the HDT SAM (Figure S14 D). Figuratively speaking the bacteria could be described as more wrinkled and flatter when incubated on the Cu-SURMOF 2.

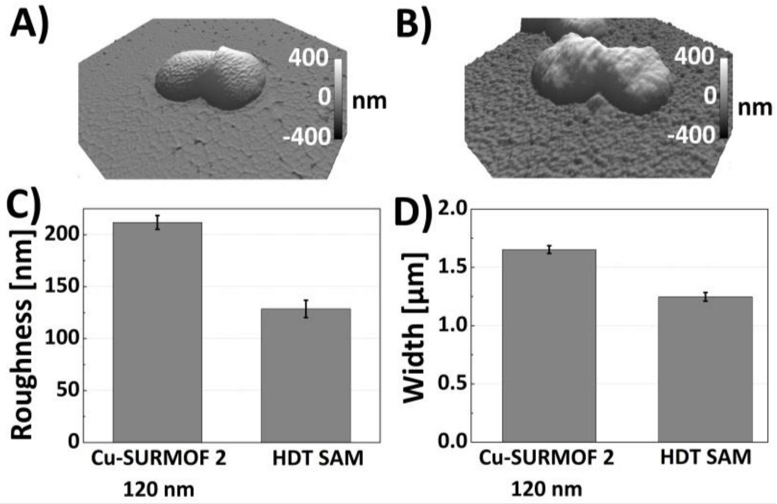

Figure S14: Analysis of the bacterial width and height after incubation on a Cu-SURMOF 2 substrate. AFM images of the bacteria on (A) HDT SAM and (B) Cu-SURMOF 2. (C) Mean roughness and (D) mean width of the bacteria. Measurements were obtained on seven individual bacteria. Error bars are the standard errors.[304]

The impression of a deformation of the bacteria upon incubation on a Cu-SURMOF 2 surface was further supported by measurement of the height profiles as shown in Figure S15. Here, it can be seen again that the bacteria incubated on the Cu-SURMOF 2 surface were flatter than those incubated on the HDT SAM reference. Analysis of an overview of a Cu-SURMOF 2 surface on which the bacteria had been cultured for 2 h showed that the SURMOF layer was still present. Such an overview is shown in Figure S16 A. The Cu-SURMOF 2 sample used for this analysis had an initial thickness of approximately 160 nm, the typical thickness of a Cu-SURMOF 2 consisting of 20 layers. From the height profile shown in Figure S16 B it can be seen that this height was still measureable after incubation with the bacteria. A possibility to consider the observation of an intact SURMOF layer after incubation with the bacteria, while still explaining the deformation of the bacteria, is a localised disassembly of the SURMOF upon contact with the bacteria.

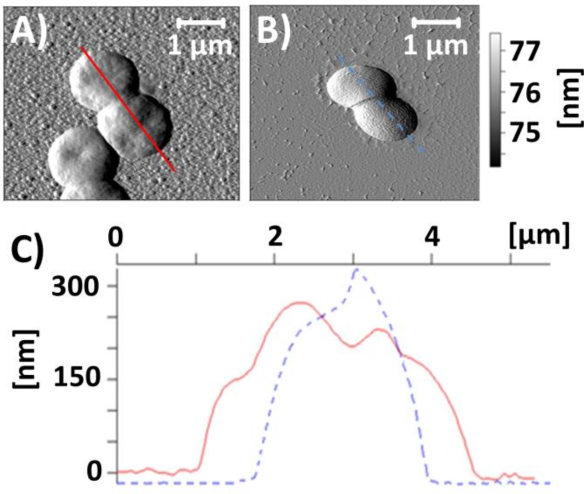

Figure S15: Analysis of the bacterial morphology. AFM images of *C. marina* on a Cu-SURMOF 2 (A) and on an HDT SAM (B). Height profile (C) indicated by the blue dotted and red line in (A) and (B).[304]

Figure S17 presents the proposed mechanism for this localised disassembly. The overview is the same as shown in Figure 97 with SEM images of bacteria appropriate to the scenario depicted shown. In the process of attaching to a surface *C. marina* secrete extracellular polymeric substances (EPS) composed of macromolecules (mostly polysaccharides[305] such as alginic acid (AA)[306]) functioning as glue for the bacteria to the surface. This may then induce a localised disassembly of the Cu-SURMOF 2 in the direct vicinity of the bacteria. The copper ions released by this disassembly are toxic for the bacteria and are the reason for the deformation of the same.

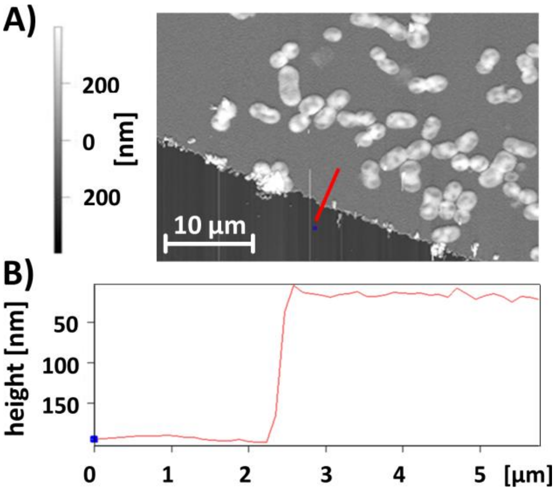

Figure S16: AFM measurement of the SURMOF 2 height after bacteria incubation. AFM image of a Cu-SURMOF 2 substrate incubated with C. marina for 2 h (A) and the height profile (B) along the red line shown in (A).[304]

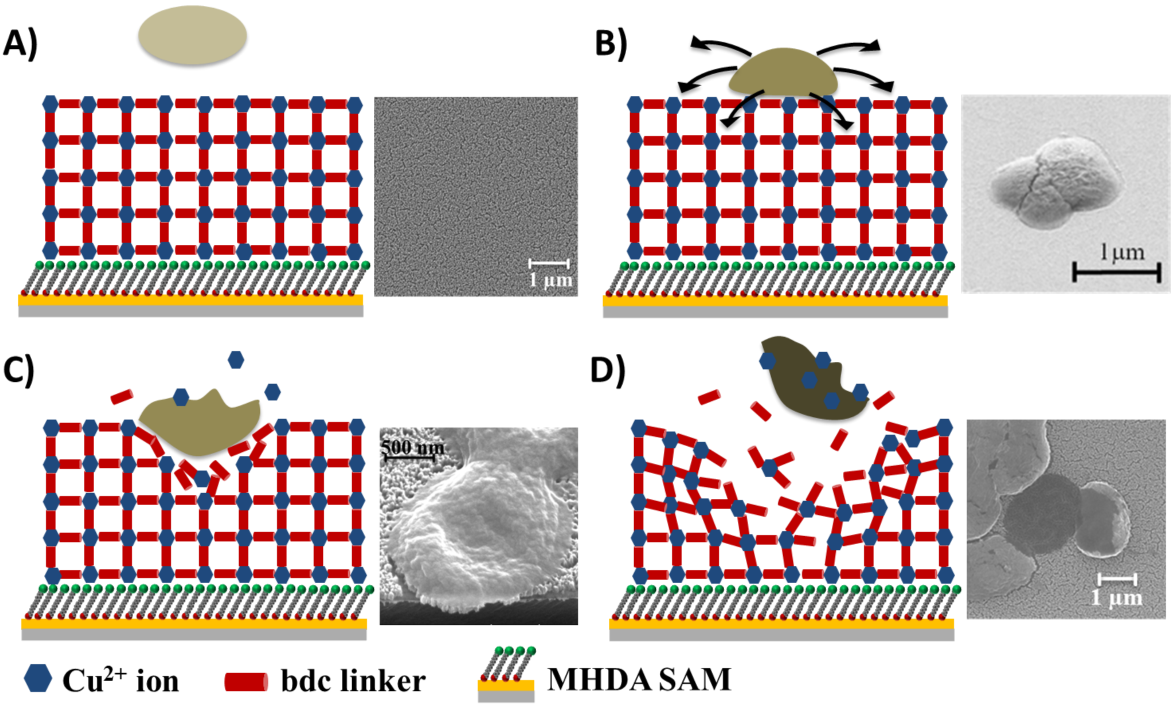

Figure S17: Proposed mechanism for the release of copper from a Cu-SURMOF 2 substrate by *C. marina*. (A) Healthy bacteria in initial contact with the SURMOF. The SEM image shows a pristine Cu-SURMOF 2. (B) Bacteria settled on an intact SURMOF begin secretion of EPS and other molecules. The SEM image shows a unaffected bacterium on a HDT reference SAM. (C) Disassembly of the SURMOF and release of Cu2+ ions. The SEM image shows a bacterium on a Cu-SURMOF 2 surface after 2 h incubation on the substrate. The bacterium is clearly deformed. (D) Adverse effect on bacteria leading to reduced viability and adhesion strength. The SEM image shows a bacterium with adhesion weakened by the SURMOF 2 so that it detached during preparation for the SEM leaving behind a dark spot.[304]

To undergird the notion of a dying of the bacteria due to the copper ions released from the SURMOF, the viability of the bacteria on a MHDA SAM reference was compared to that on a Cu-SURMOF 2 substrate. Figure S18 A, B show the fluorescence microscopy images acquired after a 2 h incubation of the bacteria on these substrates. The images show a large number of damaged bacteria on the Cu-SURMOF 2 substrate. The ratio of damaged versus all bacteria was determined by evaluating the fluorescence signal in the microscopy images. A majority of the bacterial population was damaged on the Cu-SURMOF 2 (88 %). In contrast, the fraction of dead bacteria was only 0.9 % on the MHDA SAM. To further validate this finding microfluidic detachment assays were performed on Cu-SURMOF 2 (thickness ~ 120 nm and ~ 80 nm) and on HDT and MHDA SAMs as copper-free controls. Additionally, two types of surfaces with known low adhesion strength were included, polyethylene glycol (PEG)[302] and hyaluronic acid (HA).[244] Both surfaces were known for their protein and cell resistance, thus, providing suitable controls as typical inert surfaces. As shown in Figure S18 C, the shear stress needed to detach 50 % of the bacteria (τ_{50}) was significantly lower for both Cu-SURMOF 2 coatings of differing thicknesses compared to the HDT and MHDA SAM controls. Even though the trend was similar within the error bars, it seems the 120 nm thick Cu-SURMOF 2 reduced adhesion more effectively than the 80 nm thick sample. The shear stress required to detach the bacteria was also in the range of the PEG and HA controls demonstrating the low interaction between the bacteria and the SURMOF.

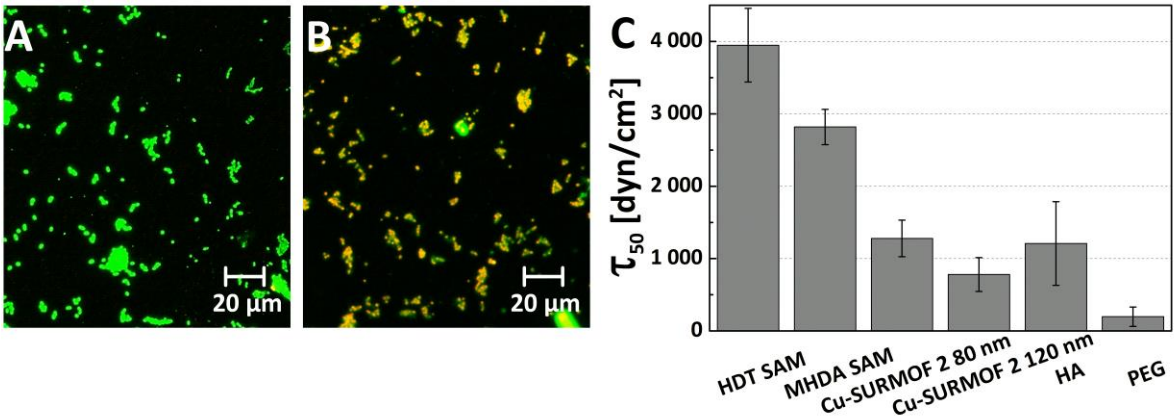

Figure S18: Viability and adhesion strength analysis of C. marina. Fluorescence microscopy images of adherent bacteria after BacLightTM bacterial viability staining on (A) MHDA SAM and (B) Cu-SURMOF 2 (15 layers). (C) Critical shear stress (τ_{50}) required to remove the bacteria from Cu-SURMOF 2 surfaces for different controls. Error bars indicate the standard error of the mean of six experiments in the case of Cu SURMOF 2 (10 layers) and HDT SAM, and four experiments for all other surfaces.[304]

7.4 BIBLIOGRAPHY

[1] G. Juliusson, P. Antunovic, A. Derolf, S. Lehmann, L. Mollgard, D. Stockelberg, U. Tidefelt, A. Wahlin, M. Hoglund, Age and acute myeloid leukemia: real world data on decision to treat and outcomes from the Swedish Acute Leukemia Registry, *Blood* **2009**, *113*, 4179-4187.

[2] A. van Rhenen, N. Feller, A. Kelder, A. H. Westra, E. Rombouts, S. Zweegman, M. A. van der Pol, Q. Waisfisz, G. J. Ossenkoppele, G. J. Schuurhuis, High stem cell frequency in acute myeloid leukemia at diagnosis predicts high minimal residual disease and poor survival, *Clinical Cancer Research* **2005**, *11*, 6520-6527.

[3] B. Löwenberg, J. D. Griffin, M. S. Tallman, Acute myeloid leukemia and acute promyelocytic leukemia, *Hematology American Society of Hematology Education Program* **2003**, 82-101.

[4] F. Ishikawa, S. Yoshida, Y. Saito, A. Hijikata, H. Kitamura, S. Tanaka, R. Nakamura, T. Tanaka, H. Tomiyama, N. Saito, M. Fukata, T. Miyamoto, B. Lyons, K. Ohshima, N. Uchida, S. Taniguchi, O. Ohara, K. Akashi, M. Harada, L. D. Shultz, Chemotherapy-resistant human AML stem cells home to and engraft within the bone-marrow endosteal region, *Nature Biotechnology* **2007**, *25*, 1315-1321.

[5] D. S. Krause, D. T. Scadden, F. I. Preffer, The hematopoietic stem cell niche--home for friend and foe?, *Cytometry Part B: Clinical Cytometry* **2013**, *84*, 7-20.

[6] L. Q. Jin, K. J. Hope, Q. L. Zhai, F. Smadja-Joffe, J. E. Dick, Targeting of CD44 eradicates human acute myeloid leukemic stem cells, *Nature Medicine* **2006**, *12*, 1167-1174.

[7] D. S. Krause, K. Lazarides, U. H. von Andrian, R. A. Van Etten, Requirement for CD44 in homing and engraftment of BCR-ABL-expressing leukemic stem cells, *Nature Medicine* **2006**, *12*, 1175-1180.

[8] T. Matsunaga, N. Takemoto, T. Sato, R. Takimoto, I. Tanaka, A. Fujimi, T. Akiyama, H. Kuroda, Y. Kawano, M. Kobune, J. Kato, Y. Hirayama, S. Sakamaki, K. Kohda, K. Miyake, Y. Niitsu, Interaction between leukemic-cell VLA-4 and stromal fibronectin is a decisive factor for minimal residual disease of acute myelogenous leukemia, *Nature Medicine* **2003**, *9*, 1158-1165.

[9] A. Avigdor, P. Goichberg, S. Shivtiel, A. Dar, A. Peled, S. Samira, O. Kollet, R. Hershkoviz, R. Alon, I. Hardan, H. Ben-Hur, D. Naor, A. Nagler, T. Lapidot, CD44 and hyaluronic acid cooperate with SDF-1 in the trafficking of human CD34(+) stem/progenitor cells to bone marrow, *Blood* **2004**, *103*, 2981-2989.

[10] C. Christophis, I. Taubert, G. Meseck, M. Schubert, M. Grunze, A. D. Ho, A. Rosenhahn, Shear stress regulates adhesion and rolling of CD44-expressing

leukemic and hematopoietic progenitor cells on hyaluronan, *Biophysical Journal* **2011**, *101*, 585-593.

[11] C. Christophis, M. Grunze, A. Rosenhahn, Quantification of the adhesion strength of fibroblast cells on ethylene glycol terminated self-assembled monolayers by a microfluidic shear force assay, *Physical Chemistry Chemical Physics* **2010**, *12*, 4498-4504.

[12] C. Christophis, Quantification of cell adhesion strength on artificial surfaces with a microfluidic shear force device., PhD Thesis, Ruperto Carola University Heidelberg (Heidelberg), **2011**.

[13] W. G. Wagner, C. Roderburg, F. Wein, A. Diehlmann, M. Frankhauser, R. Schubert, V. Eckstein, A. D. Ho, Molecular and secretory profiles of human mesenchymal stromal cells and their abilities to maintain primitive hematopoietic progenitors, *Stem Cells* **2007**, *25*, 2638-2647.

[14] S. Gottschling, R. Saffrich, A. Seckinger, U. Krause, K. Horsch, K. Miesala, A. D. Ho, Human mesenchymal stromal cells regulate initial self-renewing divisions of hematopoietic progenitor cells by a beta1-integrin-dependent mechanism, *Stem Cells* **2007**, *25*, 798-806.

[15] R. F. Wynn, C. A. Hart, C. Corradi-Perini, L. O'Neill, C. A. Evans, J. E. Wraith, L. J. Fairbairn, I. Bellantuono, A small proportion of mesenchymal stem cells strongly expresses functionally active CXCR4 receptor capable of promoting migration to bone marrow, *Blood* **2004**, *104*, 2643-2645.

[16] A. Aiuti, I. J. Webb, C. Bleul, T. Springer, J. C. Gutierrez-Ramos, The chemokine SDF-1 is a chemoattractant for human CD34+ hematopoietic progenitor cells and provides a new mechanism to explain the mobilization of CD34+ progenitors to peripheral blood, *The Journal of Experimental Medicine* **1997**, *185*, 111-120.

[17] G. Brooke, H. Tong, J. P. Levesque, K. Atkinson, Molecular trafficking mechanisms of multipotent mesenchymal stem cells derived from human bone marrow and placenta, *Stem Cells Dev* **2008**, *17*, 929-940.

[18] C. H. Kim, H. E. Broxmeyer, In vitro behavior of hematopoietic progenitor cells under the influence of chemoattractants: stromal cell-derived factor-1, steel factor, and the bone marrow environment, *Blood* **1998**, *91*, 100-110.

[19] M. Sharma, F. Afrin, N. Satija, R. P. Tripathi, G. U. Gangenahalli, Stromal-derived factor-1/CXCR4 signaling: indispensable role in homing and engraftment of hematopoietic stem cells in bone marrow, *Stem Cells and Development* **2011**, *20*, 933-946.

[20] J. Wang, P. Zhan, J. Ouyang, B. Chen, R. Zhou, Prophylactic use of granulocyte colony-stimulating factor after induction chemotherapy in patients with newly diagnosed acute myeloid leukemia may increase the complete remission rate: a

meta-analysis of five randomised controlled trials, *Clinical Lymphoma, Myeloma & Leukemia* **2009**, *50*, 457-459.

[21] E. Klyuchnikov, N. Kroger, Sensitising leukemic cells by targeting microenvironment, *Clinical Lymphoma, Myeloma & Leukemia* **2009**, *50*, 319-320.

[22] Y. Saito, N. Uchida, S. Tanaka, N. Suzuki, M. Tomizawa-Murasawa, A. Sone, Y. Najima, S. Takagi, Y. Aoki, A. Wake, S. Taniguchi, L. D. Shultz, F. Ishikawa, Induction of cell cycle entry eliminates human leukemia stem cells in a mouse model of AML, *Nature Biotechnology* **2010**, *28*, 275-280.

[23] E. Weisberg, A. K. Azab, P. W. Manley, A. L. Kung, A. L. Christie, R. Bronson, I. M. Ghobrial, J. D. Griffin, Inhibition of CXCR4 in CML cells disrupts their interaction with the bone marrow microenvironment and sensitizes them to nilotinib, *Leukemia* **2012**, *26*, 985-990.

[24] M. Kondo, A. J. Wagers, M. G. Manz, S. S. Prohaska, D. C. Scherer, G. F. Beilhack, J. A. Shizuru, I. L. Weissman, Biology of hematopoietic stem cells and progenitors: implications for clinical application, *Annual Review of Immunology* **2003**, *21*, 759-806.

[25] A. L. Lennard, G. H. Jackson, Science, medicine, and the future: Stem cell transplantation, *British Medical Journal* **2000**, *321*, 1331-1331.

[26] Y. Junying, A. Thomson, J. Domen, A. Wagners, I. L. Wieissman, D. M. Panchision, T. P. Zwaka, M. L. Rohrbaugh, C. A. Goldthwaite, J. F. Battey, L. K. Cole, Regenerative Medicine*, Vol.*, **2006**.

[27] W. Wagner, The Stromal Activity of Mesenchymal Stromal Cells, *Transfusion Medicine and Hemotherapy* **2008**, *35*, 185-193.

[28] C. C. Hofmeister, J. Zhang, K. L. Knight, P. Le, P. J. Stiff, Ex vivo expansion of umbilical cord blood stem cells for transplantation: growing knowledge from the hematopoietic niche, *Bone Marrow Transplant* **2007**, *39*, 11-23.

[29] H. Ema, H. Takano, K. Sudo, H. Nakauchi, In vitro self-renewal division of hematopoietic stem cells, *The Journal of Experimental Medicine* **2000**, *192*, 1281-1288.

[30] H. Glimm, C. J. Eaves, Direct evidence for multiple self-renewal divisions of human in vivo repopulating hematopoietic cells in short-term culture, *Blood* **1999**, *94*, 2161-2168.

[31] C. C. Fraser, C. J. Eaves, S. J. Szilvassy, R. K. Humphries, Expansion in vitro of retrovirally marked totipotent hematopoietic stem cells, *Blood* **1990**, *76*, 1071-1076.

[32] C. L. Miller, C. J. Eaves, Expansion in vitro of adult murine hematopoietic stem cells with transplantable lympho-myeloid reconstituting ability, *Proceedings of the*

National Academy of Sciences of the United States of America **1997**, *94*, 13648-13653.

[33] E. Conneally, J. Cashman, A. Petzer, C. Eaves, Expansion in vitro of transplantable human cord blood stem cells demonstrated using a quantitative assay of their lympho-myeloid repopulating activity in nonobese diabetic-scid/scid mice, *Proceedings of the National Academy of Sciences of the United States of America* **1997**, *94*, 9836-9841.

[34] M. Yagi, K. A. Ritchie, E. Sitnicka, C. Storey, G. J. Roth, S. Bartelmez, Sustained ex vivo expansion of hematopoietic stem cells mediated by thrombopoietin, *Proceedings of the National Academy of Sciences of the United States of America* **1999**, *96*, 8126-8131.

[35] M. E. Davis, Zeolite-based catalysts for chemicals synthesis, *Microporous and Mesoporous Materials* **1998**, *21*, 173-182.

[36] Y. Y. Li, F. Cunin, J. R. Link, T. Gao, R. E. Betts, S. H. Reiver, V. Chin, S. N. Bhatia, M. J. Sailor, Polymer Replicas of Photonic Porous Silicon for Sensing and Drug Delivery Applications, *Science* **2003**, *299*, 2045-2047.

[37] V. S.-Y. Lin, K. Motesharei, K.-P. S. Dancil, M. J. Sailor, M. R. Ghadiri, A Porous Silicon-Based Optical Interferometric Biosensor, *Science* **1997**, *278*, 840-843.

[38] A. Jane, R. Dronov, A. Hodges, N. H. Voelcker, Porous silicon biosensors on the advance, *Trends in Biotechnology* **2009**, *27*, 230-239.

[39] S. Kaskel, K. Schlichte, Porous Silicon Nitride as a Superbase Catalyst, *Journal of Catalysis* **2001**, *201*, 270-274.

[40] J. A. Lercher, R. A. van Santen, H. Vinek, Carbonium ion formation in zeolite catalysis, *Catalysis Letters* **1994**, *27*, 91-96.

[41] Y. Izumi, K. Urabe, Catalysis of heteropoly acids entrapped in activated carbon, *Chemistry Letters* **1981**, *10*, 663-666.

[42] A. Yamashita, Y. Mori, T. Oshima, Y. Baba, Preparation of activated carbon with high surface area using crab shell and shochu waste and the development of methane storage technology, *Carbon* **2014**, *76*, 469.

[43] S. L. James, Metal-organic frameworks, *Chemical Society Reviews* **2003**, *32*, 276-288.

[44] J. R. Long, O. M. Yaghi, The pervasive chemistry of metal-organic frameworks, *Chemical Society Reviews* **2009**, *38*, 1213-1214.

[45] A. M. Spokoyny, D. Kim, A. Sumrein, C. A. Mirkin, Infinite coordination polymer nano- and microparticle structures, *Chemical Society Reviews* **2009**, *38*, 1218-1227.

[46] L. Dean, *Blood groups and red cell antigens*, National Center for Biotechnology Information (US), Bethesda (MD), **2005**.

[47] E. Gunsilius, G. Gastl, A. L. Petzer, Hematopoietic stem cells, *Biomedicine & Pharmacotherapy* **2001**, *55*, 186-194.

[48] K. Ikuta, N. Uchida, J. Friedman, I. L. Weissman, Lymphocyte Developement from Stem-Cells, *Annual Review of Immunology* **1992**, *10*, 759-783.

[49] A. D. Ho, Kinetics and symmetry of divisions of hematopoietic stem cells, *Experimental Hematology* **2005**, *33*, 1-8.

[50] J. A. Knoblich, Asymmetric cell division during animal development, *Nature Reviews Molecular Cell Biology* **2001**, *2*, 11-20.

[51] T. Yin, L. Li, The stem cell niches in bone, *Journal of Clinical Investigation* **2006**, *116*, 1195-1201.

[52] S. H. Cheshier, S. J. Morrison, X. Liao, I. L. Weissman, In vivo proliferation and cell cycle kinetics of long-term self-renewing hematopoietic stem cells, *Proceedings of the National Academy of Sciences of the United States of America* **1999**, *96*, 3120-3125.

[53] H. R. Horvitz, I. Herskowitz, Mechanisms of asymmetric cell division: Two Bs or not two Bs, that is the question, *Cell* **1992**, *68*, 237-255.

[54] A. Atala, R. Lanza, *Handbook of Stem Cells*, Academic Press, Massachusettes, USA, **2012**.

[55] R. Schofield, The relationship between the spleen colony-forming cell and the haematopoietic stem cells., *Blood Cells* **1978**, *4*, 7-25.

[56] M. Punzel, D. Liu, T. Zhang, V. Eckstein, K. Miesala, A. D. Ho, The symmetry of initial divisions of human hematopoietic progenitors is altered only by the cellular microenvironment, *Experimental Hematology* **2003**, *31*, 339-347.

[57] T. Walenda, S. Bork, P. Horn, F. Wein, R. Saffrich, A. Diehlmann, V. Eckstein, A. D. Ho, W. Wagner, Co-culture with mesenchymal stromal cells increases proliferation and maintenance of haematopoietic progenitor cells, *Journal of Cellular and Molecular Medicine* **2010**, *14*, 337-350.

[58] S. Huang, P. Law, K. Francis, B. O. Palsson, A. D. Ho, Symmetry of initial cell divisions among primitive hematopoietic progenitors is independent of ontogenic age and regulatory molecules, *Blood* **1999**, *94*, 2595-2604.

[59] A. A. Maximow, Relation of blood cells to connecttive tissues and endothelium, *Physiological Reviews* **1924**, *4*, 533-563.

[60] J. W. Goodman, G. S. Hodgson, Evidence for stem cells in the peripheral blood of mice, *Blood* **1962**, *19*, 702-714.

[61] C. M. Richman, R. S. Weiner, R. A. Yankee, Increase in circulating stem cells following chemotherapy in man, *Blood* **1976**, *47*, 1031-1039.

[62] E. Lorenz, D. Uphoff, T. R. Reid, E. Shelton, Modification of irradiation injury in mice and guinea pigs by bone marrow injections, *Journal of the National Cancer Institute* **1951**, *12*, 197-201.

[63] M. B. Lawrence, T. A. Springer, Leukocytes roll on a selectin at physiologic flow rates: Distinction from and prerequisite for adhesion through integrins, *Cell* **1991**, *65*, 859-873.

[64] K. Ley, C. Laudanna, M. I. Cybulsky, S. Nourshargh, Getting to the site of inflammation: the leukocyte adhesion cascade updated, *Nature Reviews Immunology* **2007**, *7*, 678-689.

[65] T. A. Springer, Traffic signals for lymphocyte recirculation and leukocyte emigration: the multistep paradigm, *Cell* **1994**, *76*, 301-314.

[66] T. Yago, A. Leppanen, H. Y. Qiu, W. D. Marcus, M. U. Nollert, C. Zhu, R. D. Cummings, R. P. McEver, Distinct molecular and cellular contributions to stabilizing selectin-mediated rolling under flow, *Journal of Cell Biology* **2002**, *158*, 787-799.

[67] T. Yago, J. H. Wu, C. D. Wey, A. G. Klopocki, C. Zhu, R. P. McEver, Catch bonds govern adhesion through L-selectin at threshold shear, *Journal of Cell Biology* **2004**, *166*, 913-923.

[68] J. Barrett, in *Essential biology of stem cell transplantation* (Ed.: J. Treleaven), Elsevier Ltd., **2008**, p. 512.

[69] T. Sugiyama, H. Kohara, M. Noda, T. Nagasawa, Maintenance of the hematopoietic stem cell pool by CXCL12-CXCR4 chemokine signaling in bone marrow stromal cell niches, *Immunity* **2006**, *25*, 977-988.

[70] D. A. Sipkins, X. Wei, J. W. Wu, J. M. Runnels, D. Cote, T. K. Means, A. D. Luster, D. T. Scadden, C. P. Lin, In vivo imaging of specialized bone marrow endothelial microdomains for tumour engraftment, *Nature* **2005**, *435*, 969-973.

[71] W. Wagner, F. Wein, C. Roderburg, R. Saffrich, A. Faber, U. Krause, M. Schubert, V. Benes, V. Eckstein, H. Maul, A. D. Ho, Adhesion of Hematopoietic Progenitor Cells to Human Mesenchymal Stem Cells as a Model for Cell-Cell Interaction., *Experimental Hematology* **2007**, *35*, 314-325.

[72] Y. Muguruma, T. Yahata, H. Miyatake, T. Sato, T. Uno, J. Itoh, S. Kato, M. Ito, T. Hotta, K. Ando, Reconstitution of the functional human hematopoietic microenvironment derived from human mesenchymal stem cells in the murine bone marrow compartment, *Blood* **2006**, *107*, 1878-1887.

[73] D. Jing, A. V. Fonseca, N. Alakel, F. A. Fierro, K. Muller, M. Bornhauser, G. Ehninger, D. Corbeil, R. Ordemann, Hematopoietic stem cells in co-culture with mesenchymal stromal cells--modeling the niche compartments in vitro, *Haematologica* **2010**, *95*, 542-550.

[74] S. Mendez-Ferrer, T. V. Michurina, F. Ferraro, A. R. Mazloom, B. D. MacArthur, S. A. Lira, D. T. Scadden, A. Ma/'ayan, G. N. Enikolopov, P. S. Frenette, Mesenchymal and haematopoietic stem cells form a unique bone marrow niche, *Nature* **2010**, *466*, 829-834.

[75] A. Ehninger, A. Trumpp, The bone marrow stem cell niche grows up: mesenchymal stem cells and macrophages move in, *The Journal of Experimental Medicine* **2011**, *208*, 421-428.

[76] M. Dominici, K. Le Blanc, I. Mueller, I. Slaper-Cortenbach, F. Marini, D. Krause, R. Deans, A. Keating, D. Prockop, E. Horwitz, Minimal criteria for defining multipotent mesenchymal stromal cells. The International Society for Cellular Therapy position statement, *Cytotherapy* **2006**, *8*, 315-317.

[77] W. Wagner, F. Wein, A. Seckinger, M. Frankhauser, U. Wirkner, U. Krause, J. Blake, C. Schwager, V. Eckstein, W. Ansorge, A. D. Ho, Comparative characteristics of mesenchymal stem cells from human bone marrow, adipose tissue, and umbilical cord blood, *Experimental Hematology* **2005**, *33*, 1402-1416.

[78] K. A. Moore, I. R. Lemischka, Stem cells and their niches, *Science* **2006**, *311*, 1880-1885.

[79] T. Reya, S. J. Morrison, M. F. Clarke, I. L. Weissman, Stem cells, cancer, and cancer stem cells, *Nature* **2001**, *414*, 105-111.

[80] K. J. Hope, L. Jin, J. E. Dick, Human acute myeloid leukemia stem cells, *Archives of Medical Research* **2003**, *34*, 507-514.

[81] M. L. Guzman, C. T. Jordan, Considerations for targeting malignant stem cells in leukemia, *Cancer Control* **2004**, *11*, 97-104.

[82] D. T. Scadden, Cancer stem cells refined, *Nature Immunology* **2004**, *5*, 701-703.

[83] E. Passegue, C. H. Jamieson, L. E. Ailles, I. L. Weissman, Normal and leukemic hematopoiesis: are leukemias a stem cell disorder or a reacquisition of stem cell characteristics?, *Proceedings of the National Academy of Sciences of the United States of America* **2003**, *1*, 11842-11849.

[84] M. Al-Hajj, M. W. Becker, M. Wicha, I. Weissman, M. F. Clarke, Therapeutic implications of cancer stem cells, *Current Opinion in Genetics & Development* **2004**, *14*, 43-47.

[85] B. Löwenberg, J. R. Downing, A. Burnett, Acute Myeloid Leukemia, *New England Journal of Medicine* **1999**, *341*, 1051-1062.

[86] J. M. Bennett, D. Catovsky, M. T. Daniel, G. Flandrin, D. A. Galton, H. R. Gralnick, C. Sultan, Proposals for the classification of the myelodysplastic syndromes, *British Journal of Haematology* **1982**, *51*, 189-199.

[87] J. W. Vardiman, J. Thiele, D. A. Arber, R. D. Brunning, M. J. Borowitz, A. Porwit, N. L. Harris, M. M. Le Beau, E. Hellstrom-Lindberg, A. Tefferi, C. D. Bloomfield, The 2008 revision of the World Health Organization (WHO) classification of myeloid neoplasms and acute leukemia: rationale and important changes, *Blood* **2009**, *114*, 937-951.

[88] N. L. Harris, E. S. Jaffe, J. Diebold, G. Flandrin, H. K. Muller-Hermelink, J. Vardiman, T. A. Lister, C. D. Bloomfield, The World Health Organization classification of neoplastic diseases of the hematopoietic and lymphoid tissues. Report of the Clinical Advisory Committee meeting, Airlie House, Virginia, November, 1997, *Annals of Oncology* **1999**, *10*, 1419-1432.

[89] C. I. Civin, L. C. Strauss, C. Brovall, M. J. Fackler, J. F. Schwartz, J. H. Shaper, Antigenic analysis of hematopoiesis. III. A hematopoietic progenitor cell surface antigen defined by a monoclonal antibody raised against KG-1a cells, *The Journal of Immunology* **1984**, *133*, 157-165.

[90] F. E. Katz, R. Tindle, D. R. Sutherland, M. F. Greaves, Identification of a membrane glycoprotein associated with haemopoietic progenitor cells, *Leukemia Research* **1985**, *9*, 191-198.

[91] L. W. Terstappen, S. Huang, M. Safford, P. M. Lansdorp, M. R. Loken, Sequential generations of hematopoietic colonies derived from single nonlineage-committed CD34+CD38- progenitor cells, *Blood* **1991**, *77*, 1218-1227.

[92] I. L. Weissman, Translating Stem and Progenitor Cell Biology to the Clinic: Barriers and Opportunities, *Science* **2000**, *287*, 1442-1446.

[93] W. C. Liles, H. E. Broxmeyer, E. Rodger, B. Wood, K. Hubel, S. Cooper, G. Hangoc, G. J. Bridger, G. W. Henson, G. Calandra, D. C. Dale, Mobilization of hematopoietic progenitor cells in healthy volunteers by AMD3100, a CXCR4 antagonist, *Blood* **2003**, *102*, 2728-2730.

[94] H. E. Broxmeyer, C. M. Orschell, D. W. Clapp, G. Hangoc, S. Cooper, P. A. Plett, W. C. Liles, X. Li, B. Graham-Evans, T. B. Campbell, G. Calandra, G. Bridger, D. C. Dale, E. F. Srour, Rapid mobilization of murine and human hematopoietic stem and progenitor cells with AMD3100, a CXCR4 antagonist, *The Journal of Experimental Medicine* **2005**, *201*, 1307-1318.

[95] I. Pusic, J. F. DiPersio, Update on clinical experience with AMD3100, an SDF-1/CXCL12-CXCR4 inhibitor, in mobilization of hematopoietic stem and progenitor cells, *Currrent Opinion in Hematology* **2010**, *17*, 319-326.

[96] J. O. Trent, Z. X. Wang, J. L. Murray, W. Shao, H. Tamamura, N. Fujii, S. C. Peiper, Lipid bilayer simulations of CXCR4 with inverse agonists and weak partial agonists, *Journal of Biological Chemistry* **2003**, *278*, 47136-47144.

[97] W. B. Zhang, J. M. Navenot, B. Haribabu, H. Tamamura, K. Hiramatu, A. Omagari, G. Pei, J. P. Manfredi, N. Fujii, J. R. Broach, S. C. Peiper, A point mutation that confers constitutive activity to CXCR4 reveals that T140 is an inverse agonist and that AMD3100 and ALX40-4C are weak partial agonists, *Journal of Biological Chemistry* **2002**, *277*, 24515-24521.

[98] R. S. Y. Wong, V. Bodart, M. Metz, J. Labrecque, G. Bridger, S. P. Fricker, Comparison of the Potential Multiple Binding Modes of Bicyclam, Monocylam, and Noncyclam Small-Molecule CXC Chemokine Receptor 4 Inhibitors, *Molecular Pharmacology* **2008**, *74*, 1485-1495.

[99] T. Lapidot, A. Dar, O. Kollet, How do stem cells find their way home?, *Blood* **2005**, *106*, 1901-1910.

[100] J. P. Levesque, F. M. Helwani, I. G. Winkler, The endosteal /`osteoblastic/' niche and its role in hematopoietic stem cell homing and mobilization, *Leukemia* **2010**, *24*, 1979-1992.

[101] P. J. Quesenberry, G. Colvin, M. Abedi, Perspective: fundamental and clinical concepts on stem cell homing and engraftment: a journey to niches and beyond, *Experimental Hematology* **2005**, *33*, 9-19.

[102] S. Huang, D. E. Ingber, The structural and mechanical complexity of cell-growth control, *Nature Cell Biology* **1999**, *1*, E131-138.

[103] J. C. Adams, F. M. Watt, Regulation of development and differentiation by the extracellular matrix, *Development* **1993**, *117*, 1183-1198.

[104] D. A. Lauffenburger, A. F. Horwitz, Cell migration: a physically integrated molecular process, *Cell* **1996**, *84*, 359-369.

[105] B. M. Gumbiner, Cell Adhesion: The Molecular Basis of Tissue Architecture and Morphogenesis, *Cell* **1996**, *84*, 345-357.

[106] R. P. McEver, Adhesive interactions of leukocytes, platelets, and the vessel wall during hemostasis and inflammation, *Thrombosis and Haemostasis* **2001**, *86*, 746-756.

[107] B. Felding-Habermann, Integrin adhesion receptors in tumor metastasis, *Clinical and Experimental Metastasis* **2003**, *20*, 203-213.

[108] C. M. Verfaillie, J. B. McCarthy, P. B. McGlave, Mechanisms underlying abnormal trafficking of malignant progenitors in chronic myelogenous leukemia. Decreased adhesion to stroma and fibronectin but increased adhesion to the basement

membrane components laminin and collagen type IV, *Journal of Clinical Investigation* **1992**, *90*, 1232-1241.

[109] R. L. Juliano, Signal transduction by cell adhesion receptors and the cytoskeleton: Functions of integrins, cadherins, selectins, and immunoglobulin-superfamily members, *Annual Review of Pharmacology and Toxicology* **2002**, *42*, 283-323.

[110] A. E. Aplin, A. Howe, S. K. Alahari, R. L. Juliani, Signal transduction and signal modulation by cell adhesion receptors: The role of integrins, cadherins, immunoglobulin-cell adhesion molecules, and selectins, *Pharmacological Reviews* **1998**, *50*, 197-263.

[111] H. Du Trochet, *Recherches anatomiques et physiologiques sur la structure intime des animaux et des végétaux et sur leur motilité*, J.B. Baillière, Paris, **1824**.

[112] R. Wagner, *Erläuterungstafeln zur Physiologie und Entwicklungsgeschichte: mit vozüglicher Rücksicht auf seine Lehrbücher über Physiologie und vergleichende Anatomie*, Leipzig, **1839**.

[113] K. Ley, D. Vestweber, in *The selectins as rolling receptors (in "The selectins: initiators of leukocyte endothelial adhesion")*, Harwood Academic Publishers, London, **1997**.

[114] J. B. Freund, Leukocyte margination in a model microvessel, *Physics of Fluids* **2007**, *19*.

[115] S. M. Albelda, C. W. Smith, P. A. Ward, Adhesion Molecules and Inflammatory Injury, *Faseb Journal* **1994**, *8*, 504-512.

[116] E. B. Finger, K. D. Puri, R. Alon, M. B. Lawrence, U. H. von Andrian, T. A. Springer, Adhesion through L-selectin requires a threshold hydrodynamic shear, *Nature* **1996**, *379*, 266-269.

[117] M. B. Lawrence, G. S. Kansas, E. J. Kunkel, K. Ley, Threshold Levels of Fluid Shear Promote Leukocyte Adhesion through Selectins (CD62L,P,E), *Journal of Cell Biology* **1997**, *136*, 717-727.

[118] C. Zhu, T. Yago, J. Z. Lou, V. I. Zarnitsyna, R. P. McEver, Mechanisms for flow-enhanced cell adhesion, *Annals of Biomedical Engineering* **2008**, *36*, 604-621.

[119] H. C. DeGrendele, P. Estess, L. J. Picker, M. H. Siegelman, CD44 and its ligand hyaluronate mediate rolling under physiologic flow: A novel lymphocyte-endothelial cell primary adhesion pathway, *Journal of Experimental Medicine* **1996**, *183*, 1119-1130.

[120] K. Ley, D. C. Bullard, M. L. Arbones, R. Bosse, D. Vestweber, T. F. Tedder, A. L. Beaudet, Sequential contribution of L- and P-selectin to leukocyte rolling in vivo, *Journal of Experimental Medicine* **1995**, *181*, 669-675.

[121] K. Ley, P. Gaehtgens, Endothelial, not hemodynamic, differences are responsible for preferential leukocyte rolling in rat mesenteric venules, *Circulation Research* **1991**, *69*, 1034-1041.

[122] J. P. A. D. C. K. P. Gaboury, Molecular mechanisms involved in superoxide-induced leukocyte-endothelial cell interactions in vivo, *American Journal of Physiology - Heart and Circulatory Physiology* **1994**, *266*, H637-H642.

[123] R. Johnson, T. Mayadas, P. Frenette, R. Mebius, M. Subramaniam, A. Lacasce, R. Hynes, D. Wagner, Blood cell dynamics in P-selectin-deficient mice, **1995**, *86*, 1106-1114.

[124] H. N. Mayrovitz, *Leukocyte rolling: a prominent feature of venules in intact skin of anesthetized hairless mice*, **1992**.

[125] M. A. Perry, D. N. Granger, Role of CD11/CD18 in shear rate-dependent leukocyte-endothelial cell interactions in cat mesenteric venules, *Journal of Clinical Investigation* **1991**, *87*, 1798-1804.

[126] E. E. Schmidt, I. C. MacDonald, A. C. Groom, Interactions of leukocytes with vessel walls and with other blood cells, studied by high-resolution intravital videomicroscopy of spleen, *Microvascular Research* **1990**, *40*, 99-117.

[127] A. J. Day, G. D. Prestwich, Hyaluronan-binding proteins: tying up the giant, *Journal of Biological Chemistry* **2002**, *277*, 4585-4588.

[128] M. Morra, Engineering of biomaterials surfaces by hyaluronan, *Biomacromolecules* **2005**, *6*, 1205-1223.

[129] C. B. Underhill, B. P. Toole, Binding of Hyaluronate to the Surface of Cultured Cells, *Journal of Cell Biology* **1979**, *82*, 475-484.

[130] A. Aruffo, I. Stamenkovic, M. Melnick, C. B. Underhill, B. Seed, CD44 is the Principal Cell-Surface Receptor for Hyaluronate, *Cell* **1990**, *61*, 1303-1313.

[131] K. Miyake, P. W. Kincade, A new cell adhesion mechanism involving hyaluronate and CD44, *Current Topics in Microbiology and Immunology* **1990**, *166*, 87-90.

[132] K. Miyake, K. L. Medina, S. Hayashi, S. Ono, T. Hamaoka, P. W. Kincade, Monoclonal antibodies to Pgp-1/CD44 block lympho-hemopoiesis in long-term bone marrow cultures, *The Journal of Experimental Medicine* **1990**, *171*, 477-488.

[133] U. V. Goodison S., Tarin D., CD44 Cell Adhesion Molecules, *Journal of Clinical Pathology* **1999**, *52*, 189-196.

[134] S. Ishii, R. Ford, P. Thomas, A. Nachman, G. Steele, Jr., J. M. Jessup, CD44 participates in the adhesion of human colorectal carcinoma cells to laminin and type IV collagen, *Surgical Oncology* **1993**, *2*, 255-264.

[135] S. Jalkanen, M. Jalkanen, Lymphocyte CD44 binds the COOH-terminal heparin-binding domain of fibronectin, *The Journal of Cell Biology* **1992**, *116*, 817-825.

[136] G. F. Weber, S. Ashkar, M. J. Glimcher, H. Cantor, Receptor-ligand interaction between CD44 and osteopontin (Eta-1), *Science* **1996**, *271*, 509-512.

[137] A. Droll, S. T. Dougherty, R. K. Chiu, J. F. Dirks, W. H. McBride, D. L. Cooper, G. J. Dougherty, Adhesive interactions between alternatively spliced CD44 isoforms, *The Journal of Biological Chemistry* **1995**, *270*, 11567-11573.

[138] C. B. Knudson, W. Knudson, Hyaluronan-binding proteins in development, tissue homeostasis, and disease, *Faseb Journal* **1993**, *7*, 1233-1241.

[139] P. Ruiz, C. Schwarzler, U. Gunthert, CD44 isoforms during differentiation and development, *Bioessays* **1995**, *17*, 17-24.

[140] R. Goshen, I. Ariel, S. Shuster, A. Hochberg, I. Vlodavsky, N. de Groot, Z. Ben-Rafael, R. Stern, Hyaluronan, CD44 and its variant exons in human trophoblast invasion and placental angiogenesis, *Molecular Human Reproduction* **1996**, *2*, 685-691.

[141] U. Günthert, C. Schwarzler, B. Wittig, J. Laman, P. Ruiz, R. Stauder, A. Bloem, F. Smadja-Joffe, M. Zoller, A. Rolink, Functional involvement of CD44, a family of cell adhesion molecules, in immune responses, tumour progression and haematopoiesis, *Advances in Experimental Medicine and Biology* **1998**, *451*, 43-49.

[142] S. Ghaffari, F. Smadja-Joffe, R. Oostendorp, J. P. Levesque, G. Dougherty, A. Eaves, C. Eaves, CD44 isoforms in normal and leukemic hematopoiesis, *Experimental Hematology* **1999**, *27*, 978-993.

[143] E. Pure, C. A. Cuff, A crucial role for CD44 in inflammation, *Trends in Molecular Medicine* **2001**, *7*, 213-221.

[144] W. Holloway, A. R. Martinez, D. J. Oh, K. Francis, R. Ramakrishna, B. O. Palsson, Key adhesion molecules are present on long podia extended by hematopoietic cells, *Cytometry* **1999**, *37*, 171-177.

[145] S. Khaldoyanidi, A. Denzel, M. Zoller, Requirement for CD44 in proliferation and homing of hematopoietic precursor cells, *Journal of Leukocyte Biology* **1996**, *60*, 579-592.

[146] U. Günthert, M. Hofmann, W. Rudy, S. Reber, M. Zoller, I. Haussmann, S. Matzku, A. Wenzel, H. Ponta, P. Herrlich, A new variant of glycoprotein CD44 confers metastatic potential to rat carcinoma cells, *Cell* **1991**, *65*, 13-24.

[147] J. Lesley, R. Hyman, N. English, J. B. Catterall, G. A. Turner, CD44 in inflammation and metastasis, *Glycoconjugate Journal* **1997**, *14*, 611-622.

[148] G. R. Screaton, M. V. Bell, D. G. Jackson, F. B. Cornelis, U. Gerth, J. I. Bell, Genomic Structure of DNA Encoding the Lymphocyte Homing Receptor CD44 Reveals at least 12 Alternatively Spliced Exons, *Proceedings of the National Academy of Sciences of the United States of America* **1992**, *89*, 12160-12164.

[149] S. T. Jalkanen, R. F. Bargatze, L. R. Herron, E. C. Butcher, A lymphoid cell surface glycoprotein involved in endothelial cell recognition and lymphocyte homing in man, *European Journal of Immunology* **1986**, *16*, 1195-1202.

[150] M. B. Omary, I. S. Trowbridge, M. Letarte, M. F. Kagnoff, C. M. Isacke, Structural heterogeneity of human Pgp-1 and its relationship with p85, *Immunogenetics* **1988**, *27*, 460-464.

[151] G. S. Kansas, G. S. Wood, M. O. Dailey, A family of cell-surface glycoproteins defined by a putative anti-endothelial cell receptor antibody in man, *The Journal of Immunology* **1989**, *142*, 3050-3057.

[152] D. F. Zhou, J. F. Ding, L. J. Picker, R. F. Bargatze, E. C. Butcher, D. V. Goeddel, Molecular cloning and expression of Pgp-1. The mouse homolog of the human H-CAM (Hermes) lymphocyte homing receptor, *The Journal of Immunology* **1989**, *143*, 3390-3395.

[153] E. J. Quackenbush, S. Vera, A. Greaves, M. Letarte, Confirmation by peptide sequence and co-expression on various cell types of the identity of CD44 and P85 glycoprotein, *Molecular Immunology* **1990**, *27*, 947-955.

[154] R. L. Camp, T. A. Kraus, E. Pure, Variations in the cytoskeletal interaction and posttranslational modification of the CD44 homing receptor in macrophages, *The Journal of Cell Biology* **1991**, *115*, 1283-1292.

[155] V. B. Lokeshwar, L. Y. Bourguignon, Post-translational protein modification and expression of ankyrin-binding site(s) in GP85 (Pgp-1/CD44) and its biosynthetic precursors during T-lymphoma membrane biosynthesis, *The Journal of Biological Chemistry* **1991**, *266*, 17983-17989.

[156] D. G. Jackson, J. Buckley, J. I. Bell, Multiple variants of the human lymphocyte homing receptor CD44 generated by insertions at a single site in the extracellular domain, *The Journal of Biological Chemistry* **1992**, *267*, 4732-4739.

[157] G. R. Screaton, M. V. Bell, J. I. Bell, D. G. Jackson, The identification of a new alternative exon with highly restricted tissue expression in transcripts encoding the mouse Pgp-1 (CD44) homing receptor. Comparison of all 10 variable exons between mouse, human, and rat, *The Journal of Biological Chemistry* **1993**, *268*, 12235-12238.

[158] C. Tölg, M. Hofmann, P. Herrlich, H. Ponta, Splicing choice from ten variant exons establishes CD44 variability, *Nucleic Acids Research* **1993**, *21*, 1225-1229.

[159] K. L. Bennett, B. Modrell, B. Greenfield, A. Bartolazzi, I. Stamenkovic, R. Peach, D. G. Jackson, F. Spring, A. Aruffo, Regulation of CD44 binding to hyaluronan by glycosylation of variably spliced exons, *The Journal of Cell Biology* **1995**, *131*, 1623-1633.

[160] J. Bajorath, B. Greenfield, S. B. Munro, A. J. Day, A. Aruffo, Identification of CD44 residues important for hyaluronan binding and delineation of the binding site, *Journal of Biological Chemistry* **1998**, *273*, 338-343.

[161] S. Banerji, A. J. Day, J. D. Kahmann, D. G. Jackson, Characterization of a Functional Hyaluronan-Binding Domain from the Human CD44 Molecule Expressed inEscherichia coli, *Protein Expression and Purification* **1998**, *14*, 371-381.

[162] P. Teriete, S. Banerji, M. Noble, C. D. Blundell, A. J. Wright, A. R. Pickford, E. Lowe, D. J. Mahoney, M. I. Tammi, J. D. Kahmann, I. D. Campbell, A. J. Day, D. G. Jackson, Structure of the regulatory hyaluronan binding domain in the inflammatory leukocyte homing receptor CD44, *Molecular Cell* **2004**, *13*, 483-496.

[163] S. Banerji, A. J. Wright, M. Noble, D. J. Mahoney, I. D. Campbell, A. J. Day, D. G. Jackson, Structures of the CD44-hyaluronan complex provide insight into a fundamental carbohydrate-protein interaction, *Nature Structural & Molecular Biology* **2007**, *14*, 234-239.

[164] S. Ogino, N. Nishida, R. Umemoto, M. Suzuki, M. Takeda, H. Terasawa, J. Kitayama, M. Matsumoto, H. Hayasaka, M. Miyasaka, I. Shimada, Two-State Conformations in the Hyaluronan-Binding Domain Regulate CD44 Adhesiveness under Flow Condition, *Structure* **2010**, *18*, 649-656.

[165] D. Naor, R. V. Sionov, D. Ish-Shalom, CD44: structure, function, and association with the malignant process, *Advances in cancer research* **1997**, *71*, 241-319.

[166] S. Katoh, Z. Zheng, K. Oritani, T. Shimozato, P. W. Kincade, Glycosylation of CD44 negatively regulates its recognition of hyaluronan, *The Journal of Experimental Medicine* **1995**, *182*, 419-429.

[167] J. Lesley, N. English, A. Perschl, J. Gregoroff, R. Hyman, Variant cell lines selected for alterations in the function of the hyaluronan receptor CD44 show differences in glycosylation, *The Journal of Experimental Medicine* **1995**, *182*, 431-437.

[168] I. Trowbridge, J. Lesley, R. Schulte, R. Hyman, J. Trotter, Biochemical characterization and cellular distribution of a polymorphic, murine cell-surface glycoprotein expressed on lymphoid tissues, *Immunogenetics* **1982**, *15*, 299-312.

[169] J. Lesley, R. Schulte, R. Hyman, Binding of Hyaluronic-Acid to Lymphoid-Cell Lines is Inibited by Monoclonal-Antibodies against PGP-1, *Experimental Cell Research* **1990**, *187*, 224-233.

[170] K. Miyake, C. B. Underhill, J. Lesley, P. W. Kincade, Hyaluronate can function as a cell adhesion molecule and CD44 participates in hyaluronate recognition, *Journal of Experimental Medicine* **1990**, *172*, 69-75.

[171] J. Lesley, Q. He, K. Miyake, A. Hamann, R. Hyman, P. W. Kincade, Requirements for hyaluronic acid binding by CD44: a role for the cytoplasmic domain and activation by antibody, *The Journal of Experimental Medicine* **1992**, *175*, 257-266.

[172] O. Thoumine, J. J. Meister, Dynamics of adhesive rupture between fibroblasts and fibronectin: microplate manipulations and deterministic model, *European Biophysics Journal* **2000**, *29*, 409-419.

[173] O. Thoumine, P. Kocian, A. Kottelat, J. J. Meister, Short-term binding of fibroblasts to fibronectin: optical tweezers experiments and probabilistic analysis, *European Biophysics Journal* **2000**, *29*, 398-408.

[174] N. Walter, C. Selhuber, H. Kessler, J. P. Spatz, Cellular unbinding forces of initial adhesion processes on nanopatterned surfaces probed with magnetic tweezers, *Nano Letters* **2006**, *6*, 398-402.

[175] K. L. Sung, M. K. Kwan, F. Maldonado, W. H. Akeson, Adhesion strength of human ligament fibroblasts, *Journal of Biomechanical Engineering* **1994**, *116*, 237-242.

[176] K. V. Christ, K. T. Turner, Methods to Measure the Strength of Cell Adhesion to Substrates, *Journal of Adhesion Science and Technology* **2010**, *24*, 2027-2058.

[177] H. Schlichting, K. Gersten, *Grenzschicht-Theorie*, Springer, **2006**.

[178] T. A. Horbett, J. J. Waldburger, B. D. Ratner, A. S. Hoffman, Cell adhesion to a series of hydrophilic-hydrophobic copolymers studied with a spinning disc apparatus, *Journal of Biomedical Materials Research* **1988**, *22*, 383-404.

[179] A. J. Garcia, P. Ducheyne, D. Boettiger, Quantification of cell adhesion using a spinning disc device and application to surface-reactive materials, *Biomaterials* **1997**, *18*, 1091-1098.

[180] A. S. Goldstein, P. A. Dimilla, Application of fluid mechanic and kinetic models to characterize mammalian cell detachment in a radial-flow chamber, *Biotechnology and Bioengineering* **1997**, *55*, 616-629.

[181] A. S. Goldstein, P. A. DiMilla, Comparison of converging and diverging radial flow for measuring cell adhesion, *AIChE Journal* **1998**, *44*, 465-473.

[182] J. P. Bearinger, D. G. Castner, S. L. Golledge, A. Rezania, S. Hubchak, K. E. Healy, P(AAm-co-EG) Interpenetrating Polymer Networks Grafted to Oxide Surfaces: Surface Characterization, Protein Adsorption, and Cell Detachment Studies, *Langmuir* **1997**, *13*, 5175-5183.

[183] G. A. Truskey, J. S. Pirone, The effect of fluid shear-stress upon cell-adhesion to fibronectin-treated surfaces, *Journal of Biomedical Materials Research* **1990**, *24*, 1333-1353.

[184] T. G. van Kooten, J. M. Schakenraad, H. C. Van der Mei, H. J. Busscher, Development and use of a parallel-plate flow chamber for studying cellular adhesion to solid surfaces, *Journal of Biomedical Materials Research Part B: Applied Biomaterials* **1992**, *26*, 725-738.

[185] W. M. Deen, *Analysis of Transport Phenomena*, OUP USA, **1998**.

[186] R. K. Shah, A. L. London, *Laminar flow forced convection in ducts*, Academic Press, New York, **1978**.

[187] E. W. K. Young, A. R. Wheeler, C. A. Simmons, Matrix-dependent adhesion of vascular and valvular endothelial cells in microfluidic channels, *Lab on a Chip* **2007**, *7*, 1759-1766.

[188] E. W. K. Young, M. W. L. Watson, S. Srigunapalan, A. R. Wheeler, C. A. Simmons, Technique for Real-Time Measurements of Endothelial Permeability in a Microfluidic Membrane Chip Using Laser-Induced Fluorescence Detection, *Analytical Chemistry* **2010**, *82*, 808-816.

[189] K. S. W. Sing, D. H. Everett, R. A. W. Haul, L. Moscou, R. A. Pierotti, J. Rouquerol, T. Siemieniewska, Reporting physisorption data for gas/solid systems with special reference to the determination of surface area and porosity (Recommendations 1984), *Pure and Applied Chemistry* **1985**, *57*, 603-619.

[190] H. Deng, S. Grunder, K. E. Cordova, C. Valente, H. Furukawa, M. Hmadeh, F. Gándara, A. C. Whalley, Z. Liu, S. Asahina, H. Kazumori, M. O’Keeffe, O. Terasaki, J. F. Stoddart, O. M. Yaghi, Large-Pore Apertures in a Series of Metal-Organic Frameworks, *Science* **2012**, *336*, 1018-1023.

[191] O. Shekhah, J. Liu, R. A. Fischer, C. Woell, MOF thin films: existing and future applications, *Chemical Society Reviews* **2011**, *40*, 1081-1106.

[192] D. Zacher, R. Schmid, C. Wöll, R. A. Fischer, Surface Chemistry of Metal-Organic Frameworks at the Liquid-Solid Interface, *Angewandte Chemie-International Edition* **2011**, *50*, 176-199.

[193] M. Eddaoudi, J. Kim, N. Rosi, D. Vodak, J. Wachter, M. O'Keeffe, O. M. Yaghi, Systematic design of pore size and functionality in isoreticular MOFs and their application in methane storage, *Science* **2002**, *295*, 469-472.

[194] J. L. C. Rowsell, O. M. Yaghi, Metal-organic frameworks: a new class of porous materials, *Microporous and Mesoporous Materials* **2004**, *73*, 3-14.

[195] S. Hermes, F. Schroder, S. Amirjalayer, R. Schmid, R. A. Fischer, Loading of porous metal-organic open frameworks with organometallic CVD precursors: inclusion

compounds of the type [LnM]a@MOF-5, *Journal of Materials Chemistry* **2006**, *16*, 2464-2472.

[196] G. Ferey, Hybrid porous solids: past, present, future, *Chemical Society Reviews* **2008**, *37*, 191-214.

[197] C. Serre, F. Millange, S. Surble, G. Ferey, A route to the synthesis of trivalent transition-metal porous carboxylates with trimeric secondary building units, *Angewandte Chemie-International Edition* **2004**, *43*, 6286-6289.

[198] P. Horcajada, C. Serre, G. Maurin, N. A. Ramsahye, F. Balas, M. Vallet-Regi, M. Sebban, F. Taulelle, G. Ferey, Flexible porous metal-organic frameworks for a controlled drug delivery, *Journal of the American Chemical Society* **2008**, *130*, 6774-6780.

[199] Y. K. Park, S. B. Choi, H. Kim, K. Kim, B. H. Won, K. Choi, J. S. Choi, W. S. Ahn, N. Won, S. Kim, D. H. Jung, S. H. Choi, G. H. Kim, S. S. Cha, Y. H. Jhon, J. K. Yang, J. Kim, Crystal structure and guest uptake of a mesoporous metal-organic framework containing cages of 3.9 and 4.7 nm in diameter, *Angewandte Chemie-International Edition* **2007**, *46*, 8230-8233.

[200] R. A. Fischer, C. Wöll, Schicht-für-Schicht-Flüssigphasenepitaxie von kristallinen Koordinationspolymeren an Oberflächen, *Angewandte Chemie* **2009**, *121*, 6321 - 6324.

[201] S. Hermes, F. Schröder, R. Chelmowski, C. Woll, R. A. Fischer, Selective nucleation and growth of metal-organic open framework thin films on patterned COOH/CF3-terminated self-assembled monolayers on Au(111), *Journal of the American Chemical Society* **2005**, *127*, 13744-13745.

[202] S. Hermes, D. Zacher, A. Baunemann, C. Wöll, R. A. Fischer, Selective growth and MOCVD loading of small single crystals of MOF-5 at alumina and silica surfaces modified with organic self-assembled monolayers, *Chemistry of Materials* **2007**, *19*, 2168-2173.

[203] S. Hermes, M. K. Schroter, R. Schmid, L. Khodeir, M. Muhler, A. Tissler, R. W. Fischer, R. A. Fischer, Metal@MOF: loading of highly porous coordination polymers host lattices by metal organic chemical vapor deposition, *Angewandte Chemie International Edition* **2005**, *44*, 6237-6241.

[204] D. Zacher, O. Shekhah, C. Wöll, R. A. Fischer, Thin films of metal-organic frameworks, *Chemical Society Reviews* **2009**, *38*, 1418-1429.

[205] S. Kitagawa, R. Matsuda, Chemistry of coordination space of porous coordination polymers, *Coordination Chemistry Reviews* **2007**, *251*, 2490-2509.

[206] O. Shekhah, Layer-by-Layer Method for the Synthesis and Growth of Surface Mounted Metal-Organic Frameworks (SURMOFs), *Materials* **2010**, *3*, 1302-1315.

[207] O. Shekhah, H. Wang, S. Kowarik, F. Schreiber, M. Paulus, M. Tolan, C. Sternemann, F. Evers, D. Zacher, R. A. Fischer, C. Wöll, Step-by-step route for the synthesis of metal-organic frameworks, *Journal of the American Chemical Society* **2007**, *129*, 15118-+.

[208] H. K. Arslan, O. Shekhah, J. Wohlgemuth, M. Franzreb, R. A. Fischer, C. Wöll, High-Throughput Fabrication of Uniform and Homogenous MOF Coatings, *Advanced Functional Materials* **2011**, *21*, 4228-4231.

[209] H. K. Arslan, O. Shekhah, D. C. F. Wieland, M. Paulus, C. Sternemann, M. A. Schroer, S. Tiemeyer, M. Tolan, R. A. Fischer, C. Wöll, Intercalation in Layered Metal–Organic Frameworks: Reversible Inclusion of an Extended π-System, *Journal of the American Chemical Society* **2011**, *133*, 8158-8161.

[210] O. Shekhah, H. Wang, D. Zacher, R. A. Fischer, W. C., Wachstumsmechanismen Metall-organischer Gerüststrukturen: Einblicke in die Keimbildung anhand einer schrittweisen Methodik, *Angewandte Chemie* **2009**, *121*, 5138 -5142.

[211] T. Young, An Essay on the Cohesion of Fluids., *Philosophical Transactions of the Royal Society of London* **1805**, *95*, 65-87.

[212] R. N. Wenzel, Resistance of Solid Surfaces to Wetting by Water, *Industrial & Engineering Chemistry* **1936**, *28*, 988-994.

[213] A. B. D. Cassie, S. Baxter, Wettability of porous surfaces, *Transactions of the Faraday Society* **1944**, *40*, 546-551.

[214] H. Fujiwara, *Spectroscopic Ellipsometry - Principles and Applications*, John Wiley & Sons Ltd., Chichester, U.K., **2007**.

[215] H. G. Tomkins, E. A. Irene, *Handbook of Ellipsometry*, William Andrew Publishing, Norwich, NY, USA, **2005**.

[216] H. G. Tompkins, *A User´s Guide to Ellipsometry*, Academic Press Inc., SanDiego, CA, **2006**.

[217] J. N. Hilfiker, N. Singh, T. Tiwald, D. Convey, S. M. Smith, J. H. Baker, H. G. Tompkins, Survey of methods to characterize thin absorbing films with Spectroscopic Ellipsometry, *Thin Solid Films* **2008**, *516*, 7979-7989.

[218] S. Bauer, Inerte Oberflächen auf der Basis von immobilisierten Polysacchariden, Diploma Thesis, Ruperto Carola University Heidelberg (Heidelberg), **2011**.

[219] http://www.jawoollam.com/tutorial_1.html, retrieved: **9.1.2011**

[220] K. L. Prime, G. M. Whitesides, Self-assembled organic monolayers - model systems for studying adsorption of proteins at surfaces, *Science* **1991**, *252*, 1164-1167.

[221] S. Fruehauf, J. Toplay, A. Wilmes, A. D. Ho, *Durchflusszytometrische Diagnostik maligner hämatologischer Erkrankungen*, Ecomed Verlag.

[222] M. Ardenne, Das Elektronen-Rastermikroskop, *Zeitschrift für Physik* **1938**, *109*, 553-572.

[223] P. J. Goodhew, J. H. Beanland, R. Beanland, *Electron Microscopy and Anylysis*, Taylor & Francis, London, **2001**.

[224] E. Abbe, VII.—On the Estimation of Aperture in the Microscope, *Journal of the Royal Microscopical Society* **1881**, *1*, 388-423.

[225] L.-V. de Broglie, Recherches sur la theorie des quanta, Translation: A.F. Kracklauer, *Annales de Physique* **1925**, *10 t. III*.

[226] B. D. Ratner, D. G. Castner, in *Electron Spectroscopy for chemical analysis* (Ed.: J. C. Vickerman), John Wiley & Sons, Chichester, UK, **2011**.

[227] A. Beer, Bestimmung der Absorption des rothen Lichts in farbigen Flüssigkeiten, *Annalen der Physik und Chemie* **1852**, *86*, 78-88.

[228] M. P. Seah, W. A. Dench, Quantitative electron spectroscopy of surfaces: A standard data base for electron inelastic mean free paths in solids, *Surface and Interface Analysis* **1979**, *1*, 2-11.

[229] D. A. Shirley, High-Resolution X-Ray Photoemission Spectrum of the Valence Bands of Gold, *Physical Review B* **1972**, *5*, 4709-4714.

[230] W. L. Bragg, The Diffraction of Short Electromagnetic Waves by a Crystal, *Proceedings of the Cambridge Philosophical Society* **1913**, *17*, 43-57.

[231] E. J. Mittemeijer, U. Welzel, The "state of the art" of the diffraction analysis of crystallite size and lattice strain*, Vol. 223*, **2008**, p. 552.

[232] J. Nölte, *ICP OES Emmisionsspektroskopie für Praktiker*, WILEY-VCH Verlag GmBH, Weinheim, **2002**.

[233] J. R. E. Fraser, T. C. Laurent, U. B. G. Laurent, Hyaluronan: Its nature, distribution, functions and turnover, *Journal of Internal Medicine* **1997**, *242*, 27-33.

[234] M. Mason, K. P. Vercruysse, K. R. Kirker, R. Frisch, D. M. Marecak, G. D. Prestwich, W. G. Pitt, Attachment of hyaluronic acid to polypropylene, polystyrene, and polytetrafluoroethylene, *Biomaterials* **2000**, *21*, 31-36.

[235] K. Meyer, J. W. Palmer, The polysaccharide of the vitreous humor, *Journal of Biological Chemistry* **1934**, *107*, 629-634.

[236] B. M. Weissman, K., The structure of hyalobiuronic acid and of hyaluronic acid from umbicial cord, *Journal of the American Chemical Society* **1954**, *76*, 1753-1757.

[237] R. K. Reed, K. Lilja, T. C. Laurent, Hyaluronan in the rat with special reference to the skin, *Acta Physiologica Scandinavica* **1988**, *134*, 405-411.

[238] C. Schiraldi, D. Cimini, M. De Rosa, Production of chondroitin sulfate and chondroitin, *Applied Microbiology and Biotechnology* **2010**, *87*, 1209-1220.

[239] K. L. Shephard, Functions for Fish Muncus, *Reviews in Fish Biology and Fisheries* **1994**, *4*, 401-429.

[240] A. Albersdorfer, E. Sackmann, Swelling behavior and viscoelasticity ultrathin grafted hyaluronic acid films, *European Physical Journal B* **1999**, *10*, 663-672.

[241] R. A. Stile, T. A. Barber, D. G. Castner, K. E. Healy, Sequential robust design methodology and X-ray photoelectron spectroscopy to analyze the grafting of hyaluronic acid to glass substrates, *Journal of Biomedical Materials Research* **2002**, *61*, 391-398.

[242] Z. Grabarek, J. Gergely, Zero-length crosslinking procedure with the use of active esters, *Analytical Biochemistry* **1990**, *185*, 131-135.

[243] X. Y. Cao, M. E. Pettit, S. L. Conlan, W. Wagner, A. D. Ho, A. S. Clare, J. A. Callow, M. E. Callow, M. Grunze, A. Rosenhahn, Resistance of Polysaccharide Coatings to Proteins, Hematopoietic Cells, and Marine Organisms, *Biomacromolecules* **2009**, *10*, 907-915.

[244] S. Bauer, M. P. Arpa-Sancet, J. A. Finlay, M. E. Callow, J. A. Callow, A. Rosenhahn, Adhesion of Marine Fouling Organisms on Hydrophilic and Amphiphilic Polysaccharides, *Langmuir* **2013**.

[245] G. Albert, Herstellung Und Charakterisierung Polykristalliner Goldschichten Zur Verwendung in Der Nanolithographie, Master Thesis, University of Heidelberg (Heidelberg), **1996**.

[246] A. Ulman, Formation and Structure of Self-Assembled Monolayers, *Chemical Reviews* **1996**, *96*, 1533-1554.

[247] J. C. Love, L. A. Estroff, J. K. Kriebel, R. G. Nuzzo, G. M. Whitesides, Self-assembled monolayers of thiolates on metals as a form of nanotechnology, *Chemical Reviews* **2005**, *105*, 1103-1169.

[248] C. D. Bain, G. M. Whitesides, Modelling organic-surfaces with self-assembled monolayers, *Angewandte Chemie-International Edition in English* **1989**, *28*, 506-512.

[249] R. Nuzzo, B. Zegarski, L. Dubois, Fundamental studies of the chemisorption of organosulfur compounds on gold(111). Implications for molecular self-assembly on gold surfaces, *Journal of the American Chemical Society* **1987**, *109*, 733-740.

[250] M. Jaschke, H. Schönherr, H. Wolf, H. J. Butt, E. Bamberg, M. K. Besocke, H. Ringsdorf, Structure of Alkyl and Perfluoroalkyl Disulfide and Azobenzenethiol Monolayers on Gold(111) Revealed by Atomic Force Microscopy, *The Journal of Physical Chemistry* **1996**, *100*, 2290-2301.

[251] L. H. Dubois, R. G. Nuzzo, Synthesis, Structure, and Properties of Model Organic Surfaces, *Annual Review of Physical Chemistry* **1992**, *43*, 437-463.

[252] G. Hähner, M. Kinzler, C. Thümmler, C. Wöll, M. Grunze, Structure of self-organizing organic films: A near edge x-ray absorption fine structure investigation of thiol layers adsorbed on gold, *Journal of Vacuum Science & Technology A* **1992**, *10*, 2758-2763.

[253] R. Arnold, W. Azzam, A. Terfort, C. Wöll, Preparation, Modification, and Crystallinity of Aliphatic and Aromatic Carboxylic Acid Terminated Self-Assembled Monolayers, *Langmuir* **2002**, *18*, 3980-3992.

[254] Y. Xia, G. M. Whitesides, Soft Lithography, *Annual Review of Materials Science* **1998**, *28*, 153-184.

[255] P. Horcajada, T. Chalati, C. Serre, B. Gillet, C. Sebrie, T. Baati, J. F. Eubank, D. Heurtaux, P. Clayette, C. Kreuz, J. S. Chang, Y. K. Hwang, V. Marsaud, P. N. Bories, L. Cynober, S. Gil, G. Ferey, P. Couvreur, R. Gref, Porous metal-organic-framework nanoscale carriers as a potential platform for drug delivery and imaging, *Nature Materials* **2010**, *9*, 172-178.

[256] J. Y. An, S. J. Geib, N. L. Rosi, Cation-Triggered Drug Release from a Porous Zinc-Adeninate Metal-Organic Framework, *Journal of the American Chemical Society* **2009**, *131*, 8376-+.

[257] C. Munuera, O. Shekhah, H. Wang, C. Woll, C. Ocal, The controlled growth of oriented metal-organic frameworks on functionalized surfaces as followed by scanning force microscopy, *Physical Chemistry Chemical Physics* **2008**, *10*, 7257-7261.

[258] R. B. H. P. Koeffler, A. J. Lusis, R. Sparkes and D. W. Golde, An Undifferentiated Variant Derived from the Human Acute Myelogenous Leukemia Cell Line (Kg-1). *Blood* **1980**, *56*, 265-273.

[259] H. P. Koeffler, Induction of Differentiation of Human Acute Myelogenous Leukemia Cells: Therapeutic Implications., *Blood* **1983**, *62*, 709-721.

[260] A. Weiss, R. L. Wiskocil, J. D. Stobo, The role of T3 surface molecules in the activation of human T cells: a two-stimulus requirement for IL 2 production reflects events occurring at a pre-translational level, *The Journal of Immunology* **1984**, *133*, 123-128.

[261] H. Asou, S. Tashiro, K. Hamamoto, A. Otsuji, K. Kita, N. Kamada, Establishment of a human acute myeloid leukemia cell line (Kasumi-1) with 8;21 chromosome translocation, *Blood* **1991**, *77*, 2031-2036.

[262] J. B. R. Franza, K. Maruyama, J. I. Garrels and H. E. Ruley, In Vitro Establishment Is Not a Sufficient Prerequisite for Transformation by Activated Ras Oncogenes., *Cell* **1986**, *44*, 409-418.

[263] P. Gassmann, J. Haier, K. Schlueter, B. Domikowsky, C. Wendel, U. Wiesner, R. Kubitza, R. Engers, S. W. Schneider, B. Homey, A. Mueller, CXCR4 Regulates the Early Extravasation of Metastatic Tumor Cells In Vivo, *Neoplasia* **2009**, *11*, 651-U652.

[264] W. Wagner, F. Wein, C. Roderburg, R. Saffrich, A. Diehlmann, V. Eckstein, A. D. Ho, Adhesion of human hematopoietic progenitor cells to mesenchymal stromal cells involves CD44, *Cells Tissues Organs* **2008**, *188*, 160-169.

[265] I. Taubert, Einfluss der CD44-Standardisoform und der CD44-varianten Isoformen auf den Erhalt des hämatopoetischen und leukämischen Stammzellpotenzials, PhD Thesis, Ruperto Carola University Heidelberg (Heidelberg), **2011**.

[266] M. Hanke, I. Hoffmann, C. Christophis, M. Schubert, V. T. Hoang, A. Zepeda-Moreno, N. Baran, V. Eckstein, P. Wuchter, A. Rosenhahn, A. D. Ho, Differences between healthy hematopoietic progenitors and leukemia cells with respect to CD44 mediated rolling versus adherence behavior on hyaluronic acid coated surfaces, *Biomaterials* **2014**, *35*, 1411-1419.

[267] V. C. Hirschfeld-Warneken, Induction of Cell Polarization and Directed Migration by Nanoscale Gradients of Adhesive Ligands, PhD Thesis, Ruperto Carola University Heidelberg (Heidelberg), **2009**.

[268] M. P. Arpa Sancet, Influence of surface properties on adhesion of Cobetia marina and accumulation of marine microfoulers in the ocean, PhD Thesis, Ruperto Carola University Heidelberg (Heidelberg), **2013**.

[269] M. Alles, Mikrofluidische Adhäsionsstärkemessungen der Diatomee *Navicula perminuta*, PhD Thesis, Ruperto Carola University Heidelberg (Heidelberg), **2014**.

[270] J. E. Silbert, G. Sugumaran, Biosynthesis of chondroitin/dermatan sulfate, *Iubmb Life* **2002**, *54*, 177-186.

[271] S. J. Wang, V. B. Wreesmann, L. Y. Bourguignon, Association of CD44 V3-containing isoforms with tumor cell growth, migration, matrix metalloproteinase expression, and lymph node metastasis in head and neck cancer, *Head Neck* **2007**, *29*, 550-558.

[272] V. Orian-Rousseau, L. Chen, J. P. Sleeman, P. Herrlich, H. Ponta, CD44 is required for two consecutive steps in HGF/c-Met signaling, *Genes & Development* **2002**, *16*, 3074-3086.

[273] M. H. Siegelman, H. C. DeGrendele, P. Estess, Activation and interaction of CD44 and hyaluronan in immunological systems, *Journal of Leukocyte Biology* **1999**, *66*, 315-321.

[274] M. Milinkovic, J. H. Antin, C. A. Hergrueter, C. B. Underhill, R. Sackstein, CD44-hyaluronic acid interactions mediate shear-resistant binding of lymphocytes to dermal endothelium in acute cutaneous GVHD, *Blood* **2004**, *103*, 740-742.

[275] C. E. Orsello, D. A. Lauffenburger, D. A. Hammer, Molecular properties in cell adhesion: a physical and engineering perspective, *Trends in Biotechnology* **2001**, *19*, 310-316.

[276] R. F. Thorne, J. W. Legg, C. M. Isacke, The role of the CD44 transmembrane and cytoplasmic domains in co-ordinating adhesive and signalling events, *Journal of Cell Science* **2004**, *117*, 373-380.

[277] B. P. Toole, Hyaluronan: from extracellular glue to pericellular cue, *Nat Rev Cancer* **2004**, *4*, 528-539.

[278] R. Tammi, D. MacCallum, V. C. Hascall, J. P. Pienimaki, M. Hyttinen, M. Tammi, Hyaluronan bound to CD44 on keratinocytes is displaced by hyaluronan decasaccharides and not hexasaccharides, *The Journal of Biological Chemistry* **1998**, *273*, 28878-28888.

[279] D. Liu, M. S. Sy, A cysteine residue located in the transmembrane domain of CD44 is important in binding of CD44 to hyaluronic acid, *The Journal of Experimental Medicine* **1996**, *183*, 1987-1994.

[280] C. B. Underhill, The interaction of hyaluronate with the cell surface: the hyaluronate receptor and the core protein, *Ciba Foundation symposium* **1989**, *143*, 87-99.

[281] B. P. Toole, Hyaluronan-CD44 Interactions in Cancer: Paradoxes and Possibilities, *Clinical Cancer Research* **2009**, *15*, 7462-7468.

[282] V. V. Glinsky, G. V. Glinsky, O. V. Glinskii, V. H. Huxley, J. R. Turk, V. V. Mossine, S. L. Deutscher, K. J. Pienta, T. P. Quinn, Intravascular metastatic cancer cell homotypic aggregation at the sites of primary attachment to the endothelium, *Cancer Research* **2003**, *63*, 3805-3811.

[283] S. Legras, J. P. Levesque, R. Charrad, K. Morimoto, C. LeBousse, D. Clay, C. Jasmin, F. SmadjaJoffe, CD44-mediated adhesiveness of human hematopoietic progenitors to hyaluronan is modulated by cytokines, *Blood* **1997**, *89*, 1905-1914.

[284] G. S. Kansas, Selectins and their ligands: Current concepts and controversies, *Blood* **1996**, *88*, 3259-3287.

[285] A. Wilson, E. Laurenti, G. Oser, R. C. van der Wath, W. Blanco-Bose, M. Jaworski, S. Offner, C. F. Dunant, L. Eshkind, E. Bockamp, P. Lio, H. R. Macdonald, A. Trumpp, Hematopoietic stem cells reversibly switch from dormancy to self-renewal during homeostasis and repair, *Cell* **2008**, *135*, 1118-1129.

[286] L. J. Bendall, K. F. Bradstock, D. J. Gottlieb, Expression of CD44 variant exons in acute myeloid leukemia is more common and more complex than that observed in normal blood, bone marrow or CD34+ cells, *Leukemia* **2000**, *14*, 1239-1246.

[287] M. Mohamadzadeh, H. DeGrendele, H. Arizpe, P. Estess, M. Siegelman, Proinflammatory stimuli regulate endothelial hyaluronan expression and CD44/HA-dependent primary adhesion, *Journal of Clinical Investigation* **1998**, *101*, 97-108.

[288] K. Fuchs, A. Hippe, A. Schmaus, B. Homey, J. P. Sleeman, V. Orian-Rousseau, Opposing effects of high- and low-molecular weight hyaluronan on CXCL12-induced CXCR4 signaling depend on CD44, *Cell Death & Disease* **2013**, *4*.

[289] P. Wuchter, C. Leinweber, R. Saffrich, M. Hanke, V. Eckstein, A. Ho, M. Grunze, A. Rosenhahn, Plerixafor induces the rapid and transient release of stromal cell-derived factor-1 alpha from human mesenchymal stromal cells and influences the migration behavior of human hematopoietic progenitor cells, *Cell and Tissue Research* **2013**, 1-12.

[290] J. F. DiPersio, E. A. Stadtmauer, A. Nademanee, I. N. Micallef, P. J. Stiff, J. L. Kaufman, R. T. Maziarz, C. Hosing, S. Fruehauf, M. Horwitz, D. Cooper, G. Bridger, G. Calandra, Plerixafor and G-CSF versus placebo and G-CSF to mobilize hematopoietic stem cells for autologous stem cell transplantation in patients with multiple myeloma, *Blood* **2009**, *113*, 5720-5726.

[291] N. Flomenberg, S. M. Devine, J. F. Dipersio, J. L. Liesveld, J. M. McCarty, S. D. Rowley, D. H. Vesole, K. Badel, G. Calandra, The use of AMD3100 plus G-CSF for autologous hematopoietic progenitor cell mobilization is superior to G-CSF alone, *Blood* **2005**, *106*, 1867-1874.

[292] S. Fruehauf, M. R. Veldwijk, T. Seeger, M. Schubert, S. Laufs, J. Topaly, P. Wuchter, F. Dillmann, V. Eckstein, F. Wenz, H. Goldschmidt, A. D. Ho, G. Calandra, A combination of granulocyte-colony-stimulating factor (G-CSF) and plerixafor mobilizes more primitive peripheral blood progenitor cells than G-CSF alone: results of a European phase II study, *Cytotherapy* **2009**, *11*, 992-1001.

[293] M. Vallet-Regí, F. Balas, D. Arcos, Mesoporous Materials for Drug Delivery, *Angewandte Chemie International Edition* **2007**, *46*, 7548-7558.

[294] E. J. Anglin, L. Cheng, W. R. Freeman, M. J. Sailor, Porous silicon in drug delivery devices and materials, *Advanced Drug Delivery Reviews* **2008**, *60*, 1266-1277.

[295] J. Liu, B. Lukose, O. Shekhah, H. K. Arslan, P. Weidler, H. Gliemann, S. Braese, S. Grosjean, A. Godt, X. Feng, K. Muellen, I.-B. Magdau, T. Heine, C. Woell, A novel series of isoreticular metal organic frameworks: realizing metastable structures by liquid phase epitaxy, *Scientific Reports* **2012**, *2*.

[296] M. Hanke, H. K. Arslan, S. Bauer, O. Zybaylo, C. Christophis, H. Gliemann, A. Rosenhahn, C. Wöll, The Biocompatibility of Metal–Organic Framework Coatings: An Investigation on the Stability of SURMOFs with Regard to Water and Selected Cell Culture Media, *Langmuir* **2012**, *28*, 6877-6884.

[297] K. L. Prime, G. M. Whitesides, Adsorption of proteins onto surfaces containing end-attached oligo(ethylene oxide) - a model system using self-assembled monolayers, *Journal of the American Chemical Society* **1993**, *115*, 10714-10721.

[298] J. I. Garrels, B. R. Franza, The REF52 Protein Database - Methods of Database Construction and Analysis using the Quest System and Characterizations of Protein-Patterns from Proliferating and Quiescent REF52 Cells, *Journal of Biological Chemistry* **1989**, *264*, 5283-5298.

[299] E. A. Cavalcanti-Adam, T. Volberg, A. Micoulet, H. Kessler, B. Geiger, J. P. Spatz, Cell spreading and focal adhesion dynamics are regulated by spacing of integrin ligands, *Biophysical Journal* **2007**, *92*, 2964-2974.

[300] L. K. Ista, H. Fan, O. Baca, G. P. Lopez, Attachment of bacteria to model solid surfaces: oligo(ethylene glycol) surfaces inhibit bacterial attachment, *FEMS Microbiology Letters* **1996**, *142*, 59-63.

[301] L. K. Ista, S. Mendez, G. P. Lopez, Attachment and detachment of bacteria on surfaces with tunable and switchable wettability, *Biofouling* **2010**, *26*, 111-118.

[302] M. P. Arpa-Sancet, C. Christophis, A. Rosenhahn, Microfluidic Assay to Quantify the Adhesion of Marine Bacteria, *Biointerphases* **2012**, *7*, 1-9.

[303] J. T. Trevors, C. M. Cotter, Copper toxicity and uptake in microorganisms, *Journal of Industrial Microbiology* **1990**, *6*, 77-84.

[304] M. P. Arpa Sancet, M. Hanke, Z. Wang, S. Bauer, C. Azucena, H. Arslan, M. Heinle, H. Gliemann, C. Woll, A. Rosenhahn, Surface anchored metal-organic frameworks as stimulus responsive antifouling coatings, *Biointerphases* **2013**, *8*, 29.

[305] C. Shea, L. J. Lovelace, H. E. Smithsomerville, Deleya maria as a model organism for studies of bacterial colonisation and biofilm formation, *Journal of Industrial Microbiology* **1995**, *15*, 290-296.

[306] L. Baumann, R. D. Bowditch, P. Baumann, Description of Deleya gen. nov. Created to Accommodate the Marine Species Alcaligenes aestus, A. pacificus, A. cupidus, A. venustus, and Pseudomonas marina, *International Journal of Systematic Bacteriology* **1983**, *33*, 793-802.

[307] J. Kim, R. C. Hayward, Mimicking dynamic in vivo environments with stimuli-responsive materials for cell culture, *Trends in Biotechnology* **2012**, *30*, 426-439.

[308] M. Ravi, P. V, K. Sr, A. E, S. F. D. Paul, 3D Cell Culture Systems - Advantages and Applications, *Journal of Cellular Physiology* **2014**, n/a-n/a.

[309] K. A. Cychosz, A. J. Matzger, Water Stability of Microporous Coordination Polymers and the Adsorption of Pharmaceuticals from Water, *Langmuir* **2010**, *26*, 17198-17202.

[310] M. Tsotsalas, J. Liu, B. Tettmann, S. Grosjean, A. Shahnas, Z. Wang, C. Azucena, M. Addicoat, T. Heine, J. Lahann, J. Overhage, S. Bräse, H. Gliemann, C. Wöll, Fabrication of Highly Uniform Gel Coatings by the Conversion of Surface-Anchored Metal–Organic Frameworks, *Journal of the American Chemical Society* **2013**, *136*, 8-11.

[311] M. W. Johnson, Porous stent drug delivery system, Scimed Life Systems Inc. (Minnesota), USA, **1999**, patent no. US5972027 (A)

[312] D. Meschede, *Gerthsen Physik*, 24. ed., **2010**.

[313] D. Brkić, Review of explicit approximations to the Colebrook relation for flow friction, *Journal of Petroleum Science and Engineering* **2011**, *77*, 34-48.

[314] S. E. Haaland, Simple and Explicit Formulas for the Friction Factor in Turbulent Pipe Flow, *Journal of Fluids Engineering* **1983**, *105*, 89-90.

[315] M. O. Lacort, *Descriptive and Inferential Statistics - Summaries of Theory and Excersises solved*, **2004**.

[316] H. Dohner, E. H. Estey, S. Amadori, F. R. Appelbaum, T. Buchner, A. K. Burnett, H. Dombret, P. Fenaux, D. Grimwade, R. A. Larson, F. Lo-Coco, T. Naoe, D. Niederwieser, G. J. Ossenkoppele, M. A. Sanz, J. Sierra, M. S. Tallman, B. Lowenberg, C. D. Bloomfield, Diagnosis and management of acute myeloid leukemia in adults: recommendations from an international expert panel, on behalf of the European LeukemiaNet, *Blood* **2010**, *115*, 453-474.

[317] J. M. Foran, New prognostic markers in acute myeloid leukemia: perspective from the clinic, *Hematology ASH Education Program* **2010**, 47.

[318] R. G. Greenler, Infrared Study of Adsorbed Molecules on Metal Surfaces by Reflection Techniques, *The Journal of Chemical Physics* **1966**, *44*, 310-315.

[319] F. M. Hoffmann, Infrared reflection-absorption spectroscopy of adsorbed molecules, *Surface Science Reports* **1983**, *3*, 107-192.

[320] S. Nagarkar, G. A. Williams, Comparative techniques to quantify cyanobacteria dominated epilithic biofilms on tropical rocky shores, *Marine Ecology-Progress Series* **1997**, *154*, 281-291.

[321] T. Nishino, E. Ikemoto, K. Kogure, Application of Atomic Force Microscopy to Observation of Marine Bacteria, *Journal of Oceanography* **2004**, *60*, 219-225.

[322] M. Berney, F. Hammes, F. Bosshard, H. U. Weilenmann, T. Egli, Assessment and interpretation of bacterial viability by using the LIVE/DEAD BacLight Kit in combination with flow cytometry, *Applied Environmental Microbiology* **2007**, *73*, 3283-3290.

[323] L. Boulos, M. Prevost, B. Barbeau, J. Coallier, R. Desjardins, LIVE/DEAD BacLight : application of a new rapid staining method for direct enumeration of viable and total bacteria in drinking water, *Journal of Microbiological Methods* **1999**, *37*, 77-86.

7.5 ABBREVIATIONS

AFM	Atomic force microscope
AML	Acute myeloid leukaemia
a.u.	Arbitrary units
BE	Backscattered electrons
BM	Bone marrow
BP	Band Pass Filter
CB	(umbilical) Cord blood
CD44	Cluster of differentiation 44
CD44s	Standard isoform of CD44
CD44v	Variant isoform of CD44
DM	Dichroic Mirror
ECM	Extra cellular matrix
FACS	Fluorescence activated cell sorting
FSC	Forward Scatter
GAG	Glycosaminoglycan
HA	Hyaluronic Acid
HSCT	Haematopoietic stem cell transplantation
HPC	Haematopoietic progenitor cell
ICP OES	Plasma optical emission spectrometry
IRMOF	isoreticular metal-organic framework
LP	Long Pass Filter
LSC	Leukemic Stem Cell
MNC	Mononuclear cell
MOF	Metal-organic framework
mPB	Mobilised peripheral blood
MSC	Mesenchymal stromal cell

NOD/SCID	Non-obese diabetic/severe combined immunodeficiency
PB	Peripheral blood
Ph	Phase contrast
Pi	Propidium iodide
SAM	Self-assembled monolayer
SD	Standard deviation
SE	Secondary electron
SEM	Scanning electron microscope
SSC	Side Scatter
SP	Short Pass Filter
SURMOF	Surface anchored metal-organic framework
XPS	X-ray photoelectron spectroscopy
XRD	X-ray diffraction

7.6 CHEMICALS & REAGENTS

Abbreviation	*Full name*	*Details*	*Company*
Alkanethiols			
DDT	Dodecane-1-thiol	$HS-(CH_2)_{11}-CH_3$	Prochimia, Sopot, Poland
HDT	16-Hexadecanethiol	$HS-(CH_2)_{15}-CH_3$	Sigma-Aldrich, Munich, Germany
HUDT	11-mercapto-1-undecanthiol	$HS-(CH_2)_{11}-OH$	Prochimia, Sopot, Poland
MHDA	Mercaptohexadecanoic acid	$HS-(CH_2)_{15}-COOH$	Sigma-Aldrich, Munich, Germany
Chemical Reagents			
AA	Alginic acid sodium salt from brown algae	Kat. No. 05550	Sigma-Aldrich, Munich, Germany
APTMS	3-Aminopropyltrimethoxy-silane	$H_2N(CH_2)_3Si(OCH_3)_3$	Sigma-Aldrich, Munich, Germany
bdc	benzene-1,4-bicarboxylic acid; terephthalic acid	Kat. No. 185361	Sigma-Aldrich, Munich, Germany
btc	benzene-1,3,5-tricarboxylic acid	Kat. No. 482749	Sigma-Aldrich, Munich, Germany
$Cu(II)Ac_2 \cdot 2H_2O$	Copper(II)acetate	$Cu(CH_3COO)_2 \cdot 2H_2O$	Sigma-Aldrich, Munich, Germany
EDC	*N*-(3-dimethylaminopropyl) -*N'*-ethylcarbodiimide hydrochloride	$C_8H_{17}N_3$ HCl	Sigma-Aldrich, Munich, Germany
HA	Hyaluronic acid sodium salt from *streptococcus equii*	Kat. No. 53747 ($M = 1{,}63 \cdot 10^6$ Da)	Sigma-Aldrich, Munich, Germany
HS	Heparan sulphate		Sigma-Aldrich, Munich, Germany
KS	Keratan sulphate		Sigma-Aldrich, Munich, Germany
NHS	N-Hydroxysuccinimide	$C_4H_5NO_3$	Sigma-Aldrich, Munich, Germany

Abbreviation	*Full name*	*Details*	*Company*
Solvents			
AcOH	Acetic acid 99.9 %	$C_2H_4O_2$	Merck, Darmstadt, Germany
EtOH	Ethanol absolute 99.9 %	C_2H_5OH	Sigma-Aldrich, Munich, Germany
i-Propanol	2-Propanol 99.9 %	C_3H_7OH	Sigma-Aldrich, Munich, Germany
2% Extran	30 % alkaline Extran, diluted with MilliQ® water	Aqueous detergent	Merck KGaA, Darmstadt ,Germany
HEPES	4-(2-Hydroxyethyl)piperazine-1-ethanesulfonic acid	$C_8H_{18}N_2O_4S$	Sigma-Aldrich, Munich, Germany
Milli-Q water	Deionized water filtered by a MilliQ® plus filter system	H_2O	Millipore, Schwalbach, Germany
PBS	Phosphate buffered saline pH 7.4 (Tablets dissolved in MilliQ® water)	Kat. No. 18912	Invitrogen, Karlsruhe, Germany
Proteins, Cell Culture Reagents and Antibodies			
	BacLight$^{\text{TM}}$ bacterial viability kit	Kat. No. L7007	Invitrogen, Karlsruhe, Germany
BD Pharm Lyse	Lysing buffer	Kat. No. 555899	Becton Dickinson, Heidelberg, Germany
BSA	Bovine serum albumin	Kat. No. A7030	Sigma-Aldrich, Munich, Germany
BU52	Monoclonal anti-CD44 antibody, clone BU52, mouse anti human	Kat. No. MCA2504	AbD Serotec, Düsseldorf, Germany
BU52-FITC	Fluorescein isothiocyanate-marked monoclonal anti-CD44 antibody, clone BU52, mouse anti human	Kat. No. MCA2504F	AbD Serotec, Düsseldorf, Germany
CD44pan siRNA	5’-CTGAAATTAGGGCCCAATT-3’; 5’-AATGGTGCATTTGGTGAAC-3’; 5’-CAGAAACTCCAGACCAGTT-3’	Kat. No. SI00012775; SI03037419; SI03062661	Qiagen, Hilden, Germany
CD44v3 siRNA	5’-TGAAGATGAAAGAGACAGA-3’; 5’-AGGCATTGATGATGATGAA-3’		Qiagen, Hilden, Germany

Abbreviation	*Full name*	*Details*	*Company*
CD44v6 siRNA	5’-GGATATC GCCAAACACCCA-3’;5’-AGTAGTACAACGGAAGAAA-3’		Qiagen, Hilden, Germany
Control siRNA	5’-UAAUGUAUUGGAACGCAUAUU-3’; 5’-AGGUAGUGUAAUCGCCUUGUU-3’; 5’-UGCGCUAGGCCUCGGUUGCUU-3’		Eurofins MWG GmbH, Ebersberg, Germany
DMEM	Dulbecco’s Modified Eagle Medium, high glucose	Kat. No. 10938	Invitrogen, Karlsruhe, Germany
FCS	Fetal calf serum also fetal bovine serum	Kat. No. 10270	Invitrogen, Karlsruhe, Germany
fibrinogen	Fibrinogen from bovine plasma Type I-S, 65-85 % protein	Kat. No. F8630	Sigma-Aldrich, Munich, Germany
Ficoll-Hypaque	Biocoll Separation Solution		Biochrom, Berlin, Germany/Merck, Darmstadt, Germany
Flt-3L	Fms-like tyrosine kinase-3 Ligand	Kat. No. 308-FK	R&D Systems, Wiesbaden-Nordenstadt, Germany
G-CSF	Granulocyte-Colony Stimulating Factor	Kat. No. 17-5483	PAA Laboratories GmbH, Pasching, Austria
Hoechst 33342	2’-(4-Ethoxyphenyl)-5-(4-methyl-1-piperazinyl)-2,5’-bi-1*H*-benzimidazole trihydrochloride	Kat. No. B2261	Sigma-Aldrich, Munich, Germany
---	L-glutamine	Kat. No. 25030	Invitrogen, Karlsruhe, Germany
Lipofectamin 2000	Transfection reagent	Kat. No. 11668	Life technologies, Carlsbad, California, USA
LTBMC	Long-Term Bone Marrow Culture	self-mixed medium	University of Heidelberg
PenStrep	Penicillin/streptomycin	Kat. No. 15140	Invitrogen, Karlsruhe, Germany

Abbreviation	*Full name*	*Details*	*Company*
PFA	Paraformaldehyde	$HO(CH_2O)_nH$	Sigma-Aldrich, Munich, Germany
Abbreviation	Full name	Details	Company
RPMI	Roswell Park Memorial Institute Media 1640	Kat. No. 31870	Invitrogen, Karlsruhe, Germany
SCF	Stem cell factor		PAA Laboratories GmbH, Pasching, Austria
STAR	Goat anti mouse IgG (h/l):FITC (multi species adsorbed)	Kat. No. STAR117F	AbD Serotec, Düsseldorf, Germany
Stemline™ II medium	Stemline™ II Haematopoietic Cell Expansion Medium	Kat. No. S0192	Sigma-Aldrich, Munich, Germany
TPO	Thrombopoetin		PAA Laboratories GmbH, Pasching, Austria
Trypsin/ EDTA	0.05 % Trypsin–EDTA solution	Kat. No. 25300	Invitrogen, Karlsruhe, Germany

7.7 MATERIALS

Name	*Description*	*Company*
Au	99.99 % pure gold	Chempur, Karlsruhe, Germany
Nexterion®	Ultra flat polished, clean room float glass	Schott AG, Mainz, Germany
COOH- PS-beads	Carboxylate terminated polystyrene microspheres, 4.5 µm	Polysciences, Eppelheim, Germany
PDMS	poly-dimethoxysiloxane, elastomer and curing agent Sylgard 184	Dow Corning, MI, USA
EasyFlasks™	tissue culture flasks 25 cm^2, 75 cm²	Nunc, Langenselbold, Germany
Pattex	Powerkleber Repair Extreme	Henkel, Düsseldorf, Germany
Gas Metering Valve	back regulated precision gas pressure valve	Pressluft Götz, Mannheim, Germany
Heating Cable	Teflon covered and metal meshwork protected 3 mm wire	Fritz-Schwarz GmbH, Schwabach, Germany
Medium Reservoir	screw cap, GL 45, 4 port and DURAN® -pressure plus	Schott, Mainz, Germany
Luer Lock Adapter	Upchurch LuerTight (P-836 & P-836)	IDEX Health & Science LLC, Oak Harbor, USA
Multifold	Upchurch 7-Port (P-150)	IDEX Health & Science LLC, Oak Harbor, USA
Selection Valve	Valco Cheminert C25-3186	VICI AG, Schenkoon, Switzerland
Silicon wafers for HA referencing	Silicon wafer [100] p-doped with boron	CrysTec, Germany
Silicon wafers for MOF preparation	Silicon wafer	Wacker Chemie AG, Germany
PFA tubing	1/16 ” OD, 0.04 ” ID	VICI AG, Schenkoon, Switzerland
Pump-Syringe	60 mL Luer Lock, silicon rubber stamp	Becton Dickinson, Heidelberg, Germany
T-connector	2-way and 3-way Luer Lock connection	Neolab, Heidelberg, Germany

7.8 FINANCIAL SUPPORT

This work was supported by the Sander Stiftung (D10051281).

7.9 SUPPLEMENTARY CD

This CD contains the supplementary video material as well as digital versions of the papers published connected to this work.

7.10 LIST OF PUBLICATIONS RELATED TO THIS WORK

Conference Contributions

M. Hanke, M. Alles, M. P. Arpa Sancet, C. Christophis, M. Grunze, A. Rosenhahn. Microfluidics in Biofouling and Life Sciences, ***Poster**, Bunsenmeeting,* Heidelberg, Germany, **2011**

M. Hanke, C. Christophis, I. Taubert, A.D. Ho, M. Grunze, A. Rosenhahn. Shear Stress induced Rolling of CD44 expressing Leukaemic Cells, ***Poster**, Cellular Nanosciences*, Heidelberg, Germany, **2011**

M. Hanke, C. Christophis, N. Baran, I. Taubert, P. Wuchter, A.D. Ho, A. Rosenhahn. Microfluidic Adhesion Assay Reveals Catch Bond Activated CD44-Hyaluron Interaction in Leukemic Cells, ***Poster**, Microfluidics,* EMBL Heidelberg, Germany, **2012**

M. Hanke, C. Christophis, C. Leinweber, N. Baran, I. Taubert, P. Wuchter, A.D. Ho, A. Rosenhahn. Microfluidic Adhesion Assay Reveals Catch Bond Activated CD44-Hyaluron Interaction in Leukemic Cells, ***Poster**, Bunsentagung,* Leipzig, Germany, **2012**

M. Hanke, C. Christophis, I. Taubert, S. Maleschijski, N. Baran, P. Wuchter, A.D. Ho, A. Rosenhahn. Microfluidic Adhesion Assay Reveals Catch Bond Activated CD44-Hyaluron Interaction in Leukemic Cells, ***Poster**, American Vacuum Society,* Tampa, Florida, USA, **2012**

M. Hanke, I. Hoffmann, C. Christophis, N. Baran, P. Wuchter, A.D. Ho, A. Rosenhahn. When Stem Cells Roll: A Microfluidic Analysis of the Catch Bond Mediated Interaction between CD44 and Hyaluronic Acid, ***Talk**, Bunsentagung,* Karlsruhe, Germany, **2013**

Published articles

The articles listed here can be found as digital version on the supplementary CD (page 201).

M. Hanke, H. K. Arslan, S. Bauer, O. Zybaylo, C. Christophis, H. Gliemann, A. Rosenhahn, C. Wöll, The Biocompatibility of Metal–Organic Framework Coatings: An Investigation on the Stability of SURMOFs with Regard to Water and Selected Cell Culture Media, *Langmuir* **2012**, *28*, 6877-6884.

C. Christophis, E. Cavalcanti-Adam, **M. Hanke**, K. Kitamura, A. Gruverman, M. Grunze, P. Dowben, A. Rosenhahn, Adherent cells avoid polarization gradients on periodically poled LiTaO3 ferroelectrics, *Biointerphases* **2013**, *8*, 27.

P. Wuchter, C. Leinweber, R. Saffrich, **M. Hanke**, V. Eckstein, A. Ho, M. Grunze, A. Rosenhahn, Plerixafor® induces the rapid and transient release of stromal cell-derived factor-1 alpha from human mesenchymal stromal cells and influences the migration behavior of human haematopoietic progenitor cells, *Cell and Tissue Research* **2013**, 1-12.

M. Arpa Sancet**†**, **M. Hanke†**, Z. Wang, S. Bauer, C. Azucena, H. Arslan, M. Heinle, H. Gliemann, C. Woll, A. Rosenhahn, Surface anchored metal-organic frameworks as stimulus responsive antifouling coatings, *Biointerphases* **2013**, *8*, 29.

M. Hanke, I. Hoffmann, C. Christophis, M. Schubert, V. T. Hoang, A. Zepeda-Moreno, N. Baran, V. Eckstein, P. Wuchter, A. Rosenhahn, A. D. Ho, Differences between healthy haematopoietic progenitors and leukemia cells with respect to CD44 mediated rolling versus adherence behavior on hyaluronic acid coated surfaces, *Biomaterials* **2014**, *35*, 1411-1419.

† indicates a shared first authorship

Articles in preparation

M. Hanke, K. Fuchs, S. Maleschlijski, J. Sleeman, V. Orian-Rousseau, A. Rosenhahn, CD44 mediates the Flow Induced Rolling of HepG2 Epithelial Cancer Cells on Hyaluronan, *in preparation*

DANKSAGUNG

Zumindest der praktische Teil der Arbeit ist erst einmal geschafft und nun ich möchte mich bei allen bedanken, die daran mitgewirkt haben.

Besonders bedanken möchte ich mich bei Prof. Axel Rosenhahn für die Aufnahme in die Arbeitsgruppe und seine Unterstützung während der gesamten Promotion. Vielen Dank für die Möglichkeit an einem solch interessanten, interdisziplinären Projekt mitwirken zu dürfen. Danke außerdem für die Hilfestellungen, die Motivation und die Korrektur der Publikationen und natürlich auch dieser Arbeit.

Bei Prof. Joachim P. Spatz danke ich mich herzlich für die Übernahme des Zweitgutachtens.

Mein großer Dank gilt außerdem Prof. Anthony D. Ho und Dr. Patrick Wuchter für die freundliche Aufnahme in der Med. V des Universitätsklinikums Heidelberg und für die gute Zusammenarbeit im Rahmen unseres Projekts. Danke für die Hilfestellungen und Anregungen bezüglich der Zielgestaltung und die kompetente Unterstützung bei deren Erreichen.

Auch Prof. Christof Wöll und Dr. Hartmut Gliemann danke ich ganz herzlich, nicht nur für die freundliche Aufnahme am Institut für funktionelle Grenzflächen am KIT, sondern auch für Möglichkeit bei einem so spannenden Projekt mitwirken zu dürfen. Danke für die interessanten und zielführenden Gespräche sowie die Unterstützung beim Schreiben der Publikationen.

Besonders bedanken möchte ich mich auch bei Dr. Christof Christophis und bei Dr. Isabel Hoffmann, die mir als meine „Postdocs“ während der Arbeit mit Rat und Tat zur Seite standen. Danke euch beiden für die tolle Zusammenarbeit. Ich habe von euch viel gelernt und hatte dabei noch mehr Spaß!

An dieser Stelle möchte ich mich bei all denjenigen Kooperationspartnern bedanken, die ich noch nicht genannt habe. Dankbar bin ich nicht nur für die vielfältigen Projekte an denen ich teilhaben durfte, sondern auch für die fachlich kompetente und freundliche Unterstützung die mir dabei von allen Seiten zuteilwurde. Ich bedanke mich ganz herzlich bei…

…Dr. Véronique Orian-Rousseau, Dr. Katharina Fuchs (ITG, KIT), Prof. Jonathan Sleeman (Universität Heidelberg und ITG, KIT) für die Zusammenarbeit am HepG2Iso Projekt.

…Dr. Hasan K. Arslan, Zhengbang Wang, Marita Heinle, Dr. Carlos Azucena und Olexandra Zybaylo (IFG, KIT), sowie Dr. Maria Pilar Arpa Sancet (ehemals AK Rosenhahn) und Stella Bauer danke ich für die Zusammenarbeit am SURMOF 2 Projekt.

…Dr. Elisabetta Ada Cavalcanti-Adam (Max-Planck-Institut für Intelligente Systeme, Stuttgart), Prof. Kenji Kitamura (National Institute for Materials Science, Japan), Dr. Alexei Gruverman, Prof. Peter A. Dowben (University of Nebraska-Lincoln, USA) und Prof. Michael Grunze (Angewandte Physikalische Chemie, Universität Heidelberg) für die Zusammenarbeit an den Lithiumtantalaten.

…Dr. Christina Leinweber (ehemals AK Rosenhahn), Dr. Rainer Saffrich, Dr. Volker Eckstein (Universitätsklinikum Heidelberg) und Prof. Michael Grunze (Angewandte Physikalische Chemie, Universität Heidelberg für die Zusammenarbeit am Plerixafor/MSC Projekt.

…Dr. Mario Schubert, Dr. Van T. Hoang, Natalia Baran, Volker Eckstein (Universitätsklinikum Heidelberg) und Dr. Abraham Zepeda-Moreno (Child and Youth Cancer Research Institute, Mexico) für die Zusammenarbeit am CD44-Hyaluronsäure Interaktionsprojekt.

Prof. Joachim P. Spatz, Dr. Véronique Orian-Rousseau und Dr. Cornelia Lee-Thedieck danke ich ganz herzlich für die Großzügigkeit die Zellkultureinrichtungen mitbenutzen zu dürfen.

Ein großes Dankeschön auch an Angela Lenze, Katrin Barth-Miesala und Karina Borowski für das Isolieren und das Sortieren der HPC, der leukämischen Blasten und der Leukozyten. Danke sowohl euch als auch Van und natürlich Isabel dafür, dass ich mich in meiner „zweiten Gruppe“ immer willkommen gefühlt habe und ich lernen durfte, dass man in einem Krankenhaus auch Spaß haben kann.

Für das Korrekturlesen bedanke ich mich bei Maria, Stella, Isabel und Stojan. Danke dafür, dass ihr mir die Bäume gezeigt habt wenn ich sie vor lauter Wald nicht mehr sehen konnte.

Stella bei dir möchte ich mich für die angenehme Zeit im Labor bedanken. Gerade bei den Zuckerslideaktionen hat man gemerkt: Zu zweit geht es nicht nur schneller es ist auch noch witziger!

Stojan bei dir möchte ich mich für nicht nur für die vielen hilfreichen Diskussion und Hinweise, sondern vor allem auch für die Dönertouren, die Pausen und generell die gute Zeit bedanken.

Isabel, dir danke ich nicht nur dafür, dass du mir diese Gruppe vorgeschlagen und mich während des Studiums und der Promotion tatkräftig unterstützt hast, sondern vor allem für die Freundschaft, die hoffentlich nicht abreißt wenn wir mit Arbeiten beschäftigt sind.

Bei der ganzen Gruppe möchte ich mich für die tolle Zeit bedanken. Ich danke euch für die Motivation und die Unterstützung, die Tipps und die Tricks, die Kaffeepausen und die Kuchen, das Grillfleisch und die Grillbananen, die Spaziergänge und die Dönertouren, den Klatsch und den Tratsch, schlicht für dreieinhalb tolle Jahre die ich nicht missen möchte.

Ganz besonders danke ich meiner Familie. Danke, dass ihr immer an mich geglaubt und mich unterstützt habt. Ihr wart mir wirklich eine Stütze und eine große Hilfe auf dem Weg hierher!

I thank my entire family for always believing in me. You were a real support and a big help on the journey to the PhD defence.

Thank you, Grandi and Granddad, for being a real inspiration for me.

Dir, Ilona, danke ich für die Geduld und die Unterstützung die du mir während des Studiums und der Promotion entgegengebracht hast. Danke auch dafür, dass du mir unsere süße, kleine Prinzessin (unser kleines, dickes Stinkerchen) Marlene geschenkt hast. Danke euch beiden, dass ihr mich immer wieder zum Lachen bringt! Ich liebe euch!

Eidesstattliche Versicherung gemäß § 8 der Promotionsordnung der Naturwissenschaftlich-Mathematischen Gesamtfakultät der Universität Heidelberg

1. Bei der eingereichten Dissertation zu dem Thema

How Stem Cells Roll: A Microfluidic Characterisation of the
CD44-Hyaluronic Acid Interaction and its Role in Leukaemia

handelt es sich um meine eigenständig erbrachte Leistung.

2. Ich habe nur die angegebenen Quellen und Hilfsmittel benutzt und mich keiner unzulässigen Hilfe Dritter bedient. Insbesondere habe ich wörtlich oder sinngemäß aus anderen Werken übernommene Inhalte als solche kenntlich gemacht.

3. Die Arbeit oder Teile davon habe ich ~~wie folgt~~/bislang nicht[1] an einer Hochschule des In- oder Auslands als Bestandteil einer Prüfungs- oder Qualifikationsleistung vorgelegt.

Titel der Arbeit:______________________________

Hochschule und Jahr:______________________________

Art der Prüfungs- oder Qualifikationsleistung:____________________

4. Die Richtigkeit der vorstehenden Erklärungen bestätige ich.

5. Die Bedeutung der eidesstattlichen Versicherung und die strafrechtlichen Folgen einer unrichtigen oder unvollständigen eidesstattlichen Versicherung sind mir bekannt.

Ich versichere an Eides statt, dass ich nach bestem Wissen die reine Wahrheit erklärt und nichts verschwiegen habe.

Wiesloch, 13.9.2014

Ort und Datum   Unterschrift

---

[1] Nicht Zutreffendes streichen. Bei Bejahung sind anzugeben: der Titel der andernorts vorgelegten Arbeit, die Hochschule, das Jahr der Vorlage und die Art der Prüfungs- oder Qualifikationsleistung.